COPPE
Instituto Alberto Luiz Coimbra de Pós-Graduação e Pesquisa de Engenharia
UFRJ

MODELING OF SUSPENSION POLYMERIZATIONS IN CONTINUOUS OSCILLATORY BAFFLED REACTORS

Jonildo dos Santos Silva

Tese de Doutorado apresentada ao Programa de Pós-graduação em Engenharia Química, COPPE, da Universidade Federal do Rio de Janeiro, como parte dos requisitos necessários à obtenção do título de Doutor em Engenharia Química.

Orientadores: José Carlos Costa da Silva Pinto
Príamo Albuquerque Melo Jr.

Rio de Janeiro
Março de 2024

MODELING OF SUSPENSION POLYMERIZATIONS IN CONTINUOUS OSCILLATORY BAFFLED REACTORS

Jonildo dos Santos Silva

TESE SUBMETIDA AO CORPO DOCENTE DO INSTITUTO ALBERTO LUIZ COIMBRA DE PÓS-GRADUAÇÃO E PESQUISA DE ENGENHARIA DA UNIVERSIDADE FEDERAL DO RIO DE JANEIRO COMO PARTE DOS REQUISITOS NECESSÁRIOS PARA A OBTENÇÃO DO GRAU DE DOUTOR EM CIÊNCIAS EM ENGENHARIA QUÍMICA.

Orientadores: José Carlos Costa da Silva Pinto
Príamo Albuquerque Melo Jr.

Aprovada por: Prof. José Carlos Costa da Silva Pinto
Prof. Príamo Albuquerque Melo Jr.
Prof. Marcio Nele de Souza
Prof. Reinaldo Giudici
Dr. Normando José Castro de Jesus

RIO DE JANEIRO, RJ – BRASIL
MARÇO DE 2024

dos Santos Silva, Jonildo

Modeling of Suspension Polymerizations in Continuous Oscillatory Baffled Reactors/Jonildo dos Santos Silva. – Rio de Janeiro: UFRJ/COPPE, 2024.

XIV, 248 p.: il.; 29, 7cm.

Orientadores: José Carlos Costa da Silva Pinto
Príamo Albuquerque Melo Jr.

Tese (doutorado) – UFRJ/COPPE/Programa de Engenharia Química, 2024.

1. Polimerização. 2. Suspensão. 3. COBR. I. Carlos Costa da Silva Pinto, José *et al.* II. Universidade Federal do Rio de Janeiro, COPPE, Programa de Engenharia Química. III. Título.

Acknowledgements

It has been a long journey! In fact, the seed that originated this Thesis was planted in my mind over 20 years ago. I don't remember exactly who said to me that a person would have to study over twenty years (from kindergarten to graduate school) to obtain a doctorate, but from that moment afterward, I spent hours daydreaming about getting it. I am very grateful that the Lord put many great and helpful people along my path. First of all, I would like to thank the support I received from Dad and Mom throughout these long years I've been away from home. I am also very thankful to my elder brother, Junior, and his family for giving me all kinds of support. Professor Frede Carvalho, a very wise man, also played a role in this by encouraging me to come to Rio de Janeiro. I really enjoy his good advices.

I would like to thank Mary for being nice and making my day better every time she came around and asked how I was doing. I will never forget your kindness. Lucas was also a very helpful friend and gave me hours of support to keep my workstation operating. From the technical side, I want to thank R. Marinho for providing support and valuable data that served as a basis for writing Chapter 2 of this Thesis. A special thanks goes to my advisors, Zé Carlos and Príamo. For me, both represent the epitome of stoicism. Your support, patience, and warm-heartedness were crucial for developing this work. I will always be indebted to you.

Finally, and most importantly, I thank the Lord for putting very nice people on my way. All of you will be in my prayers. As I sit down and finish writing this document, my eyes are wet with tears of gratitude. A huge thanks to all of you!

This study was financed in part by the Coordenação de Aperfeiçoamento de Pessoal de Nível Superior – Brasil (CAPES) – Finance Code 001.

Resumo da Tese apresentada à COPPE/UFRJ como parte dos requisitos necessários para a obtenção do grau de Doutor em Ciências (D.Sc.)

MODELAGEM DE POLIMERIZAÇÕES EM SUSPENSÃO EM REATORES OSCILATÓRIOS COMPARTIMENTADOS CONTÍNUOS

Jonildo dos Santos Silva

Março/2024

Orientadores: José Carlos Costa da Silva Pinto
Príamo Albuquerque Melo Jr.

Programa: Engenharia Química

Processos de polimerização em suspensão são utilizados para produzir polímeros de importância comercial como, por exemplo, poli(cloreto de vinila), poli(acetato de vinila), poli(metacrilato de metila) e poliestireno. Apesar da importância econômica desses polímeros, tanques agitados de elevado volume operando em batelada são utilizados industrialmente nos processos de produção atuais. No entanto, processos em batelada possuem desvantagens em comparação aos processos contínuos. Por exemplo, a produtividade é prejudicada devido ao tempo ocioso de enchimento, evacuação e limpeza. Por outro lado, reatores tubulares podem ser operados continuamente; a razão área/volume é elevada, facilitando o controle de temperatura; e o volume reacional é menor, ocasionando menores riscos de operação. Dadas as vantagens da produção contínua em reatores tubulares, este trabalho objetiva o desenvolvimento de modelos fenomenológicos de polimerização em suspensão em Reatores Oscilatórios Compartimentados Contínuos. Mais especificamente, uma representação completa da cinética, transferência de calor e distribuição de tamanhos de partículas é desenvolvida na tentativa de facilitar o desenvolvimento de processos industriais de produção de polímeros em suspensão em modo contínuo.

Abstract of Thesis presented to COPPE/UFRJ as a partial fulfillment of the requirements for the degree of Doctor of Science (D.Sc.)

MODELING OF SUSPENSION POLYMERIZATIONS IN CONTINUOUS OSCILLATORY BAFFLED REACTORS

Jonildo dos Santos Silva

March/2024

Advisors: José Carlos Costa da Silva Pinto
Príamo Albuquerque Melo Jr.

Department: Chemical Engineering

Suspension polymerization is the process utilized to produce commercially important polymers such as poly(vinyl chloride), poly(vinyl acetate), poly(methyl methacrylate) and polystyrene. In spite of the economic importance of these polymers, large stirred tank reactors operating in batch mode are employed in the current industrial production processes. However, batch processes show many disadvantages in comparison to continuous ones. For instance, the productivity is impaired due to the idle time during filling, evacuation and cleaning. On the other hand, tubular reactors can be operated continuously; the area-to-volume ratio is larger, which improves temperature control, and the equipment size is usually smaller, minimizing operational risks. Given the advantages of continuous production in tubular reactors, this work aims at developing comprehensive phenomenological models to represent suspension polymerizations in Continuous Oscillatory Baffled Reactors (COBR). More specifically, a complete representation of the kinetics, heat transfer and particle size distributions in these systems is pursued in an attempt to bridge the gap that currently exists between laboratory scale and industrial scale production of suspension polymers in continuous mode.

Contents

List of Figures **x**

List of Tables **xiv**

1 Introduction **1**

1.1 Batch *versus* Continuous Processing 2

1.2 Thesis Organization 6

1.3 References 7

2 The Current Batch Suspension Polymerization Process: An Industrial Example **10**

2.1 Introduction 11

2.2 Literature Review 14

2.2.1 PVC Polymerization Modeling 14

2.2.2 Population Balance Modeling 19

2.3 Model Development 23

2.3.1 Kinetic Model 23

2.3.2 Equilibrium Relationships 23

2.3.3 Mass Balances 26

2.3.4 Moment Equations 26

2.3.5 Reaction Rates 28

2.3.6 Polymer Properties 31

2.3.7 Population Balance Model 33

2.3.8 Initial Condition 37

2.4 Results and Discussion 37

2.4.1 Estimation of Kinetic Parameters 37

2.4.2 Estimation of Breakage and Coalescence Parameters 41

2.4.3 Effect of Process Variables 46

2.4.4 Evolution of Mean Particle and Droplet Diameters 47

2.5 Concluding Remarks 49

2.6 References 52

3 Literature Review and Theoretical Foundations 63
3.1 Continuous Suspension Polymerization . . . 64
3.2 Oscillatory Baffled Reactors . . . 66
3.2.1 Oscillatory Flow Mixing . . . 69
3.2.2 Heat Transfer . . . 82
3.2.3 Power Dissipation . . . 87
3.2.4 Droplet Size Distribution . . . 92
3.2.5 Scale-up . . . 95
3.2.6 Applications of OBRs to Suspension Polymerization . . . 98
3.3 Concluding Remarks . . . 104
3.4 References . . . 105

4 Poly(vinyl acetate) Suspension Polymerization in an Oscillatory Baffled Reactor 117
4.1 Model Development . . . 118
4.1.1 Kinetic Model . . . 119
4.1.2 Mass Balances . . . 121
4.1.3 Moment Balances . . . 123
4.1.4 Energy Balances . . . 126
4.1.5 Dimensionless Groups . . . 128
4.1.6 Heat Transfer . . . 129
4.1.7 Regulatory Control . . . 133
4.2 Literature Data . . . 136
4.3 Results and Discussion . . . 138
4.3.1 Effect of Backflow and Number of Tanks . . . 138
4.3.2 Fitting Experimental Data . . . 143
4.3.3 Effect of Initiator Type . . . 145
4.3.4 Effect of Oscillation Velocity . . . 152
4.4 Concluding Remarks . . . 152
4.5 References . . . 156

5 Poly(vinyl chloride) Suspension Polymerization in an Oscillatory Baffled Reactor 162
5.1 Model Development . . . 163
5.1.1 Kinetic Model . . . 163
5.1.2 Equilibrium Calculations . . . 164
5.1.3 Mass Balances . . . 166
5.1.4 Moment Balances . . . 169
5.1.5 Energy Balances . . . 171
5.1.6 Reaction Rates . . . 173

5.1.7 Dimensionless Groups . . . 176
5.1.8 Heat Transfer . . . 178
5.1.9 Regulatory Control . . . 181
5.2 Results and Discussion . . . 184
5.2.1 Effect of Backflow and Number of Tanks . . . 184
5.2.2 Effect of Residence Time . . . 188
5.2.3 Effect of Initiator Type . . . 195
5.2.4 Effect of Oscillation Velocity . . . 198
5.3 Concluding Remarks . . . 198
5.4 References . . . 203

6 Droplet and Particle Size Distributions in an Oscillatory Baffled Reactor: Population Balance Model 210
6.1 Model Development . . . 211
6.1.1 Distributed Population Balance Model . . . 211
6.1.2 Breakage and Coalescence Rates . . . 213
6.1.3 Power Dissipation . . . 215
6.1.4 Daughter Droplet Distribution . . . 215
6.1.5 Mean Diameters . . . 216
6.1.6 Initial Condition . . . 217
6.2 Results and Discussion . . . 217
6.2.1 Breakage and Coalescence Parameters . . . 217
6.2.2 Effect of Power Dissipation . . . 220
6.2.3 Effect of Dispersed Phase Fraction . . . 223
6.2.4 Effect of Suspending Agent Flow Rate . . . 225
6.3 Concluding Remarks . . . 226
6.4 References . . . 227

7 Conclusions 231

A Demonstration of the Moment Equations 233
A.1 Living Polymer Balances . . . 234
A.2 Dead Polymer Balances . . . 236

B Output Flow Rate: Vinyl Acetate Polymerization 242

C Output Flow Rate: Vinyl Chloride Polymerization 245

List of Figures

1.1 Advantages of implementing Process Intensification (Al Azri *et al.*, 2022). 3
1.2 Schematic representation of a continuous oscillatory baffled reactor (McGlone *et al.*, 2015). 4
1.3 Effect of the flow regime on the polymer properties (Reis *et al.*, 2019). 5

2.1 Reactors utilized to carry out suspension polymerization. From early technology (a) to more recent (d) (Saeki and Emura, 2002). 12
2.2 PVC production flowsheet (Carroll *et al.*, 2017). 13
2.3 Reactor pressure and monomer conversion obtained experimentally and predicted by the proposed model. (A) F1, (B) F2 and (C) F3. Gray and orange shadowed areas represent the ranges of $x \leq x_f$ and $x > x_f$, respectively. 39
2.4 Values of VK obtained experimentally and predicted by the proposed model. (A) F1, (B) F2 and (C) F3. Gray and orange shadowed areas represent the ranges of $x \leq x_f$ and $x > x_f$, respectively. 39
2.5 Variation of suspension properties in F1. 40
2.6 Polymerization rate and heat released in the three industrial grade formulations. 40
2.7 Experimental and simulated final cumulative particle size distributions obtained with parameters shown in Table 2.7. 42
2.8 Breakage rate constant ($\eta_c = 5 \times 10^{-4}$ Pa s, $\rho_d = 840$ kg m^{-3}, $\sigma = 4.0 \times 10^{-3}$ N m^{-1}) for different dispersed phase volume fractions calculated with parameter set PS1. 44
2.9 Coalescence rate constant ($\eta_c = 5 \times 10^{-4}$ Pa s, $\rho_d = 840$ kg m^{-3}, $\sigma = 4.0 \times 10^{-3}$ N m^{-1}) for different dispersed phase volume fractions calculated with parameter set PS1. 45
2.10 Coalescence rate constant ($\eta_c = 5 \times 10^{-4}$ Pa s, $\rho_d = 840$ kg m^{-3}, $\sigma = 4.0 \times 10^{-3}$ N m^{-1}) for different dispersed phase volume fractions calculated with parameter set PS2. 45

2.11 Experimental and simulated sieve data with the parameters in Table 2.7. 46
2.12 Effect of impeller rotation and PVA concentration on particle size distribution in F1, (A) and (B), respectively. Effect of impeller rotation and PVA concentration on particle size distribution in F2, (C) and (D), respectively. 47
2.13 Evolution of Sauter mean diameter of the droplets . Effect of impeller rotation and PVA concentration in F1, (A) and (B), respectively. Effect of impeller rotation and PVA concentration in F2, (C) and (D), respectively. Pink, gray and orange shadowed areas represent the ranges of conversion $x \leq 30\%$, $30 < x \leq x_f$ and $x > x_f$, respectively. . 48
2.14 Evolution of Sauter mean diameter of the particles . Effect of impeller rotation and PVA concentration in F1, (A) and (B), respectively. Effect of impeller rotation and PVA concentration in F2, (C) and (D), respectively. Pink, gray and orange shadowed areas represent the ranges of conversion $x \leq 30\%$, $30 < x \leq x_f$ and $x > x_f$, respectively. . 48

3.1 Baffle types commonly used. A) from González-Juárez *et al.* (2018), B,C) from González-Juárez *et al.* (2017), D) from Solano *et al.* (2012), E) from Ahmed *et al.* (2018a), F) from Lobry *et al.* (2013), G,H) from McDonough *et al.* (2015), and I) from Ahmed *et al.* (2018b). 68
3.2 Eddies formation mechanism (Jian and Ni, 2005). 68
3.3 Experimental apparatus used by Mackley and Ni (1993). 74
3.4 Experimental apparatus used by Ni and Pereira (2000). 76
3.5 Different geometries investigated by Zhang *et al.* (2022). 81
3.6 Experimental apparatus used by Lobry *et al.* (2015) to perform liquid-liquid dispersions. 103
3.7 Experimental apparatus used by Lobry *et al.* (2015) to perform suspension polymerization reactions. 103

4.1 Tanks-in-series with backflow representation of the COBR. 118
4.2 Cross section view of the reactor and jacket. 130
4.3 Conversion data at the outlet stream (A) and along the reactor length (B) (Lobry *et al.*, 2015; Lobry, 2012). 137
4.4 Effect of k on dynamic conversion profile at the reactor outlet. 138
4.5 Effect of k on the steady state temperature profile. 139
4.6 Effect of $F_{b,n}$ on dynamic conversion profile at the reactor outlet. . . . 140
4.7 Effect of $F_{b,n}$ on the steady state temperature profile. 140

4.8 Effect of $F_{b,n}$ on dynamic conversion profile at the reactor outlet. Controlled temperatures located at intermediate positions in zones 1 and 2. 141
4.9 Effect of $F_{b,n}$ on the steady state temperature profile. Controlled temperatures located at intermediate positions in zones 1 and 2. . . . 142
4.10 Calculated and experimental conversion values. 143
4.11 Steady state model predictions for Mn (left axis) and Mw (right axis) values in Exp. 1 (solid line) and Exp. 2 (dashed line). 144
4.12 Simulated reactor (A,C) and jacket temperatures (B,D) in Exp. 1 (A,B) and Exp. 2 (C,D). 145
4.13 Effect of initiator type on dynamic conversion profile at the reactor outlet. 146
4.14 Effect of initiator type on the steady state conversion profile. 147
4.15 Effect of initiator type on the steady state reactor temperature profile. 147
4.16 Controlled temperature in each zone. 148
4.17 Jacket inlet temperature. 149
4.18 Heat generation profile in the simulation performed with DIBP. . . . 150
4.19 Heat generation profile in the simulation performed with DIBP and two initiator feed points. 151
4.20 Comparison between steady state profiles in simulations performed with single initiator and two initiator feeds. A) Conversion, B) Reactor temperature, C) Number average molar mass, and D) Initiator. 151
4.21 Effect of $\chi_o f_o$ on the reactor side Nusselt number and heat transfer coefficients. 153

5.1 Effect of k on dynamic conversion profile at the reactor outlet. . . . 185
5.2 Effect k on the steady state temperature profile. 186
5.3 Effect of $F_{b,n}$ on dynamic conversion profile at the reactor outlet. . . 187
5.4 Effect of $F_{b,n}$ on the steady state temperature profile. 188
5.5 Effect of residence time on dynamic conversion profile at the reactor outlet. 189
5.6 Effect of residence time on the steady state initiator amount profile. 189
5.7 Effect of residence time on the steady state conversion profile. 190
5.8 Effect of residence time on the steady state K-Value profile. 191
5.9 Effect of residence time on the steady state weight average molar mass profile. 191
5.10 Steady state polymerization rate profile simulated with different residence times. 193

5.11 Spatial-temporal evolution of the polymerization rates in the simulation performed with residence time of 3 h. 193
5.12 Spatial-temporal evolution of the polymerization rates in the simulation performed with residence time of 1 h. 194
5.13 Steady state volume fractions of the phases that compose the organic phase. 194
5.14 Effect of initiator type on the reaction performance. A) conversion, B) K-Value, C) initiator, and D) weight average molar mass. 195
5.15 Effect of initiator feed strategy on the reaction performance. A) conversion, B) reactor temperature, C) initiator, and D) weight average molar mass. 197
5.16 Steady state polymerization rates simulated with different initiator feed strategies. 197
5.17 Effect of oscillation velocities on the heat transfer coefficients ($Re = 100$). 199
5.18 Effect of oscillation velocities on the heat transfer coefficients ($Re = 50$). 200

6.1 Schematic representation of the droplets and particles in the COBR. 212
6.2 Predicted Sauter mean diameter by different correlations. 218
6.3 Breakage rate constant evaluated at different droplet diameters and dispersed phase fractions. 219
6.4 Coalescence rate constant evaluated at different droplet diameters and dispersed phase fractions. 220
6.5 Steady state conversion profile. 221
6.6 Dynamic droplet size distribution at the reactor outlet. 221
6.7 Steady state droplet size distribution along the reactor length. . . . 222
6.8 Effect of the power dissipation. A) particle size cumulative distribution function, B) particle size probability density function, C) steady state Sauter mean diameter of the particles, and D) steady state Sauter mean diameter of the droplets. 223
6.9 Effect of the dispersed phase fraction. A) particle size cumulative distribution function B), particle size probability density function, C) steady state Sauter mean diameter of the particles, and D) steady state Sauter mean diameter of the droplets. 224
6.10 Effect of the suspending agent concentration. A) particle size cumulative distribution function B), particle size probability density function, C) steady state Sauter mean diameter of the particles, and D) steady state Sauter mean diameter of the droplets. 225

List of Tables

2.1 Kinetic mechanism (Yuan *et al.*, 1991). 23
2.2 Equilibrium calculations at the different reaction stages. 25
2.3 Additional constitutive relationships and parameters. 32
2.4 Data used for parameter estimation. 33
2.5 Parameters in the initiator decomposition rate constant [1]. 33
2.6 Search region and estimated parameters. 38
2.7 Search region and estimated parameters in the breakage and coalescence rate equations. 42

4.1 Kinetic model used to represent the polymerization of vinyl acetate (Teymour, 1989). 119
4.2 Kinetic rate constants used to perform the simulations. 120
4.3 Suspension properties (poly(vinyl acetate)/vinyl acetate/water system). 134
4.4 Additional constitutive relationships and parameters (poly(vinyl acetate)/vinyl acetate/water system). 135
4.5 Experimental conditions (Lobry *et al.*, 2015; Lobry, 2012). 137

5.1 Equilibrium calculations at the different reaction stages in poly(vinyl chloride) polymerization. 165
5.2 Suspension properties (poly(vinyl chloride)/vinyl chloride/water system). 182
5.3 Additional constitutive relationships and parameters (poly(vinyl chloride)/vinyl chloride/water system). 183

6.1 Some mean droplet size correlations. 218

A.1 Free radical polymerization mechanism. 233
A.2 Auxiliary table[1], $\kappa = 0$. 237
A.3 Auxiliary table, $\kappa = 1$ 238
A.4 Auxiliary table, $\kappa = 2$. 240

Chapter 1

Introduction

"Now go; I will help you speak and will teach you what to say."

Exodus 4:12

In this introductory chapter, an overview of the motivations and the contextualization of this work are summarized in a concise manner. Additionally, the way that the work is organized is presented for the sake of didactics and, eventually, to serve as a guide to the reader who wants to skip specific parts of this Thesis. It is also worth mentioning that one of the key points of this chapter is to establish a connection between Process Intensification (PI) strategies and the modeling approaches that will be developed in the upcoming chapters emphasizing their relevance and putting the scope of this Thesis in perspective. Caution must be paid to the fact that an in-depth description of PI methods is out of the scope of this work. For this purpose, the interested reader can consult some of the references listed in Section 1.3.

1.1 Batch *versus* Continuous Processing

The subject of batch vs. continuous processing has been on debate for many years (Englund, 1982; Goršek and Glavič, 1997; Calabrese and Pissavini, 2011; Chen, 2017). In the past decades, this topic has gained more attention as it is being addressed within a broader discipline/area of chemical engineering called Process Intensification (PI) (Al Azri *et al.*, 2022). More specifically, PI is a term coined by Colin Ramshaw in the 1970s at Imperial Chemical Industries referring to "the strategy of reducing the size of chemical plant needed to achieve a given production objective" (Cross and Ramshaw, 1986). Over time, the definition of PI has evolved as recently reviewed by Keil (2018). One of the most concise definitions is due to Stankiewicz and Moulijn (2000):

> *Process intensification consists of the development of novel apparatuses and techniques that, compared to those commonly used today, are expected to bring dramatic improvements in manufacturing and processing, substantially decreasing equipment- size/production-capacity ratio, energy consumption, or waste production, and ultimately resulting in cheaper, sustainable technologies.* (Stankiewicz and Moulijn, 2000)

Generally speaking, according to the concept presented, there is no doubt that moving from batch to continuous operation can be beneficial. Figure 1.1 illustrates some of the advantages of continuous processing in comparison to batch operation. First of all, continuous reactors are smaller (Rossetti and Compagnoni, 2016), as a result, the safety of operation is improved since dealing with smaller inventories becomes safer (Baldea *et al.*, 2017). Secondly, the operational costs are reduced and the productivity is increased (McMillin *et al.*, 2020). For instance, one of the greatest barriers towards maximizing profits in industrial suspension polymerization plants is related to the idle time due to filling, evacuation and cleaning (Ilare and Sponchioni, 2020). Lastly, but not least important, the variability of final properties from batch to batch can be mitigated (Rogers and Jensen, 2019).

The safety appeal is particularly true if hazardous chemicals are used as reactants (Ilare and Sponchioni, 2020). For instance, monomers such as vinyl chloride, vinyl acetate and styrene used as raw materials to produce suspension polymers show harmful effects to the human health (Nelson *et al.*, 2011). Additionally, the azo compounds used as initiator systems also add operational risks due to their high reactivity which can cause explosions (Liu *et al.*, 2015). Moreover, polymerization

reactions are exothermic, consequently, failure to remove the heat released by the reaction from the system can cause the so called runaway (Ilare and Sponchioni, 2020).

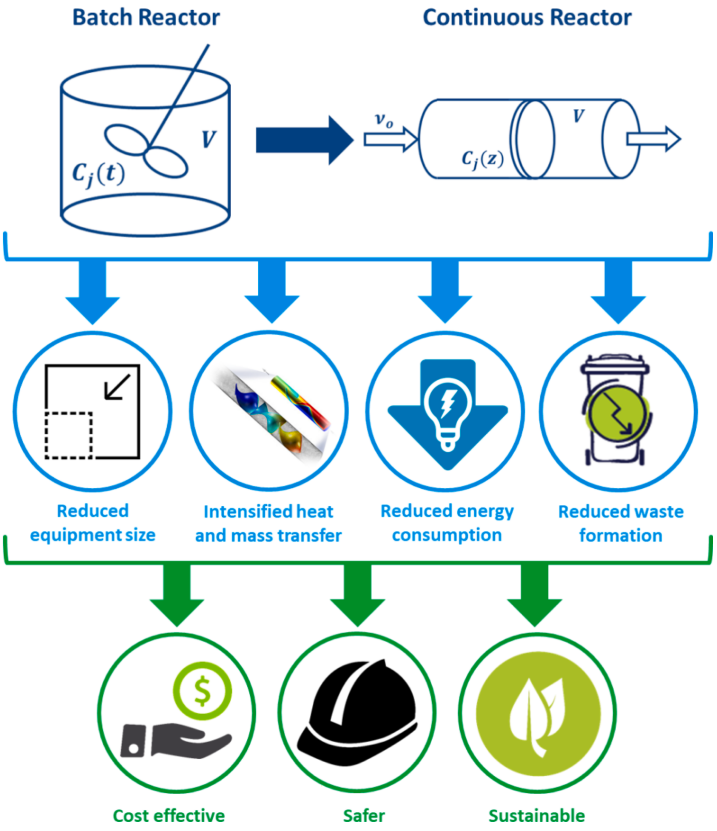

Figure 1.1: Advantages of implementing Process Intensification (Al Azri *et al.*, 2022).

Substituting batch processes by continuous ones constitutes a PI method (Florit *et al.*, 2020). In this context, the Continuous Oscillatory Baffled Reactor (COBR) has gaining increasing attention in the last decades as a way to move from batch to continuous operation. Figure 1.2 shows a schematic representation of this device. The COBR is essentially a tubular reactor equipped with equally spaced baffles (Smith and Mackley, 2006; Jian and Ni, 2005). Differently from standard tubular reactors, it presents two superimposed flow components, namely a net flow and an oscillatory flow (Stonestreet and Harvey, 2002). The net flow component is provided by a pump whereas the oscillatory flow component can be provided by a piston, bellow or diaphragm (Jian and Ni, 2005). By superimposing an oscillatory flow component, the result is the creation of vortices in the volume spaces located between consecutive baffles providing more intense mixing. Consequently, these volume spaces located between baffles can be regarded as small stirred tanks connected

in series (Dickens *et al.*, 1989). As a result, this reactor can achieve plug flow regime at net flow laminar conditions (Harvey *et al.*, 2001). This design can significantly enhance heat and mass transfer rates in comparison to similar conventional tubular reactors (Ahmed *et al.*, 2018a; Ahmed *et al.*, 2018b). The ability to deal with solid formation also constitutes a competitive advantage of this reactor design (Slavnić *et al.*, 2019). For this reason, this technology is gaining attention in areas where plug flow regime and long reaction times are desired (Stonestreet and Harvey, 2002; Ni *et al.*, 2003). As an example, suspension polymerization processes might take advantage of these characteristics because it produces solid beads that should remain suspended in the liquid phase and also because it is usually desired that particle size distributions and particle properties be uniform at the outlet stream. Figure 1.3 illustrates qualitatively how the flow regime and residence time distribution affect the final polymer properties.

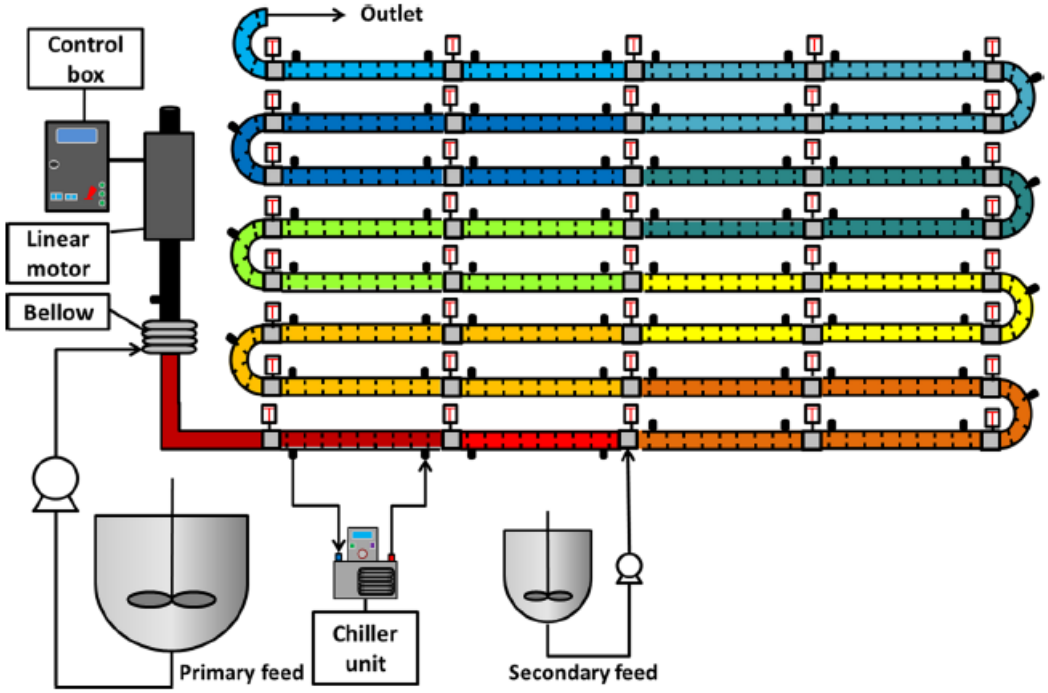

Figure 1.2: Schematic representation of a continuous oscillatory baffled reactor (McGlone *et al.*, 2015).

The previous paragraphs described the subject of batch to continuous transition in an utopian way. In other words, it was presumably assumed that there exists a continuous process whose performance at delivering products with identical final properties as those obtained in batch mode is readily available. However, as per Ilare and Sponchioni (2020) and Rossetti and Compagnoni (2016), there is still

a knowledge gap that must be filled in order to migrate from batch to continuous processing without loss on the desired final properties. Generally speaking, the size of this gap depends on the process under consideration and its nuances. Regarding suspension polymerizations, a full understanding of how continuous operation affects particle size distribution and molar mass distribution is of paramount importance in this undertaking.

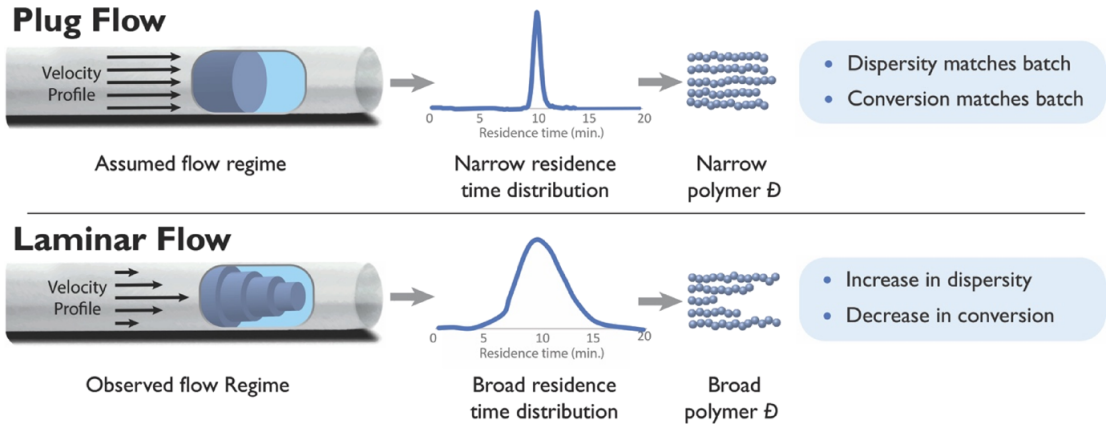

Figure 1.3: Effect of the flow regime on the polymer properties (Reis *et al.*, 2019).

The importance of model-based strategies have been recognized as a way of facilitating the development and implementation of PI strategies. For instance, Ouyang *et al.* (2022) proposed a general methodology, i.e., that can be applied to different processes, based on laboratory scale experiments, computational fluid dynamics simulations, optimization, process simulation, and assessment. In addition to the lower costs associated, process modeling allows the investigation and evaluation of different setups (Ilare and Sponchioni, 2020; Rossetti and Compagnoni, 2016).

Based on the previous paragraphs, the main contribution of this Thesis is the development of comprehensive phenomenological models to help the transition of suspension polymerizations from batch to continuous operation. More specifically, the goal is to understand how the continuous operation of Oscillatory Baffled Reactors affects the polymerization reaction. Furthermore, the models intend to give a thorough representation of the kinetics, heat transfer, polymer properties as well as particle size distributions. It is also expected that the modeling strategies developed here be used in the future for scale-up purposes. To achieve such goals, this work is organized as follows.

1.2 Thesis Organization

This Thesis is organized in seven chapters, including this short introduction. In Chapter 2, an overview of the current industrial batch process employed to produce suspension polymers is presented. More specifically, focus is given on the polymerization of vinyl chloride (the most important polymer produced by the suspension process). Several important concepts will be introduced in this chapter. Additionally, a comprehensive kinetic model will be developed and validated with industrial data. Furthermore, a population balance model will be implemented and solved using a discretization technique to describe the product particle/droplet size distributions obtained in three industrial grade formulations. Even though focus is given to the batch process, the Chapter 2 is important because of two main reasons. Firstly, a set of reliable kinetic parameters to represent the polymerization of vinyl chloride will be estimated and will be used to describe the polymerization of this monomer in a continuous oscillatory baffled reactor in Chapter 5. Secondly, the numerical strategy to solve the population balance will be extended in Chapter 6 to describe the particle/droplet size distributions in oscillatory baffled reactors.

In Chapter 3, a comprehensive literature review covering continuous suspension polymerizations and oscillatory baffled reactors is presented. This chapter is a turning point of this work since it marks the transition where, afterwards, full attention will be given to continuous suspension polymerization systems rather than batch processes. In this part of the work, emphasis is given on the challenges regarding suspension polymerization and the advances in oscillatory baffled reactor technology. One entire section of this chapter will be devoted to studies that attempted to carry out suspension polymerizations in these devices.

In Chapter 4, a mathematical model to represent the suspension polymerization of vinyl acetate in a COBR will be developed and the model predictions will be compared with available experimental data found in the literature. The model developed in Chapter 4, will be extended in Chapter 5 to represent vinyl chloride suspension polymerizations. Even though both reactions show similar kinetic mechanisms, the polymerization of vinyl chloride shows more complex heterogeneous phenomena due to the fact that poly(vinyl chloride) is insoluble in its monomer. Consequently, an additional phase is present. This is the main reason why these mathematical models are presented in different chapters.

In Chapter 6, the mathematical model presented in Chapter 5 will be further extended to describe the particle/droplet size distributions, a key aspect that can

not be disregarded in poly(vinyl chloride) suspension polymerization. A spatially distributed population balance model will be developed and solved to investigate the effects of key operational parameters on the final product size distributions.

Finally, in Chapter 7, the main conclusions of this Thesis are summarized in a concise manner. Additionally, some suggestions for future works are highlighted.

1.3 References

Al Azri, N.; Patel, R.; Ozbuyukkaya, G.; Kowall, C.; Cormack, G.; Proust, N.; Enick, R.; Veser, G. Batch-to-continuous transition in the specialty chemicals industry: impact of operational differences on the production of dispersants. Chemical Engineering Journal, 445, 136775, 2022.

Ahmed, S.M.R.; Law, R.; Phan, A.N.; Harvey, A.P. Thermal performance of meso-scale oscillatory baffled reactors. Chemical Engineering and Processing: Process Intensification, 132, 25-33, 2018a.

Ahmed, S.M.R.; Phan, A.N.; Harvey, A.P. Mass transfer enhancement as a function of oscillatory baffled reactor design. Chemical Engineering and Processing: Process Intensification, 130, 229-239, 2018b.

Baldea, M.; Edgar, T.F.; Stanley, B.L.; Kiss, A.A. Modular manufacturing processes: status, challenges, and opportunities. AIChE Journal, 63, 10, 4262-4272, 2017.

Calabrese, G.S.; Pissavini, S. From batch to continuous flow processing in chemicals manufacturing. AIChE Journal, 57, 4, 828-834, 2011.

Chen, S. Comparison of batch versus continuous process in the pharmaceutical industry based on safety consideration. Master Thesis, Texas A&M University, United States, May 2017.

Cross, W.T.; Ramshaw, C. Process intensification: laminar flow heat transfer. Chemical Engineering Research and Design, 64, 4, 293-301, 1986.

Dickens, A.W.; Mackley, M.R.; Williams, H.R. Experimental residence time distribution measurements for unsteady flow in baffled tubes. Chemical Engineering Science, 44, 7, 1471-1479, 1989.

Englund, S.M. Chemical processing - batch or continuous. Journal of Chemical Education, 59, 9, 766-768, 1982.

Florit, F.; Busini, V.; Rota, R. Kinetics-free process intensification: from semi-batch to series of continuous chemical reactors. Chemical Engineering and Processing: Process Intensification, 154, 108014, 2020.

Goršek, A.; Glavič, P. Design of batch versus continuous processes part I: single-purpose equipment. Trans IChemE, 75, Part A, 709-717, 1997.

Harvey, A.P.; Mackley, M.R.; Stonestreet, P. Operation and optimization of an oscillatory flow continuous reactor. Industrial and Engineering Chemistry Research, 40, 5371-5377, 2001.

Ilare, J.; Sponchioni, M. From batch to continuous free-radical polymerization: recent advances and hurdles along the industrial transfer. Advances in Chemical Engineering, 56, 1, 229-257, 2020.

Jian, H.; Ni, X. A numerical study on the scale-up behaviour in oscillatory baffled columns. Chemical Engineering Research and Design, 83, A10, 1163-1170, 2005.

Keil, F.J. Process intensification. Reviews in Chemical Engineering, 34, 2, 135-200, 2018.

Liu, S.H.; Shu, C.M.; Hou, H.Y. Applications of thermal hazard analyses on process safety assessments. Journal of Loss Prevention in the Process Industries, 33, 59-69, 2015.

McGlone, T.; Briggs, N.E.B.; Clark, C.A.; Brown, C.J.; Sefcik, J.; Florence, A.J. Oscillatory flow reactors (OFRs) for continuous manufacturing and crystallization. Organic Process Research and Development, 19, 1186-1202, 2015.

McMillin, R.E.; Luxon, A.R.; Ferri, J.K. Enabling intensification of multiphase chemical processes with additive manufacturing. Advances in Colloid and Interface Science, 285, 102294, 2020.

Nelson, C.P.; Patton, G.W.; Arvidson, K.; Lee, H.; Twaroski, M.L. Assessing the toxicity of polymeric food-contact substances. Food and Chemical Toxicology, 49, 1877-1897, 2011.

Ni, X.; Harvey, M.R.; Stonestreet, A.P.; Baird, M.H.I.; Rao, N.R. Mixing through oscillations and pulsations - a guide to achieve process enhancements in the chemical and process industries. Chemical Engineering Research and Design, 81, 3, 373-383, 2003.

Ouyang, Y.; Heynderickx, G.J.; Van Geem, K.M. Development of intensified reactors: a process intensification methodology perspective. Chemical Engineering and Processing - Process Intensification, 181, 109164, 2022.

Reis, M.H.; Leibfarth, F.A.; Pitet, L.M. Polymerizations in continuous flow: recent advances in the synthesis of diverse polymeric materials. ACS Macro Letters, 9, 123-133, 2020.

Rogers, L.; Jensen, K.F. Continuous manufacturing - the Green Chemistry promise?. Green Chemistry, 21, 3481-3498, 2019.

Rossetti, I.; Compagnoni, M. Chemical reaction engineering, process design, scale-up issues at the frontier of synthesis: flow chemistry. Chemical Engineering Journal, 296, 56-70, 2016.

Slavnić, D.; Bugarski, B.; Nikačević. Solids flow pattern in continuous oscillatory baffled reactor. Chemical Engineering and Processing - Process Intensification, 135, 108-119, 2019.

Smith, K.B.; Mackley, M.R. An experimental investigation into the scale-up of oscillatory flow mixing in baffled tubes. Chemical Engineering Research and Design, 84, A11, 1001-1011; 2006.

Stankiewicz, A.I.; Moulijn, J.A. Process intensification: transforming chemical engineering. Chemical Engineering Progress, 96, 2, 22-34, 2000.

Stonestreet, P.; Harvey, A.P. A mixing-based design methodology for continuous oscillatory flow reactors. Chemical Engineering Research and Design, 80, 1, 31-44, 2002.

Chapter 2

The Current Batch Suspension Polymerization Process: An Industrial Example

In this chapter, an overview of the current suspension polymerization process is given. More specifically, the key aspects of the industrial process are introduced in a concise way. Emphasis is given on the phenomena that occur in the reaction vessel, consequently, downstream and upstream processing/purification steps are not deeply discussed. Afterward, a mathematical model based on first principles is developed and validated with actual industrial data to comprehend the relationships between process variables and the specification of the final resins. To achieve this goal, firstly, a literature review on the previous works is performed and the current status of kinetic as well as population balance models applied to suspension polymerizations is assessed. Parts of this chapter have been published as "Silva *et al.* Modeling of particle size distributions in industrial poly(vinyl chloride) suspension polymerization reactors. Processes, 11, 5, 2023."

2.1 Introduction

Poly(vinyl chloride) (PVC) belongs to the group of the most important commercial plastic materials. It is surpassed only by poly(ethylene) (PE) and poly(propylene) (PP) in terms of worldwide production (Guo *et al.*, 2021). From an economic standpoint, the global PVC market is expected to grow at a compounded annual growth rate (CAGR) of 4.4% from 2022 to 2030 reaching 9.95 billion dollars (Precedence Research, 2023). Furthermore, the economic importance of PVC is linked to its numerous areas of application (Kanking *et al.*, 2021; Kwon *et al.*, 2021; Ekelund *et al.*, 2007; Islam *et al.*, 2018; Hakkarainen, 2003; Chiellini *et al.*, 2013). Mijangos *et al.* (2023) and Abreu *et al.* (2018) performed reviews on the current status of PVC production emphasizing the problems that still exist and the perspectives for the future.

Nearly 80% of the worldwide PVC production is achieved through suspension polymerization (Kiparissides and Pladis, 2022). At industrial level, large reaction vessels with volumes of order 200 m^3 are employed as shown in Figure 2.1. According to the suspension polymerization technique, the monomer and oil soluble initiators are dispersed in water (continuous phase) by proper agitation and suspending agents (Yuan *et al.*, 1991; Machado *et al.*, 2007; Pinto *et al.*, 2013). Afterward, the reaction starts when the temperature is increased until the desired value and the polymer chains are formed inside the dispersed monomer droplets (Yuan *et al.*, 1991; Machado *et al.*, 2007). Consequently, at the microscopic level, each monomer droplet behaves as a small bulk reactor (Machado *et al.*, 2007). Therefore, bulk and suspension polymerizations share closely akin kinetic features (Crosato-Arnaldi *et al.*, 1968).

The continuous aqueous phase has the task of improving heat transfer and reducing the viscosity of the suspension (Machado *et al.*, 2007). The level of agitation (Guo *et al.*, 2017; Marinho *et al.*, 2018) and surfactant type and concentration (Chatzi and Kiparissides, 1994; Lerner and Nemet, 1999) make the control of particle morphology possible, and it is one of the reasons why this technology is successfully widespread. Commercially, spherical polymer particles with characteristic diameters ranging from 50 to 500 μm are produced (Kiparissides, 1996). Furthermore, the particle porosity plays an important role in the final application of the resin, since it controls the rates of plasticizer adsorption and the interaction of the resin with the plasticizers, affecting the performances of processing stages and the final properties of PVC pieces (Darvish *et al.*, 2015). This explains the interest in the development of techniques to monitor the properties of the particles inside the reactor (Faria *et al.*, 2009a, 2009b, 2009c, 2010a, 2010b).

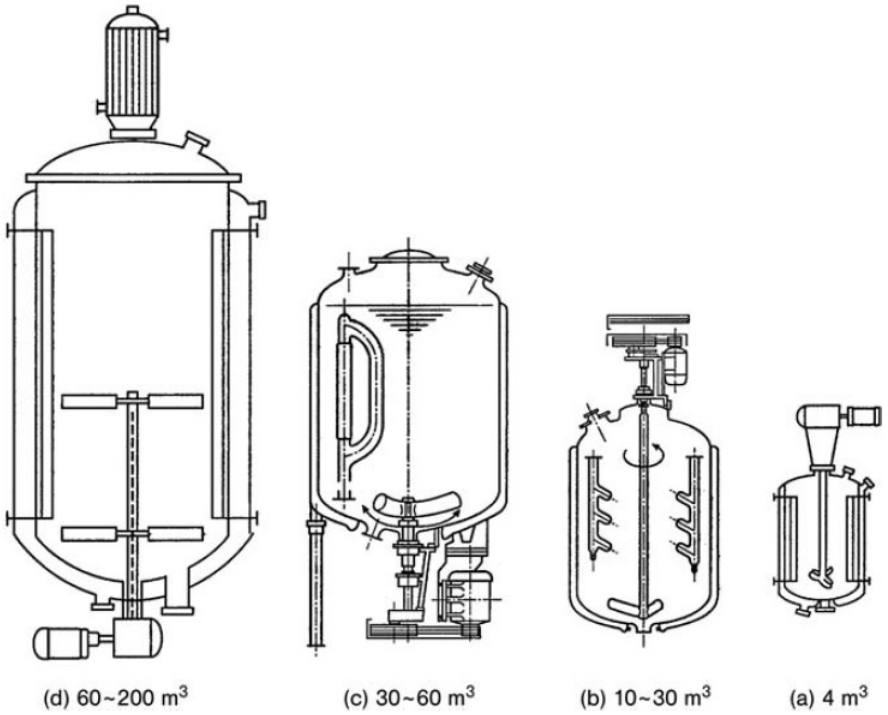

Figure 2.1: Reactors utilized to carry out suspension polymerization. From early technology (a) to more recent (d) (Saeki and Emura, 2002).

When dealing with batch systems, it is of paramount importance for the plant economics to reduce the batch time without compromising the final product specification. In this respect, decreasing batch time inevitably means increasing polymerization rate. However, this implies that a greater amount of heat must be removed from the system in a shorter period of time as the polymerization reaction is highly exothermic and a peak of heat generation is expected at higher conversion. Moreover, either increasing temperature or the amount of initiator brings concern about the final product specification (Kobayashi *et al.*, 1998). More specifically, higher temperature implies that polymer with lower molecular mass will be obtained due to the high values of chain transfer to monomer (Abdel-Alim and Hamielec, 1972). Furthermore, increasing the amount of initiator increases the profile of heat generation and excess residuals can prejudice the final resin properties (Saeki and Emura, 2002). In other words, heat removal constitutes a process constraint (Tacidelli *et al.*, 2009).

In order to circumvent the aforementioned problems, investigators have developed strategies to increase the process productivity guaranteeing the final product specification and safety constraints. For instance, Pinto and Giudici (2000) proposed a strategy based on optimizing a mixture fast and slow initiators to obtain uniform heat generation profiles. By doing so, these authors expected to improve

the operability of the cooling system. Additionally, Tacidelli *et al.* (2009) studied the possibility of increasing the temperature near the end of the reaction and the addition extra monomer during the polymerization. Bijhanmanesh and Etsami (2016) investigated the continuous addition of a fast initiator in order to decrease the batch time.

In Figure 2.2, a simplified representation of the steps in PVC polymerization is shown. The use of water to improve heat removal, introduces the necessity of wastewater treatment units which increase the number of equipments and operational costs associated (Saeki and Emura, 2002). The content of residual VCM in the PVC slurry also constitutes an issue of concern as safety standards require very low levels of unreacted monomer in the final resins. More specifically, VCM content below 1 ppm are permitted (Wypych, 2015). The stripping of residual VCM requires treating the slurry at elevated temperature and low pressure (Feldman *et al.*, 1980; Hughes, 1980). In recent plants, this process is performed in stripping towers (Wypych, 2015). After the removal of residual monomer, the water content is centrifuged off and the resin is dried.

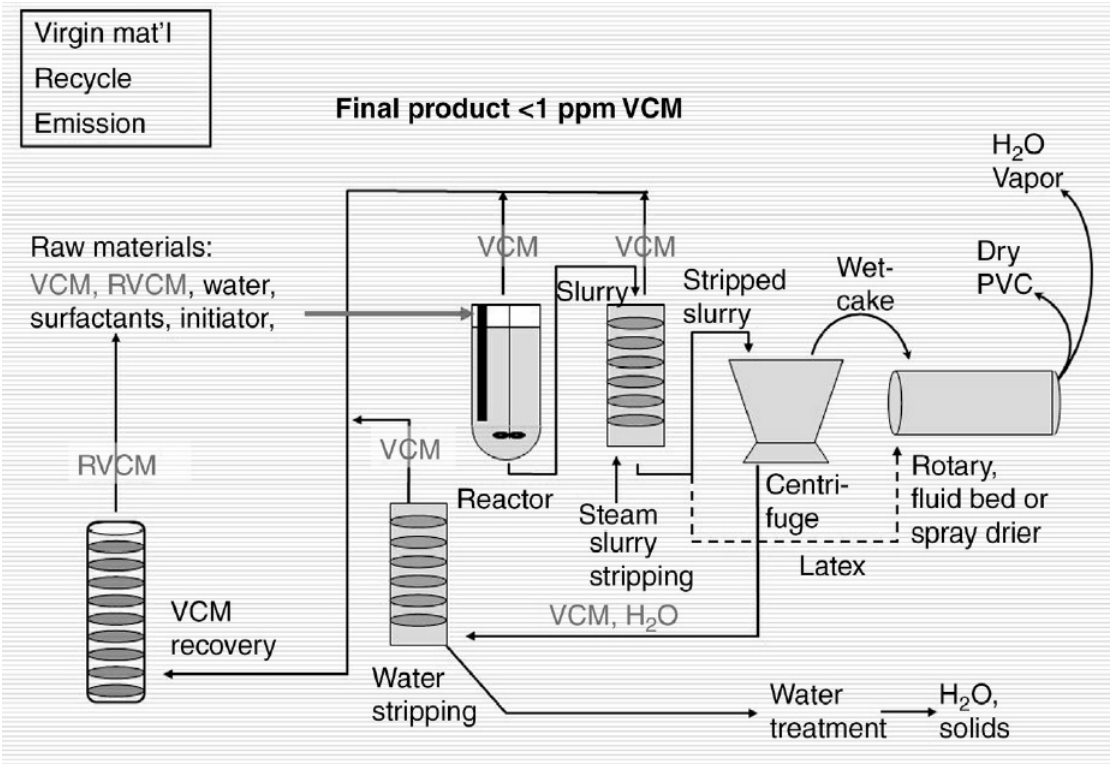

Figure 2.2: PVC production flowsheet (Carroll *et al.*, 2017).

2.2 Literature Review

Before addressing the proposed mathematical model development, a comprehensive literature review that covers the area of PVC polymerization modeling and population balances is provided. Regarding the population balances, the review focuses initially on some of the basic concepts, while afterward the subject is narrowed down to applications on suspension polymerizations.

2.2.1 PVC Polymerization Modeling

The literature related to modeling of PVC polymerization dates back to the 1960s. Firstly, Talamini (1966) investigated the bulk polymerization of vinyl chloride monomer (VCM) and proposed a currently classical two-phase model to describe the conversion of monomer. According to this two-phase model, the polymerization takes place in the concentrated phase (polymer-rich) and in the diluted phase (monomer-rich) at different rates. The reaction rate in the concentrated phase is higher due to the well-know gel effect that reduces the rates of termination of polymer radicals in the polymer particles. This model was able to predict experimental data accurately up to conversions of 30%.

Crosato-Arnaldi *et al.* (1968), following the work by Talamini (1966), studied bulk and suspension polymerizations of VCM using different initiators. These authors concluded that the autocatalytic behavior observed in VCM polymerization is due only to phase separation and does not depend on the type of initiator. It was observed that the equation employed to describe the overall conversion agreed accurately with available data up to conversions of 50-60%. However, beyond this value, the fit was not satisfactory. In spite of that, the authors did not provide a clear explanation to this fact. Additionally, it was shown that the kinetics of bulk and suspension polymerizations are equivalent. This was concluded based on the observation that the conversion curves of bulk and suspension polymerizations overlap when plotted against time multiplied by the square root of the initiator concentration. Data related to VCM polymerizations and reported in prior literature were fitted with fair accuracy by the developed model.

Abdel-Alim and Hamielec (1972) investigated the bulk polymerization of VCM with emphasis on average molar mass and molar mass distributions (MMD). These authors developed a model to predict conversion based on the model presented originally by Talamini (1966). In their model, the effects of volume change and

molecular diffusion on the kinetic constants were also considered. By doing so, the rate of propagation was assumed to be null near the glass transition point. Consequently, their model was able to accurately predict conversions in the range where the model proposed by Crosato-Arnaldi *et al.* (1968) was not able to.

Ugelstad *et al.* (1973) studied the bulk polymerizations of VCM. These investigators considered the possible effects of adsorption and desorption of radicals from the polymer-rich phase. Furthermore, based on experimental data, it was concluded that the model used to predict the conversion was more accurate than the one proposed by Crosato-Arnaldi *et al.* (1968). In fact, the new model was equivalent to the one proposed by Crosato-Arnaldi *et al.* (1968) only if two assumptions were made. Firstly, if the termination rate in the polymer-rich phase were lower than its counterpart in the monomer-rich phase, which was true according to available experimental data. Secondly, if the volume change during polymerization were neglected. In fact, during the development of the model equations used to predict the conversion, it was assumed that the volumes of the phases could vary with conversion, which is an aspect that can not be disregarded in bulk and, consequently, suspension VCM polymerizations.

Kuchanov and Bort (1973) performed a critical analysis of the previously published manuscripts and kinetic data regarding bulk and suspension VCM polymerizations. These authors emphasized that several authors made fundamental mistakes related to some of the assumptions used to derive the kinetic equations to explain the bulk and suspension polymerizations of VCM. One of the errors, according to these authors, was the use of homogeneous kinetic theory in an inherently heterogeneous reaction system. Additionally, these authors argued that Talamini's assumption (Talamini, 1966; Crosato-Arnaldi *et al.*, 1968) that the radical concentration in both phases present was independent of conversion could not be supported by available experimental data. Furthermore, the assumption that the radicals were not initiated inside the polymer particles was also criticized, as this assumption was inadmissible out the low conversion range.

Hamielec *et al.* (1982) focused on the effects of diffusion limitations on the kinetic constants of the reaction. These authors proposed a detailed kinetic mechanism to explain VCM polymerization and included parameters in the rate constants to account for the effects of diffusion limitations. According to these authors, it was well established that the termination rate decreased with conversion, resulting in increasing number of radicals, which explained the autocatalytic behavior noticed by previous investigators. Additionally, as the glass transition point of the polymer is approached, the propagation rate falls due to the effect of the decreasing free

volume, which impairs the mobility of the monomer molecules to the active centers. In fact, these observations are very important for the operation of batch reactors because, as the conversion approaches higher values, the molecular properties (molar mass and branching distributions, for instance) of PVC, which relate to thermal stability, are deteriorated due to the mentioned diffusion effects. Based on these observations, the authors proposed operation policies to operate a batch reactor in a fashion designed to ensure the improvement of the final molecular properties.

Sidiropoulou and Kiparissides (1990) developed a general model for the VCM suspension polymerization to predict the main molecular properties of PVC. The employed kinetic mechanism was identical to the one used by Hamielec *et al.* (1982). More specifically, the proposed model comprised the mass balances of growing and terminated radicals, initiator and monomer. To overcome the problem of solving a large number of equations, the authors employed the method of moments to obtain a smaller number of ordinary differential equations. The authors emphasized that their model was a generalization of previous models. In order to validate their work, simulations were performed and the results were compared to those provided by previous models found in the literature. Lastly, these investigators also considered the effects of diffusion control at higher conversions. For comparative purposes, the authors quantified the deviations caused by disregarding the diffusion effects on the kinetic rate constants.

Pinto (1990a) developed a simplified model based on the work of Abdel-Alim and Hamielec (1972) and investigated strategies to carry out polymerizations at constant rate in a batch reactor. The author investigated several strategies and concluded that it was almost impossible to keep the polymerization rate constant in an industrial batch reactor because of the heat transfer limitations. The author also pointed out that a proper initiator choice and feed strategy would help in this undertaking. In posterior works, Pinto (1990b, 1990c) performed a dynamic analysis in continuous VCM polymerizations in a stirred vessel. The author was able to identify the ranges in the parameter space where complex phenomena occurred, i.e., limit cycles, isolas and multiple steady states.

Xie *et al.* (1991a, 1991b, 1991c, 1991d, 1991e) investigated several aspects of VCM polymerizations. These authors were able to develop a comprehensive model by including the kinetic mechanism, multi-phase phenomena and molar mass distributions. Several experiments were performed in order to evaluate the model prediction capabilities. One of the most successful representations of the diffusional effects of the VCM polymerization at high conversions can be attributed to these authors. Additionally, the partition coefficient of the initiator among the polymer-

rich and monomer-rich phases was estimated based on the dynamic evolution of conversion data.

Dimian *et al.* (1995) were apparently the first to implement a model to describe an industrial VCM suspension polymerization reactor based on the work of Xie *et al.* (1991a). The authors investigated the polymerization from a process control perspective. A cascade PID controller was employed to keep temperature variations within a $\pm$ 1 % margin. The effects of the heat balance on the molecular properties and the molar mass distributions were investigated.

Chung and Jung (1996) used the same kinetic scheme described previously by Sidiropoulou and Kiparissides (1990) to investigate the abnormal behavior observed in bulk VCM polymerization in a large-scale reactor. More specifically, this abnormal behavior was related to suppression of the autocatalytic phenomena. In this work, it is argued that the autocatalytic behavior is observed in large-scale suspension polymerizations, but not in large-scale bulk polymerizations. The authors proposed that this abnormal behavior was due to the absence of thermodynamic equilibrium between the monomer recirculated through the condenser and the polymeric phase already present inside the reactor.

Giving special emphasis to the operability of a batch suspension polymerization reactor, Lewin (1996) investigated the effects of temperature control and initiator loading on the operation of an industrial reactor. This author used a simplified model that was similar to the one proposed initially by Abdel-Alim and Hamielec (1972) to perform the simulations and incorporated an energy balance into the system of equations. The model parameters were calibrated with real plant data. Using this simple model, the author was able to characterize the operability space of the process and identify the regions of thermal runaway. Furthermore, the simple model allowed the selection of proper amounts of the two distinct initiators considered in the study.

Kiparissides *et al.* (1997) developed a model that was able to predict molecular properties, conversion, temperature and pressure of a batch suspension PVC polymerization reactor. Differently from Sidiropoulou and Kiparissides (1990), these authors incorporated the vapour phase and the energy balance equations in the modeling framework, rendering a more realistic representation of the process because reactor pressure and temperature play important roles in PVC suspension polymerization plants and are the only variables measured during operation. The model was validated with data obtained in a laboratory scale reactor. The authors were able to get relevant information regarding the composition of the phases present during the course of the polymerization reaction. Furthermore, the capability of the

model to optimize the production of PVC was shown through an illustrative example. The goal of the example was to find the proportion of initiators (fast and slow initiator) to minimize the peak in the heat released profile. By using their model, the authors were able to predict a smoother curve of heat released, which proved the efficiency of the model.

Talamini *et al.* (1998) performed a thorough investigation regarding the validity of the two-phase model proposed by Talamini (1966) to describe bulk and suspension polymerizations of VCM. The authors argued against previous criticism regarding the main assumptions made when the balance equations were derived to describe the reaction behavior. The criticisms were mainly related to the assumption of equilibrium between the phases, constant ratio of radicals in both phases and the resulting partition coefficient of the initiator among them. The authors used theoretical and experimental evidences to controvert the arguments against their model.

Mejdell *et al.* (1999) modeled an industrial batch reactor and paid special attention to aspects related to the heat transfer and energy balances. The model developed by these authors shared many similarities with the model originally proposed by Kiparissides *et al.* (1997). In order to estimate the heat transfer coefficients, the authors filled the reactor with pure water and performed heating and cooling experiments. The simulations with the model were compared to real plant data and fair agreement was observed. The authors compared conversion data estimated solely with the heat balance and conversion data measured experimentally and found noticeable deviations in the range of higher conversions. These investigators attributed this effect to the fact that diffusion control on the rates of termination and propagation were not included in their model.

Wieme *et al.* (2007) developed a complete model to simulate pilot scale and industrial scale reactors. These authors proposed the detailed modeling of the suspension properties, energy balances and temperature control loops. Based on the simulations, it was possible to get insights on the importance of the reflux condenser as well as fouling on the reactor walls for the operability of the process.

Among the works mentioned above, the models described by Sidiropoulou and Kiparissides (1990), Xie *et al.* (1991a, 1991b, 1991c, 1991d, 1991e) and Kiparissides *et al.* (1997) can be reliably used to describe the reactor behavior up to higher conversions. For this reason, the model developed here is based on these previous works with minor differences mainly related to the description of the gas phase and the definition of conversion. Here, the gas phase is represented as an ideal gas

mixture, and the conversion is expressed as the ratio between polymer mass and the sum of the monomer and polymer masses instead of the ratio between the polymer mass and the initial amount of monomer, which is only valid for perfect batches. The latter modification is important if additional monomer feeds are added during the reaction.

2.2.2 Population Balance Modeling

Valentas *et al.* (1966) developed a classic study to investigate the relationship between the breakage mechanism and the final droplet size distributions in an agitated vessel. The population balance model was developed considering only the breakage mechanism. Additionally, a numerical integration formula was used to solve the integrals in the population balance model. A log-normal distribution was assumed as initial condition. The authors investigated the effects of impeller speed and temperature on the final droplet size distributions. It was shown that temperature exerted a minor effect on the particle size distributions because the properties related to breakage such as interfacial tension, density and viscosity varied very little with temperature in the studied system (benzene-water).

Valentas and Amundson (1966) introduced a coalescence mechanism in the previously described model and noticed significant changes in the final droplet size distributions obtained through simulation. The authors modeled the effect of temperature on coalescence efficiency, and a noticeable response was observed when they compared the effect of this variable in the breakage process. Additionally, it was shown that the existence of a limiting maximum droplet size for coalescence generated bimodalities in the final distributions.

Coulaloglou and Tavlarides (1977) developed phenomenological models of breakage and coalescence to predict droplet size distributions in a continuous stirred vessel. The breakage and coalescence models considered that the efficiencies of these phenomena depend on the degree of turbulence of the system. The authors were able to correlate the rates of breakage and coalescence with fluid properties and the operation conditions. Good agreement was obtained between the model predictions and the available experimental data.

Narsimham *et al.* (1979) developed a model for droplet transitional breakage in dispersions with low dispersed phase concentration. The authors focused solely on the breakage process since coalescence can be neglected when the dispersed phase

concentration is low. However, when comparing their model results with experimental data, the obtained final droplet size distributions presented much lower variance. The authors attributed this phenomenon to the assumptions made during the solution of the population balance equations.

Hsia and Tavlarides (1980) used a Monte Carlo based population balance model to represent droplet size distributions in stirred vessels. The droplet breakup and coalescence as well as flows of droplets in and out of the control volume were considered. In their study, the rates of breakage and coalescence were the same proposed by Coulaloglou and Tavlarides (1977). Hsia and Tavlarides (1983) improved their previous simulation model in order to represent bivariate distributions. By doing so, the authors were able to get more insights on the previously employed breakage and coalescence models and proposed improvements in these equations.

Sovová (1981) improved the model described by Coulaloglou and Tavlarides (1977) by incorporating a new effect on the efficiency of collisions. This effect accounts for the collision between two droplets in addition to the film drainage effect described by Coulaloglou and Tavlarides (1977). By doing this, and performing parameter estimation, the new model was able to represent literature data more accurately.

Based on the previous works, Alvarez *et al.* (1994) developed breakage and coalescence rate constant equations to describe particle size distributions in suspension polymerization reactors. These authors described and modeled some of the suspension properties, including surface tension and viscoelasticity, and included these properties in the rate equations. This approach allowed the authors to represent the evolution of particle size distributions in suspension polymerizations with good accuracy, based on the available experimental data.

Based on the work of Alvarez *et al.* (1994), Maggioris *et al.* (2000) developed a two compartment model to represent particle size distributions in suspension polymerization reactors. More specifically, the impeller and the circulation regions were modeled as connected compartments with different rates of energy dissipation per mass, which results in different breakage and coalescence rates in each compartment. This was an attempt to represent the non-homogeneity of turbulence inside the vessel. These authors were able to compare their model predictions with experimental data and a fair agreement was observed for the investigated systems, including PVC polymerization. Subsequently, Kotoulas and Kiparissides (2006) further improved the model described by Maggioris *et al.* (2000), incorporating the change in surface tension due to conversion. The model was able to describe the evolution of the

particle size distributions for styrene and VCM polymerizations.

Machado *et al.* (2000) employed a population balance modeling approach to describe poly(styrene) particle size distributions. These authors employed previously published coalescence and breakage rate models and used an orthogonal collocation based discretization scheme to solve the population balance equation. The effects of suspension rheology on the final particle size distribution were also analysed.

Kiparissides *et al.* (2004) and Kiparissides (2006) discussed some of the difficulties to describe particulate systems and suspension polymerizations through population balance modeling. These publications provide overviews of the topic and some perspectives on numerical methods used to solve population balances.

Alexopoulos and Kiparissides (2007) developed a population balance model to represent the primary particle size distribution inside the polymerizing monomer droplets in PVC polymerizations. The population balance model considered nucleation, growth and aggregation of the primary particles. Through this modeling approach, these investigators were able to determine the conversion at which massive particle aggregation of primary particles occurs.

Bárkányi *et al.* (2013) developed a population balance model coupled with the kinetic model from Sidiropoulou and Kiparissides (1990) to investigate the effect of initiator distribution among the droplets on the mean conversion. The droplet breakage and coalescence events were simulated with a Monte Carlo method. As expected, it was found that non homogeneous distribution of initiator among the droplets affected the conversion. More specifically, higher deviations from homogeneity resulted in lower mean conversions.

Kiparissides (2018) developed a multiscale modeling approach combining the kinetic model developed previously by Kiparissides *et al.* (1997) and the population balance model developed by Kotoulas and Kiparissides (2006) and Alexopoulos and Kiparissides (2007). The author investigated several aspects of PVC polymerization, including: the effects of operation variables on the particle size distributions and grain porosity.

Koolivand *et al.* (2019) used a population balance model and a kinetic model to represent the particle size distributions and MMD of polystyrene produced in suspension polymerization. The effects of impeller rotation speed, chain transfer agent, initiator and temperature were investigated. Given the predictive capabilities of their model, the authors developed an optimization strategy to obtain tailored

MMD and particle size distributions.

Kim *et al.* (2021) studied poly(methyl methacrylate) (PMMA) suspension polymerization in a 1L reactor using a computational fluid dynamics (CFD) model combined with population balances and reaction kinetics. More specifically, the authors investigated different blade angles and their effects on the final particle size distributions. It was found that higher blade angles resulted in smaller particles due to the effect of increasing energy dissipation in the impeller zone. It was also pointed out that higher blade angles generated inefficient mixing inside the reactor.

At this point, it is very important to emphasize that none of the previously published studies investigated the performances of population balance models in large-scale industrial PVC polymerization reactors. Particularly, it is not obvious that models developed in the laboratory scale will perform well in the large scale, because the flow conditions are not homogeneous and unavoidable spatial temperature and concentration gradients can develop inside vessels of large dimensions (Kiparissides, 2006; Kim *et al.*, 2021). Besides, CFD models may not be sufficient to represent these systems, as agreement has yet to be achieved regarding the correct functional forms of breakage and coalescence rate kernels. For these reasons, population balance models are not scalable yet, in the sense that functional forms and model parameters used to describe laboratory scale reactors are not necessarily suitable to describe the phenomena that occur in much larger vessels. Finally, the use of top condensers for removal of the reaction heat can generate new droplets and introduce non-equilibrium mass and heat transfer effects that can impact the performances of these models. Consequently, it can be relevant to investigate the performance of population balance models in industrial scale suspension PVC polymerization reactors.

In the following sections, although some authors argue that suspension polymerization systems are not homogeneous in terms of mixing and rates of energy dissipation (Alexopoulos *et al.*, 2002; Kiparissides, 2006), the agitated vessels investigated in this work will be considered homogeneous, so that the suspension properties will be assumed to be independent of position. Additionally, in order to assure the scalability of the proposed model, proper parameter estimation procedures will be employed to describe particle size distributions of polymer powders produced in large scale reactors. In spite of the significant simplification imposed on the model, it will be shown that the proposed strategy is capable of representing actual industrial data accurately, being useful for development of operation strategies at plant site.

2.3 Model Development

2.3.1 Kinetic Model

The PVC polymerization mechanism is based on a free radical polymerization scheme that involves initiator decomposition, chain initiation, propagation, transfer to monomer and bimolecular termination reactions. The kinetic mechanism assumed in this study was originally proposed by Yuan *et al.* (1991) and is shown in Table 2.1. More detailed models are available in the literature, if one is interested in more detailed description of the molecular properties of the final product, including the degree of branching and the tacticity distribution (Xie *et al.*, 1991a; Xie *et al.*, 1991b; Xie *et al.*, 1991c; Xie *et al.*, 1991d; Xie *et al.*, 1991e; Kiparissides *et al.*, 1997).

Transfer to monomer plays an important role in controlling the polymer molar mass (Abdel-Alim and Hamielec, 1972). Disproportionation is the major mode of termination (Burgess, 1982). According to Park and Smith (1970), 75% of the termination reactions are due to disproportionation and 25% by combination.

Table 2.1: Kinetic mechanism (Yuan *et al.*, 1991).

Reaction Step	Mechanism[1]
Initiator decomposition	$I \xrightarrow{kd} 2I^*$
Chain initiation	$I^* + M \xrightarrow{ki} R_1$
Propagation	$R_x + M \xrightarrow{kp} R_{x+1}$
Transfer to monomer	$R_x + M \xrightarrow{ktm} P_x + R_1$
Termination by disproportionation	$R_x + R_y \xrightarrow{ktd} P_x + P_y$
Termination by combination	$R_x + R_y \xrightarrow{ktc} P_{x+y}$

[1] R and P represent living and dead polymer chains, respectively.
I^* and M represent the free radical and monomer, respectively.

2.3.2 Equilibrium Relationships

The suspension polymerization of VCM is a heterogeneous process due to the low solubility of VCM in water. In addition, the polymer is also insoluble in its own monomer. It is believed that the first polymer molecules precipitate at the onset of the reaction (Yuan *et al.*, 1991). At conversions x (Equation (2.1)) below 0.1%, the polymerization reaction proceeds in the monomer-rich phase (Phase 1) only. Following the definition of Sidiropoulou and Kiparissides (1990) and Kiparissides *et al.* (1997), this stage of the reaction is called Stage 1. In this stage, the volume of

Phase 1 is nearly the volume of the overall monomer. The first column of Table 2.2 describes the system composition at this stage.

$$x = \frac{p}{m_t + p} \tag{2.1}$$

$$x_s = \frac{\varphi_p \rho_p}{\varphi_p \rho_p + (1 - \varphi_p)\rho_m} \tag{2.2}$$

$$x_f = x_s \left[\frac{1}{1 + \frac{m_3 + m_4}{m_2}(1 - x_s)} \right] \tag{2.3}$$

As the reaction proceeds, the polymer precipitated forms the polymer-rich phase (Phase 2). The appearance of this polymer-rich phase characterizes the so called Stage 2. Let x_f represent the critical conversion (Equation (2.3)), then from $x > 0.001$ to $x \leq x_f$, Phases 1 and 2 are in equilibrium, so that the concentrations remain constant until x_f is reached (Kiparissides *et al.*, 1997). The fraction of polymer in Phase 2 (Equation (2.2)) is temperature dependent according to the Flory-Huggins interaction parameter (χ) (Xie *et al.*, 1991a) (see Table 2.2) . This stage is characterized by the agglomeration of small particles (domains) to originate larger polymer particles (Yuan *et al.*, 1991). As the conversion increases, the volume of the polymeric phase increases and monomer from Phase 1 is transferred to Phase 2 to maintain the equilibrium. If the reaction is carried out at isothermal conditions, the pressure of the reactor remains constant until x_f.

When the critical conversion is surpassed, the monomer-rich phase disappears and the reaction continues in the polymer-rich phase only (Stage 3) (Table 2.2). This stage is characterized by the continuous drop of the reactor pressure, since the monomer from the gas phase migrates to the polymer-rich phase. In this stage, the polymerization reaction becomes diffusion controlled due to the decreasingly lower mobility of the molecules.

Table 2.2: Equilibrium calculations at the different reaction stages.

Stage 1: $x \leq 0.001$	Stage 2: $0.001 < x \leq x_f$	Stage 3: $x > x_f$
$m_t = m_1 + m_2 + m_3 + m_4$	$m_t = m_1 + m_2 + m_3 + m_4$	$m_t = m_1 + m_2 + m_3 + m_4$
$V_t = V_1 + V_2 + V_3 + V_4$	$V_t = V_1 + V_2 + V_3 + V_4$	$V_t = V_1 + V_2 + V_3 + V_4$
$w_t = w_3 + w_4$	$w_t = w_3 + w_4$	$w_t = w_3 + w_4$
$m_2 = 0$	$m_2 = p\left(\frac{1-\varphi_p}{\varphi_p}\right)\left(\frac{\rho_m}{\rho_p}\right)$	$m_1 = 0$
$m_3 = k_s \frac{Z_t}{Z_m^{sat}} w_3$	$m_3 = k_s \frac{Z_t}{Z_m^{sat}} w_3$	$m_2 = p\left(\frac{1-\varphi_p}{\varphi_p}\right)\left(\frac{\rho_m}{\rho_p}\right)$
$m_4 = \frac{y_m Z_t M M_m V_4}{RT}$	$m_4 = \frac{y_m Z_t M M_m V_4}{RT}$	$m_3 = k_s \frac{Z_t}{Z_m^{sat}} w_3$
$V_1 = \frac{m_1}{\rho_m}$	$V_1 = \frac{m_1}{\rho_m}$	$m_4 = \frac{y_m Z_t M M_m V_4}{RT}$
$V_2 = 0$	$V_2 = \frac{m_2}{\rho_m} + \frac{p}{\rho_p}$	$V_1 = 0$
$V_3 = \frac{w_3}{\rho_w} + \frac{m_3}{\rho_m}$	$V_3 = \frac{w_3}{\rho_w} + \frac{m_3}{\rho_m}$	$V_2 = \frac{m_2}{\rho_m} + \frac{p}{\rho_p}$
$w_4 = \frac{y_w Z_t M M_w V_4}{RT}$	$w_4 = \frac{y_w Z_t M M_w V_4}{RT}$	$V_3 = \frac{w_3}{\rho_w} + \frac{m_3}{\rho_m}$
$Z_t = Z_m^{sat} + Z_w^{sat}$	$Z_t = Z_m^{sat} + Z_w^{sat}$	$w_4 = \frac{y_w Z_t M M_w V_4}{RT}$
$y_m = \frac{Z_m^{sat}}{Z_t}$	$y_m = \frac{Z_m^{sat}}{Z_t}$	$Z_t = Z_m^{sat} e^{ln(1-\varphi_p)+\varphi_p+\chi\varphi_p^2} + Z_w^{sat}$
$y_w + y_m = 1$	$y_w + y_m = 1$	$y_m = \frac{Z_m^{sat}}{Z_t}$
	$ln(1-\varphi_p) + \varphi_p + \chi\varphi_p^2 = 0$	$y_w + y_m = 1$
	$\chi = \frac{1286.4}{T} - 3.02$	$\chi = \frac{1286.4}{T} - 3.02$

2.3.3 Mass Balances

The following mass balances are generalized to account for multiple initiators (Equations (2.4)–(2.6)). Additionally, the initiator partition coefficient is also included for the calculation of initiator distribution among the phases (Xie *et al.*, 1991a). Since the system under consideration is heterogeneous, the overall initiator, monomer and polymer balances must account for the rates of consumption or generation in both Phases 1 and 2 (Equations (2.6)–(2.8)).

$$I_{k,1} = \frac{I_k V_1}{V_1 + k_I V_2} \tag{2.4}$$

$$I_{k,2} = I_k - I_{k,1} \tag{2.5}$$

$$\frac{dI_k}{dt} = -\sum_{j=1}^{2} kd_{k,j} I_{k,j} \tag{2.6}$$

$$\frac{dM}{dt} = -\sum_{j=1}^{2} kp_j \frac{M_j}{V_j} \frac{\lambda_{0,j}}{V_j} V_j \tag{2.7}$$

$$\frac{dP}{dt} = \sum_{j=1}^{2} kp_j \frac{M_j}{V_j} \frac{\lambda_{0,j}}{V_j} V_j \tag{2.8}$$

2.3.4 Moment Equations

As any polymerization system deals with molecules of different chain lengths, generating a chain length distribution (CLD), sometimes it becomes infeasible to consider every individual chain length to describe the molar mass distribution (MMD). In order to avoid the inconveniences of representing the whole MMD, the method of moments can be applied as a means of describing the averages of the MMD (Equations (2.9)–(2.14)). Compared to other MMD modeling approaches, the method of moments is of considerable simplicity and allows the calculation of the main polymer properties, which depend mostly on the number average molar

mass (Mn) and the weight average molar mass (Mw) (Bachmann *et al.*, 2016). According to Mastan and Zhu (2015), one of the major advantages of the method of moments relies on the fact that it avoids solving a high number of mass balances (one for each chain length). Nonetheless, the cost of doing so is the loss of the whole MMD representation. The detailed development of the moment equations is given in the Appendix A.

$$\frac{d\lambda_{0,j}}{dt} = \sum_{k=1}^{nk} 2f_{k,j}kd_{k,j}I_{k,j} - (ktc_j + ktd_j)\frac{\lambda_{0,j}}{V_j}\frac{\lambda_{0,j}}{V_j}V_j \quad (j = 1, 2) \tag{2.9}$$

$$\begin{aligned}\frac{d\lambda_{1,j}}{dt} &= \sum_{k=1}^{nk} 2f_{k,j}kd_{k,j}I_{k,j} + kp_j\frac{M_j}{V_j}\frac{\lambda_{0,j}}{V_j}V_j + ktm_j\frac{M_j}{V_j}\frac{(\lambda_{0,j} - \lambda_{1,j})}{V_j}V_j \\ &\quad - (ktc_j + ktd_j)\frac{\lambda_{0,j}}{V_j}\frac{\lambda_{1,j}}{V_j}V_j\end{aligned} \tag{2.10}$$

$$\begin{aligned}\frac{d\lambda_{2,j}}{dt} &= \sum_{k=1}^{nk} 2f_{k,j}kd_{k,j}I_{k,j} + kp_j\frac{M_j}{V_j}\frac{(2\lambda_{1,j} + \lambda_{0,j})}{V_j}V_j + ktm_j\frac{M_j}{V_j}\frac{(\lambda_{0,j} - \lambda_{2,j})}{V_j}V_j \\ &\quad - (ktc_j + ktd_j)\frac{\lambda_{0,j}}{V_j}\frac{\lambda_{2,j}}{V_j}V_j\end{aligned} \tag{2.11}$$

$$\frac{d\mu_0}{dt} = \sum_{j=1}^{2}\left[ktm_j\frac{M_j}{V_j}\frac{\lambda_{0,j}}{V_j}V_j + \left(ktd_j + \frac{ktc_j}{2}\right)\frac{\lambda_{0,j}}{V_j}\frac{\lambda_{0,j}}{V_j}V_j\right] \tag{2.12}$$

$$\frac{d\mu_1}{dt} = \sum_{j=1}^{2}\left[ktm_j\frac{M_j}{V_j}\frac{\lambda_{1,j}}{V_j}V_j + (ktc_j + ktd_j)\frac{\lambda_{0,j}}{V_j}\frac{\lambda_{1,j}}{V_j}V_j\right] \tag{2.13}$$

$$\frac{d\mu_2}{dt} = \sum_{j=1}^{2}\left[ktm_j\frac{M_j}{V_j}\frac{\lambda_{2,j}}{V_j}V_j + ktc_j\left(\frac{\lambda_{0,j}}{V_j}\frac{\lambda_{2,j}}{V_j}V_j + \frac{\lambda_{1,j}}{V_j}\frac{\lambda_{1,j}}{V_j}V_j\right) + ktd_j\frac{\lambda_{0,j}}{V_j}\frac{\lambda_{2,j}}{V_j}V_j\right] \tag{2.14}$$

2.3.5 Reaction Rates

In order to model the effect of diffusion limitations on the reaction rates, Xie *et al.* (1991a) made use of the Free Volume Theory (Vrentas and Duda, 1977; Bueche, 1962). The free volume is a measure of the impairment of mobility of the molecules. Large free volumes indicate that the molecules can diffuse more freely and that individual reaction rates are higher. Over the course of the reaction, as the polymer fraction increases, the free volume diminishes considerably. The calculation of the free volume takes into account the glass transition temperature of monomer and polymer (Equations (2.15)–(2.19)) (Xie *et al.*, 1991a; Fedors, 1979; Reding *et al.*, 1979; Ceccorulli *et al.*, 1977).

$$T_{g,m} = 70.74 \tag{2.15}$$

$$T_{g,p} = 87.1 - 0.132(T - 273.15) + 273.15 \tag{2.16}$$

$$V_{f,m} = 0.025 + 9.98 \times 10^{-4}(T - T_{g,m}) \tag{2.17}$$

$$V_{f,p} = 0.025 + 5.47 \times 10^{-4}(T - T_{g,p}) \tag{2.18}$$

$$V_f = V_{f,p}\varphi_p + V_{f,m}(1 - \varphi_p) \tag{2.19}$$

In the present study, kt and kp were taken from the works of Burnett and Wright (1954) and Sidiropoulou and Kiparissides (1990), respectively. Burnett and Wright (1954) also estimated a propagation rate constant, but the obtained value seemed too high according to Ugelstad *et al.* (1973) and Si (2007). Their termination rate constant was also employed by Xie *et al.* (1991a). ktm was taken from Abdel-Alim and Hamielec (1972). The termination rate constant in the polymer-rich phase (Phase 2) was estimated based on the available data, considering that non-equilibrium conditions might develop. In the rate equations presented below,

Equations (2.20)–(2.38), the value of the universal gas constant R is already included in the exponential term. The activation energies in the free volume parameters A, B, B_f and C (E_1, E_2, E_3 and E_4)(Xie *et al.*, 1991a) (Equations (2.35)–(2.38)) were estimated. It was also assumed that $ktc = 0.25kt$ and $ktd = 0.75kt$ (Park and Smith, 1970).

If $x \leq x_f$

$$kt_1 = 1.3 \times 10^{12} exp\left(\frac{-2113.7}{T}\right) \tag{2.20}$$

$$kt_2 = kt_{ref} = \frac{kt_1}{F} \tag{2.21}$$

$$kp_j = kp_{ref} = 5.0 \times 10^7 exp\left(\frac{-3320}{T}\right) \tag{2.22}$$

$$ktm_j = ktm_{ref} = 5.78 exp\left(\frac{-2768}{T}\right) kp_j \tag{2.23}$$

$$kd_{k,j} = kd_{ref,k} = kd_{0,k} exp\left(\frac{-E_{0,k}}{T}\right) \tag{2.24}$$

$$ktd_j = 0.75kt_j \tag{2.25}$$

$$ktc_j = 0.25kt_j \tag{2.26}$$

$$f_{k,j} = f_{ref} \tag{2.27}$$

At conversions higher than x_f, the reaction rates become diffusion controlled, thus the reaction rates (Equations (2.28)–(2.34)) become dependent upon the free volume and parameters A, B, B_f and C as described by Equations (2.35)–(2.38).

If $x > x_f$

$$kt_2 = kt_{ref} exp\left(-A\left(\frac{1}{V_f} - \frac{1}{V_{f,xf}}\right)\right) \tag{2.28}$$

$$kp_2 = kp_{ref} exp\left(-B\left(\frac{1}{V_f} - \frac{1}{V_{f,xf}}\right)\right) \tag{2.29}$$

$$ktm_2 = ktm_{ref} exp\left(-B\left(\frac{1}{V_f} - \frac{1}{V_{f,xf}}\right)\right) \tag{2.30}$$

$$kp_2 f_{k,2}^{1/2} = \left(kp_{ref} f_{ref}^{1/2}\right) exp\left(-B_f\left(\frac{1}{V_f} - \frac{1}{V_{f,xf}}\right)\right) \tag{2.31}$$

$$kd_{k,2} = kd_{k,ref} exp\left(-C\left(\frac{1}{V_f} - \frac{1}{V_{f,xf}}\right)\right) \tag{2.32}$$

$$ktd_2 = 0.75 kt_2 \tag{2.33}$$

$$ktc_2 = 0.25 kt_2 \tag{2.34}$$

$$A = 6.64 \times 10^6 exp\left(\frac{-E_1}{T}\right) \tag{2.35}$$

$$B = 1.85 \times 10^3 exp\left(\frac{-E_2}{T}\right) \tag{2.36}$$

$$B_f = 4.01 \times 10^4 exp\left(\frac{-E_3}{T}\right) \tag{2.37}$$

$$C = 477exp\left(\frac{-E_4}{T}\right) \tag{2.38}$$

2.3.6 Polymer Properties

The main properties used to describe the polymer quality are the number average molar mass (Mn), weight average molar mass (Mw) and the K-Value (VK), Equations (2.39), (2.40) and (2.41), respectively. The VK is a measurement of the viscosity of dilute polymer solutions made in standard experimental conditions (Burgess, 1982). This variable is used to make inferences about the polymer molecular mass. Moreover, it specifies the different PVC grades produced. Equation (2.41) was fitted with data from Skillicorn *et al.* (1993) as reported by Abi-Ramia (2012) and Castor (2014).

$$Mn = MM_m \frac{\sum_{j=1}^{2} \lambda_{1,j} + \mu_1}{\sum_{j=1}^{2} \lambda_{0,j} + \mu_0} \tag{2.39}$$

$$Mw = MM_m \frac{\sum_{j=1}^{2} \lambda_{2,j} + \mu_2}{\sum_{j=1}^{2} \lambda_{1,j} + \mu_1} \tag{2.40}$$

$$VK = 0.8482 Mw^{0.385611} \tag{2.41}$$

In addition to Equations (2.1)–(2.41), the constitutive relationships and parameters in Table 2.3 were used to calculate the physical and suspension properties. Data regarding three industrial grade formulations (F1, F2 and F3), as described in Tables 2.4 and 2.5, were used for parameter estimation. Regarding the surface tension, the system VCM/water surface tension is 32 mN m^{-1} (Nilsson *et al.*, 1985). However, this work assumed that the data regarding the system MMA/water/PVA studied by Lazrak *et al.* (1998) represents well the system VCM/PVA/Water in the range of PVA concentrations employed in this study.

Table 2.3: Additional constitutive relationships and parameters.

Equation/Parameter[1]	References
$log_{10}(\eta_w) = -4.64779 + \frac{262.37}{T-133.98}$	Korosi and Fabuss (1968)
$ln(\eta_m) = 0.26297 + \frac{276.55}{T} - 1.7282ln(T)$	Green and Perry (2008)
$\eta_c = \eta_w \left(1 + \frac{\sum[\eta]_{pva,i} C_{pva,i}}{1-0.45\sum[\eta]_{pva,i} C_{pva,i}}\right)$	Okaya (1992) apud Kotoulas and Kiparissides (2006)
$\eta_d = \eta_m \left(1 + 2.5\varphi_{eff} + 6.2\varphi_{eff}^2\right)$; $\varphi_{eff} = 1.8\varphi_{p,d}$	Batchelor and Green (1972), Kiparissides and Pladis (2022)
$[\eta]_{pva} = 1.332 \times 10^{-4} Mw_{pva}^{0.566}$	Nagy (1993)
$\eta_s = \frac{\eta_c}{1-\Phi}\left(1 + \frac{1.5\eta_d\Phi}{\eta_d+\eta_c}\right)$	Vermeulen *et al.* (1955)
$\rho_m = 947 - 1.746(T - 273.15)$	Kiparissides *et al.* (1997)
$\rho_p = 10^3 exp(0.4296 - 3.274 \times 10^{-4} T)$	Kiparissides *et al.* (1997)
$\rho_w = 1011 - 0.4484(T - 273.15)$	Kiparissides *et al.* (1997)
$\frac{1}{\rho_d} = \frac{x}{\rho_p} + \frac{1-x}{\rho_m}$	Kotoulas and Kiparissides (2006)
$\rho_s = (1 - \Phi)\rho_w + \Phi\rho_d$	Bouyatiotis and Thornton (1967)
$Z_w^{sat} = exp(73.64 - \frac{7258.2}{T} - 7.3ln(T) + 4.16 \times 10^{-6} T^2)$	Green and Perry (2008)
$Z_m^{sat} = exp(91.43 - \frac{5141.7}{T} - 10.9ln(T) + 1.43 \times 10^{-6} T^2)$	Green and Perry (2008)
$\sigma_{ref} = -4.41 \times 10^{-5} T + 2.7 \times 10^{-2}$	fitted with data from Lazrak *et al.* (2008)
$K_\sigma = 6.637 \times 10^{-6} T + 8.122 \times 10^{-3}$	fitted with data from Lazrak *et al.* (2008)
$K_A = 1.042 \times 10^{-4} T - 2.519 \times 10^{-2}$	fitted with data from Lazrak *et al.* (2008)
$\sigma = \sigma_{ref} - K_\sigma \frac{K_A C_{pva}}{1+K_A C_{pva}}$	Lazrak *et al.* (2008)
$F^{1/2} = 41.2 - 0.0104(T - 273.15)^2 + 0.2656(T - 273.15)$	This work
$k_I = 0.77$	Xie *et al.* (1991a)
$k_s = 0.0088$	Nilsson *et al.* (1978)
$R = 8.314 \times 10^3$	Green and Perry (2008)
$-\Delta H = 106$	Kiparissides *et al.* (1997)
$f_{ref} = 0.7$	This work

[1] Units are given in the list of symbols.

Table 2.4: Data used for parameter estimation.

Component/Condition [1]	F1	F2	F3
Φ[-]	0.49	0.41	0.41
Initiator 01 [kg]	18.75	0	0
Initiator 02 [kg]	0	6.38	8.29
Initiator 03 [kg]	0	9.64	6.90
Initiator 04 [kg]	0	9.38	11.54
C_{pva} [kg m^{-3}]	-	-	-
Impeller diam., L [m]	-	-	-
Rotation, N^* [Hz]	-	-	-
Reactor vol., V_t [m^3]	-	-	-
Final conv., x[%]	87	84	90
Final K-Value, VK[-]	67	59	57

[1] PVA concentration, impeller diameter, rotation and reactor volume were omitted due to confidentiality reasons.

Table 2.5: Parameters in the initiator decomposition rate constant [1].

Name [2]	kd_0	E_0
Initiator 01 (k = 1)	1.52×10^{14}	13888.60
Initiator 02 (k = 2)	7.09×10^{14}	14865.28
Initiator 03 (k = 3)	1.83×10^{15}	14728.17
Initiator 04 (k = 4)	2.84×10^{15}	15436.61

[1] Units are given in the list of symbols. [2] Names were omitted due to confidentiality reasons.

2.3.7 Population Balance Model

A detailed derivation of the population balance model based on different principles was presented by Solsvik and Jakobsen (2015). The population balance model employed in the present study is shown in Equation (2.42) (Valentas *et al.*, 1966; Valentas and Amundson, 1966; Coulaloglou and Tavlarides, 1977). According to this representation, $N(\vartheta)$ represents the number of droplets of mass ϑ; $kc(\zeta, \vartheta)$ represents the coalescence rate constant of droplets with masses ζ and ϑ, respectively; $kb(\vartheta)$ represents the breakage rate constant of droplets of mass ϑ; $\beta(\zeta, \vartheta)$ is the daughter droplet distribution, representing the probability of a droplet of mass ϑ to be obtained from the breakage of a droplet of mass ζ; $\gamma(\zeta)$ is the number of daughter droplets resulting from the breakage of droplet of mass ζ; and V_s is the suspension volume ($V_t - V_4$). Therefore, the first term on the right-hand side of Equation (2.42) represents the appearance of droplets of mass ϑ due to coalescence of smaller ones. By analogy, the second term represents the disappearance of droplets of mass ϑ due to coalescence with other droplets. Finally, the third term represents the appearance of droplets of mass ϑ due to the breakage of bigger droplets and the last term

represents the disappearance due to breakage. This balance has no inlet and outlet terms since we are dealing with a batch reaction system.

$$\frac{dN(\vartheta)}{dt} = \frac{1}{2}\int_0^{\vartheta} kc(\zeta, \vartheta-\zeta)\frac{N(\zeta)}{V_s}\frac{N(\vartheta-\zeta)}{V_s}V_s d\zeta - \int_0^{\infty} kc(\zeta,\vartheta)\frac{N(\zeta)}{V_s}\frac{N(\vartheta)}{V_s}V_s d\zeta + \int_{\vartheta}^{\infty} kb(\zeta)\beta(\zeta,\vartheta)\gamma(\zeta)\frac{N(\zeta)}{V_s}V_s d\zeta - kb(\vartheta)\frac{N(\vartheta)}{V_s}V_s \tag{2.42}$$

In addition to Equation (2.42), the following restriction (Equation (2.43)) must me satisfied in order to conserve the mass after breakage (Kotoulas and Kiparissides, 2006):

$$\int_0^{\zeta} \vartheta\gamma(\zeta)\beta\left(\zeta,\vartheta\right)d\vartheta = \zeta \tag{2.43}$$

The breakage and coalescence rate models used in the present work were proposed by Coulaloglou and Tavlarides (1977) and used by Hsia and Tavlarides (1980, 1983) (Equations (2.44) and (2.45)). After breakage, it is assumed that two unequal droplets are formed, so that $\gamma(\zeta) = 2$ (binary breakage). The daughter droplet distribution, Equation (2.46), was proposed by Mikos *et al.* (1986). In Equation (2.46), $\bar{\vartheta} = \frac{\zeta}{\gamma(\zeta)}$ and $\sigma_\beta = 0.4\bar{\vartheta}$. In the original paper, these rates were expressed in terms of droplet volume. However, in Equation (2.42) the rates are dependent on the droplet mass variable. Since mass is proportional to volume for a spherical droplet, the exponents of the mass variable were kept the same, cf. Equations (2.44) and (2.45). The parameters c_1, c_2, c_3 and c_4 depend on the selected internal variable and will be estimated with actual plant data.

$$kb'(\zeta) = c_1\zeta^{-2/9}\frac{N^* L^{2/3}}{1+\Phi}exp\left(-c_2\frac{\sigma(1+\Phi)^2}{\rho_d\zeta^{5/9}N^{*2}L^{4/3}}\right) \tag{2.44}$$

$$kc'(\zeta,\vartheta) = c_3\left(\zeta^{1/3}+\vartheta^{1/3}\right)^2\left(\zeta^{2/9}+\vartheta^{2/9}\right)^{1/2}\frac{N^*L^{2/3}}{1+\Phi}\times exp\left(-c_4\frac{\eta_c\rho_c}{\sigma^2}\frac{N^{*3}L^2}{(1+\Phi)^3}\left(\frac{\zeta^{1/3}\vartheta^{1/3}}{\zeta^{1/3}+\vartheta^{1/3}}\right)^4\right) \tag{2.45}$$

$$\beta(\zeta,\vartheta) = \frac{1}{\sigma_\beta\sqrt{2\pi}} exp\left(-\frac{\left(\vartheta-\bar{\vartheta}\right)^2}{2\sigma_\beta^2}\right) \tag{2.46}$$

Equations (2.44) and (2.45) were proposed for a non-reacting system, although the polymerization of VCM constitutes a reacting system, so that the properties and morphology of the droplets change with the increase of conversion. As a matter of fact, the morphology of polymerizing PVC droplets has been extensively studied. For instance, Darvish *et al.* (2015) presented a detailed literature review on the morphology of PVC particles produced through suspension technologies. As described before, since PVC is insoluble in its monomer, the first PVC molecules precipitate to form microdomains with average diameters around 10 nm Darvish *et al.* (2015). Afterwards, these unstable particles aggregate to form primary particles nuclei (domains). For conversions between 0.1 and 1% these domains aggregate to form primary particles Smallwood (1986). It was observed that after 30% conversion the mean droplet diameter of the suspension remains constant independently of the stirring speed (Máriási, 1986; Guo *et al.*, 2017). This occurs because the droplet becomes rigid. In order to account for this effect in the model, the Equations (2.44) and (2.45) were modified in the form of Equations (2.47) and (2.48).

$$kb(\zeta) = \begin{cases} kb'(\zeta)\left(1-\frac{x}{0.3}\right)^2 & \text{if } x \leq 0.3 \\ 0 & \text{otherwise} \end{cases} \tag{2.47}$$

$$kc(\zeta,\vartheta) = \begin{cases} kc'(\zeta,\vartheta)\left(1-\frac{x}{0.3}\right)^2 & \text{if } x \leq 0.3 \\ 0 & \text{otherwise} \end{cases} \tag{2.48}$$

By discretizing the internal variable mass as $\zeta_i = i\Delta\zeta$, $i = 1, ..., nc$ with $\Delta\zeta = \zeta_{max}/nc$, the following set of differential equations can be obtained (Equations (2.49) and (2.50)). This discretization approach is based on the mean value theorem (MI approach) on number frequency (Kumar and Ramkrishna, 1996). Hidy (1965) and Gelbard and Seinfeld (1979) used similar approaches to solve population balances. It is worth to mention that, in the present model, if $\zeta_l + \zeta_i > \zeta_{max}$ then $kc(\zeta_l, \zeta_i) = 0$ to avoid forming particles with masses outside of the discretization range. In the present work, $nc = 100$ was used to generate the discretization grid.

$$\frac{dN(\zeta_i)}{dt} = \frac{1}{2}\sum_{l=1}^{i-1} kc(\zeta_l, \zeta_{i-l})\frac{N(\zeta_l)}{V_s}\frac{N(\zeta_{i-l})}{V_s}V_s - \sum_{i=1}^{nc} kc(\zeta_l, \zeta_i)\frac{N(\zeta_l)}{V_s}\frac{N(\zeta_i)}{V_s}V_s + \sum_{l=i+1}^{nc} kb(\zeta_l)\beta(\zeta_l, \zeta_i)\gamma(\zeta_l)\frac{N(\zeta_l)}{V_s}V_s - kb(\zeta_i)\frac{N(\zeta_i)}{V_s}V_s \tag{2.49}$$

$$\sum_{l=1}^{i} \zeta_l \gamma(\zeta_i)\beta(\zeta_i, \zeta_l) = \zeta_i \tag{2.50}$$

Finally, assuming that the particles are of spherical shape, the particle and droplet diameters can be calculated as Equations (2.51) and (2.52). Equation (2.53) was proposed by assuming that the PVC particles are spherical and a bed of these particles has a porosity of 40%. Since at $x \leq x_f$ the droplet has monomer and polymer, in this range of conversion $\epsilon = \epsilon_f$ if $\epsilon_m > \epsilon_f$; otherwise, $\epsilon = \epsilon_m$. Equation (2.55) represents the Sauter mean diameter (d_{32}) which is an average diameter.

$$d_{p,i} = \left[\frac{6x\zeta_i}{(1-\epsilon)\rho_p\pi}\right]^{1/3} \tag{2.51}$$

$$d_{d,i} = \left(\frac{6\zeta_i}{\rho_d\pi}\right)^{1/3} \tag{2.52}$$

$$\epsilon_f = 0.4 + 0.6\,(1-\varphi_p) \tag{2.53}$$

$$\epsilon_m = \frac{\frac{1-x}{\rho_m}}{\frac{1-x}{\rho_m} + \frac{x}{\rho_p}} \tag{2.54}$$

$$d_{32} = \frac{\sum_{i=1}^{nc} N(\zeta_i)d_i^3}{\sum_{i=1}^{nc} N(\zeta_i)d_i^2} \tag{2.55}$$

2.3.8 Initial Condition

In order to solve the model equations, a set of initial conditions is required. For the component balances, the data in Table 2.4 was employed. The initial droplet size distribution was assumed to follow the Gaussian distribution (Equation (2.56)). In Equation (2.56), $\sigma_0^2 = 3.0 \times 10^{-10}$ and $\bar{\zeta} = 1.25 \times 10^{-9}$, in accordance with available plant data. The system of differential-algebraic equations was solved with the DASSL solver (Petzold, 1982) in a Fortran environment.

$$N_0(\zeta_i) = \frac{\Omega_i}{\sqrt{2\pi\sigma_0^2}} exp\left(-\frac{\left(\zeta_i - \bar{\zeta}\right)^2}{2\sigma_0^2}\right) \tag{2.56}$$

2.4 Results and Discussion

2.4.1 Estimation of Kinetic Parameters

The Particle Swarm Optimization Algorithm (PSO)(Kennedy and Eberhart, 1995; Schwaab *et al.*, 2008) was used to solve the optimization problem (Equation (2.57)) to estimate the kinetic parameters. The total swarm size was 30 and the hyperparameters were the same proposed by Schwaab *et al.* (2008). The inferior and superior limits of the search region are shown in Table 2.6. By solving the optimization problem, the kinetic parameters in Table 2.6 were obtained. In comparison to the parameters described by Xie *et al.* (1991a), the estimated values were very similar to the published values, which is very consistent, and the largest correction regarded E_3, which is related to initiator efficiency. This can be related to the fact that the initiator systems employed in the present work were different from those used by Xie *et al.* (1991a). Comparisons between model response and experimental data are shown in Figures 2.3 and 2.4. In Figure 2.3, the model prediction of the pressure dynamics for the three formulations is impressive. The model is also able to predict the final conversion accurately. In industrial environments, operators use the pressure variable to make inferences about the conversion since gravimetric analyses are time consuming. The accuracy that the model has shown representing the pressure and conversion data, make it suitable for the development of process control and monitoring studies in future works. The gray and orange shadowed areas in Figures 2.3 and 2.4 represent the ranges of conversion $x \leq x_f$ and

$x > x_f$, respectively. The identification of this critical conversion is very important for the polymerization of PVC since it defines the point where the monomer starts to migrate from the gaseous phase to the polymer-rich phase causing a drop in reactor pressure. The increase in pressure near the end of the polymerization runs in Figure 2.3 parts A and C is a consequence of the increase in temperature as shown in Figure 2.4 parts A and C. This is a common practice used in industry to cause an increase in conversion called "heat-kick" (Tacidelli *et al.*, 2009).

$$\min_{E_1,E_2,E_3,E_4} \sum_{i=1}^{3} \left[\left(\frac{VK_i - VK_{i,exp}}{VK_{i,exp}} \right)^2 + \left(\frac{x_i - x_{i,exp}}{x_{i,exp}} \right)^2 + \sum \left(\frac{Z_{t,i} - Z_{t,i,exp}}{Z_{t,i,exp}} \right)^2 \right] \tag{2.57}$$

Subject to:

Dynamic model

Table 2.6: Search region and estimated parameters.

	E_1	E_2	E_3	E_4
Inferior limit	1000	500	1000	500
Superior limit	7000	5000	10000	5000
This work [1]	4850	2450	4081	2681
Xie *et al.* (1991a)	4986	2595	3464	2291

[1] Units are given in the list of symbols.

In Figure 2.4, the temperatures and VK of the three formulations are shown. In this case, the temperature data profiles were used as model inputs in the parameter estimation strategy because the model presented in this work does not contemplate an energy balance so far. The obtained fits of VK can be regarded as very satisfactory. As expected, it is possible to observe that the VK of the resin varies inversely with temperature which shows the model consistency once again.

To conclude this section, Figure 2.5 shows a plot of suspension viscosity and surface tension for one the studied industrial grade formulations. In Figure 2.6, the polymerization rate (R_{pol}) and the amount of heat released ($\dot{Q} = -R_{pol}\Delta H$) due to the reaction are shown. It is possible to notice that as the reaction time is decreased (from F3 to F1), the peak in heat generated becomes steeper which means that the cooling system needs to operate close to its maximum capacity. In fact, this is one of the main challenges in increasing the process productivity as discussed in the introduction.

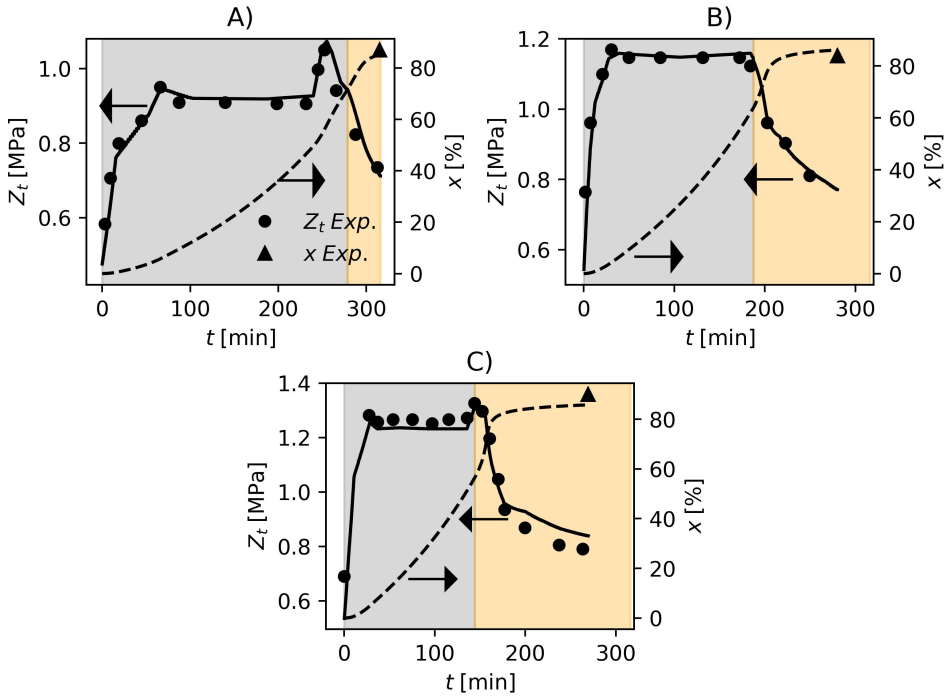

Figure 2.3: Reactor pressure and monomer conversion obtained experimentally and predicted by the proposed model. (A) F1, (B) F2 and (C) F3. Gray and orange shadowed areas represent the ranges of $x \leq x_f$ and $x > x_f$, respectively.

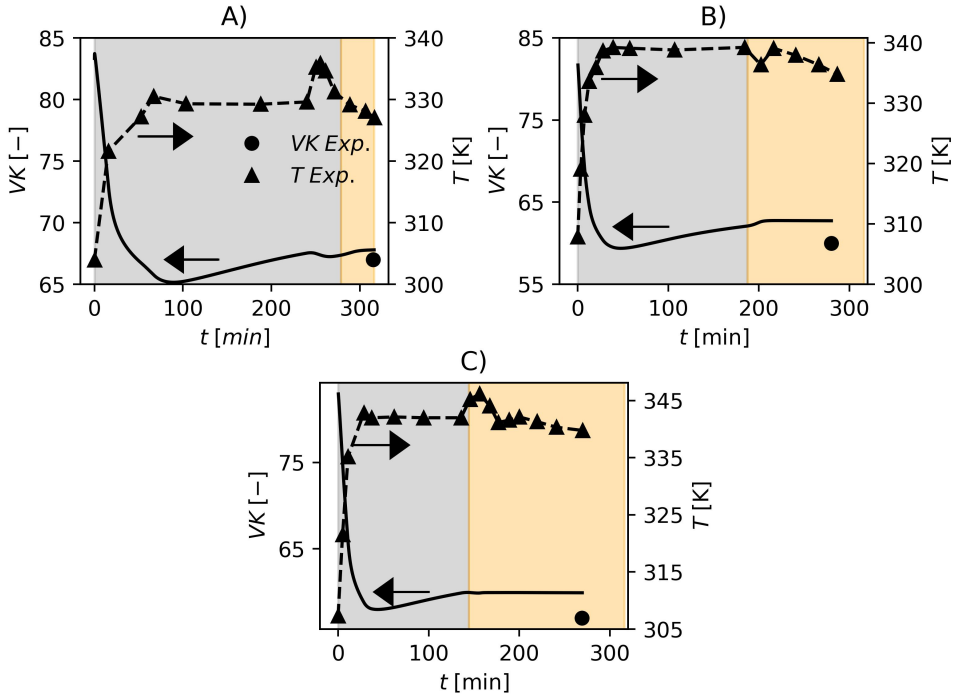

Figure 2.4: Values of VK obtained experimentally and predicted by the proposed model. (A) F1, (B) F2 and (C) F3. Gray and orange shadowed areas represent the ranges of $x \leq x_f$ and $x > x_f$, respectively.

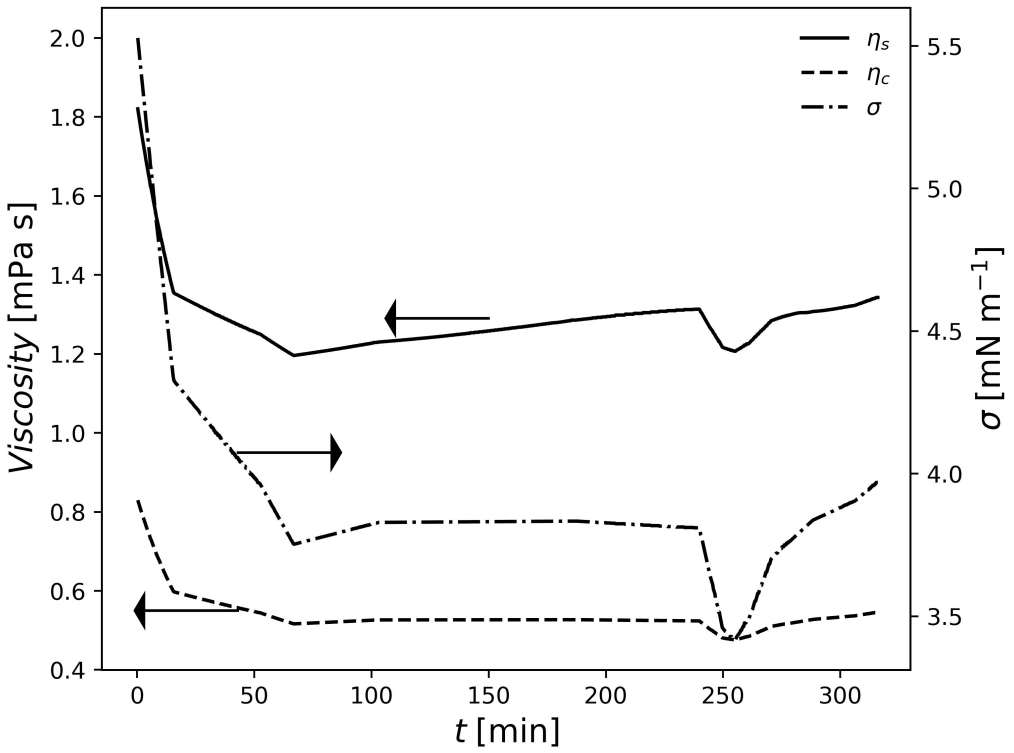

Figure 2.5: Variation of suspension properties in F1.

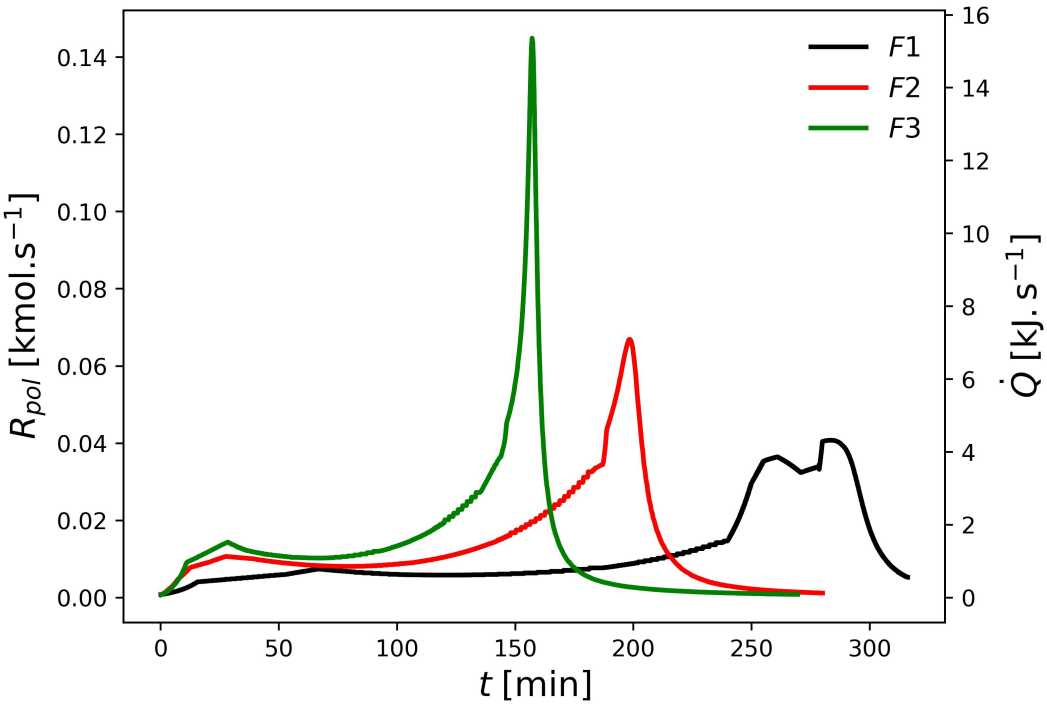

Figure 2.6: Polymerization rate and heat released in the three industrial grade formulations.

2.4.2 Estimation of Breakage and Coalescence Parameters

In the present work, two reactor types were considered. The formulation 1 (F1) was carried out in a reactor equipped with a reflux condenser on its top, while the second and third formulations (F2 and F3) were carried out in a reactor equipped only with a cooling jacket for temperature control. The top reflux condenser can significantly affect the particle nucleation mechanism (as a flow of cold monomer is continuously fed into the reactor) and the rates of breakage and coalescence inside the vessel. For instance, Cheng and Langsam (1985) observed coarsening of the particle size distribution when a top reflux condenser was used in their experiments. Moreover, these authors also found that the percentage of coarse particles was proportional to the reflux rate and this effect became negligible when the operation of the top reflux condenser was initiated after conversion of 30%, when the polymer particle approached the particle identification point, i.e., when droplet breakage and coalescence cease. Therefore, the parameter estimations were performed for each type of reactor independently. Two types of data were available for the present study: sieve tests and distributions obtained by laser scattering (Mastersizer 3000, Malvern Penalytical, UK). More specifically, the sieve tests for the three formulations were available whereas the particle size distributions by laser scattering were available only for F1 and F2 (due to internal regulations, the laser scattering tests were about to be replaced by sieve tests). In order to perform the parameter estimation, the problem 2.58 was solved with the PSO algorithm (Eberhart and Kennedy, 1995; Schwaab *et al.*, 2008) with the same parameters employed previously, except the search region, obviously. In Equation 2.58, ξ represents the final cumulative particle size distribution. The estimated parameters were c_1, c_2, c_3 and c_4 in Equations (2.47) and (2.48).

$$\min_{c_1,c_2,c_3,c_4} \sum \left(\frac{\xi_i - \xi_{i,exp}}{\xi_{i,exp}} \right)^2 \tag{2.58}$$

Subject to:

Dynamic model

The parameter sets PS1 and PS2 in Table 2.7 were estimated based on laser scattering data provided by industrial runs F1 and F2. The obtained fits are shown in Figure 2.7. According to the figure, these two parameter sets can represent the available industrial data accurately, which illustrates the flexibility of the proposed modeling approach. Even though it is tempting to compare the estimated parameter

Table 2.7: Search region and estimated parameters in the breakage and coalescence rate equations.

Parameter Set[1]	c_1	c_2	c_3	c_4
Inferior limit	1.0×10^{-7}	1.0×10^{-1}	1.0×10^{-5}	1.0×10^{5}
Superior limit	1.0×10^{-1}	1.0×10^{2}	1.0×10^{-10}	1.0×10^{10}
PS1	7.05×10^{-4}	2.85×10^{1}	8.51×10^{-8}	1.78×10^{7}
PS2	7.10×10^{-4}	2.88×10^{1}	1.56×10^{-8}	1.22×10^{7}
Coul. and Tav. (1977) [2]	8.67×10^{-2}	1.75×10^{-3}	5.90×10^{-10}	1.83×10^{13}

[1] Units are given in the list of symbols. [2] The units in Coulaloglou and Tavlarides (1977) were converted to match the units used in the present work.

sets with the values reported by Coulaloglou and Tavlarides (1977), such a comparison may not be informative due to four main reasons. Firstly, in their original work, the authors represented the breakage, coalescence and daughter droplet distributions in terms of droplet volume, as discussed previously. Secondly, the vessel employed in their study had only 12 L, while the industrial vessels considered in the present work have tens of cubic meters. Thirdly, a different system was employed in their study (water-kerosene-dichlorobenzene). Lastly, these investigators worked with very dispersed systems, where $0.025 \leq \Phi \leq 0.15$; so that Φ was significantly smaller than the values used in the present work ($\Phi \approx 0.5$)

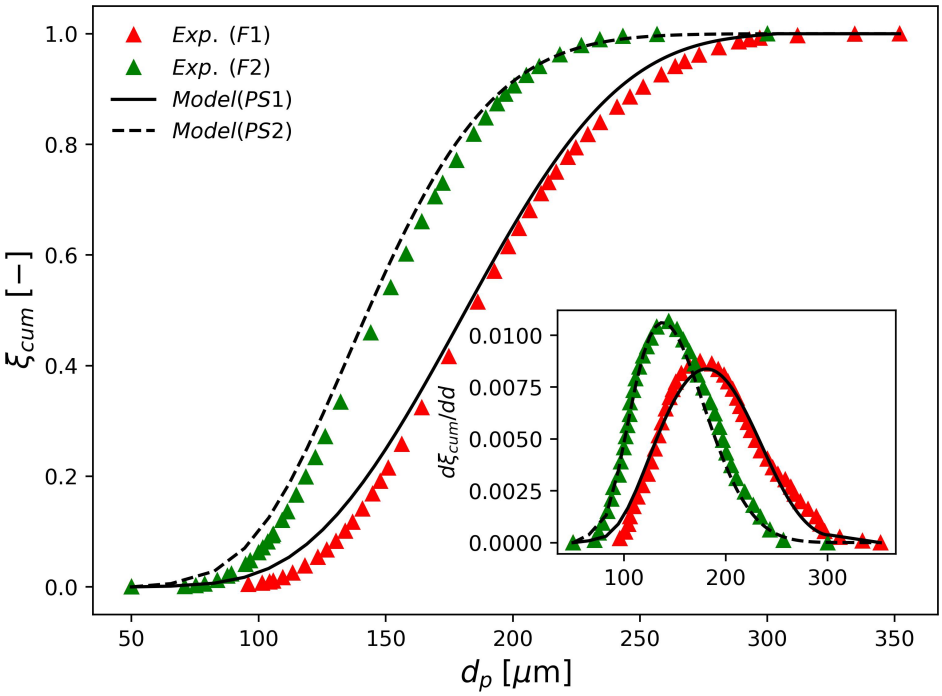

Figure 2.7: Experimental and simulated final cumulative particle size distributions obtained with parameters shown in Table 2.7.

In spite of that, as c_1 and c_3 represent the frequencies of breakage and coalescence, respectively; and c_2 and c_4 represent the efficiencies of breakage and coalescence, respectively; it can be noticed that the breakage efficiencies in the two polymerization reactors are very similar. Additionally, the breakage frequency in the reactor equipped with a top reflux condenser is also very similar to its counterpart in the reactor without a top reflux condenser, which puts in evidence the fact that the breakage mechanism in both vessels is very similar. Moreover, just to put it into perspective, the breakage efficiency proposed by Coulaloglou and Tavlarides (1977) is nearly four orders of magnitude greater than the breakage efficiencies in the industrial reactors (pay attention to the negative sings of the exponential terms in Equations (2.44) and (2.45)) whereas the breakage frequency is two orders of magnitude higher. This can be attributed to the small hold up in the smaller reactor, which favors breakage (Alvarez *et al.*, 1994; Narsimhan *et al.*, 1979; Coulaloglou and Tavlarides, 1977) and the fact that the smaller reactor is more homogeneous and have less stagnation zones. Furthermore, regarding the industrial reactors, the coalescence efficiency in the polymerization reactor with a top reflux condenser is smaller even tough the coalescence frequency is higher. This can be attributed to the effect of the top reflux condenser on the rates, as discussed previously. The coalescence efficiencies in the polymerization reactors are notably higher (6 orders of magnitude) than the efficiencies in the vessel from Coulaloglou and Tavlarides (1977), which can be attributed to larger hold up and volume also discussed previously. The coalescence frequencies in the polymerization reactors are two orders of magnitude higher than that in the smaller vessel. To the best of our knowledge, this has never been discussed in the polymerization literature.

In Figure 2.8, the droplet breakage rate constant for different hold up fractions and calculated with parameters PS1 is plotted against the droplet diameter at zero conversion. It can be seen that larger droplets are more prone to breakage, as expected. Additionally, as the hold up increases the breakage rate constant decreases which is a very known effect according to the literature (Alvarez *et al.*, 1994; Narsimhan *et al.*, 1979; Coulaloglou and Tavlarides, 1977). In Figure 2.9, the coalescence rate constant calculated with parameters PS1 is shown. According to this set of parameters, the highest coalescence rate constants are obtained between large and small droplets. On the other hand, the smaller droplets are less likely to coalesce with other small droplets. Furthermore, as the hold up fraction increases, the coalescence rate constant of droplets of intermediate sizes also increases. The coalescence rate constant plotted is symmetrical around the secondary diagonal of the plot, as expected, since $kc(\zeta, \vartheta) = kc(\vartheta, \zeta)$. As discussed in the development of the population balance model, the coalescence rate of droplets with masses ζ and

ϑ such that $\zeta + \vartheta > \zeta_{max}$ is zero because it would result in particles with masses outside the discretization range. This is the reason why the upper part of the plots are ignored.

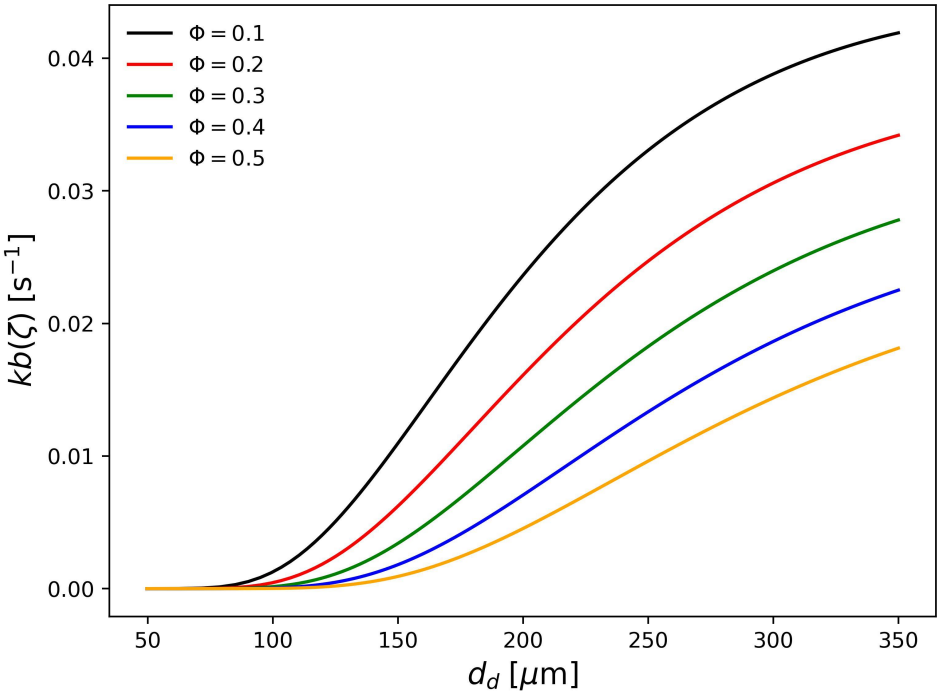

Figure 2.8: Breakage rate constant ($\eta_c = 5 \times 10^{-4}$ Pa s, $\rho_d = 840$ kg m^{-3}, $\sigma = 4.0 \times 10^{-3}$ N m^{-1}) for different dispersed phase volume fractions calculated with parameter set PS1.

In order to emphasize the difference in coalescence rates due to cold monomer refluxing, in Figure 2.10 the coalescence rate constant calculated with parameters PS2 is shown. In this case, a much more uniform profile is observed where the coalescence rate of large and small droplets is nearly the same of droplets of intermediate sizes. Based on the colorbars of the Figures 2.9 and 2.10 it is possible to affirm that the coalescence rate constant in the reactor equipped with a top reflux condenser is roughly 5 times higher than its counterpart in the reactor without cold monomer refluxing.

In Figure 2.11, it is shown the experimental and predicted sieve data for the three formulations. Even though the parameters sets PS1 and PS2 were estimated with the laser scattering data, these sets of parameters also represent the sieve data with remarkable accuracy, specially F1 and F3. The sieve data in F2 shows a slightly lower average than the model prediction, this can be attributed to additional breakage that occurs due to the shaking of the equipment during the test.

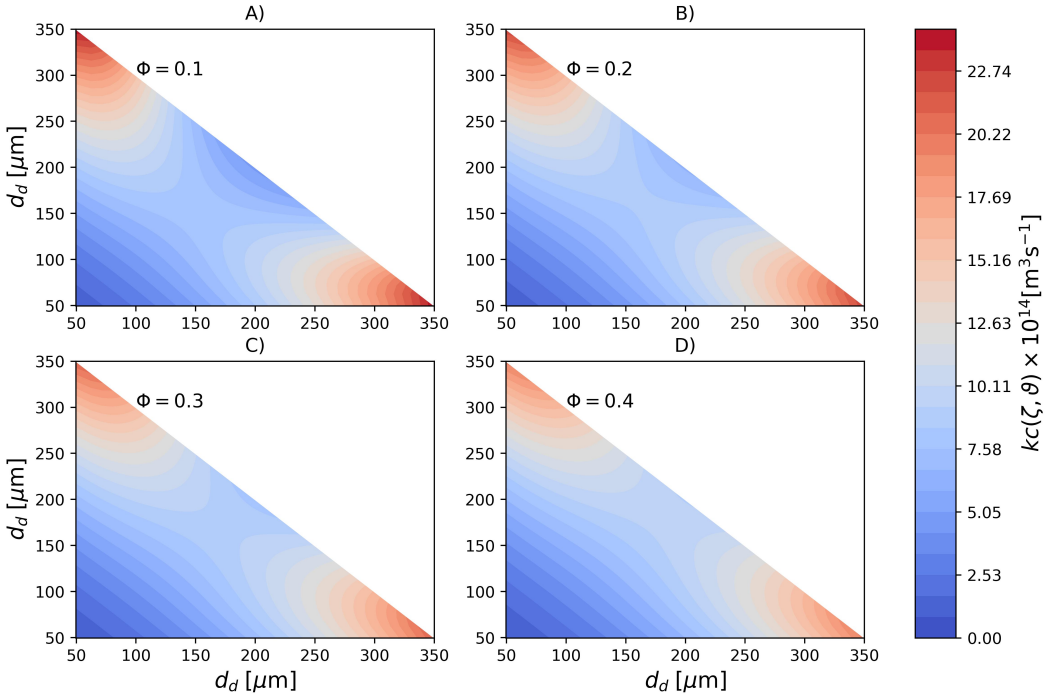

Figure 2.9: Coalescence rate constant ($\eta_c = 5 \times 10^{-4}$ Pa s, $\rho_d = 840$ kg m^{-3}, $\sigma = 4.0 \times 10^{-3}$ N m^{-1}) for different dispersed phase volume fractions calculated with parameter set PS1.

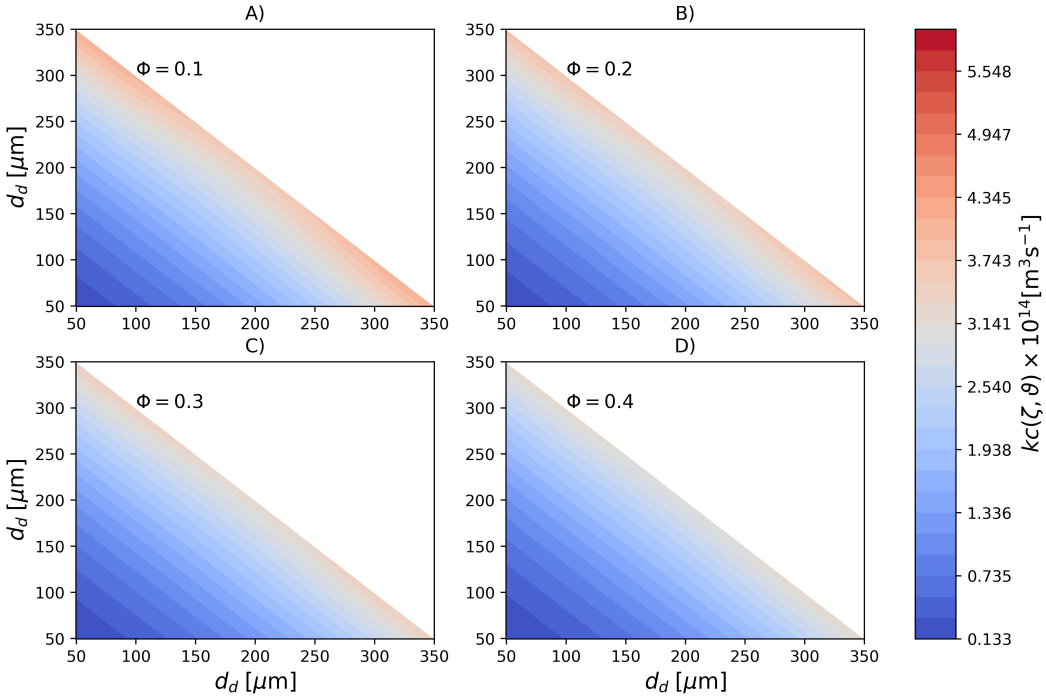

Figure 2.10: Coalescence rate constant ($\eta_c = 5 \times 10^{-4}$ Pa s, $\rho_d = 840$ kg m^{-3}, $\sigma = 4.0 \times 10^{-3}$ N m^{-1}) for different dispersed phase volume fractions calculated with parameter set PS2.

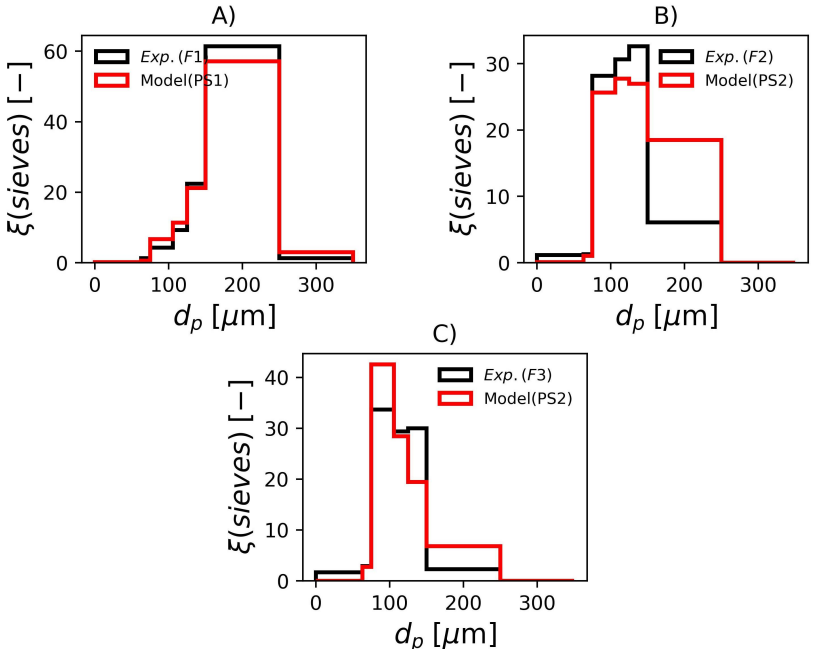

Figure 2.11: Experimental and simulated sieve data with the parameters in Table 2.7.

2.4.3 Effect of Process Variables

To be useful at the plant site, the proposed model must be able to represent the effect of operation variables on the final product properties. For this reason, in the present section, the effect of perturbations on particle properties is investigated. According to Figure 2.12, when the rotation speed is reduced by 10%, $d_{32,p}$ is increased by about 11% in operation conditions F1. On the other hand, an increase of 10% in impeller rotation causes a decrease of 8.7% in $d_{32,p}$. Regarding F2, $d_{32,p}$ increases 13.6% when the impeller speed drops by 10% and decreases by 10% when impeller rotation increases 10%. In the studied conditions, the magnitude of the change in impeller rotation causes similar changes in the particle mean diameter. However, since the formulations are different, i.e., different amounts of PVA, temperature, initiator and dispersed phase fraction, it becomes difficult to analyse the effect of the impeller speed on the rates solely. Additionally, the relationships between these variables in the rate equations is nonlinear. Consequently, to compare the rates and their effects on both reactors, it would be necessary that the same formulations be produced on each of them.

The model predictions appear to be less sensitive to changes in PVA concentration. Still regarding Figure 2.12, decreasing the PVA concentration by 50% causes a 14.4% increase in $d_{32,p}$ in F1. Additionally, an increase of 50% causes a 7% decrease

in $d_{32,p}$. With respect to F2, the 50% decrease in PVA causes 19.3% increase in $d_{32,p}$ and an increase of 50% causes 10% decrease in $d_{32,p}$. The influence of PVA concentration might be underestimated/overestimated because the model does not consider the degree of hydrolysis in the equation that represents the surface tension (σ), see Table 2.3.

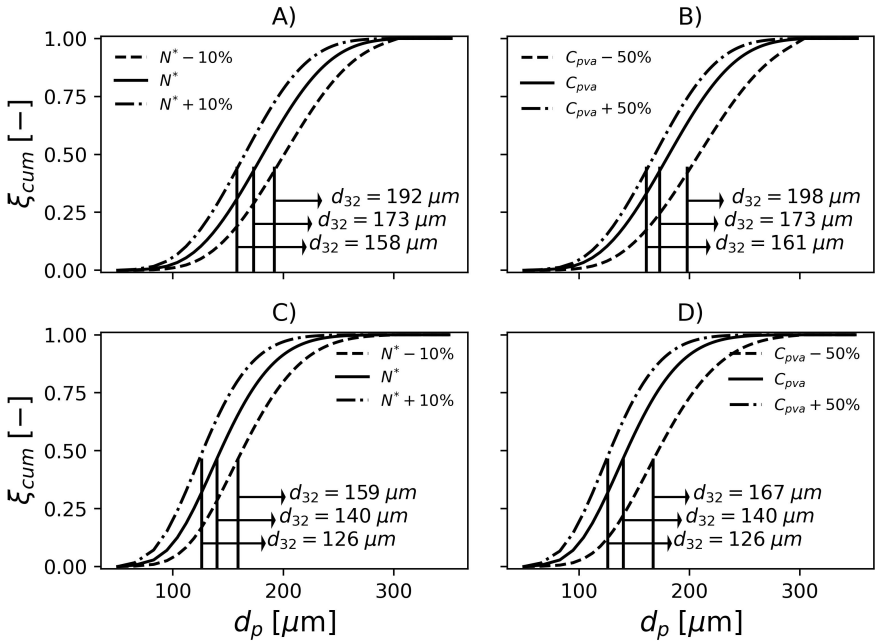

Figure 2.12: Effect of impeller rotation and PVA concentration on particle size distribution in F1, (A) and (B), respectively. Effect of impeller rotation and PVA concentration on particle size distribution in F2, (C) and (D), respectively.

2.4.4 Evolution of Mean Particle and Droplet Diameters

In Figures 2.13 and 2.14, it is shown the evolution of droplet and particle mean diameters for the conditions studied in the previous section, respectively. Additionally, the results are compared with those obtained in formulations F1 and F2. Regarding Figure 2.13, the beginning of the reaction is marked by strong droplet coalescence. Then the breakage mechanism becomes predominant until 30% conversion. The transition from pink to gray in these figures marks the point where 30% conversion is surpassed. At this point, the polymerizing monomer droplets become rigid and are not prone to breakage and coalescence according to the present model. It is possible to notice a decrease in droplet diameter as conversion advances. In fact, this is a consequence of the increasing droplet density, as the fraction of polymer increases and the density of PVC is higher than that of VCM. This shrinking phenomena continues until the end of the reaction when $x > x_f$. In Figure 2.14, it

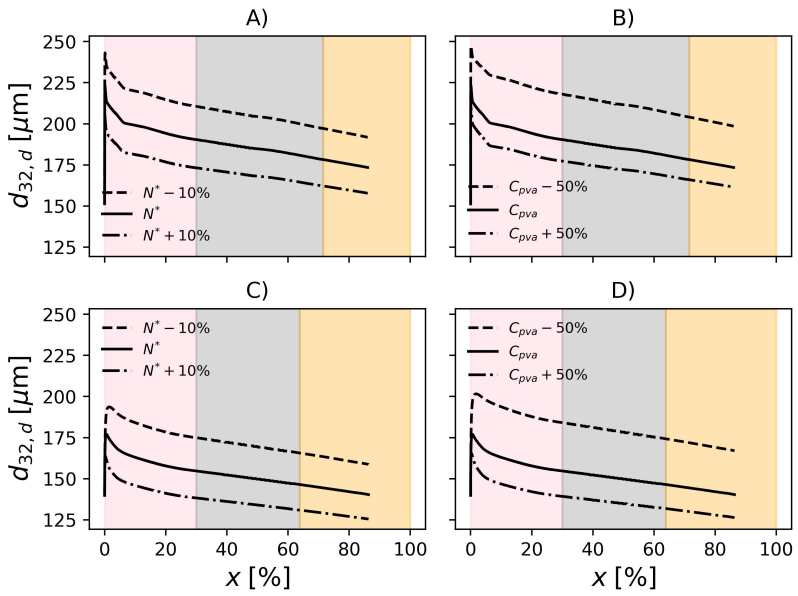

Figure 2.13: Evolution of Sauter mean diameter of the droplets . Effect of impeller rotation and PVA concentration in F1, (A) and (B), respectively. Effect of impeller rotation and PVA concentration in F2, (C) and (D), respectively. Pink, gray and orange shadowed areas represent the ranges of conversion $x \leq 30\%$, $30 < x \leq x_f$ and $x > x_f$, respectively.

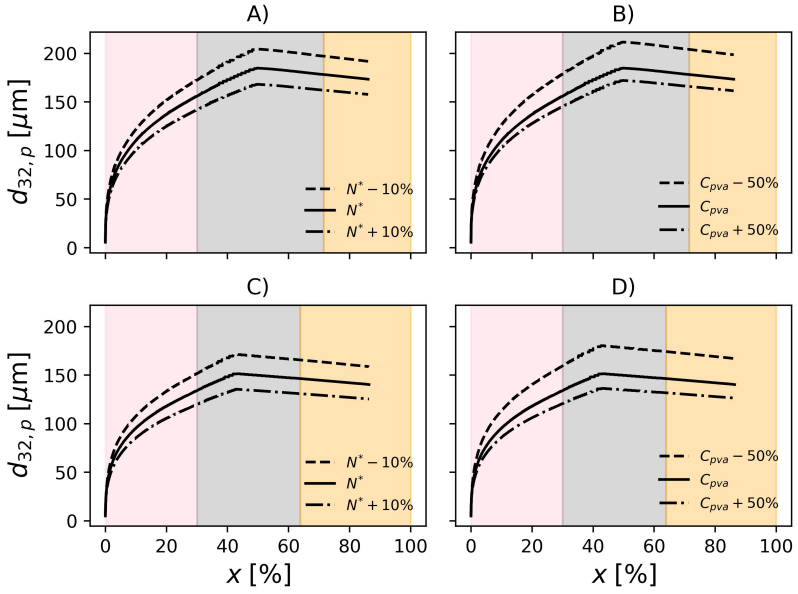

Figure 2.14: Evolution of Sauter mean diameter of the particles . Effect of impeller rotation and PVA concentration in F1, (A) and (B), respectively. Effect of impeller rotation and PVA concentration in F2, (C) and (D), respectively. Pink, gray and orange shadowed areas represent the ranges of conversion $x \leq 30\%$, $30 < x \leq x_f$ and $x > x_f$, respectively.

is possible to observe that the particle size increases with conversion, as expected, due agglomeration of primary particles to form the agglomerates, in accordance with Xie *et al.* (1991a) and Cebollada *et al.* (1989). The slight decrease $d_{32,p}$ is a consequence of the decrease in particle porosity as monomer is consumed and the particle becomes denser.

2.5 Concluding Remarks

In the present chapter, a model was built and implemented to represent the trajectories of mass inventories, pressures and polymer properties, with emphasis on the final particle size distributions in industrial scale PVC suspension polymerization reactors for the first time. It was shown that, after proper parameter estimation, the model is able to represent the operation of industrial scale reactors and describe the final particle size distributions, as measured through sieve tests and laser scattering analyses. Even tough turbulence homogeneity was assumed in the entire vessel, the obtained model predictions can be regarded as very good. Particularly, it was shown for the first time that the frequency and efficiency of breakage in the reactor equipped with a top reflux condenser were very similar to their counterparts in the reactor without a reflux condenser. However, the coalescence frequency was larger in the reactor with a top reflux condenser, which emphasizes that refluxing cold monomer to the vessel favors coalescence and tends to result in larger particles.

List of Abbreviations

Abbreviation	Meaning
CAGR	Compound Annual Growth Rate
CFD	Computational Fluid Dynamics
CLD	Chain Length Distribution
MMA	Methyl Methacrylate
MMD	Molar Mass Distribution
PE	Poly(ethylene)
PMMA	Poly(methyl methacrylate)
PP	Poly(propylene)
PVA	Poly(vinyl alcohol)
PVC	Poly(vinyl chloride)
PSO	Particle Swarm Optimization
VCM	Vinyl Chloride Monomer

List of Symbols

Symbol	Meaning
A	Free volume parameter used in kt equation [-]
B	Free volume parameter used in kp equation [-]
B_f	Free volume parameter used in $kp_2 f^{1/2}$ equation [-]
C	Free volume parameter used in kd equation [-]
c_1, c_2, c_3, c_4	Empirical constants [-]
C_{pva}	PVA concentration [kg m^{-3}]
d_p	Particle diameter [m]
d_d	Droplet diameter [m]
d_{32}	Sauter mean diameter [m]
E_1, E_2, E_3, E_4	Activation energies in the free volume parameters [K]
f	Initiator efficiency [-]
I	Initiator [kmol]
k_s	Monomer solubility [kg kg^{-1}]
k_I	Initiator partition coefficient [-]
kc	Coalescence rate constant [m^3 s^{-1}]
kb	Breakage rate constant [s^{-1}]
kp	Propagation rate constant [m^3 $kmol^{-1}$ s^{-1}]
kd	Initiator decomposition rate constant [s^{-1}]
ktm	Transfer to monomer rate constant [m^3 $kmol^{-1}$ s^{-1}]
kt	Termination rate constant [m^3 $kmol^{-1}$ s^{-1}]
ktc	Termination by combination rate constant [m^3 $kmol^{-1}$ s^{-1}]
ktd	Termination by disproportionation rate constant [m^3 $kmol^{-1}$ s^{-1}]
L	Impeller diameter [m]
m	Monomer [kg]
M	Monomer [kmol]
MM	Molar mass [kg $kmol^{-1}$]
Mn	Number average molar mass [kg $kmol^{-1}$]
Mw	Weight average molar mass [kg $kmol^{-1}$]
nk	Number of initiators [-]
nc	Number of mass classes [-]
N	Number of droplets [-]
N^*	Impeller rotation speed [Hz]
p	Polymer [kg]
P	Polymer [kmol]
$\dot{Q}$	Heat released by the reaction [kJ s^{-1}]
R	Ideal gas constant [m^3 Pa $kmol^{-1}$ K^{-1}]

R_{pol}	Polymerization rate [kmol s^{-1}]
t	Time [s]
T	Temperature [K]
T_g	Glass transition temperature [K]
V	Volume [m^3]
V_s	Suspension volume [m^3]
VK	K-Value [-]
V_f	Free volume [-]
V_{f,x_f}	Free volume at $x = x_f$ [-]
x	Conversion [-]
x_f	Critical conversion [-]
y	Volume fraction [-]
w	Water [kg]
Z	Pressure [Pa]

Subscripts	
j	Relative to phase j
1	Relative to phase 1 (monomer-rich)
2	Relative to phase 2 (polymer-rich)
3	Relative to phase 3 (aqueous phase)
4	Relative to phase 4 (gaseous phase)
m	Monomer
p	Polymer
w	Water
s	Suspension
d	Dispersed phase
c	Continuous phase
t	Total
k	Initiator type ($k = 1, ..., nk$)

Greek symbols	
ΔH	Enthalpy of reaction [kJ $kmol^{-1}$]
ϵ	Porosity [-]
λ_q	q^{th} order living polymer moment [kmol]
μ_q	q^{th} order dead polymer moment [kmol]
φ_p	Polymer volume fraction in phase 2 [-]
$\varphi_{p,d}$	Polymer volume fraction in the dispersed phase [-]
Φ	Dispersed phase volume fraction [-]
χ	Flory-Huggins interaction parameter [-]

η	Viscosity [Pa s]
$[\eta]$	Intrinsic viscosity [m^3 kg^{-1}]
ρ	Density [kg m^{-3}]
β	Daughter droplet distribution [-]
ζ, ϑ	Droplet mass [kg]
σ	Surface tension [N m^{-1}]
σ_0^2	Variance [kg^2]
Ω_i	Total mass of particles of mass i [kg]
ξ	Particle size distribution [-]

2.6 References

Abdel-Alim, A.H.; Hamielec, A.E. Bulk polymerization of vinyl chloride. Journal of Applied Polymer Science, 16, 783–799, 1972.

Abi-Ramia, N.M. Modelagem, Simulação e Otimização da Polimerização em Suspensão do PVC, Master Thesis, Universidade Federal do Rio de Janeiro, May of 2012.

Abreu, C.M.R.; Fonseca, A.C.; Rocha, N.M.P.; Guthrie, J.T.; Serra, A.C.; Coelho, J.F.J. Poly(vinyl chloride): Current status and future perspectives via reversible deactivation radical polymerization methods. Progress in Polymer Science, 87, 34-69, 2018.

Alexopoulos, A.H.; Maggioris, D.; Kiparissides, C. CFD analysis of turbulence non-homogeneity in mixing vessels a two-compartment model. Chemical Engineering Science, 57, 10, 1735-1752, 2002.

Alexopoulos, A.H.; Kiparissides, C. On the prediction of internal particle morphology in suspension polymerization of vinyl chloride. Part I: The effect of primary particle size distribution. Chemical Engineering Science, 62, 15, 3970-3983, 2007.

Alvarez, J.; Alvarez, J.; Hernández, M. A population balance approach for the description of particle size distribution in suspension polymerization reactors. Chemical Engineering Science, 49, 1, 99-113, 1994.

Bachmann, R.; Melchiors, M.; Avtomonov, E. Modelling and optimization of

nonlinear polymerization processes. Macromolecular Symposia, 370, 135-143, 2016.

Bárkányi, A.; Németh, S.; Lakatos, B.G. Modeling and simulation of suspension polymerization of vinyl chloride via population balance model. Computers and Chemical Engineering, 59, 5, 211-218, 2013.

Batchelor, G.; Green, J. The hydrodynamic interaction of two small freely-moving spheres in a linear flow field. Journal of Fluid Mechanics, 56, 2, 375-400, 1972.

Bijhanmanesh, M.J.; Etesami, N. Continuous Dosing of Fast Initiator During Vinyl Chloride Suspension Polymerization: Polymerization Rate and PVC Properties. Journal of Applied Polymer Science, 133, 41, 44079, 2016.

Bouyatiotis, B.A.; Thornton, J.D. Liquid-liquid extraction studies in stirred tanks. part I. droplet size and hold-up measurements in a seven-inch diameter baffled vessel. Institution of Chemical Engineers Symposium Series, 26, 43-50, 1967.

Bueche, F. Physical Properties of Polymers. Interscience Publishers: New York, NY, USA, pp. 112-120, 1962.

Burgess, R.H. Suspension polymerization of vinyl chloride. In: Manufacturing and Processing of PVC, Eds.: Burgess, R.H., Elsevier: Barking, England, pp. 1-27, 1982.

Burnett, G.M.; Wright, W.W. The photosensitized polymerization of vinyl chloride in tetrahydrofuran solution. III. determination of the kinetic coefficients. Proceedings of the Royal Society London. Series A. Mathematical and Physical Sciences, 221, 1144, 41-53, 1954.

Carroll, W.F.; Johnson, R.W.; Moore, S.S.; Paradis, R.A. 4 - Poly(vinyl chloride). In: Applied Plastics Engineering Handbook, Eds.: Kutz, M., William Andrew Publishing: Norwich, NY, USA, pp. 73-89, 2017.

Castor, C.A. Investigação Experimental e Modelagem de Sistemas Não-convencionais da Polimerização em Suspensão do Cloreto de Vinila. PhD Thesis, Universidade Federal do Rio de Janeiro, July of 2014.

Cebollada, A.F.; Schmidt, M.J.; Farber, J.N.; Capiati, N.J.; Vallés, E.M. Suspension Polymerization of Vinyl Chloride. I. Influence of Viscosity of Suspension Medium on Resin Properties. Journal of Applied Polymer Science, 37, 145-166,

1989.

Ceccorulli, G.; Pizzoli, M.; Pezzin, G. Effect of thermal history on T_g and corresponding C_P changes in PVC of different stereoregularities. Journal of Macromolecular Science Part B: Physics, 14, 4, 499-510, 1977.

Chatzi, E.G.; Kiparissides, C. Drop size distribution in high holdup fraction dispersion systems: Effect of the degree of hydrolysis of PVA stabilizer. Chemical Engineering Science, 49, 24, 5039-5052, 1994.

Cheng, J.T.; Langsam, M. Particle structure of PVC based on cellulosic suspension system. III. effect of monomer refluxing. Journal of Applied Polymer Science, 30, 4, 1365-1378, 1985.

Chiellini, F.; Ferri, M.; Morelli, A.; Dipaola, L.; Latini, G. Perspectives on alternatives to phthalate plasticized poly(vinyl chloride) in medical devices applications. Progress in Polymer Science, 38, 7, 1067-1088, 2013.

Chung, S.T.; Jung, S.H. Kinetic modeling of commercial scale mass polymerization of vinyl chloride. Journal of Vinyl and Additive Technology, 2, 295-303, 1996.

Coulaloglou, C.A.; Tavlarides, L.L. Description of interaction processes in agitated liquid-liquid dispersions. Chemical Engineering Science, 32, 11, 1289-1297, 1977.

Crosato-Arnaldi, A.; Gasparini, P.; Talamini, G. The bulk and suspension polymerization of vinyl chloride. Die Makromolekulare Chemie: Macromolecular Chemistry and Physics, 117, 1, 140-152, 1968.

Darvish, R.; Esfahany, M.N.; Bagheri, R. S-PVC grain morphology: A review. Industrial and Engineering Chemistry Research and Design, 54, 44, 10953-10963, 2015.

Dimian, A.; van Diepen, D.; van der Wal, G.A. Dynamic simulation of a PVC suspension reactor. Computers and Chemical Engineering, 19, 427-432, 1995.

Ekelund, M.; Edin, H.; Gedde, U.W. Long-term performance of poly(vinyl chloride) cables Part 1: Mechanical and Electrical Performances. Polymer Degradation and Stability, 92, 4, 617-629, 2007.

Faria, J.M., Jr.; Lima, E.L.; Pinto, J.C.; Machado, F. Monitoramento in situ e em tempo real de variáveis morfológicas do poli(cloreto de vinila) usando espectroscopia NIR. Polímeros, 19, 95-104, 2009.

Faria Jr, J.M.; Machado, F.; Lima, E.L.; Pinto, J.C. Monitoring of vinyl chloride suspension polymerization using NIRS 1. prediction of morphological properties. Computer Aided Chemical Engineering, 27, 327-332, 2009.

Faria Jr, J.M.; Machado, F.; Lima, E.L.; Pinto, J.C. Monitoring of vinyl chloride suspension polymerization using NIRS 2. proposition of a scheme to control morphological properties.Computer Aided Chemical Engineering, 27, 1329-1334, 2009.

Faria Jr, J.M.; Machado, F.; Lima, E.L.; Pinto, J.C. In-line monitoring of vinyl chloride suspension polymerization with near infrared spectroscopy, 1–Analysis of morphological properties. Macromolecular Reaction Engineering, 4, 1, 11-24, 2010.

Faria, J.M., Jr.; Machado, F.; Lima, E.L.; Pinto, J.C. In-line monitoring of vinyl chloride suspension polymerization with near infrared spectroscopy, 2–Design of an advanced control strategy. Macromolecular Reaction Engineering, 4, 8, 486-498, 2010.

Fedors, R.F. A universal reduced glass transition temperature for liquids. Journal of Polymer Science, 17, 719-722, 1979.

Feldman, M.L.; Goodman, D.; Koral, M.; Miller, R.S.; Stanaback, R.J. Process for the removal of vinyl chloride from aqueous slurries of vinyl chloride polymers. Tenneco Chemicals, United States Patent Number 4229569, 1980.

Gelbard, F.; Seinfeld, J.H. The general dynamic equation for aerosols. theory and application to aerosol formation and growth. Journal of Colloid and Interface Science, 68, 2, 363-382, 1979.

Green, D.W.; Perry, R.H. Perry's Chemical Engineers' Handbook, 8th ed.; McGraw Hill: New York, USA, 2008.

Guo, Y.; Leroux, F.; Tian, W.; Li, D.; Tang, P.; Feng, Y. Layered double hydroxides as thermal stabilizers for poly(vinyl chloride): A review. Applied Clay Science, 211, 106198, 2021.

Guo, R.; Yu, E.; Liu, J.; Wei, Z. Agitation transformation during vinyl chloride

suspension polymerization: Aggregation morphology and PVC properties. RSC Advances, 7, 24022, 2017.

Hakkarainen, M. New PVC materials for medical applications—The release profile of PVC/polycaprolactone-polycarbonate aged in aqueous environments. Polymer Degradation and Stability, 80, 3, 451-458, 2003.

Hamielec, A.E.; Gomez-Vaillard, R.; Marten, F.L. Diffusion-controlled free radical polymerization. effect on polymerization rate and molecular properties of polyvinyl chloride. Journal of Macromolecular Science - Chemistry, 17, 6, 1005-1020, 1982.

Hidy, G.M. On the theory of the coagulation of noninteracting particles in brownian motion. Journal of Colloid Science, 20, 123-144, 1965.

Hsia, M.A.; Tavlarides, L.L. A simulation model for homogeneous dispersions in stirred tanks. Chemical Engineering Journal, 20, 3, 225-236, 1980.

Hsia, M.A.; Tavlarides, L.L. Simulation analysis of drop breakage, coalescence and micromixing in liquid-liquid stirred tanks. Chemical Engineering Journal, 26, 3, 189-199, 1983.

Hughes, W.G. Process for the removal of vinyl chloride from aqueous dispersions of vinyl chloride resins. Tenneco Chemicals, United States Patent Number 4228273, 1980.

Islam, I.; Sultana, S.; Ray, S.W.; Nur, H.P.; Hossain, M.T.; Ajmotgir, W.M. Electrical and tensile properties of carbon black reinforced polyvinyl chloride conductive composites. Journal of Carbon Research, 4, 1, 2018.

Kanking, S.; Pulngern, T.; Rosarpitak, V.; Sombatsompop, N. Temperature profiles and electric energy consumption for wood/Poly(vinyl chloride) composite and fibre cement board houses. Journal of Building Engineering, 42, 102784, 2021.

Kennedy, J.; Eberhart, R. Particle Swarm Optimization. Proceedings of the IEEE International Conference on Neural Networks, 4, 1942-1948, 1995.

Kim, S.H.; Lee, J.H.; Braatz, R.D. Multi-scale fluid dynamics simulation based on MP-PIC-PBE method for PMMA suspension polymerization. Computers and Chemical Engineering, 152, 107391, 2021.

Kiparissides, C. Challenges in particulate polymerization reactor modeling and optimization: A population balance perspective. Journal of Process Control, 16, 3, 205-224, 2006.

Kiparissides, C.; Alexopoulos, A.; Roussos, A.; Dompaziz, G.; Kotoulas, C. Population balance modeling of particulate polymerization processes. Industrial and Engineering Chemistry Research, 43, 23, 7290-7302, 2004.

Kiparissides, C. Modeling of suspension vinyl chloride polymerization: From kinetics to particle size distribution and PVC grain morphology. Advances in Polymer Science, 280, 121-194, 2018.

Kiparissides, C. Polymerization reactor modeling: A review of recent developments and future directions. Chemical Engineering Science, 51, 10, 1637-1659, 1996.

Kiparissides, C.; Pladis, P. On the prediction of suspension viscosity, grain morphology, and agitation power in SPVC reactors. Canadian Journal of Chemical Engineering, 100, 4, 714-730, 2022.

Kiparissides, C.; Daskalakis, G.; Achilias, D.S.; Sidiropoulou, E. Dynamic simulation of industrial poly(vinyl chloride) batch suspension polymerization reactors. Industrial and Engineering Chemistry Research and Design, 36, 4, 1253-1267, 1997.

Kobayashi, T.; Amano, T.; Okuno, Y.; Kurihara, H.; Kurokawa, T. Process for preparing vinyl chloride polymer under specified pressure. Shin-Etsu Chemical Co., United States Patent Number 005739222A, 1998.

Koolivand, A.; Shahrokhi, M.; Farahzadi, H. Optimal control of molecular weight and particle size distributions in a batch suspension polymerization reactor. Iranian Polymer Journal, 28, 735-745, 2019.

Korosi, A.; Fabuss, B.M. Viscosity of liquid water from 25^{o} to 150^{o}. measurements in pressurized glass capillary viscometer. Analytical Chemistry, 40, 1, 157-162, 1968.

Kotoulas, C.; Kiparissides, C. A generalized population balance model for the prediction of particle size distribution in suspension polymerization reactors. Chemical Engineering Science, 61, 2, 332-346, 2006.

Kuchanov, S.I.; Bort, D.N. Kinetics and mechanism of bulk polymerization of

vinyl chloride. Vysokomol. Soyed., A15, 10, 2393-2412, 1973.

Kumar, S.; Ramkrishna, D. On the solution of population balance equations by discretization - I. a fixed pivot technique. Chemical Engineering Science, 51, 8, 1311-1332, 1996.

Kwon, C.W.; Chang, P. Influence of alkyl chain length on the action of acetylated monoglycerides as plasticizers for poly (vinyl chloride) food packaging film. Food Packaging and Shelf Life, 27, 100619, 2021.

Lazrak, N.; Le Bolay, N.; Ricard, A. Droplet stabilization in high holdup fraction suspension polymerization reactors. European Polymer Journal, 34, 11, 1637-1647, 1998.

Lerner, F.; Nemet, S. Effects of poly(vinyl acetate) suspending agents on suspension polymerisation of vinyl chloride monomer. Plastics, Rubber and Composites, 28, 3, 100-104, 1999.

Lewin, D.R. Modelling and control of an industrial PVC suspension polymerization reactor. Computers and Chemical Engineering, 20, S865-S870, 1996.

Machado, F.; Lima, E.L.; Pinto, J.C. A review on suspension polymerization processes. Polimeros, 17, 166-179, 2007.

Machado, R.A.F.; Pinto, J.C.; Araújo, P.H.H.; Bolzan, A. Mathematical modeling of polystyrene particle size distribution produced by suspension polymerization. Brazilian Journal of Chemical Engineering, 17, 395-407, 2000.

Maggioris, D.; Goulas, A.; Alexopoulos, A.H.; Chatzi, E.G.; Kiparissides, C. Prediction of particle size distribution in suspension polymerization reactors: Effect of turbulence nonhomogeneity. Chemical Engineering Science, 55, 20, 4611-4627, 2000.

Máriási, B. On the particle formation mechanism of poly(vinyl chloride)(PVC) powder produced by suspension polymerization-development of external morphology of particles. Journal of Vinyl Technology, 8, 1, 20-26, 1986.

Marinho, R.; Horiuchi, L.; Pires, C.A. Effect of stirring speed on conversion and time to particle stabilization of poly(vinyl chloride) produced by suspension polymerization process at the beginning of reaction. Brazilian Journal of Chemical Engineering, 35, 631-640, 2018.

Mastan, E.; Zhu, S. Method of moments: A versatile tool for deterministic modeling of polymerization kinetics. European Polymer Journal, 68, 139-160, 2015.

Mejdell, T.; Pettersen, T.; Naustdal, C.; Svendsen, H.F. Modelling of industrial S-PVC reactor. Chemical Engineering Science, 54, 13-14, 2459-2466, 1999.

Mijangos, C.; Calafel, I.; Santamaría, A. Poly(vinyl chloride), a historical polymer still evolving. Polymer, 266, 125610, 2023.

Mikos. A.G.; Takoudis, C.G.; Peppas, N.A. Reaction engineering aspects of suspension polymerization. Journal of Applied Polymer Science, 31, 8, 2647-2659, 1986.

Nagy, D.J. A Mark-Houwink equation for poly(vinyl alcohol) from sec-viscometry. Journal of Liquid Chromatography, 16, 14, 3041-3058, 1993.

Narsimhan, G.; Gupta, J.P.; Ramkrishna, D. A model for transitional breakage probability of droplets in agitated lean liquid-liquid dispersions. Chemical Engineering Science, 34, 2, 257-265, 1979.

Nilsson, H.; Silvergreen, C.; Törnell, B. Swelling of PVC latex particles by VCM. European Polymer Journal, 14, 9, 737-741, 1978.

Nilsson, H.; Silvergren, C.; Tornell, B. Suspension stabilizers for PVC production I: Interfacial tension measurements. Journal of Vinyl Technology, 7, 3, 112-118, 1985.

Okaya, T. Modification of Polyvinyl Alcohol by Copolymerization. In: Polyvinyl Alcohol Developments; Ed.: Finch, C.A.; Wiley: Hoboken, New Jersey, USA, 1992.

Park, G.S.; Smith, D.G. Vinyl chloride studies. II. initiation and termination in the homogeneous polymerization of vinyl chloride. Die Makromolekulare Chemie: Macromolecular Chemistry and Physics, 131, 1, 1-6, 1970.

Petzold, L.R. Description of DASSL: A differential/Algebraic System Solver; Sandia National Labs.: Livermore, CA, USA, 1982.

Pinto, M.C.C.; Santos, J.G.F., Jr.; Machado, F.; Pinto, J.C. Suspension polymerization processes. In: Encyclopedia of Polymer Science and Technology; Wiley: Hoboken, New Jersey, USA, 2013.

Pinto, J.C. Vinyl chloride suspension polymerization with constant rate. a numerical study of batch reactors. Journal of Vinyl Technology, 12, 1, 7-12, 1990.

Pinto, J.C. Dynamic behavior of continuous vinyl chloride bulk and suspension polymerization reactors. a simple model analysis. Polymer Engineering and Science, 30, 5, 291-302, 1990.

Pinto, J.C. Dynamic behavior of continuous vinyl chloride suspension polymerization reactors: effects of segregation. Polymer Engineering and Science, 30, 15, 925-930, 1990.

Pinto, J.M.; Giudici, R. Optimization of a cocktail of initiators for suspension polymerization of vinyl chloride in batch reactors. Chemical Engineering Science, 56, 3, 1021-1028, 2001.

Precedence Research. Available online: `https://www.precedenceresearch.com/pvc-pipes-market` (accessed on 7 February 2023).

Reding, F.P.; Walter, E.R.; Welch, F.J. Glass transition and melting point of poly(vinyl chloride). Journal of Polymer Science, 56, 163, 225-231, 1962.

Saeki, Y.; Emura, T. Technical progresses for PVC production. Progress in Polymer Science, 27, 10, 2055-2131, 2002.

Schwaab, M.; Biscaia, E.C.; Monteiro, J.L.; Pinto, J.C. Nonlinear parameter estimation through particle swarm optimization. Chemical Engineering Science, 63, 6, 1542-1552, 2008.

Si, K. Kinetics and Mechanism of Vinyl Chloride Polymerization: Effects of additives on Polymerization Rate, Molecular Weight and Defect Concentration in the Polymer. Doctoral Dissertation, Case Western Reserve University, Cleveland, OH, USA, May 2007.

Sidiropoulou, E.; Kiparissides, C. Mathematical modeling of PVC suspension polymerization: a unifying approach and some new results. Journal of Macromolecular Science - Chemistry, 27, 3, 257-288, 1990.

Skillicorn, D.E.; Perkins, G.G.A.; Slark, A.; Dawkins, J.V. Molecular weight and solution viscosity characterization of PVC. Journal of Vinyl Technology, 15, 2, 105-108, 1993.

Smallwood, P.V. The formation of grains of suspension poly(vinyl chloride). Polymer, 27, 10, 1609-1618, 1986.

Solsvik, J.; Jakobsen, H.A. The foundation of the population balance equation: a review. Journal of Dispersion Science and Technology, 36, 4, 510-520, 2015.

Sovová, H. Breakage and coalescence of drops in a batch stirred vessel-II comparison of model and experiments. Chemical Engineering Science, 36, 9, 1567-1573, 1981.

Tacidelli, A.R.; Alves, J.J.N.; Vasconcelos, L.G.S.; Brito, R.P. Increasing PVC suspension polymerization productivity - an industrial application. Chemical Engineering Processing: Process Intensification, 48, 1, 485-492, 2009.

Talamini, G. The heterogeneous bulk polymerization of vinyl chloride. Journal of Polymer Science, 4, 3, 535-537, 1966.

Talamini, G.; Visentini, A.; Kerr, J. Bulk and suspension polymerization of vinyl chloride: the two-phase model. Polymer, 39, 10, 1879-1891, 1998.

Ugelstad, J.; Flogstad, H.; Hertzberg, T.; Sund, E. On the bulk polymerization of vinyl chloride. Die Makromoleckulare Chemie: Macromolecular Chemistry and Physics, 164, 1, 171-181, 1973.

Valentas, K.J; Bilous, O.; Amundson, N.R. Analysis of breakage in dispersed phase systems. Industrial and Engineering Chemistry Fundamentals, 5, 2, 271-279, 1966.

Valentas, K.J.; Amundson, N.R. Breakage and coalescence in dispersed phase systems. Industrial and Engineering Chemistry Fundamentals, 5, 4, 533-542, 1966.

Vermeulen, T.; Williams, G.M.; Langlois, G.E. Interfacial area in liquid-liquid and gas-liquid agitation. Chemical Engineering Progress, 51, 85-94, 1955.

Vrentas, J.S.; Duda, J.L. Diffusion in polymer-solvent systems. I. Reexamination of the free-volume theory. Journal of Polymer Science, 15, 403-416, 1977.

Wieme, J.; De Roo, T.; Marin, G.B.; Heynderickx, G.J. Simulation of pilot- and industrial-scale vinyl chloride batch suspension polymerization reactors. Industrial and Engineering Chemistry Research, 46, 4, 1179-1196, 2007.

Wypych, G. PVC Degradation and Stabilization, 3rd ed.; ChemTec Publishing: Toronto, Canada, 2015; pp. 25–45, 2015.

Xie, T.Y.; Hamielec, A.E.; Wood, P.E.; Woods, D.R. Experimental investigation of vinyl chloride polymerization at high conversion: Mechanism, kinetics and modelling. Polymer, 32, 2, 537-557, 1991a.

Xie, T.Y.; Hamielec, A.E.; Wood, P.E.; Woods, D.R. Experimental investigation of vinyl chloride polymerization at high conversion—Reactor dynamics. Journal of Applied Polymer Science, 43, 7, 1259-1269, 1991b.

Xie, T.Y.; Hamielec, A.E.; Wood, P.E.; Woods, D.R. Experimental investigation of vinyl chloride polymerization at high conversion: Semi-batch reactor modelling. Polymer, 32, 11, 2087-2095, 1991c.

Xie, T.Y.; Hamielec, A.E.; Wood, P.E.; Woods, D.R. Experimental investigation of vinyl chloride polymerization at high conversion: Molecular-weight development. Polymer, 32, 6, 1098-1111, 1991d.

Xie, T.Y.; Hamielec, A.E.; Wood, P.E.; Woods, D.R. Suspension, bulk, and emulsion polymerization of vinyl chloride—Mechanism, kinetics, and reactor modelling. Journal of Vinyl Technology, 13, 1, 2-25, 1991e.

Yuan, H.G.; Kalfas, G.; Ray, W.H. Suspension Polymerization. Journal of Macromolecular Science, Part C: Polymer Reviews, 31, 2-3, 215-299, 1991.

Chapter 3

Literature Review and Theoretical Foundations

This chapter presents a comprehensive literature review of the state-of-the-art in continuous suspension polymerization and Oscillatory Baffled Reactors (OBR). Regarding continuous suspension polymerization, it is shown that very few works are found in the open literature. This can be mainly attributed to the inherent technological problems that pertain this subject. Concerning OBR technology, an attempt is made to offer a chronological perspective of the field, initially focusing on the works that laid down the theoretical foundations for the development of this technology. For the sake of conciseness, the OBR section was divided into six subsections: oscillatory flow mixing, heat transfer, power dissipation, droplet size distributions, scale-up, and applications to suspension polymerizations. The reader must be aware that throughout this chapter, the terms Oscillatory Baffled Reactor, Oscillatory Flow Reactor (OFR), Oscillatory Baffled Column (OBC), and Oscillatory Baffled Tube (OBT) will be used interchangeably. The choice of the term will depend on the preference of the author being reviewed. Attention must also be paid to the fact that the acronym OBR itself is insufficient to describe the equipment studied since there are different baffle types, configurations, geometries, and operation modes. Consequently, when discussing specific works, emphasis will also be given to the extra information that characterizes the device. Naturally, this review tries to reach a compromise between what is necessary to understand the OBR and what is relevant to this Thesis. As such, the works were selected based on this criterion.

3.1 Continuous Suspension Polymerization

To the best of our knowledge, no commercial industrial process is currently available to produce suspension polymers in continuous mode. In addition, few articles and patent applications explore this topic, as recently reviewed by Lima *et al.* (2023). Particularly, the scarce patent documents are mostly focused on the polymerization of vinyl chloride.

Shanta (1954) disclosed a device for conducting continuous polymerization of vinyl monomers such as vinyl acetate, acrylonitrile, methyl methacrylate, dichlorostyrene, and styrene. The reaction device comprised a cylindrical vessel with a height larger than the diameter and an extension of a smaller diameter. The agitation of the suspension was guaranteed by the use of a stirrer and bubbling inert gas from the bottom of the device. Furthermore, a cooling jacket was employed to guarantee the control of the temperature.

Stark (1961) disclosed a system formed by a series of connected vessels to carry out the continuous suspension polymerization of vinyl monomers. According to the author, the number of vessels should range from 5 to 10. The reactor contents should flow by gravity from one vessel to another, and each vessel should contain an independent stirring device to ensure homogeneity. To avoid clogging, the author recommends using an inert gas stream in the first vessel to ensure that the system pressure is higher than the vapor pressure of the reacting mixture. Consequently, the gas flow rate should guarantee the suspension flow in the whole system.

Krause and Wolf (1966) presented a rotationally symmetrical device to perform the continuous emulsion or suspension polymerization of unsaturated monomers, including vinyl chloride and vinyl acetate. The apparatus consisted of a vertical tower with a central shaft and discs attached. The discs were separated from the walls by narrow annular openings. The system was designed to avoid backmixing among the spaces between two consecutive discs (chambers).

Wolf and Goetze (1975) disclosed a very complex device that comprised a vertical tower where a vertical shaft was installed. This tubular reacting space was additionally divided into chambers. These chambers were connected by openings in the separating elements. Each chamber was equipped with ring pipelines which were connected by the opposite sides of the chamber.

Hatate *et al.* (1981) studied the effects of ultrasonic irradiation on the interaction among droplets and the reactor walls in batch and continuous mode in styrene suspension polymerization. The authors found that ultrasonic irradiation prevented agglomeration and sticking of droplets to the reactor walls in the range of analyzed operational conditions. These results were particularly interesting because droplet deposition on the walls can impair the continuous operation of these processes. Despite that, this technology has not gained widespread use, possibly due to the high costs of ultrasonic irradiation devices. In a posterior work, Hatate *et al.* (1984) employed a Monte Carlo method to investigate the continuous suspension polymerization of styrene.

Klippert *et al.* (1984) described a device comprising three zones for vinyl chloride polymerization. The first zone was a vertical tank where monomer conversions should attain values around 10 wt%. The last two zones were constituted by tubular reactors with length to diameter ratio of at least 4. The authors emphasized the absence of internals in the tubular reactors and the operation in plug flow regime to avoid incrustation and to achieve narrow particle size distributions, respectively.

Pinto (1990) investigated the dynamic behavior of continuous vinyl chloride suspension polymerization. The author developed a simple dynamic model and identified ranges where complex phenomena, including the development of limit cycles and steady-state isolas, might occur in adiabatic and non-adiabatic reactors. The effects of operation parameters, such as residence time and heat exchange coefficient, on the observed complex nonlinear responses were investigated.

Dowding *et al.* (2000) investigated the continuous suspension polymerizations of divinylbenzene in a continuous tubular reactor. The authors argued that using a reactor made of poly(tetrafluoroethylene) might allow the minimization of fouling. Additionally, the use of additives to increase the density of the organic phase might also mitigate fouling. Compared to samples obtained in batch mode, the particle size distributions of the particles obtained in continuous mode were narrower. Similar results were obtained in a posterior work by Dowding *et al.* (2001), where the emulsion feed was prepared with the help of a purpose-built cross-flow membrane.

Liu *et al.* (2011) studied the polymerization of butyl acrylate in a coaxial capillary microreactor. The authors emphasized the improvements in polymer properties, such as the molar mass distribution, compared to polymers produced in standard batch vessels. The improved heat transfer of this type of reactor was also pointed out.

Dirix *et al.* (2016) presented a method to carry out either polymerization or copolymerization of vinyl chloride using at least two reactors in series. The authors argued that the first continuous stirred tank reactor should preferably achieve conversion of up to 60 wt.%. Additionally, this arrangement would achieve higher molar masses than the equivalent batch process and use less initiator.

Hong *et al.* (2019) presented a method to produce poly(vinyl chloride) (PVC) through suspension polymerization utilizing at least three zones of microreactors connected in series. Each microreactor set comprised several microchannels. The authors emphasized that the diameter of the microchannels should be sufficiently large to avoid clogging due to the unavoidable agglomeration of droplets that inherently occur in PVC suspension polymerizations. The temperature control of each of these zones was performed independently.

Lima *et al.* (2023) presented a comprehensive survey on the challenges regarding continuous suspension polymerization of vinyl chloride monomer. The authors investigated both patent and article documents. It was found that one of the main problems associated with the continuous production of suspension polymers is the deposition of material on the walls of the reactor. Furthermore, the authors pointed out that microreactor technology and continuous oscillatory baffled reactors (COBR) are very promising in tackling the problems associated with continuous operation.

3.2 Oscillatory Baffled Reactors

Before addressing specific aspects of OBRs, it is important to overview this mixing/reaction device briefly. The basic idea behind the development of this technology is that the rates of mixing in a tube equipped with baffle inserts can be enhanced by imposing an oscillatory flow component. This idea has gained increasing attention since the 1980s, as shown in the next sections, and several investigators have attempted to investigate different operation modes, baffle types, and geometric parameters that affect the performance of these vessels.

Regarding the operation mode, either batch or continuous can be performed. In the latter case, the oscillatory flow is superimposed on a net flow component. In order to obtain efficient mixing, the oscillatory flow must dominate over the net flow. Since the earlier works used mainly single-orifice sharp-edged baffles, it is common to find definitions such as in Avila *et al.* (2022): "The continuous oscillatory baffled reactor (OBR) is a particular type of tubular reactor, typically equipped

with periodically located sharp-edged baffles along its length." According to this definition, even though not clearly stated, it can be implied that other baffle types can be used as inserts. Moreover, there are configurations where the pulsation is achieved by moving the baffles attached to rods instead of oscillating the fluid by means of a piston.

To facilitate the comprehension of the upcoming sections, Figure 3.1 shows the common baffle types used by different investigators. This figure must be used as a reference throughout this chapter. Additionally, Figure 3.2 taken from the work of Jian and Ni (2005) illustrates the mechanism that gives rise to efficient mixing in a tube with shape-edged orifice baffles and oscillatory flow provided by a piston (even though a piston is not shown). According to Figure 3.2, as the piston accelerates, pulling the fluid upward, in situation A to B, vortex rings, or eddies are formed downstream of the baffles and start to fill the space between them. Then, as the piston reaches its maximum position and begins the downward movement (flow reversal), in situation C to D, the vortex formed is swept in the main bulk flow and interacts with other vortices before repeating the cycle. This mechanism of vortice formation and how they interact with each other governs the mixing regime (Jian and Ni, 2005).

Based on an ingenuous investigation of Figure 3.2, a few provocative questions may arise. Firstly, how do the oscillatory conditions (frequency and amplitude) influence the size of the eddies formed? How does the distance between baffles affect the way eddies interact? How does the size of the orifice influence this process? Is the cavity inter-baffles behaving as a perfectly stirred tank? How can the mixing regime be quantified in terms of the operation conditions? In the case of continuous operation, what is the contribution of the continuous net flow to this process? How are the heat and mass transfers affected? In a liquid-liquid dispersion, how is the nature of the droplets affected? Lastly, but not least importantly, how does this mechanism occur in a tube with another baffle type? In fact, these are some of the questions the investigators have attempted to answer in the last three decades. Without further ado and with the concepts of the previous paragraphs and these questions in mind, a comprehensive literature review of this topic is presented in the next subsections.

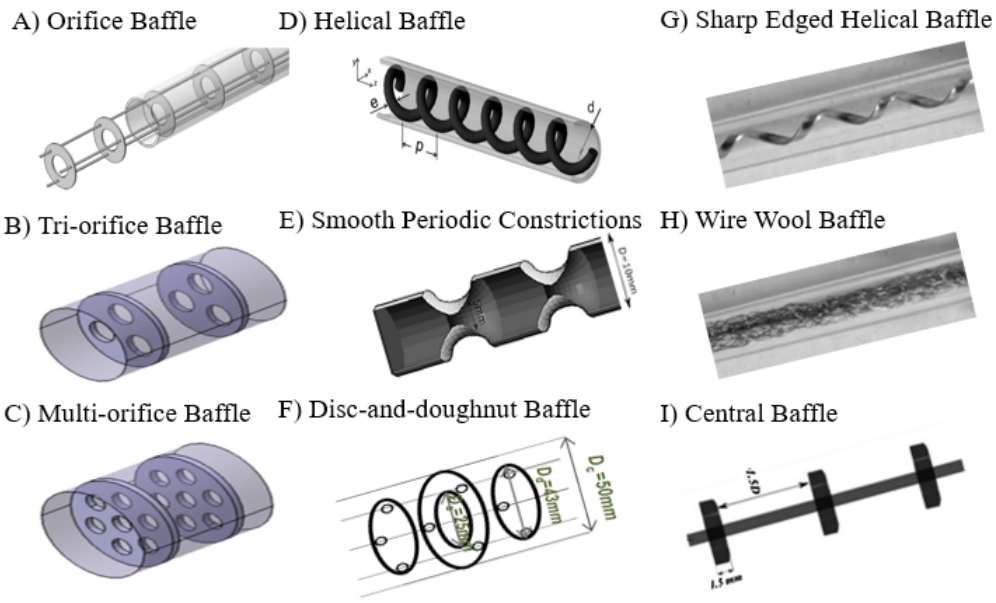

Figure 3.1: Baffle types commonly used. A) from González-Juárez *et al.* (2018), B,C) from González-Juárez *et al.* (2017), D) from Solano *et al.* (2012), E) from Ahmed *et al.* (2018a), F) from Lobry *et al.* (2013), G,H) from McDonough *et al.* (2015), and I) from Ahmed *et al.* (2018b).

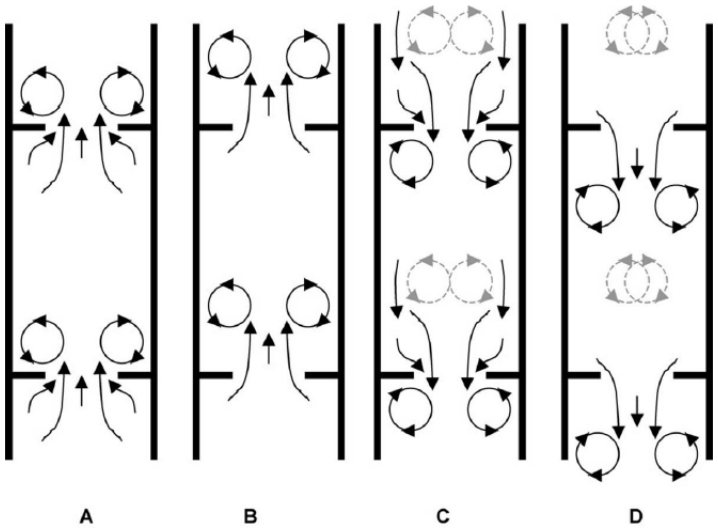

Figure 3.2: Eddies formation mechanism (Jian and Ni, 2005).

3.2.1 Oscillatory Flow Mixing

The second half of the 1980s witnessed the onset of interest in investigating oscillatory flow in non-smooth tubes following the pioneering work of Knott and Mackley (1980), who observed earlier that this type of flow on sharp-edged geometries gives rise to complex flow patterns. The first attempt to investigate in detail the flow patterns and energy losses in such devices was provided by Brunold *et al.* (1989). More specifically, these authors investigated experimentally how flow oscillations influence fluid patterns in ducts containing baffles and sharp edges individually. In the first experimental setup, the authors considered a manometer-type rectangular sectioned geometry containing sharp edges at the bottom. According to the results obtained in this experiment, the authors concluded that fluid oscillation can generate complex fluid patterns and flow separation near the sharp edges. The same was not observed when the experiment was conducted without sharp edges. Based on their observations, the authors were able to scratch the eddy formation mechanism and their injection from the edges into the main flow.

Regarding the circular duct geometry, the authors conducted experiments with and without orifice baffles inserted in the central lower tube. In this setup, Brunold and co-workers were able to track the formation of eddies at different oscillation amplitudes. Additionally, different inter-baffle spacings were tested, and it was concluded that 1.5 tube diameters was the configuration that gave the most effective mixing in the radial direction. Indeed, these authors reported that intense mixing occurred in the range of oscillatory Reynolds number, Equation (3.1), $300 \leq Re_o \leq 100000$ and Strouhal number, Equation (3.2), $10^{-2} \leq St \leq 1$. The oscillatory Reynolds number is a modification of the conventional Reynolds number (Equation (3.3)), and it is used to describe oscillatory flows. According to Avila *et al.* (2022), the St compares the eddy propagation, related to the oscillation amplitude, and the tube diameter. Abbott *et al.* (2013) points out that large St values imply small oscillation amplitudes and poor vortex formation; the opposite situation is also true. These dimensionless groups are the main parameters that characterize the oscillatory flow regime. Ni and Gough (1997) presented a discussion on these dimensionless groups. More specifically, these authors criticized that neither the orifice diameter nor the baffle spacing were present in the definitions of these dimensionless numbers, even though these variables play an important role in the flow patterns. In Equations (3.1)–(3.3), f_o and χ_o are the frequency and center-to-peak amplitude of oscillation, respectively. Moreover, ρ is the fluid density, d is the tube diameter, η is the viscosity of the fluid, and v is the average net flow velocity.

$$Re_o = \frac{2\pi f_o \chi_o \rho d}{\eta} \tag{3.1}$$

$$St = \frac{d}{4\pi\chi_o} \tag{3.2}$$

$$Re_{net} = \frac{\rho v d}{\eta} \tag{3.3}$$

Furthermore, Brunold *et al.* (1989) investigated the energy losses in both geometries. As one would expect, by increasing the number of edges in the rectangular geometry or the number of baffles in the circular geometry apparatus, the energy loss was increased. In summary, the main result of this work was the identification of experimental conditions where good radial mixing occurs in the tube geometries utilized. The authors claimed that such a phenomenon could improve heat and mass transfer coefficients, even though no experimental evidence was given in this publication.

In an attempt to elucidate the phenomena occurring in baffled tubes due to oscillatory flow, Dickens *et al.* (1989) studied the residence time distribution (RTD) in a horizontal baffled tube using a tracer technique in experimental conditions where $Re_{net} = 110$, $0 \leq Re_o \leq 3000$ and $0.3 \leq St \leq \infty$. Experiments were carried out utilizing a fixed number of baffles and different frequencies and amplitudes of oscillation. Based on the RTD curves obtained and knowing the initial amount of tracer injected, the authors were able to identify conditions where near plug flow regime was achieved. Compared to Brunold *et al.* (1989), these authors gave a much more quantitative description of the flow regimes. The variances of the RTDs obtained and the classical result obtained by Levenspiel and Smith (1957) allowed the authors to calculate the dispersion coefficient for each experiment. With the aid of a plot relating the Peclet number ($1/Pe$) (Equation (3.4)) and the amplitudes of oscillation, the authors determined the conditions of minimum dispersion (near plug flow regime).

Additionally, by ignoring the dispersion coefficient and representing the system as a tanks-in-series model, the authors found that the number of tanks estimated to represent the system was very close to the actual number of spaces between baffles.

In other words, in the experimental conditions considered, a continuous stirred tank reactor could well represent each space between two baffles. In Equation (3.4), L and D_x represent the tube length and the diffusion coefficient, respectively.

$$Pe = \frac{vL}{D_x} \tag{3.4}$$

Mackley *et al.* (1990) investigated the effects of baffles and oscillatory flow on the heat transfer coefficients. For this purpose, a shell and tube heat exchanger apparatus was utilized. Initially, these authors investigated the heat transfer coefficient without fluid oscillation and baffles inside the tubes. In a second experiment, orifice baffles were inserted, and no fluid oscillation was applied. By comparing the Nusselt number (Nu), Equation (3.5), estimated in these two experiments, a noticeable increase was observed in the experiment with the presence of baffles. This behavior was accentuated in the $Re_{net} \geq 400$ region. In another experiment, the authors estimated Nu when no baffles were present and fluid oscillation was applied with $Re_{net} = 300$ and $0 \leq Re_o \leq 1600$. In this experiment, no effect was detected in Nu compared to the experiment with neither baffles nor oscillation. Lastly, by applying fluid oscillation with the presence of baffles, the Nu increased remarkably, confirming the hypothesis raised by Brunold *et al.* (1989) that oscillatory flow in a baffled tube could improve the heat transfer coefficients. In Equation (3.5), h is the convective heat transfer coefficient, and k is the thermal conductivity of the fluid.

$$Nu = \frac{hd}{k} \tag{3.5}$$

Howes *et al.* (1991) simulated numerically two-dimensional flow patterns in a channel with baffles and fluid oscillation. These investigators aimed to identify conditions where a high degree of radial mixing was achieved. The authors also simulated the flow pattern without baffles and oscillation for comparison purposes. By comparing the experiments with the presence and absence of oscillatory flow without baffles, the authors concluded that at a lower Re_o ($Re_o = 100$ and $Re_{net} = 100$) and ignoring the molecular diffusion, there was no change neither in the radial mixing pattern nor the dispersion, emphasizing what was observed experimentally by Brunold *et al.* (1989) and Mackley *et al.* (1990). In the presence of baffles and the absence of fluid oscillations, it was verified that by increasing Re_{net} from 100 to

300, the symmetry of the flow was broken, and a good radial mixing pattern was achieved. In another numerical experiment, by considering both fluid oscillation and baffles, it was noted that by increasing the Re_o from 100 to 300 at fixed $St = 1$ and $Re_{net} = 100$, a pattern of good radial mixing was observed and low dispersion was achieved. These authors also mentioned the fact that the transition from laminar to turbulent behavior in continuous flow occurs at $2000 \leq Re_{net} \leq 3000$, whereas in oscillatory flow, the transition from ordered to chaotic occurs at a much lower Re_o.

Mackley and Ni (1991) used a tracer technique to measure the concentration profiles in a baffled tube in both horizontal and vertical positions. The concentration profiles were measured at different tube positions, and the authors noticed that the tracer density strongly affected the flow velocity profiles that were photographed. To overcome this experimental difficulty, the authors added some sugar to the main fluid stream to balance the densities of the fluid (water) and the tracer (NaCl). In the experiments with baffles and oscillatory flow, these investigators worked in the experimental region of $Re_{net} = 128$, $0 \leq Re_o \leq 3600$ and $0.3 \leq St \leq \infty$. In one experiment with the tube in the horizontal position, it was noticed that the concentration profiles measured by the probes at different radial positions were very similar, highlighting that strong radial mixing occurred. The concentration profiles almost overlapped each other in the vertical tube arrangement with the same flow conditions. Once the region of good radial mixing was identified, the authors applied an imperfect pulse technique (Osstergaard and Michelsen, 1969) and the dispersion model to estimate the Peclet number, Equation (3.4). The estimated Peclet number gave excellent results fitting their data. Moreover, it was concluded that by decreasing St, a significant decrease in Peclet was obtained in their experimental conditions, which shows that an increase in the amplitude of oscillations causes a net increase in axial dispersion.

Hewgill *et al.* (1993) studied the effects of baffles and oscillatory flow in gas-liquid mass transfer. More specifically, they studied the transfer of gaseous oxygen to an aqueous phase. Three baffle geometries (orifice, central, and helical) were investigated (see Figure 3.1). They worked in the experimental conditions of $0 \leq Re_o \leq 7840$ and $0.1 \leq St \leq 0.5$. By analyzing the photographs taken during the experiments, these investigators concluded that the central baffles performed poorly in providing good radial mixing. On the other hand, helical and orifice baffles performed efficiently in this subject under the same conditions.

For the sake of comparison, Hewgill *et al.* (1993) conducted experiments with and without baffles without fluid oscillation. The results showed that the mass transfer is slightly increased by the presence of baffles in the experimental condi-

tions. Applying fluid oscillation in the baffled device showed a sixfold increase in mass transfer. Regarding the baffle types, the speed of oxygen uptake followed this ascending order: central < helical < orifice. Finally, to emphasize the applicability of this new device to enhance mass transfer, the authors calculated the time-averaged power dissipation based on the Bernoulli equation and showed that this device is more energy efficient than a gas-sparged stirred tank.

Mackley and Ni (1993) studied the RTDs in a series of connected baffled tubes, Figure 3.3. In the experiments considering fluid oscillation and baffles in the tube, the authors observed that a regime near plug flow could be achieved in some operation conditions. Additionally, a comparison was drawn between the conditions in which a similar regime could be attained using unbaffled tubes. To attain a regime of good radial mixing in a smooth tube, it was required to operate the system at higher Re_{net}, implying, inevitably, short residence times. In the case of utilizing a baffled tube and oscillatory flow, such conditions were feasible at much lower Re_{net}, resulting in longer residence times, yet operating in a net laminar flow regime. In fact, this is one of the main advantages of oscillatory flow in baffled tubes for performing chemical reactions. Furthermore, as performed in a previous publication (Mackley and Ni, 1991), these authors applied an imperfect pulse technique to estimate the dispersion coefficient in the dispersion model. The results showed that for a given piston displacement (amplitude of oscillation), no noticeable effect of the oscillation frequency was noticed on the dispersion coefficient. On the other hand, when the experiments were carried out in a fixed oscillation frequency and different amplitudes, a noticeable effect was observed in the dispersion coefficients. As the oscillation amplitude increased (St decreased), the dispersion coefficient passed through a minimum value and then increased. This behavior was not observed when operating the system at higher Re_{net}. In this study, an experimental setup with parallel tubes was also investigated. For this arrangement, similar results of concentration profiles were obtained, emphasizing that this new reactor design could be applied in operations where good heat exchange is required. This arrangement with a bundle of tubes was further investigated by Ni (1994).

Ni *et al.* (1995) studied the oxygen mass transfer in yeast culture in a batch OBR. The length and diameter of the reactor employed were 500 mm and 50 mm, respectively, and the volume was 1 L. A total of six orifice baffles attached to two stainless steel rods were inserted into the reactor. The spacing between the baffles was 1.5 the column diameter as proposed by Brunold *et al.* (1989). For comparison purposes, the authors also conducted experiments in similar conditions in a 2 L batch stirred tank reactor. Regarding the oscillatory baffled reactor, the authors

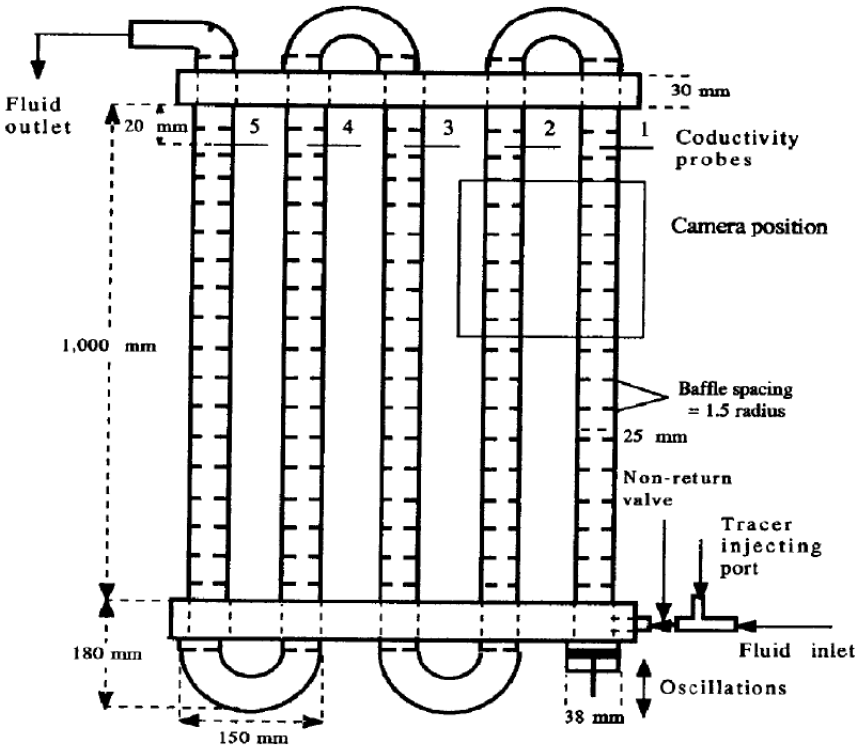

Figure 3.3: Experimental apparatus used by Mackley and Ni (1993).

observed that increasing the frequency and oscillation amplitude increased the mass transfer coefficient considerably, which proved that the oscillatory conditions play an important role in the mixing characteristics of these systems. The authors used the power dissipation as a criterion to compare the results obtained in the oscillatory baffled reactor with those obtained in the stirred tank reactor (Subsection 3.2.3). By plotting the mass transfer coefficients from both reactors against their respective power dissipations, the authors observed that for the same value of power dissipation, the mass transfer coefficient in the oscillatory baffled reactor was 75% higher than its counterpart in the stirred tank reactor.

In a posterior work, Ni and Gao (1996) investigated the mass transfer characteristics of a pilot batch OBC equipped with orifice baffles. The authors used the system air-water in the experiments. The internal diameter of the column and height were 100 mm and 1050 mm, respectively. In the experiments, the authors used different baffle spacings, more specifically, from one to two tube diameters. To avoid performing a large number of experiments, the authors fixed the oscillation amplitude at 8 mm while the frequency varied from 0 to 6 Hz. By estimating the mass transfer coefficients in the different experiments, the authors concluded that the baffle spacing of 1.8 times the tube's internal diameter gave the highest mass transfer rates. It is important to notice that since the oscillation amplitude was

fixed in this work, the St was also fixed. Consequently, this value of baffle spacing may not guarantee maximum mass transfer in other geometries and operational conditions.

Stonestreet and Van der Veeken (1999) studied the effects of oscillatory conditions on the RTDs in a 24 mm diameter and 2.8 m long reactor. To interpret their data, the authors employed the tanks-in-series model. In this approach, the authors utilized a stage-wise efficiency, which is defined as the ratio of tanks in the tanks-in-series model to the actual number of inter-baffle spacings. Based on this definition and defining a velocity ratio (Ψ) (Equation (3.6)), the authors were able to determine the regions where a near plug flow regime was achieved. More precisely, the region of $2 \leq \Psi \leq 4$ was considered more likely to promote profiles similar to plug flow. Since this work, the Ψ has been extensively used to characterize continuous oscillatory baffled reactors (COBR).

$$\Psi = \frac{Re_o}{Re_{net}} \tag{3.6}$$

Ni and Pereira (2000) used a tracer technique to investigate the dispersion characteristics in a COBR of 25 m and 40 mm diameter, Figure 3.4. A total of 287 orifice baffles with spacings of 1.8 times the tube diameter, such as in the work of Ni and Gao (1996), were present in the tube. The restriction ratio (α), defined as the ratio of orifice area to tube cross-section area (d_o^2/d^2), was 21%. The authors investigated the operational condition ranges of $1 \leq f_o \leq 4$ Hz and $0 \leq \chi_o \leq 8$ mm. In these conditions the range of Re_{net} varied from 0 to 2500, the Re_o from 0 to 8032 and St from 0.4 to ∞. The authors employed the dispersion model and the tanks-in-series with backflow to interpret their data.

Additionally, the authors defined the so-called cell Peclet number, which is defined as taking the length between two consecutive baffles instead of the length from the injection point to the probe position (see Equation (3.4)). The authors emphasized that this approach would be more conclusive for the data interpretation. Generally speaking, the authors found that increasing the oscillatory Reynolds number increased the dispersion in the system. However, at higher Re_{net}, the effect of increasing Re_o on the dispersion coefficient was less significant. Given the narrow interval of axial dispersion coefficients obtained experimentally, the authors concluded that the COBR studied under these conditions operated very close to the plug flow regime. The authors also proposed a correlation to relate the tracer

density and operational conditions to the diffusion coefficient, Equation (3.7). In Equation (3.7), the term with subscript b means energy dissipation due to baffles and bends. Similarly, the term with subscript m is due to oscillatory flow.

$$D_x = 1.8 \times 10^{-3} \rho_{tr}^{0.8} \left(\frac{\varrho}{\rho}\right)_b^{0.097} \left(\frac{\varrho}{\rho}\right)_m^{0.0156} \tag{3.7}$$

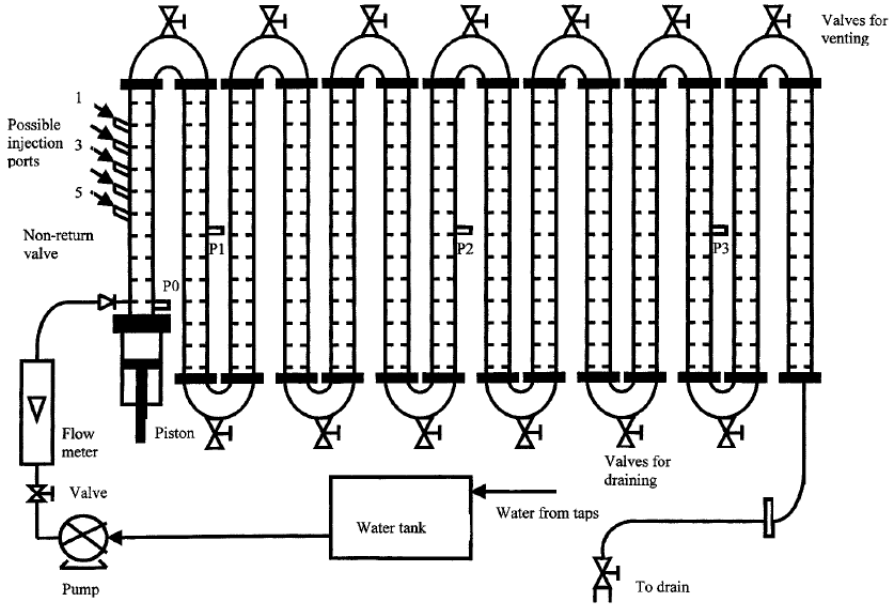

Figure 3.4: Experimental apparatus used by Ni and Pereira (2000).

Takriff and Masyithah (2002) studied the backmixing mechanism in an OBC of 282 mm height and 94 mm diameter. The authors used the Ideal Stage with Backmixing model from Xu (1994) to represent the column. It was found that the backmixing mechanism is strongly influenced by the oscillatory velocity (frequency times amplitude). It was also found that the net flow rate had the effect of decreasing it. Additionally, highly viscous fluids also lead to lower backmixing. Based on their data, Equations (3.8)–(3.9) were proposed to correlate the backmixing with the experimental conditions and fluid properties.

$$\frac{F_b \rho}{\eta d} = -57.364 + 0.1416B - 6 \times 10^{-6} B^2 \tag{3.8}$$

$$B = Re_o \left(\frac{d}{d_o} \right)^{0.1} \tag{3.9}$$

Reis *et al.* (2004) studied the RTDs in an OBR with smooth periodic constrictions. The reactor length and volume were 35 cm and 4.5 ml, respectively. The authors operated the reactor at frequencies between 0 and 20 Hz and amplitudes ranging from 0 to 3 mm. Both batch and continuous experiments were carried out. In the batch experiments, the authors used a tracer technique to characterize the mixing time and found that it was more affected by the oscillation amplitude than the frequency. The authors explained this fact by arguing that at a fixed amplitude, increasing the frequency improves the radial mixing only. On the other hand, an increase in amplitude at a fixed frequency affects the size and nature of eddies and consequently affects the dispersion coefficient. Regarding the continuous operation experiments, the authors used the differential backmixing and stagewise backmixing models from Mecklenburgh and Hartland (1968) to fit a theoretical backflow parameter (F_b/F) which represents the proportion of backflow expressed in terms of the total inlet flow rate (Equation (3.10)).

$$\frac{F_b}{F} = \frac{Re_o \eta d}{4 v \rho} \tag{3.10}$$

Zheng and Mackley (2008) studied a mesoscale OBR. The total reactor length, diameter, and orifice diameter were 9 m, 5 mm, and 2 mm, respectively. Smooth periodic constrictions were used instead of sharp-edge single-orifice baffles. The authors studied the RTDs using an imperfect pulse technique. In the operational conditions of $0 \leq Re_o \leq 800$, $0 \leq Re_{net} \leq 58$, and $0.08 \leq St \leq 0.4$, conditions of near plug flow were encountered. Based on their experimental data, Equation (3.11) was proposed to represent the dispersion coefficient.

$$\frac{D_x \rho}{\eta} = 0.026 Re_{net} + 5.91 Re_o^{0.058} St^{-1.62} + \frac{2.92 Re_{net}^2}{0.026 Re_{net} + 5.91 Re_o^{0.058} St^{-1.62}} \tag{3.11}$$

Phan and Harvey (2010) investigated the RTDs obtained by three baffle designs in a continuous mesoscale OBR. More specifically, central, helical, and orifice baffles

were investigated. These investigators worked in the region of $4.3 \leq Re_{net} \leq 34$. It was identified that at $Re_{net} \leq 10$, the oscillatory conditions played an important role in the RTDs obtained. However, this effect was not noticeable at $Re_{net} \geq 25$. Additionally, it was noticed that the conditions where near plug flow regime was achieved for the helical type baffles were different from those of central and orifice baffles.

Following these works on mesoscale oscillatory baffled reactors, several authors performed studies on this type of device. For the sake of conciseness these works will be briefly summarized. For instance, Reis *et al.* (2010) studied dispersion characteristics and used the dispersion, tanks-in-series and tanks-in-series with backflow models to interpret their results and showed that the tanks-in-series was not able to fit the data obtained. Phan and Harvey (2011, 2012) investigated to effect of geometrical parameters on the RTDs in a tube with the helical baffle design. Phan *et al.* (2011a) and Phan *et al.* (2012) investigated biodiesel production in reactors with sharp-edged helical baffles. Phan *et al.* (2011b) studied the fluid mixing at very low net flow rates in devices with orifice and central baffles. McDonough *et al.* (2015) performed a review on the use of the mesoscale OBR for process development. McDonough *et al.* (2016) integrated a heat pipe in a mesoscale OBR in order to enhance the temperature control of an exothermic reaction. McDonough *et al.* (2017) investigated the flow patterns through CFD in a tube with helical baffles. Ejim *et al.* (2017) used a factorial approach to understand how the geometry affects the dispersion and solids suspension. Eze *et al.* (2017) studied carboxylic acid esterification. McDonough *et al.* (2018) studied kinetic reaction screening. McDonough *et al.* (2019) studied the micromixing phenomenon.

Manninen *et al.* (2013) investigated the effect of viscosity of non-newtonian fluids on the dispersion coefficients in an OBR through CFD. The authors simulated tracer experiments and concluded that it was impossible to correlate the dispersion coefficient with the operational conditions when non-Newtonian fluids were used due to viscosity changes. Moreover, the authors also simulated a moving baffle device and concluded that the dispersion coefficients in this device were 17% higher than their counterparts in the moving fluid OBR.

Abbott *et al.* (2014) reported a central composite experimental design to find the conditions where plug flow would be achieved. These authors applied the same approach as Stonestreet and Van der Veeken (1999) to find the number of tanks that best fits the RTD data obtained and then fitted a second-order polynomial relating flow rate, frequency and amplitude of oscillation to the number of tanks in the model. The authors argued that this approach would be of great value to scaling

up oscillatory baffled reactors.

Mazubert *et al.* (2016a) investigated the flow patterns using CFD in an OBR using five different baffle types: single orifice, disc-and-doughnut, and 3 variations of helical baffle designs. It was shown that the disc-and-doughnut required the highest power dissipation to obtain similar mixing behaviors, whereas the single orifice required the lowest. Helical baffles required intermediate values of power dissipation. In a posterior work, Mazubert *et al.* (2016b) gave a quantitative description of the flow regimes by calculating the shear stress, the axial to radial stretching, and the RTDs.

Kacker *et al.* (2017), attempting to put in evidence the differences in mixing behavior in homogeneous and heterogeneous systems in an OBT intended to be used as a crystallizer, performed a series of experiments with a DN15 model from Nitech. In this experimental setup, the authors concluded that the conditions where the near plug flow regime was achieved were different from those recommended by Stonestreet and Van der Veeken (1999). Moreover, the maximum plug flow behavior conditions in homogeneous and heterogeneous systems differed. The authors argued that this resulted from the longer time the solids spent inside the reactor. This work investigated solid fractions of up to 10%(w/w).

Slavnic *et al.* (2017) applied a dispersion model to interpret data related to two COBRs of different dimensions. Similar to previous investigators, these authors found that amplitude has a more significant effect on the dispersion coefficient than frequency. Additionally, it was verified that keeping the oscillatory Reynolds fixed on both reactors does not imply that the resulting RTDs will be equal. To correlate the experimental conditions with the diffusion coefficient, a correlation to calculate the Peclet number as a function of flow conditions was proposed. The authors used data from previous investigators to corroborate the validity of their model, Equation (3.12).

$$\frac{1}{Pe} = 0.12 Re_o^{-0.31} St^{0.47} \Psi^{0.25} \tag{3.12}$$

Slavnic *et al.* (2019) studied the flow patterns of solids in a single orifice baffle OBR of 2 m long, 26 mm internal diameter, and 21.3% restriction ratio. The operational conditions used in this study were: $154 \leq Re_{net} \leq 597$, $619 \leq Re_o \leq 2707$, $0.16 \leq St \leq 0.68$ and $4 \leq \Psi \leq 4.5$. The authors characterized

four solid flow regimes depending on the power dissipation, oscillatory to settling velocity ratio, and concentration ratio between two adjacent cells: creeping solids flow, dense solids flow, dilute solids flow, and solids wash out. The Peclet number of the solids was estimated using the dispersion model. It was found that the solids flow regime approached plug flow by increasing the power dissipation (increasing either amplitude or frequency).

Sutherland *et al.* (2019) developed a CFD study coupled with population balances emphasizing the hydrodynamic and mixing differences in stationary baffle and moving baffle OBRs. The authors simulated different operational conditions to characterize the flow and used the Reynolds number and Strouhal number calculated having the fluid as a reference (Re_f, St_f) and the ratio of axial do radial velocity (V_R)(Equation (3.13), as described in Fitch *et al.* (2005) and Jian and Ni (2005)) to argue that the classical oscillatory dimensionless groups Re_o, St and Re are insufficient to characterize the flow in the moving baffle device. Data from Ni *et al.* (2001a) was used to validate the population balance model. In a posterior work, Sutherland *et al.* (2022) performed a more detailed investigation of both devices using the power dissipation, the ratio of axial to radial velocity, and mixing time as comparison parameters. The results showed that the stationary baffle device performed better.

$$V_R = \frac{\sum_{j=1}^{J}\sum_{i=1}^{I}|v_{axial(i,j)}|/J.I}{\sum_{j=1}^{J}\sum_{i=1}^{I}|v_{radial(i,j)}|/J.I} \tag{3.13}$$

Avila *et al.* (2020a) performed a CFD study to investigate the mixing performance by varying the position of the feed of the tracer. A COBR of 15 mm internal diameter and 7.5 mm orifice diameter with smooth periodic constrictions was investigated. The numerical experiments were performed at $6 \leq Re_{net} \leq 27$ and $24 \leq Re_{net} \leq 96$. The authors concluded that injecting the tracer at the center line of the reactor gave poor mixing performance. On the other hand, injecting the tracer near the reactor wall resulted in the best results.

Jimeno *et al.* (2022) investigated how particle size affects the dispersion coefficient in a COBR using CFD. More specifically, the solid and liquid phases were represented as Lagrangian and Eulerian, respectively. The authors aimed at understanding the effect of the solid phase in a Nitech DN15 model (www.nitechsolutions.co.uk). A total length of 752 mm and 32 baffle cells were considered in the modeling approach. The dispersion model was used to determine the dispersion coefficient.

Moreover, the perfect pulse and imperfect pulse techniques were simulated. However, the imperfect pulse technique provided more reliable results. It was found that in the simulated conditions, the larger particles tend to stay near the bottom of the device due to gravity effects. It was also found that the dispersion coefficient was smaller when larger solid particles were present. Additionally, solids volume fractions below 10% were investigated.

Avila *et al.* (2022) performed a thorough literature on the OBR technology. The authors reviewed the main parameters that affect the performance of these systems, including baffle type, geometry, and operational conditions. Based on the previous works, the authors emphasized that the operational conditions that lead to a near plug flow regime may differ depending on the reactor configuration and must be adjusted based on the requirements of the process. Some technological problems were also pointed out, such as the difficulty in operating OBRs in processes where high solids hold up are required and challenges due to highly viscous fluids. To date, the work of Avila *et al.* (2022) offers the most detailed review of these systems.

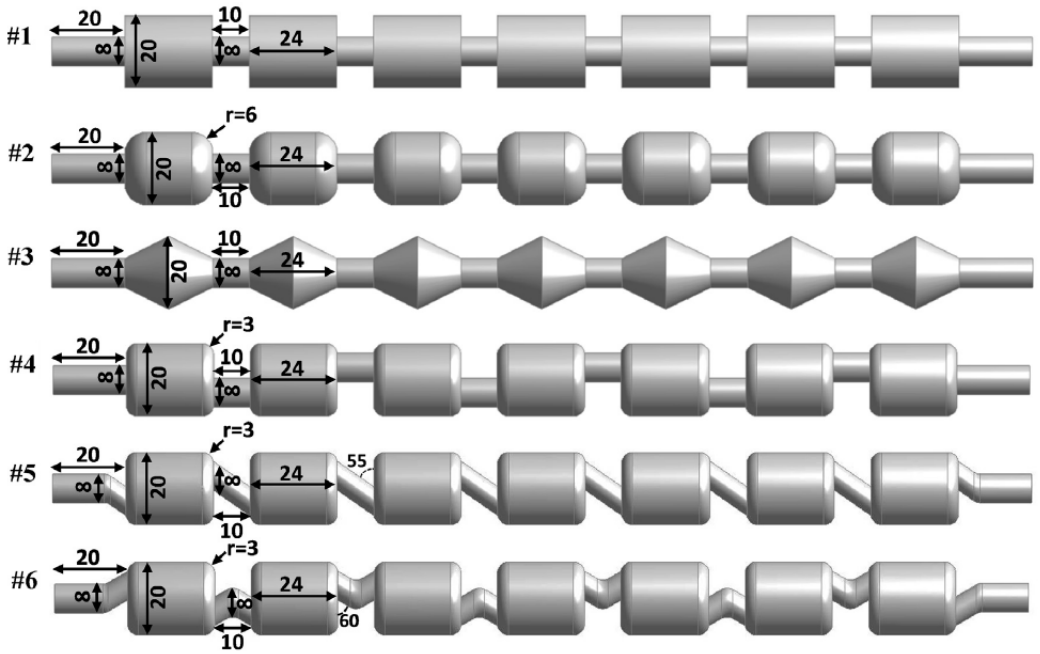

Figure 3.5: Different geometries investigated by Zhang *et al.* (2022).

Zhang *et al.* (2022) studied the effect of different cell (chamber) geometries and the types of connections in a device aimed to be used as an oscillatory baffled crystallizer through CFD (Figure 3.5). It was found that the shape of the cell did not have a significant effect on the pattern of solid suspension. This was concluded be-

cause, in the numerical experiments performed, most of the solid particles remained near the bottom of the device for all cell types. However, a remarkable effect of the position of the connections was observed. More precisely, connections positioned up and down and inclined pipe gave the best pattern of particle suspension (designs #4, #5 and #6 in Figure 3.5). Fraction of solids of up to 20% were investigated in this study.

3.2.2 Heat Transfer

Mackley and Stonestreet (1995) extended the work of Mackley *et al.* (1990) in the investigation of heat transfer performance due to oscillatory flow in a baffled heat exchanger apparatus. As reported by the previous investigators, these authors also noticed a remarkable increase in Nu due to increasing Re_{net} compared to an unbaffled tube. Additionally, by fixing Re_{net} and applying oscillation, the authors observed a strong positive effect of the Re_o on Nu. Experiments carried out at different oscillation frequencies for several fixed amplitudes highlighted that the frequency was the governing factor affecting the heat transfer, i.e., higher frequencies implied higher Nu. By performing experiments at different Re_o and different Re_{net}, it was observed that Nu obtained at each Re_o curve approached a limiting value as Re_{net} increased. The experimental range of Re_{net} was $0 \leq Re_{net} \leq 1200$. This result emphasizes that the net flow effect on the heat transfer becomes more noticeable as the regime approaches turbulent conditions. Additionally, these authors fitted their data with the following correlation, Equation (3.14).

$$Nu_{s,n} = 0.0035 Re_{net}^{0.13} Pr^{1/3} + 0.3 \left[\frac{Re_o^{2.2}}{(Re_{net} + 800)^{1.25}} \right] \tag{3.14}$$

Stephens and Mackley (2002) studied experimentally the heat transfer performance in batch OBRs. The authors investigated two configurations. In one arrangement, the baffles were fixed inside the tube and the oscillations were applied to the fluid. In the other arrangement, the oscillation was provided by moving the baffles. In the stationary configuration, single orifice baffles were employed, whereas in the moving baffles configuration, baffles with three orifices were employed. In the case of stationary baffles, the authors verified that tube side Nu increased with the oscillation velocity ($\chi_o f_o$) for different values of St, in agreement with the results of Mackley *et al.* (1990) and Mackley and Stonestreet (1995). These experiments

were conducted in the $0 \leq Re_o \leq 1000$ and $0 \leq f_o \leq 10$ Hz range. In the experiments with moving baffles, the same trend was observed. However, in this case, the oscillatory conditions were more severe. For instance, the authors mentioned a ten-fold increase in Nu at $Re_o = 28000$. It is important to emphasize that the authors mention high uncertainties in the Nu calculated at higher frequencies for both configurations due to experimental limitations. No correlation was proposed to relate the oscillation conditions with Nu.

Solano *et al.* (2012) used a CFD model to investigate the flow patterns and heat transfer in an OBR of 5 mm internal diameter equipped with helical baffles. The simulations showed that even working at $Re_{net} = 10$ and $Re_o = 320$, a four-fold heat transfer increase was obtained when compared to steady state flow in a baffled tube.

Also studying heat transfer in oscillatory baffled reactors, Law *et al.* (2018) argued that the validity of Equation (3.14) is put in doubt when the fluid has a lower Pr. The authors criticized the form of the equation proposed by Mackley and Stonestreet (1995). Moreover, it was observed that when the fluid has a low Prandtl number (water, for instance), the predictions of Nusselt for increasing net Reynolds number decreases, then reaches a minimum and, subsequently, increases. A behavior that does not have physical meaning, according to the authors. Indeed, Mackley and Stonestreet (1995) used only oil as the working fluid, which has $Pr = 73$ in their experimental conditions. Using deionized water as working fluid, Law *et al.* (2018) generated data at broader experimental conditions and proposed the following correlations to calculate Nu in oscillatory flow reactors (Equations (3.15)–(3.16)). The equation can be used with confidence in the operational conditions of $200 \leq Re_{net} \leq 1300$, $0 \leq Re_o \leq 8700$ and $4.4 \leq Pr \leq 73$. The OBR used in the experiments had a 26 mm diameter, and orifice baffles (13 mm orifice; 52 mm baffle spacing) were used.

- $0 \leq Re_o \leq 1300$

$$Nu = 0.0022 Re_{net}^{0.7} Pr^{0.3} Re_o^{0.44} \tag{3.15}$$

- $Re_o \geq 1300$

$$Nu = 0.52 Re_{net}^{0.7} Pr^{0.3} \tag{3.16}$$

The Paste, Particle and Polymer Processing Group (P4G) from Cambridge University (accessed in February of 2023) developed the following correlation to predict the Nusselt number in OBRs, Equation (3.17). There was no detail on how this correlation was fitted when this material was accessed. Avila *et al.* (2022) mentions criticism regarding the predictions of Equation (3.17) and Equation (3.14).

$$Nu = Pr^{1/3}\left[0.36Re^{0.6} + 0.8\frac{Re_o^{1.7}}{Re + 10000}\right] \tag{3.17}$$

Onyemelukwe *et al.* (2018) studied the heat transfer characteristics of a with smooth periodic constrictions. The tube diameter was 5 mm. The authors investigated the behavior of the tube at low net Reynolds numbers, more specifically, from 11 to 54. The oscillatory Reynolds number was also low (39-197). In the experiments with steady flow (no oscillatory component), a 1.4-fold heat transfer improvement was observed compared to a similar tube without periodic constrictions. In the experiments with unsteady oscillatory flow, it was observed that in the range of experimental conditions, the net Reynolds number was more significant than the oscillatory Reynolds number in improving heat transfer. Furthermore, it was shown that heat transfer was more affected by the Strouhal number than the oscillation frequency. Based on their experimental data, the authors fitted the following equation to describe the Nusselt number in the range of operational conditions used in their study, Equation (3.18).

$$Nu = 0.01616Re^{1.16}Pr^{1/3} + 0.0016\left[Re_o^{0.08}Re^{1.42}\frac{St}{1.136}\right] \tag{3.18}$$

Ahmed *et al.* (2018b) performed a study on the heat transfer in mesoscale oscillatory baffled reactors with three different baffle geometries: central, orifice, and helical baffles (see Figure 3.1). The experiments were conducted at $60 \leq Re_{net} \leq 2500$ and $0 \leq Re_o \leq 1600$. At a fixed oscillatory Reynolds number, an 11-fold increase in the Nu was observed at $Re_{net} = 1345$ with the central baffle. This increase was calculated with respect to the steady flow in a smooth tube. Beyond this Reynolds number, a 4.5 fold increase was observed at $Re_{net} = 2300$. The other baffle designs also showed significant, but smaller, enhancement in Nu. The orifice baffle showed the smallest improvement. The authors argued that greater heat transfer observed with the central baffle was due to the disruption of the axial flow in the

radial direction caused by this design. Based on the experimental data, correlations were developed to relate the oscillatory conditions with the Nu for each of the three designs (Equations (3.19) and (3.20)). In these equations, λ is a parameter that depends on the baffle design. Furthermore, a thermal performance criteria was developed to evaluate the baffle designs. This thermal performance comprised the ratio between the Nusselt number and the pressure drop. It was verified that the helical baffle had the highest thermal performance while the central had the lowest. Furthermore, the central baffle showed the highest pressure drop among the designs studied.

- $0 \leq Re_o \leq 1300$

$$Nu = \lambda Re_{net}^{0.7} Pr^{1/3} Re_o^{0.44} \tag{3.19}$$

- $Re_o \geq 1300$

$$Nu = 23.45 \lambda Re_{net}^{0.7} Pr^{1/3} \tag{3.20}$$

González-Juárez *et al.* (2018) developed a CFD study to investigate the heat transfer in a baffled tube of 25 mm diameter with orifice baffles spaced by 1.5 times the diameter. The authors noticed that the fluid properties strongly affect the tube side Nu. For instance, water and thermal oil were used as working fluids. Additionally, the authors calculated the averaged Nusselt number and compared the results with the correlations proposed by Mackley and Stonestreet (1995) and from the P4G Group. Strong deviations were observed from the calculated numerical values and predictions by the mentioned correlations, especially at lower net Reynolds numbers. Higher deviations were noticeable using the correlation from Mackley and Stonestreet (1995). Furthermore, the oscillation frequency was more significant than the amplitude, influencing the heat transfer.

Muñoz-Cámara *et al.* (2020) studied the heat transfer and flow characteristics in a three-orifice baffled device. In the experiments performed with a steady flow, the authors identified the transition point from laminar to turbulent and proposed correlations to describe the Fanning friction factor in each region. The authors conducted experiments in the experimental ranges of $10 \leq Re_{net} \leq 600$, $10 \leq Re_o \leq 440$, and $190 \leq Pr \leq 470$. The main tube diameter was 32 mm, each orifice had a diameter of 9.2 mm, and the baffles were spaced by 1.5 times the diameter. The authors identified that the oscillatory flow component can enhance heat transfer compared to the steady flow case, especially at low net Reynolds numbers. However,

the effect of the oscillatory component becomes negligible at higher net Reynolds numbers because the flow is already in the turbulent regime. Based on their data, the authors proposed the following correlation to relate the Nusselt number to the oscillatory and steady flow, Equation (3.21).

$$Nu = 0.412 Re_{net}^{0.196} Re_o^{0.583} Pr^{0.285} \tag{3.21}$$

In a posterior work, Muñoz-Cámara *et al.* (2021a) studied the heat transfer due to oscillatory flow in a tube of 32 mm diameter with circular orifice baffles spaced by 1.5 diameters. The authors used the Hydrogen Bubble Visualization and Particle Image Velocimetry to investigate the flow patterns. In the experiments with no net flow, it was observed that the transition from axisymmetric to asymmetric occurred at $Re_o = 130$ in their experimental conditions. In the absence of net flow, the authors observed that the flow presented temporal symmetry, i.e., the same pattern for the forward and backward movement of the piston. When considering a net flow, it was observed that the temporal symmetry was broken at a low velocity ratio. However, when the velocity ratio increased, the flow became more similar to the case without net flow. The authors used this information regarding the flow patterns to explain the Nusselt number observed. This study investigated the cell Nusselt number and the average Nusselt number. The authors argued that their results could not be compared with previous correlations since they worked at very low net Reynolds numbers ($Re_{net} \leq 100$). However, the Nusselt Number increased with the net Reynolds number and oscillatory Reynolds number and showed no saturation for $\Psi < 20$, which is consistent with previous studies.

Briggs *et al.* (2021) investigated the heat transfer and residence time distribution in a continuous oscillatory baffled crystallizer of 15 mm internal diameter (DN15 from Ni tech). The authors investigated the effect of the oscillation conditions on the steady state temperature profiles along the reactor length. It was pointed out that the oscillation conditions must be tuned to avoid steep temperature gradients along the length of the tube as a way of avoiding deterioration in the final properties of the crystals. Overall heat transfer coefficients of the order of 100 W m^2 K were obtained. Additionally, it was mentioned that fluid oscillation can be impaired in long tubes due to the so-called "oscillation damping," resulting from energy losses due to bends and baffles.

In continuation to the work of Zhang *et al.* (2022), Huang *et al.* (2023) studied numerically the heat transfer of novel designs of oscillatory baffled tubes. It was shown that heterogeneous systems have more efficient heat transfer than homogeneous systems. Moreover, particle concentration was more significant than particle size to enhance the heat transfer coefficients.

Muñoz-Cámara *et al.* (2024) investigated the effect of the orientation of tri-orifice baffles on the heat transfer coefficients in a 32 mm diameter tube. Experiments were conducted at net Reynolds numbers varying from 50-1000 and oscillatory Reynolds numbers ranging from 0 to 750. Two baffle configurations were investigated: aligned and opposed. At $Re_o > 150$, both configurations resulted in very close Nusselt numbers. However, at $Re_o < 150$, the opposed configuration showed a higher Nusselt number at the cost of having the highest pressure drop. The following correlation was proposed to represent the Nusselt number in the opposed baffle configuration, Equation (3.22):

$$Nu = 0.385 Re_{net}^{0.338} Re_o^{0.435} Pr^{0.285}, \Psi > 1 \tag{3.22}$$

3.2.3 Power Dissipation

In addition to studying heat transfer in OBRs, Mackley and Stonestreet (1995) investigated the power dissipation in these devices. More specifically, when analyzing the energy consumed at different oscillation amplitudes, the authors found that at higher oscillation amplitudes (i.e., 6.4 mm - lower St), a good agreement was obtained between the energy consumed and the prediction by an equation derived based on the quasi-steady state model (QSM) from Jealous and Johnson (1955)(Equation (3.23)). The QSM assumes that the pressure drop in an oscillatory flow at a specified instantaneous velocity is equal to the pressure drop at steady net flow conditions with the same instantaneous velocity (Mackley and Stonestreet, 1995; Avila *et al.*, 2022). This model is assumed valid for $0.5 \leq f_o \leq 2$ Hz and $5 \leq \chi_0 \leq 30$ mm, i.e., low frequencies and high amplitudes (Avila *et al.*, 2022). In Equation (3.23), N_b, C_D, and L represent the number of baffles, the orifice discharge coefficient, and the reactor length, respectively.

$$\varrho = \frac{2\rho N_b \left(2\pi f_o \chi_o\right)^3 \left(\frac{1}{\alpha^2} - 1\right)}{3\pi C_D^2 L} \tag{3.23}$$

When the authors plotted the tube side Nu against the power dissipation for different oscillatory conditions and compared it to the Nu obtained at laminar and turbulent flow in smooth tubes, it was found that for the same power required, the oscillation condition with amplitude 6.4 mm gave the highest Nu, showing once again that it is very advantageous to use baffles and oscillatory flow to achieve efficient heat transfer. Finally, based on a personal communication with M.H.I. Baird the authors presented Equation (3.24) to represent the factor by which the net steady flow power dissipation is increased due to the application of oscillatory flow.

$$\Xi = \left[1 + 4\left(\frac{\Psi}{\pi}\right)^3\right]^{1/3} \tag{3.24}$$

Baird and Stonestreet (1995) proposed the so-called Eddy Enhancement Model (EEM). This model was developed based on acoustic principles and is valid for low amplitudes and high frequencies, i.e., $1 \leq \chi_o \leq 5$ mm and $3 \leq f_o \leq 14$ Hz, in opposition to the QSM model (Avila *et al.*, 2022). Instead of the discharge coefficient of the QSM model (C_D), the EEM model has the mixing length (l_{mix}) as an adjustable parameter (Equation (3.25)).

$$\varrho = \frac{1.5 N_b \rho \left(2\pi f_o\right)^3 \chi_o^2 l_{mix}}{\alpha L} \tag{3.25}$$

Jimeno *et al.* (2018) investigated the accuracy of the QSM and EEM models by comparing their predictions with power dissipation data obtained through CFD simulations of a DN15 OBR model from Nitech. Based on their data, the authors proposed corrections in the QSM and EEM as in Equations (3.26) and (3.27), respectively. Regarding the QSM, the dependency of power dissipation on the number of baffles was expressed as a power law of N_b (instead of the linear relationship proposed originally), Equation (3.25). Similarly, a power law of N_b dependency was included in the EEM, and a correlation relating the baffle geometry and l_{mix} was proposed

to improve the model predictions, Equation (3.28). The authors also pointed out that the contribution of the net flow to the power dissipation was negligible in their range of simulated conditions. Moreover, instead of the L in the denominator of Equations (3.26) and (3.27), the authors used the ratio of volume to area (V/A) since this ratio may diverge from L in smooth constriction baffles.

$$\varrho = \frac{2\rho N_b^{0.7} \left(2\pi f_o \chi_o\right)^3 \left(\frac{1}{\alpha^2} - 1\right)}{3\pi C_D^2 \left(V/A\right)} \tag{3.26}$$

$$\varrho = \frac{1.5\rho N_b^{0.7} \left(2\pi f_o\right)^3 \chi_o^2 l_{mix}}{\alpha \left(V/A\right)} \tag{3.27}$$

$$l_{mix} = 0.002 \left[\alpha \frac{d_o}{\pi \chi_o}\right]^{-0.57} \tag{3.28}$$

Ahmed *et al.* (2018b) performed a study on the pressure drops in mesoscale oscillatory baffled reactors using three baffle geometries: central baffles, orifice baffles, and helical baffles. The authors conducted experiments in the $60 \leq Re_{net} \leq 2500$ and $0 \leq Re_o \leq 1600$ region. In distinct net flow conditions, it was noticed that the pressure drop falls continuously with increasing oscillatory Reynolds number and reaches a plateau at $Re_o = 500$. It was also observed that the device with central baffles had the highest pressure drop, followed by the orifice and helical baffle devices. It was also found that the Stouhal number had no significant effect on the pressure drops, i.e., the oscillation velocity was the dominant factor. Correlations were proposed to relate the pressure drop per reactor length with the oscillation conditions.

González-Juárez *et al.* (2018) studied the power dissipation in a 25 mm diameter tube with orifice baffles separated by 1.5 times the tube diameter. The authors used CFD software to evaluate the power dissipation and compared the results obtained with a previous correlation proposed by Mackley and Stonestreet (1995). Under the studied conditions, i.e., $5 \leq Re_{net} \leq 200$ and $0 \leq Re_o \leq 800$, the averaged power dissipation calculated and the predicted by the previous correlation were in agreement and errors were less than 5%.

Sutherland *et al.* (2020) emphasized the differences in the hydrodynamic behavior of moving baffles and stationary baffles OBCs and developed, for the first time, a correlation to predict the power consumption (Equation 3.29) in moving baffle OBCs and an oscillatory power number (N_{P0}), Equation (3.30). The authors pointed out that the QSM and EEM models were developed based on moving fluid devices. The power number was derived using dimensional analysis, and data obtained through CFD simulation was used to corroborate their model. In order to characterize the hydrodynamic behavior in these devices, dimensionless groups that considered the fluid as the reference, as proposed by Sutherland *et al.* (2019), were used. P, in Equation (3.30), represents total power which unit is watt.

$$\varrho = \frac{4\rho N_b \left(1-\alpha^2\right)\left(1/\alpha^2-1\right)^2}{3\pi C_D^2 L}\left(2\pi f_o \chi_o\right)^3 \tag{3.29}$$

$$N_{P0} = \frac{P}{\rho(2\pi f_o \chi_o)^3 d^2} \tag{3.30}$$

Avila *et al.* (2020b) investigated power dissipation through CFD simulations in operational conditions where $6 \leq R_{net} \leq 27$ and $24 \leq Re_o \leq 96$. These authors showed that the QSM model predicts power dissipation accurately only in the turbulent regime. In the transition and laminar regimes, however, the predictions are nonphysical, according to them. Equations (3.31)–(3.35) were developed by fitting data generated to represent the power dissipation over the whole flow regime. In Equation (3.34), ϱ^* represents the dimensionless power density, and l_b^{opt} represents the optimum baffle spacing and has a value of $1.5d$ in agreement with Brunold *et al.* (1989).

$$\varrho^* = \frac{\varrho d}{\rho\left(2\pi f_o \chi_o + v\right)^2} \tag{3.31}$$

- For laminar flow ($\alpha = 0.25$ and $l_b = 1.1d$)

$$\varrho^* = \frac{330}{Re_T} \tag{3.32}$$

$$Re_T = \frac{(2\pi f \chi_o + v)\,\rho d}{\eta}\sqrt{\frac{\beta}{\alpha}} \tag{3.33}$$

$$\beta = \frac{l_b^{opt}}{l_b} \tag{3.34}$$

- For laminar flow ($\alpha = 0.22$ and $l_b = 1.6d$)

$$\varrho^* = 1.92 \tag{3.35}$$

Muñoz-Câmara *et al.* (2021b) derived the effect of the oscillatory flow on the power dissipation in relation to the power dissipation under steady flow conditions in the fully developed regime analytically. Using a simple model, the authors found an expression describing the increase in power dissipation due to the oscillatory flow component. When compared to the equation proposed by Baird (Equation (3.24)), as described by Mackley and Stonestreet (1995), a great agreement was observed. The authors also emphasized that the derivation of the equation proposed by Baird remains unclear. Despite that, the predictions of increase in power consumption predicted by the Baird Equation are reasonably good.

Muñoz-Câmara *et al.* (2022) experimentally studied the power consumption and pressure drop in an OBR using two baffle designs: single orifice and tri-orifice. Based on the experimental data, the authors developed models to represent the power number (Equation 36), oscillatory fanning friction factor, and power dissipation. Additionally, the authors used their data to fit C_D and l_{mix} in the QSM and EEM models (Equation (37) and (38)), respectively. It was shown that these parameters depend on the oscillatory conditions and can not assume fixed values in wide ranges of operation conditions.

$$N_{P0} = \frac{C1}{Re_o} + C2 Re_o^m \left(\frac{\chi_o}{d}\right)^n \tag{3.36}$$

$$C_D^2 = \frac{1/\alpha^2 - 1}{6 N_{P0}} \tag{3.37}$$

$$l_{mix} = \frac{8\alpha}{3\pi}\chi_0 N_{P0} \tag{3.38}$$

Mortazavi and Pakzad (2023) developed a CFD study to estimate the effect of geometric and operational parameters on the average and maximum power dissipation in a moving baffle OBC. By fitting the data obtained through simulation, it was found that the effect of f_o and χ_o have different magnitudes. More specifically, the contribution of f_o was higher in the range of experimental conditions simulated. Moreover, it was also shown that the fluid viscosity did not affect the average and maximum power dissipation. Lastly, by comparing their data with the predictions of the QSM and EEM and emphasizing that these models were developed for stationary baffle devices, the authors concluded that the moving baffle OBC spends less energy, which makes it more efficient.

3.2.4 Droplet Size Distribution

Pereira and Ni (2001) studied liquid-liquid dispersions in a COBR 25 m long and 40 mm internal diameter. The water-silicone oil system was investigated. Based on their results, the authors concluded that increasing the oscillation frequency or amplitude narrows the droplet size distributions. The authors argued that such behavior is a consequence of the increase in the turbulence inside the reactor, which favors the breakage rate over the coalescence rate, resulting in smaller droplets. The experimental data obtained was used to fit a correlation relating the Sauter mean diameter of the droplets ($d_{32,d}$) to Re_{net} and Re_o (Equation (3.39)), it was found that Re_o had the dominant effect on d_{32}, putting in evidence that the oscillatory flow conditions can be adjusted in order to obtain certain particle size requirements. The authors also estimated a correlation based on the power dissipation due to oscillatory flow and net flow, Equation (3.40).

$$d_{32,d} = 1.72 \times 10^{-2} Re_o^{-0.91} Re_{net}^{-0.42} \tag{3.39}$$

$$d_{32,d} = 3.7 \times 10^{-5} \left(\frac{\varrho}{\rho}\right)^{-0.3} \left(\frac{\varrho_{net}}{\rho}\right)^{-0.14} \tag{3.40}$$

Ni *et al.* (2002a) investigated droplet breakage and coalescence rates in a continuous oscillatory baffled reactor. The total length of the reactor, including the curves connecting the straight sections, was 12.5 m, and the diameter was 40

mm. The silicone oil was used as the dispersed phase in volume fractions (hold-up) that varied from 1.6 to 6.7 %. In developing a discretized version of the population balance equations to represent the droplet size distributions, the authors assumed that there was no flow of droplets from one cell to another in the reactor. Cell refers to the space between two consecutive baffles. In the discretization process, it was assumed that the droplet volume of a given class was $\sqrt{2}$ times the volume of the previous class (Hounslow *et al.*, 1988). The authors considered binary breakage, and the two droplets resulting from breakage had half the volume of the original droplet. In the coalescence model, strong simplifications were also applied. For instance, instead of considering that all droplets can interact with each other, the authors considered only three types of interactions to avoid computational complexity. Based on the work of Tsouris and Tavlarides (1994), Equations (3.41) and (3.42) were proposed to represent the breakage and coalescence rates (kb and kc) of droplets of diameter d_d in class i. The parameters p_1, p_2, p_3 and p_4 were estimated to fit the data in the experimental conditions investigated. k and $d_{e,min}$ are additional parameters, namely eddy wave number and minimum eddy diameter capable of breaking a droplet, respectively. One of the main drawbacks of this methodology is the fact that the suspension properties are not considered in the breakage and coalescence rate equations.

$$kb(d_{d,i}) = p_1 \int_{2/d_{d,i}}^{2/d_{e,min}} \left(2/k + d_{d,i}^2\right)^2 \sqrt{8.2k^{-2/3} + 1.07d_{d,i}^{2/3}}k^2 \times exp\left(-p_2 d_{d,i}^2 k^{11/3}\right) dk \tag{3.41}$$

$$kc(d_{d,i}, d_{d,j}) = p_3 \left(d_{d,i} + d_{d,j}\right)^2 \sqrt{d_{d,i}^{2/3} + d_{d,j}^{2/3}} exp\left(-\frac{p_4}{(d_{d,i} + d_{d,j})^{2/3}}\right) \tag{3.42}$$

Showing criticism about the previous methods to estimate breakage and coalescence parameters in oscillatory reactors, Mignard *et al.* (2003) proposed a methodology in which the breakage was determined experimentally. More specifically, the authors used a high-speed camera to observe the behavior of the droplets after their passage through the baffle orifice. With this data and a defined droplet breakage probability model (Equation (3.43)), the authors determined the parameters to fit their probability data (p_1 and p_2). In a posterior step, this the authors fixed the breakage frequency, Equation (3.44), and estimated the coalescence parameters (p_3-p_6) in Equation (3.45), to represent the droplet size distributions. In this repre-

sentation, $We(d_{d,i})$ is the droplet Weber number, τ_c represents the average residence time within a cell, and $\bar{R}$ is the reduced droplet radios (more details can be found in the original work).

$$P_{br}(d_{d,i}) = p_1 \frac{d_{d,i}}{d_0} \int_{\pi/2}^{0} \left(-\frac{2}{\pi}\right) exp\left(-\frac{p_2 \alpha^2}{We(d_{d,i}) cos^2(\theta)}\right) d\theta \tag{3.43}$$

$$kb(d_i) = \frac{P_{br}(d_{d,i})}{\tau_c} \tag{3.44}$$

$$\begin{aligned} kc(d_{d,i}, d_{d,j}) = p_3 \left(d_{d,i} + d_{d,j}\right)^2 \sqrt{d_{d,i}^{2/3} + d_{d,j}^{2/3}} \times \\ \left[\frac{1 - exp\left(-p_4 \left(\frac{\varrho}{\rho}\right) \bar{R}^4 (1 - p_6 \bar{R})\right)}{1 - exp\left(-p_5 \left(\frac{\varrho}{\rho}\right) \bar{R}^4 (1 - p_6 \bar{R})\right)}\right] \end{aligned} \tag{3.45}$$

Hounslow and Ni (2004) developed a population balance model to represent the experimental data reported by Ni *et al.* (1998). The authors tested different breakage and coalescence kernels and concluded that the daughter droplet distribution resulting in four droplets of equal size per breakage event gave the best fit. However, the model used by the authors presented a few limitations. More specifically, the properties of the suspension were not included in the rate equations. This makes the model inadequate for scale-up since the estimated parameters can only be applied to the data set used in this study.

In continuation of the work of Mignard *et al.* (2003), Mignard *et al.* (2004) used the same methodology to estimate the breakage frequency in a continuous oscillatory baffled reactor. The authors proposed a very complex model to describe the breakage probabilities. More specifically, the model had five parameters that were estimated based on the available data. Due to experimental limitations, the authors could not gather data regarding the breakage probability of small droplets. It was also found that oscillation amplitude has a stronger effect on droplet breakage than frequency.

To develop a more robust droplet breakage model, Mignard *et al.* (2006) performed experiments with fluids of different physical properties. It was observed that the properties of the fluid did not influence the droplet distributions observed experimentally in their experimental conditions. Moreover, the breakage process

was the predominant phenomenon in the continuous oscillatory baffled reactor. The authors developed a model of breakage probability (Equation (3.46)) and included the droplet viscoelastic effect. The breakage frequency was defined as in Equation (3.44). In total, 3 fitting parameters were included in the model. A parameter estimation procedure was performed, and it was concluded that the parameter related to surface tension had no statistical significance. The other two had limited significance as well. Despite that, the authors claim improvements were made compared to the previous models.

$$P_{br}(d_{d,i}) = 1 - exp\left[-p_1\chi_o \frac{(2\pi f_o\chi_o)^{3/4}\, d_{d,i}^{1/3}}{(\eta_c/\rho_c)^{3/4}} \times exp\left(-p_2 \frac{\sigma}{\rho_c\,(2\pi f_o\chi_o)^2\, d_{d,i}^{5/3}} - p_3 \frac{\eta_d}{\sqrt{\rho_c\rho_d}\,(2\pi f_o\chi_o)\, d^{4/3}}\right)\right] \tag{3.46}$$

At this point, it is important to mention that the models to describe droplet size distributions, breakage, and coalescence rates in oscillatory baffled reactors are of limited use for scale-up and need further improvements. As is the case for other liquid-liquid dispersion systems, it is very unlikely that a universal model will be developed to represent the droplet behavior in these systems, mainly because there are different reactor geometries, operation conditions, and fluid properties. Consequently, how these variables influence droplet behavior is far from fully understood in these systems.

3.2.5 Scale-up

Harvey *et al.* (2001) studied the optimization of ester saponification in a COBR. A 2.9 m long reactor with orifice baffles spaced by 1.5 times the diameter was investigated. The tube and orifice diameters were 24 mm and 12 mm, respectively. The ranges of frequencies and amplitudes of oscillation in the study were $1 \leq f_o \leq 10$ Hz and $0.5 \leq \chi_o \leq 15$ mm. The authors developed a tanks-in-series model and incorporated the saponification kinetics to interpret their data. Based on their data, the authors concluded that the reaction time could be reduced by one order of magnitude compared to the industrial process, keeping the production and specification fixed. Moreover, the reactor volume required is reduced by two orders of magnitude. The authors emphasized the applicability of the continuous oscillatory baffled reactor for batch-to-continuous migration, pointing out the gains

in process safety due to the smaller reactant inventories.

Ni *et al.* (2001b) reported the dispersion characteristics of close-fit and loose-fit orifice baffles aiming at scaling up in batch mode. Available experimental data showed that in both cases, the dispersion coefficient increases linearly with respect to tube diameter. Additionally, a hydraulic diameter was defined to unify the analysis of both baffle types.

Stonestreet and Harvey (2002) developed a scale-up methodology and used two illustrative examples. More specifically, the authors studied the production of succinimide and the hydrolysis of esters to produce sterols. Their method was based on maintaining the mixing regime obtained at the laboratory scale in the scaled up process. For this undertaking, the dimensionless groups used to represent the oscillatory baffled reactor, namely Re_{net}, Re_o, St, and Ψ were utilized. The power dissipation was also taken into consideration. Spreadsheet calculations were employed to illustrate the methodology proposed. The authors compared the optimal dimensions and operational conditions of the oscillatory baffled reactor obtained with the equivalent conventional tubular reactor designed to achieve the same mixing and production requirements. It was shown that the oscillatory baffled reactor was considerably smaller than the equivalent tubular reactor and required less energy. This work is a landmark in the literature on oscillatory baffled reactors since it was the first time a detailed scale-up methodology was proposed.

Jian and Ni (2005) studied the scale-up of an oscillatory baffled tube using computational fluid dynamics. The authors argued that scaling the diameter of the tube and keeping the ratio of oscillatory Reynolds number can lead to similar flow patterns in these devices. Tube diameters of 50, 100, and 200 mm were investigated.

Smith and Mackley (2006) measured the dispersion coefficients in tubes with 24, 54, and 150 mm diameters and presented a correlation relating the oscillatory conditions to the dispersion coefficient, Equation (3.47). The lengths of the tubes were 1, 2, and 4.5 m, respectively. As a significant result, these authors concluded, based on experiments, that the magnitude of axial dispersion does not vary with tube diameter if the values of Re_{net}, Re_o and St are fixed. The authors emphasized their discovery from the point of view of scaling up from laboratory scale to larger scales. The authors emphasized that a multi-orifice baffled design can be an alternative to single-orifice tubes.

$$D_x = 7.0 \times 10^{-7} Re_{net}^{0.8} + 7.5 \times 10^{-7} Re_o e^{-0.4St} + \frac{3.0 \times 10^{-12} Re_{net}^{1.6}}{7.0 \times 10^{-7} Re_{net}^{0.8} + 7.5 \times 10^{-7} Re_o e^{-0.4St}} \quad (3.47)$$

Oliva *et al.* (2018) investigated the residence time distribution in two commercially available oscillatory baffled reactors. Principal component based image analysis was used to investigate the RTDs under different operational conditions. In this study, reactors of 37.5 mL and 312.5 mL were investigated. For comparison purposes, the mean oscillatory velocity was kept constant in both reactors. Similar to previous studies, it was found that the effect of frequency on dispersion is less significant than oscillation amplitude in affecting the dispersion coefficients. Moreover, the conditions that achieve near plug flow regime were identified for each reactor.

Sutherland *et al.* (2021) studied the scale-up of a moving baffle OBC through CFD. Similar to the work of Smith and Mackley (2006), the authors studied columns of different diameters, and the oscillatory conditions were chosen such that Re_o and St were kept constant. The response variables were the axial to radial velocity ratio, the oscillatory power number, and energy dissipation. It was shown that high frequencies and low oscillation amplitudes hinder the mixing pattern along the column. This mixing pattern was quantified through the mixing time, which is the time required to obtain homogeneous conditions inside the column. It was argued that high frequencies increase backmixing delaying the fluid propagation. Moreover, it was verified that increasing the column diameter and keeping Re_o and St unchanged preserves the dynamic conditions inside the OBC. On the other hand, the overall power density decreases, and mixing time increases due to the larger fluid volume.

Cox *et al.* (2022) developed an experimental study to gain insight into the behavior of the RTD of a COBR upon scaling up. The reactor had a diameter of 40 mm and a total length of 5740 mm, considering all the columns. The investigators used a design of experiments and used the tanks in series model to represent the number of tanks as a function of the dimensionless numbers that describe the oscillatory baffled reactor. When the RTD in a single column was evaluated, the number of tanks that fitted their data was 13.38, which was very close to the actual number of tanks present (twelve, more specifically). However, in the experiments with the whole reactor length, the best fit was obtained with 43.68 tanks instead of sixty real compartments. The maximum number of tanks occurred at a velocity ratio (Ψ)

equal to 2.27. Furthermore, the authors discussed the effect of the U-bends on the oscillation due to energy losses affecting the RTDs and pointed out some issues that need to be addressed when scaling up very long processes.

3.2.6 Applications of OBRs to Suspension Polymerization

Even though oscillatory flow reactors have also been applied to emulsion polymerization processes (Palma *et al.*, 2001; Sayer *et al.*, 2002; Carvalho *et al.*, 2010), this subsection exclusively focuses on the application of OBRs to suspension polymerizations for the sake of conciseness. Moreover, there are differences among these two processes and a detailed explanation of the aspects and mechanisms involved in emulsion polymerization is out of the scope of this work. Therefore, the next paragraphs distills the relevant work performed using OBRs to suspension polymerizations.

Ni *et al.* (1998) investigated the behavior of liquid-liquid suspensions of methyl methacrylate (MMA) and water in a batch oscillatory baffled reactor (BOBR). The authors used two recipes, one containing a high amount of surfactant and another containing less. From the dispersion point of view, the droplets of monomer prepared with high surfactant content would not coalesce when the fluid oscillation ceased, being more stable. In the first experiment performed with the high surfactant concentration recipe, the authors found that at specified oscillatory conditions, the Sauter mean diameter of droplets (d_{32}) decreased until reaching a dynamic equilibrium condition. According to this experiment, the time required to obtain stable droplets was 30 min. Furthermore, the decrease in d_{32} suggested that the breakup mechanism was predominant over coalescence during the transitional period.

Based on their data and a correlation in the literature that describes d_{32} in stirred tanks (Zerfa and Brooks, 1996), the authors were able to highlight the similarities between the transitional behavior in BOBRs and stirred tank reactors (STR). Concerning the recipe prepared with a lower amount of surfactant, the authors noticed that the transition time was not affected by the levels of surfactant. However, the surfactant amount affected the d_{32} and the droplet size distribution (DSD). The recipe prepared with the higher amount of surfactant resulted in smaller d_{32} and narrower DSDs for the same oscillatory conditions. Lastly, the effect of baffle thickness on the DSD was evaluated. By comparing baffles with thicknesses of 0.8 and 3 mm, it was noticed that the latter provided smaller droplets and narrower DSDs in the studied experimental conditions. Equations (3.48) and (3.49) were proposed to

represent the d_{32} in terms of the oscillatory velocity and power dissipation per uni mass (Equation (3.50)), respectively.

$$d_{32} = 0.966 \times 10^{-6} \left(\chi_o f_o\right)^{-1.2}, \;\; 24 \leq \chi_o f_o \leq 60 \; [\text{mm s}^{-1}] \tag{3.48}$$

$$d_{32} = 6.80 \times 10^{-5} \left(\frac{\varrho}{\rho}\right)^{-0.4} \tag{3.49}$$

$$\frac{\varrho}{\rho} = 3.82 \times 10^{4} \left(\chi_o f_o\right)^{3} \tag{3.50}$$

In a subsequent work, Ni *et al.* (1999) developed a correlation relating polymer particle size with droplet size using MMA in a BOBR. In this case, the polymerization reaction was conducted in the BOBR and the particle size was described in terms of the mean particle size of the polymer ($d_{v,0.5}$), which represents the particle size at 50% cumulative volume distribution. Initially, the authors investigated the effect of frequency of oscillation on d_{32} and $d_{v,0.5}$ at a fixed oscillation amplitude and concluded that increasing frequency might lead to the reduction of both quantities. It must be emphasized, however, that the effect of increasing oscillation frequency exerted a stronger effect on $d_{v,0.5}$. On the other hand, increasing the oscillation amplitude at a fixed frequency caused effects of equivalent magnitudes both in $d_{v,0.5}$ and d_{32}. Regarding the effects of frequency and amplitude on the PSDs, it was observed that increasing any of the two variables provided narrower particle size distributions, suggesting that both variables can be used to control this important product property.

Based on the correlation obtained in the previous works, Ni *et al.* (1999) developed a correlation relating the d_{32} and $d_{v,0.5}$, Equations (3.51) and (3.52). In other words, the proposed correlation related the droplet size in a system without reaction to the particle size in a system where polymerization took place. At the analysed experimental conditions, the proportionality constant between d_{32} and $d_{v,0.5}$ was equal to 3.11. This constant value highlighted the observation that the coalescence phenomenon occurred during the reaction; consequently, the diameters of the obtained polymer beads were larger than the diameters of the original droplets. Ni *et al.* (1999) also observed that the transient trajectories of d_{32} at different frequencies

were initiated at lower values and then increased with the course of the reaction. According to the authors, this indicated that the increase in the system viscosity due to the chemical reaction favored the coalescence phenomenon resulting in larger droplet sizes.

$$d_{v,0.5} = 3.11 \times 10^{-6} \left(\chi_o f_o\right)^{-1.2}, \quad 24 \leq \chi_o f_o \leq 60 \text{ [mm s}^{-1}\text{]} \tag{3.51}$$

$$d_{v,0.5} = 3.11 d_{32} \tag{3.52}$$

Based on the works by Ni *et al.* (1998) and Ni *et al.* (1999), Nelson *et al.* (2000) performed a similar study in a reactor of larger dimension (diameter of 210 mm). These investigators tried to comprehend the scaling up of the process. Based on the findings of the previous authors and their data, the authors were able to develop a correlation relating d_{32} to oscillation conditions and the power input, Equations (3.53) and (3.54).

$$d_{32} = 3.9 \times 10^{-6} \left(\chi_o f_o\right)^{-1.15}, \quad 27 \leq \chi_o f_o \leq 60 \text{ [mm s}^{-1}\text{]} \tag{3.53}$$

$$d_{32} = 12.1 \times 10^{-5} \left(\frac{\varrho}{\rho}\right)^{-0.35} \tag{3.54}$$

Ni *et al.* (2000) studied the inverse suspension polymerization of acrylamide in a BOBR. In contrast to previous publications, the authors employed an apparatus in which the oscillations were caused by moving baffles. As in the previous publications, it was noticed that increasing the oscillatory velocity (product of frequency and amplitude) resulted in smaller polymer particles. The authors concluded that there was a limiting value of oscillation velocity below which the mixing along the height of the reactor was not efficient. In this condition of poor mixing, a temperature gradient was observed along the reactor, which was caused by the combination of poor heat exchange and nonuniform reaction conditions. In conditions where mixing was not efficient, the authors verified that the PSDs were much larger and skewed. On the other hand, at the conditions where mixing was efficient, Gaussian PSDs were

obtained, indicating that mean particle size and PSD could be controlled by selecting the appropriate oscillatory velocity. Besides, the baffle spacing exerted little effect on the mean particle size and PSD, which was attributed to the fact that in moving baffle apparatuses the oscillatory amplitude is higher than in pulsating fluid systems. The effect of the baffle-free area on obtained PSDs was also moderate, even though 23% free area provided a minimum mean particle size. The effect of monomer addition time was approximately linear and of small magnitude on the mean particle size. The following correlations were proposed to describe the mean particle size as a function of the oscillation conditions and energy dissipation, Equations (3.55) and (3.56).

$$d_{v,0.5} = 4.4 \times 10^{-1} \left(\chi_o f_o\right)^{-1.603}, \quad 50 \leq \chi_o f_o \leq 150 \text{ [mm s}^{-1}] \tag{3.55}$$

$$d_{v,0.5} = 2.121 \times 10^{-3} \left(\frac{\varrho}{\rho}\right)^{-0.6511} \tag{3.56}$$

In a subsequent work, Ni *et al.* (2001a) extended the results of Ni *et al.* (2000) and developed a population balance model to represent interactions between droplets and the particle and droplet size distributions. Before doing that, correlations were proposed to describe the average droplet diameters (Equation (3.57) and (3.58)) and particle diameters (Equation (3.59) and (3.60)). Regarding the numerical solution of the population balance model, the authors employed the discretization method of Lister *et al.* (1995).

$$d_{32} = 2.8 \times 10^{-5} \left(\chi_o f_o\right)^{-0.96} \tag{3.57}$$

$$d_{32} = 7.26 \times 10^{-4} \left(\frac{\varrho}{\rho}\right)^{-0.32}, \; 10 \leq \frac{\varrho}{\rho} \leq 90 \text{ [W kg}^{-1}] \tag{3.58}$$

$$d_{v,0.5} = 1.44 \times 10^{-3} \left(\frac{\varrho}{\rho}\right)^{-0.55} \tag{3.59}$$

$$d_{v,0.5} = 34.85 d_{32}^{1.70} \tag{3.60}$$

Ni *et al.* (2002b) developed a population balance model for the previously described system that considered the breakage rate only. Although the authors tried to show the capabilities of the OBR for process intensification and production of tailored polymer materials, there was strong evidence that their numerical strategy could not calculate the breakage rates very efficiently. For instance, the applied numerical method resulted in negative breakage rates in some simulations.

More recently, Lobry *et al.* (2015) investigated liquid-liquid dispersions and polymerizations in a COBR. In the first part of their study, the authors studied the conditions where a suspension of oil and water might be prepared to provide stable dispersions. In this part of their study, the apparatus schematically shown in Figure 3.6 was used. A set of experimental conditions that resulted in stable suspensions were mapped. Droplet size distributions were also measured, and the d_{32} was correlated with operational conditions, Equations (3.61)-(3.62). In the polymerization study, vinyl acetate was polymerized in suspension to reach monomer conversions up to 30 wt%. The authors reported the dynamic conversion data at the reactor outlet and steady state conversions along reactor length. Although promising, several aspects of the polymerization reaction still need to be investigated in detail. For instance, data on molar mass distributions and the fouling phenomenon were not reported. The experimental apparatus used in the polymerization reactions is shown in Figure 3.7.

$$d_{32} = 51.6 \left(\frac{\varrho}{\rho} \right)^{-0.29} \tag{3.61}$$

$$\frac{d_{32}}{d_h} = 2.99 Re_o^{-0.89} We_h^{-0.08} \tag{3.62}$$

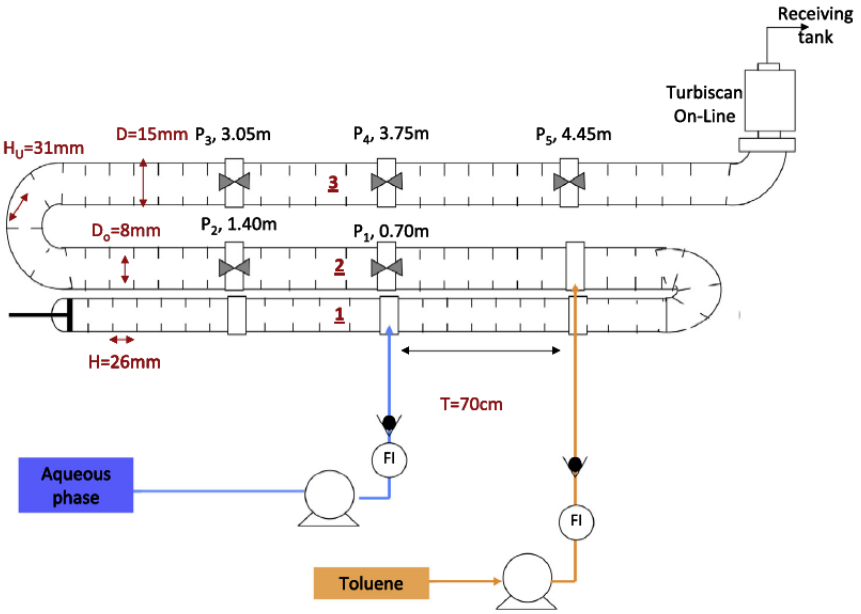

Figure 3.6: Experimental apparatus used by Lobry *et al.* (2015) to perform liquid-liquid dispersions.

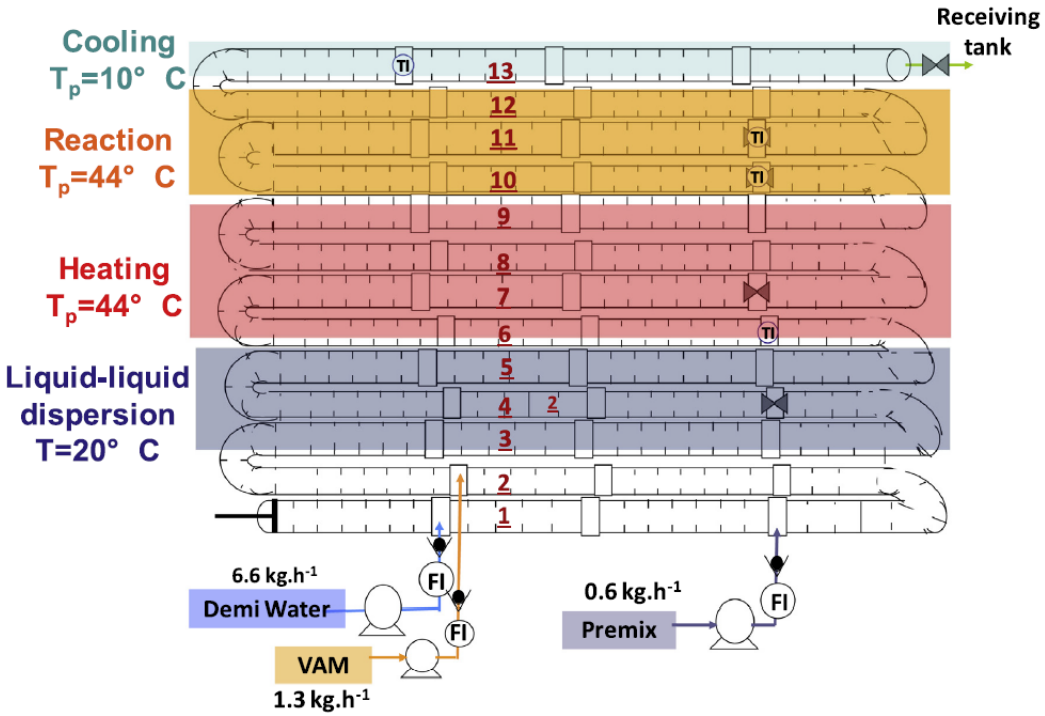

Figure 3.7: Experimental apparatus used by Lobry *et al.* (2015) to perform suspension polymerization reactions.

3.3 Concluding Remarks

Based on this literature review, it is possible to conclude that the continuous operation of suspension polymerization reactors is still a challenge. There are operational problems that need to be overcome, most notably the fouling on the reactor walls. Moreover, the literature on suspension polymerization in oscillatory baffled reactors is scarce. Even though the mixing characteristics of the oscillatory baffled reactor are attractive for conducting lengthy reactions, further investigation needs to be performed to gain insights into the behavior of the system at conditions close to the ones performed at the industrial level. More specifically, the hydrodynamic behavior of the system at higher monomer hold up and conversion has never been studied. The heat transfer is also an operational issue that needs attention. Finally, but not least important, the polymer morphology is of paramount importance for end-use applications. Therefore, a comprehensive mathematical model that includes the kinetics, heat transfer, and polymer properties can be of great value in understanding suspension polymerizations in oscillatory baffled reactors.

List of Abbreviations

Abbreviation	Meaning
BOBR	Batch Oscillatory Baffled Reactor
CFD	Computational Fluid Dynamics
COBR	Continuous Oscillatory Baffled Reactor
DSD	Droplet Size Distribution
EEM	Eddy Enhancement Model
OBR	Oscillatory Baffled Reactor
OBT	Oscillatory Baffled Tube
OFR	Oscillatory Flow Reactor
OBC	Oscillatory Baffled Column
PMMA	Poly(methyl methacrylate)
PSD	Particle Size Distribution
PVC	Poly(vinyl chloride)
PVAC	Poly(vinyl acetate)
QSM	Quasi Steady State Model
RTD	Residence Time Distribution

List of Symbols

Symbol	Meaning
d	Diameter [m]
d_h	Hydraulic diameter [m]
d_o	Orifice diameter [m]
d_{32}	Sauter mean diameter [m]
D_x	Diffusion coefficient [m^2 s^{-1}]
f_o	Frequency of oscillation [s^{-1}]
h	Convective heat transfer coefficient [J s^{-1} m^{-2} K^{-1}]
k	Thermal conductivity [J s^{-1} m^{-1} K^{-1}]
kb	Breakage rate constant [s^{-1}]
kc	Coalescence rate constant [m^3 s^{-1}]
L	Tube length [m]
Nu	Nusselt number [-]
Pe	Peclet number [-]
Pr	Prandtl number [-]
Re_o	Oscillatory Reynolds number [-]
Re	Reynolds number [-]
St	Strouhal number [-]
v	Velocity [m s^{-1}]
We_h	Weber number [-]
Greek letters	
α	Restriction ratio (d_o^2/d^2) [%]
χ_o	Center-to-peak amplitude of oscillation [m]
η	Viscosity [kg m^{-1} s^{-1}]
σ	Thermal conductivity [J m^{-1} s^{-1} K^{-1}]
ρ	Density [kg m^{-3}]
ϱ	Power dissipation [W m^{-3}]
Ψ	Velocity ratio [-]

3.4 References

Abbott, M.S.R.; Harvey, A.P.; Perez, G.V.; Theodorou, M.K. Biological processing in oscillatory baffled reactors: operation, advantages and potential. Interface Focus 3, 20120036, 2013.

Abbott, M.S.R.; Harvey, A.P.; Morrison, M.I. Rapid determination of the residence time distribution (RTD) function in an oscillatory baffled reactor (OBR) using a design of experiments (DoE) approach. International Journal of Chemical Reactor Engineering, 12, 1, 575-586, 2014.

Ahmed, S.M.R.; Phan, A.N.; Harvey, A.P. Mass transfer enhancement as a function of oscillatory baffled reactor design. Chemical Engineering and Processing: Process Intensification, 130, 229-239, 2018a.

Ahmed, S.M.R.; Law, R.; Phan, A.N.; Harvey, A.P. Thermal performance of meso-scale oscillatory baffled reactors. Chemical Engineering and Processing: Process Intensification, 132, 25-33, 2018b.

Avila, M.; Fletcher, D.F.; Poux, M.; Xuereb, C.; Aubin, J. Mixing performance in continuous oscillatory baffled reactors. Chemical Engineering Science, 219, 115600, 2020a.

Avila, M.; Fletcher, D.F.; Poux, M.; Xuereb, C.; Aubin, J. Predicting power consumption in continuous oscillatory baffled reactors. Chemical Engineering Science, 212, 115310, 2020b.

Avila, M.; Kawas, B.; Fletcher, D.F.; Poux, M.; Xuereb, C.; Aubin, J. Design, performance characterization and applications of continuous oscillatory baffled reactors. Chemical Engineering and Processing - Process Intensification, 180, 108718, 2022.

Briggs, N.E.B.; McGinty, J.; McCabe, C.; Raval, V.; Sefcik, J.; Florence, A.J. Heat transfer and residence time distribution in plug flow continuous oscillatory baffled crystallizers. ACS Omega, 6, 28, 18352-18363, 2021.

Baird, M.H.I.; Stonestreet, P. Energy dissipation in oscillatory flow within a baffled tube. Chemical Engineering Research and Design, 73, 5, 503-511, 1995.

Brunold, C.R.; Hunns, J.C.B.; Mackley, M.R.; Thompson, J.W. Experimental observations on flow patterns and energy losses for oscillatory flow in ducts containing sharp edges. Chemical Engineering Science, 44, 5, 1227-1244, 1989.

Carvalho, A.C.S.M.; Chicoma, D.L.; Sayer, C.; Giudici, R. Development of a continuous emulsion copolymerization process in a tubular reactor. Industrial and Engineering Chemistry Research, 49, 21, 10262-10273, 2010.

Cox, R.; Salonitis, K.; Rebrov, E.; Impey, S.A. Revisiting the effect of U-bends, flow parameters, and feasibility for scale-up on residence time distribution curves for a continuous bioprocessing oscillatory baffled flow reactor. Industrial and Engineering Chemistry Research, 61, 30, 11181-11196, 2022.

Dickens, A.W.; Mackley, M.R.; Williams, H.R. Experimental residence time distribution measurements for unsteady flow in baffled tubes. Chemical Engineering Science, 44, 7, 1471-1479, 1989.

Dirix, C.A.M.C.; De Jong, J.J.T.; Meulenbrugge, L.; Vanduffel, K.A.K. Continuous process for the production of vinyl chloride (co)polymers. Akzo Nobel, United States Patent (Reissued), USRE45940E, 2016.

Dowding, P.J.; Goodwin, J.W.; Vincent, B. Production of porous suspension polymers using a continuous tubular reactor. Colloid and Polymer Science, 278, 346-351, 2000.

Dowding, P.J.; Goodwin, J.W.; Vincent, B. Production of porous suspension polymer beads with a narrow size distribution using a cross-flow membrane and a continuous tubular reactor. Colloids and Surfaces A: Physicochemical and Engineering Aspects, 180, 3, 301-309, 2001.

Ejim, L.N.; Yerdelen, S.; McGlone, T.; Onyemelukwe, I.; Johnston, B.; Florence, A.J.; Reis, N.M. A factorial approach to understanding the effect of inner geometry of baffled meso-scale tubes on solids suspension and axial dispersion in continuous, oscillatory liquid-solid plug flows. Chemical Engineering Journal, 308, 669-682, 2017.

Eze, V.C.; Fisher, J.C.; Phan, A.N.; Harvey, A.P. Intensification of carboxylic acid esterification using a solid catalyst in a mesoscale oscillatory baffled reactor platform. Chemical Engineering Journal, 322, 205-214, 2017.

Fitch, A.W.; Jian, H.; Ni, X. An investigation of the effect of viscosity on mixing in an oscillatory baffled column using digital particle image velocimetry and computational fluid dynamics simulation. Chemical Engineering Journal, 112, 197-210, 2005.

González-Juárez, D.; Herrero-Martín, R.; Solano, J.P. Enhanced heat transfer and power dissipation in oscillatory-flow tubes with circular-orifice baffles: a numerical study. Applied Thermal Engineering, 141, 494-502, 2018.

González-Juárez, D.; Solano, J.P.; Herrero-Martín, R.; Harvey, A.P. Residence time distribution in multiorifice baffled tubes: a numerical study. Chemical Engineering Research and Design, 118, 259-269, 2017.

Harvey, A.P.; Mackley, M.R.; Stonestreet, P. Operation and optimization of an oscillatory flow continuous reactor. Industrial and Engineering Chemistry Research, 40, 23, 5371-5377, 2001.

Hatate, Y.; Ikari, A.; Nakashio, F.; Kondo, K. Effect of coalescence and redispersion on suspension polymerization of styrene in a continuous stirred tank reactor. Journal of Chemical Engineering of Japan, 14, 6, 493-495, 1981.

Hatate, Y.; Ikari, A.; Nakashio, F.; Kondo, K. A simulation of continuous suspension polymerization of styrene by the Monte Carlo Method. Journal of Chemical Engineering of Japan, 17, 3, 339-342, 1984.

Hewgill, M.R.; Mackley, M.R.; Pandit, A.B.; Pannu, S.S. Enhancement of gas-liquid mass transfer using oscillatory flow in a baffled tube. Chemical Engineering Science, 48, 4, 799-809, 1993.

Hong, C.; Shimin, W.; Guohua, S.; Huiyuan, X. The continuous synthesis system of suspension type polyvinyl-chloride. Yibin Tianyuan Group, Chinese Patent Number CN209501640U, 2019.

Hounslow, M.; Ni, X. Population balance modeling of droplet coalescence and break-up in an oscillatory baffled reactor. Chemical Engineering Science, 59, 4, 819-828, 2004.

Hounslow, M.J.; Ryall, R.L.; Marshall, V.R. A discretized population balance for nucleation, growth and aggregation. AIChE Journal, 34, 11, 1821-1832, 1988.

Howes, T.; Mackley, M.R.; Roberts, E.P.L. The simulation of chaotic mixing and dispersion for periodic flows in baffled channels. Chemical Engineering Science, 46, 7, 1669-1677, 1991.

Huang, W.; Zhang, C.; Li, Z.; Liang, W.; Xu, J.; Xiong, Q.; Luo, H. Assessments of the heat transfer performance of a novel continuous oscillatory baffled crystallizer via two-fluid model. Chemical Engineering Science, 275, 118701, 2023.

Jealous, A.C.; Johnson, H.F. Power requirements for pulse generation in pulse columns. Industrial and Engineering Chemistry, 47, 6, 1159-1166, 1955.

Jian, H.; Ni, X. A numerical study on the scale-up behavior in oscillatory baffled columns. Chemical Engineering Research and Design, 83, A10, 1163-1170, 2005.

Jimeno, G.; Lee, Y.C.; Ni, X. On the evaluation of power density models for oscillatory baffled reactors using CFD. Chemical Engineering and Processing: Process Intensification, 134, 153-162, 2018.

Jimeno, G.; Lee, Y.C.; Ni, X. The effect of particle size on flow in a continuous oscillatory baffled reactor using CFD. Canadian Journal of Chemical Engineering, 100, S258-S271, 2022.

Kacker, R.; Regensburg, S.I.; Kramer, H.J.M. Residence time distribution of dispersed liquid and solid phase in a continuous oscillatory flow baffled crystallizer. Chemical Engineering Journal, 317, 413-423, 2017.

Klippert, H.; Tzschoppe, E.; Paschalis, S.; Weinlich, J.; Eaglemann, M. Continuous process and device for the manufacture of a vinyl chloride polymer in aqueous suspension. Hoechst Aktiengesellschaft, United States Patent Number 4424301, 1984.

Knott, G.F.; Mackley, M.R. On eddy motions near plates and ducts, induced by water waves and periodic flows. Philosophical Transactions of the Royal Society of London. Series A, Mathematical and Physical Sciences, 294, 1412, 599-623, 1980.

Krause, H.J.; Wolf, H. Vorrichtung zur kontinuierlichen polymerisation. BASF, German Patent Number 1217069, 1966.

Law, R.; Ahmed, S.M.R.; Tang, N.; Phan, A.N.; Harvey, A.P. Development of a more robust correlation for predicting heat transfer performance in oscillatory baffled reactors. Chemical Engineering and Processing: Process Intensification, 125, 133-138, 2018.

Levenspiel, O.; Smith, W.K. Notes on the diffusion-type model for the longitudinal mixing of fluids in flow. Chemical Engineering Science, 6, 4-5, 227-235, 1957.

Lima, R.; Silva, J.; Vasconcelos, M.; Castor, C.A.; Pinto, J.C. Bibliometric survey of the PVC production - part I: the continuous polymerization challenge. Polímeros, 33, 2, 2023.

Lister, J.D.; Smit, D.J.; Hounslow, M.J. Adjustable discretized population balance for growth and aggregation. AIChemE Journal, 41, 3, 591-603, 1995.

Liu, Z.; Lu, Y.; Yang, B.; Luo, G. Controllable preparation of poly(butyl acrylate) by suspension polymerization in a coaxial capillary microreactor. Industrial and Engineering Chemistry Research, 50, 21, 11853-11862, 2011.

Lobry, E.; Gourdon, C.; Xuereb, C.; Lasuye, T. Liquid-liquid dispersion in cocurrent disc and doughnut pulsed column effect of the operating conditions, physical properties and materials parameters. Chemical Engineering Journal, 233, 24-38, 2013.

Lobry, E.; Lasuye, T.; Gourdon, C.; Xuereb, C. Liquid-liquid dispersion in a continuous oscillatory baffled reactor- application to suspension polymerization. Chemical Engineering Journal, 259, 505-518, 2015.

Mackley, M.R.; Ni, X. Mixing and dispersion in a baffled tube for steady laminar and pulsatile flow. Chemical Engineering Science, 46, 12, 3139-3151, 1991.

Mackley, M.R.; Ni, X. Experimental fluid dispersion measurements in periodic baffled tube arrays. Chemical Engineering Science, 48, 18, 3293-3305, 1993.

Mackley, M.R.; Tweddle, G.M.; Wyatt, I.D. Experimental heat transfer measurements for pulsatile flow in baffled tubes. Chemical Engineering Science, 45, 5, 1237-1242, 1990.

Mackley, M.R.; Stonestreet, P. Heat transfer and associated energy dissipation for oscillatory flow in baffled tubes. Chemical Engineering Science, 50, 14, 2211-2224, 1995.

Manninen, M.; Gorshkova, E.; Immonen, K.; Ni, X. Evaluation of axial dispersion and mixing performance in oscillatory baffled reactors using CFD. Journal of Chemical Technology and Biotechnology, 88, 4, 553-562, 2013.

Mazubert, A.; Fletcher, D.F.; Poux, M.; Aubin, J. Hydrodynamics and mixing in continuous oscillatory flow reactors - part I: effect of baffle geometry. Chemical Engineering and Processing: Process Intensification, 108, 78-92, 2016a.

Mazubert, A.; Fletcher, D.F.; Poux, M.; Aubin, J. Hydrodynamics and mixing in continuous oscillatory flow reactors - part II: characterization methods. Chemical Engineering and Processing: Process Intensification, 102, 102-116, 2016b.

McDonough, J.R.; Phan, A.N.; Harvey, A.P. Rapid process development using oscillatory baffled mesoreactors - a state-of-the-art review. Chemical Engineering Journal, 265, 110-121, 2015.

McDonough, J.R.; Phan, A.N.; Reay, D.A.; Harvey, A.P. Passive isothermalisation of an exothermic reaction in flow using a novel "heat pipe oscillatory baffled reactor (HPOBR)". Chemical Engineering and Processing: Process Intensification, 110, 201-213, 2016.

McDonough, J.R.; Ahmed, S.M.R.; Phan, A.N.; Harvey, A.P. A study of the flow structures generated by oscillating flows in a helical baffled tube. Chemical Engineering Science, 171, 160-178, 2017.

McDonough, J.R.; Phan, A.N.; Harvey, A.P. The mesoscale oscillatory baffled reactor facilitates intensified kinetics screening when the solvent is removed. Chemical Engineering and Processing: Process Intensification, 129, 51-62, 2018.

McDonough, J.R.; Oates, M.F.; Law, R.; Harvey, A.P. Micromixing in oscillatory baffled flows. Chemical Engineering Journal, 361, 508-518, 2019.

Mecklenburgh, J.C.; Hartland, S. Design of reactors with backmixing - I exact methods. Chemical Engineering Science, 23, 57-65, 1968.

Mignard, D.; Amin, L.; X. Ni. Population balance modeling of droplets in an oscillatory baffled reactor - using direct measurements of breakage rate constants. Journal of Chemical Technology and Biotechnology, 78, 2-3, 364-369, 2003.

Mignard, D.; Amin, L.; Ni, X. Modelling of droplet breakage probabilities in an oscillatory baffled reactor. Chemical Engineering Science, 59, 11, 2189-2200, 2004.

Mignard, D.; Amin, L.P.; Ni, X. Determination of breakage rates of oil droplets in a continuous oscillatory baffled tube. Chemical Engineering Science, 61, 21, 6902-6917, 2006.

Mortazavi, H.; Pakzad, L. Power consumption in a moving baffle oscillatory baffled reactor: a CFD study. Canadian Journal of Chemical Engineering, 101, 5, 2878-2895, 2023.

Muñoz-Cámara, J.; Solano, J.P.; Pérez-García, J. Experimental correlations for oscillatory-flow friction and heat transfer in circular tubes with tri-orifice taffles.

International Journal of Thermal Sciences, 156, 106480, 2020.

Muñoz-Cámara, J.; Crespí-Llorens, D.; Solano, J.P.; Vicente, P. Baffled tubes with superimposed oscillatory flow: experimental study of the fluid mixing and heat transfer at low net Reynolds numbers. Experimental Thermal and Fluid Science, 123, 110324, 2021a.

Muñoz-Cámara, J.; Solano, J.P.; Pérez-García, J. Analytical calculation of the flow superposition effect on the power consumption in oscillatory baffled reactors. Chemical Engineering Science, 229, 116084, 2021b.

Munõz-Cámara, J.; Solano, J.P.; Pérez-García, J. Non-dimensional analysis of experimental pressure drop and energy dissipation measurements in oscillatory baffled reactors. Chemical Engineering Science, 262, 118030, 2022.

Muñoz-Cámara, J.; Crespí-Llorens, D.; Solano, J.P.; Vicente, P.G. Effect of three-orifice baffles orientation on the flow and thermal-hydraulic performance: experimental analysis for net and oscillatory flows. Applied Thermal Engineering, 236, 121566, 2024.

Nelson, G.; Ni, X.; Mustafa, I. Experimental measurement of droplet size distribution of a MMA suspension in a batch oscillatory reactor of 0.21m diameter. 10^{th} European Conference on Mixing, Eds: H.E.A. van den Akker and J.J. Derksen, Elsevier, 2000.

Ni, X.; Pereira, N.E. Parameters affecting fluid dispersion in a continuous oscillatory baffled tube. AIChE Journal, 46, 1, 37-45, 2000.

Ni, X.; Bennett, D.C.; Symes, K.C.; Grey, B.D. Inverse phase suspension polymerization of acrylamide in a batch oscillatory baffled reactor. Journal of Applied Polymer Science, 76, 11, 1669-1676, 2000.

Ni, X.; Gélicourt, Y.S.; Baird, M.H.I.; Rama Rao, N.V. Scale-up of single phase axial dispersion coefficients in batch and continuous oscillatory baffled tubes. Canadian Journal of Chemical Engineering, 79, 3, 444-448, 2001b.

Ni, X.; Johnstone, J.C.; Symes, K.C.; Grey, B.D.; Bennett, D.C. Suspension polymerization of acrylamide in an oscillatory baffled reactor: from drops to particles. AIChemE Journal, 47, 8, 1746-1757, 2001a.

Ni, X.; Mignard, D.; Saye, B.; Johnstone, J.C.; Pereira, N. On the evaluation

of droplet breakage and coalescence rates in an oscillatory baffled reactor. Chemical Engineering Science, 57, 11, 2101-2114, 2002a.

Ni, X.; Murray, K.R.; Zhang, Y.; Bennett, D.; Howes, T. Polymer product engineering utilising oscillatory baffled reactors. Powder Technology, 124, 3, 281-286, 2002b.

Ni, X.; Gough, P. On the discussion of the dimensionless groups governing oscillatory flow in a baffled tube. Chemical Engineering Science, 52, 18, 3209-3212, 1997.

Ni, X. Residence time distribution measurements in a pulsed baffled tube bundle. Journal of Chemical Technology and Biotechnology, 59, 3, 213-221, 1994.

Ni, X.; Gao, S.; Cumming, R.H.; Pritchard, D.W. A comparative study of mass transfer in yeast for a batch pulsed baffled bioreactor and a stirred tank fermenter. Chemical Engineering Science, 50, 13, 2127-2136, 1995.

Ni, X.; Gao, S. Mass transfer characteristics of a pilot pulsed baffled reactor. Journal of Chemical Technology and Biotechnology, 65, 65-71, 1996.

Ni, X.; Zhang, Y.; Mustafa, I. An investigation of droplet size and size distribution in methylmethacrylate suspensions in a batch oscillatory-baffled reactor. Chemical Engineering Science, 53, 16, 2903-2919, 1998.

Ni, X.; Zhang, Y.; Mustafa, I. Correlation of polymer particle size with droplet size in suspension polymerisation of methylmethacrylate in a batch oscillatory-baffled reactor. Chemical Engineering Science, 54, 6, 841-850, 1999.

Oliva, J.A.; Pal, K.; Barton, A.; Firth, P.; Nagy, Z.K. Experimental investigation of the effect of scale-up on mixing efficiency in oscillatory flow baffled reactors (OFBR) using principal component based image analysis as a novel noninvasive residence time distribution measurement approach. Chemical Engineering Journal, 351, 498-505, 2018.

Onyemelukwe, I.I.; Benyahia, B.; Reis, N.M.; Nagy, Z.K.; Rielly, C.D. The heat transfer characteristics of a mesoscale continuous oscillatory baffled flow crystalliser with smooth periodic constrictions. International Journal of Heat and Mass Transfer, 123, 1109-1119, 2018.

Osstergaard, K.; Michelsen, M. On the use of the imperfect tracer pulse method

for determination of hold-up and axial mixing. Canadian Journal of Chemical Engineering, 47, 2, 107-112, 1969.

Palma, M.; Sayer, C.; Giudici, R. A new reactor for emulsion polymerization: effect of operational conditions on conversion and particle number. DECHEMA Monographs, 137, 625-631, 2001.

Pereira, N.E.; Ni, X. Droplet size distribution in a continuous oscillatory baffled reactor. Chemical Engineering Science, 56, 3, 735-739, 2001.

Phan, A.; Harvey, A.P.; Rawcliff, M. Continuous screening of base-catalysed biodiesel production using new designs of mesoscale oscillatory baffled reactors. Fuel Processing Technology, 92, 8, 1560-1567, 2011a.

Phan, A.; Harvey, A.; Lavender, J. Characterisation of fluid mixing in novel designs of mesoscale oscillatory baffled reactors operating at low net flow rates (0.3-0.6 ml/min). Chemical Engineering and Processing: Process Intensification, 50, 3, 254-263, 2011b.

Phan, A.; Harvey, A. Characterisation of mesoscale oscillatory helical baffled reactor - experimental approach. Chemical Engineering Journal, 180, 229-236, 2012.

Phan, A.; Harvey, A.; Eze, V. Rapid production of biodiesel in mesoscale oscillatory baffled reactors. Chemical Engineering and Technology, 35, 7, 1214-1220, 2012.

Phan, A.N.; Harvey, A. Development and evaluation of novel designs of continuous mesoscale oscillatory baffled reactors. Chemical Engineering Journal, 159, 1-3, 212-219, 2010.

Phan, A.; Harvey, A. Effect of geometrical parameters on fluid mixing in novel mesoscale oscillatory helical baffled designs. Chemical Engineering Journal, 169, 1-3, 339-347, 2011.

Pinto, J.C. Dynamic behavior of continuous vinyl chloride bulk and suspension polymerization reactors. a simple model analysis. Polymer Engineering and Science, 30, 5, 291-302, 1990.

Reis, N.; Vicente, A.A.; Teixeira, J.A. Liquid backmixing in oscillatory flow through a periodically constricted meso-tube. Chemical Engineering and Processing: Process Intensification, 49, 7, 793-803, 2010.

Reis, N.; Vicente, A.A.; Teixeira, J.A.; Mackley, M.R. Residence times and mixing of a novel continuous oscillatory flow screening reactor. Chemical Engineering Science, 59, 22-23, 4967-4974, 2004.

Sayer, C.; Palma, M.; Giudici, R. Modeling continuous vinyl acetate emulsion polymerization reactions in a pulsed sieve plate column. Industrial and Engineering Chemistry Research, 41, 7, 1733-1744, 2002.

Shanta, P.L. Process of suspension polymerization. United States Patent Number 2694700, 1954.

Slavnić, D.S.; Živković, L.V.; Bjelić, A.V.; Bugarski, B.M.; Nikačević, N.M. Residence time distribution and Peclet number correlation for continuous oscillatory flow reactors. Journal of Chemical Technology and Biotechnology, 92, 8, 2178-2188, 2017.

Slavnić, D.; Bugarski, B.; Nikačević, N. Solids flow pattern in continuous oscillatory baffled reactor. Chemical Engineering and Processing: Process Intensification, 135, 108-119, 2019.

Smith, K.B.; Mackley, M.R. An experimental investigation into the scale-up of oscillatory flow mixing in baffled tubes. Trans IChemE, 84, A11, 1001-1011, 2006.

Solano, J.P.; Herrero, R.; Espín, S.; Phan, A.N.; Harvey, A.P. Numerical study of the flow pattern and heat transfer enhancement in oscillatory baffled reactors with helical coil inserts. Chemical Engineering Research and Design, 90, 6, 732-742, 2012.

Stark, A.H. Continuous polymerization process. The Dow Chemical Company, United States Patent Number 3007903, 1961.

Stephens, G.G.; Mackley, M.R. Heat transfer performance for batch oscillatory flow mixing. Experimental Thermal and Fluid Science, 25, 8, 583-594, 2002.

Stonestreet, P.; Van der Veeken, P.M.J. The effects of oscillatory flow and bulk flow components on residence time distribution in baffled tube reactors. Trans IChemE, 77, Part A, 671-684, 1999.

Stonestreet, P.; Harvey, A.P. A mixing-based design methodology for continuous oscillatory flow reactors. Trans IChemE, 80, Part A, 31-44, 2002.

Sutherland, K.; Pakzad, L.; Fatehi, P. CFD population balance modeling and

dimensionless group analysis of a multiphase oscillatory baffled column (OBC) using moving overset meshes. Chemical Engineering Science, 199, 552-570, 2019.

Sutherland, K.; Pakzad, L.; Fatehi, P. Oscillatory power number, power density model, and effect of restriction size for a moving-baffle oscillatory baffled column using CFD modelling. Canadian Journal of Chemical Engineering, 98, 5, 1172-1190, 2020.

Sutherland, K.; Pakzad, L.; Fatehi, P. Mixing time and scale-up investigation of a moving-baffle oscillatory baffled column. Chemical Engineering and Technology, 44, 8, 1403-1411, 2021.

Sutherland, K.; Pakzad, L.; Fatehi, P. Comparison of mixing performance between stationary-baffle and moving-baffle batch oscillatory baffled columns via numerical modeling. Chemical Engineering Communications, 209, 1, 17-46, 2022.

Takriff, M.S.; Masyithah, Z. Interstage backmixing in oscillatory flow in a baffled column. Chemical Engineering Communications, 189, 12, 1640-1652, 2002.

Tsouris, C.; Tavlarides, L.L. Breakage and coalescence models for drops in turbulent dispersions. AIChE Journal, 40, 3, 395-406, 1994.

Wolf, A.; Goetze, U. Vorrichtung zur kontinuierlichen durchführung von chemischen umsetzungen, insbesondere polymerisationen. Wacker-Chemie GmbH, German Patent Number 2343788, 1975.

Xu, B.C. Interstage backmixing in compartmented agitated columns: experimental determination and correlation. Ph.D. Thesis, University of Arkansas, 1994.

Zhang, C.; Huang, W.; Li, C.; Ouyang, J.; Wang, H.; Xu, J.; Luo, H. Numerically investigating the effects of geometry on hydrodynamics and particle suspension performance in continuous oscillatory baffled crystallizers. Chemical Engineering Science, 249, 117352, 2022.

Zheng, M.; Mackley, M. The axial dispersion performance of an oscillatory flow meso-reactor with relevance to continuous flow operation. Chemical Engineering Science, 63, 7, 1788-1799, 2008.

Zerfa, M.; Brooks, B. Prediction of vinyl chloride drop sizes in stabilised liquid-liquid agitated dispersion. Chemical Engineering Science, 51, 12, 3223-3233, 1996.

Chapter 4

Poly(vinyl acetate) Suspension Polymerization in an Oscillatory Baffled Reactor

In this chapter, a phenomenological model to represent suspension polymerizations in a continuous oscillatory baffled reactor is presented for the first time. The reactor is described as a series of tanks of equal volume connected. Additionally, a backflow stream is also included to simulate a backmixing mechanism. The proposed model considers mass, energy, statistical moments balances and regulatory control loops. Furthermore, the heat transfer coefficient is modeled as a function of the oscillatory conditions and the properties of the suspension. The model predictions are compared with available experimental data and good agreement is observed. The effects of key model parameters on model responses are also investigated. It is shown that initiator type and injection points must be carefully planned to avoid excessive temperature gradients along the reactor length. Given the thorough description of kinetic and heat transfer phenomena, the model can be used for reactor design and process scale-up. Parts of this chapter have been published as "Silva *et al.* Modeling of suspension polymerizations in continuous oscillatory baffled reactors - Part I: Vinyl acetate polymerization. Chemical Engineering Science, 288, 119845, 2024".

4.1 Model Development

For modeling purposes, the reactor scheme presented in Figure 3.7 was mathematically represented as a series of k perfectly mixed stirred tanks connected in series with a backflow stream to simulate backmixing, as described in Figure 4.1. According to Mecklenburgh and Hartland (1968), this modeling approach is suitable for compartmentalized reactors. The developed model considers the reactor from the point where the heating section starts until the outlet. In this specific setup, the initial sections of the reactor have the role of stabilizing the suspension and for this reason are kept at lower temperature. At the end of the droplet stabilizing region, the temperature is increased so that the initiator starts to decompose and the reaction begins.

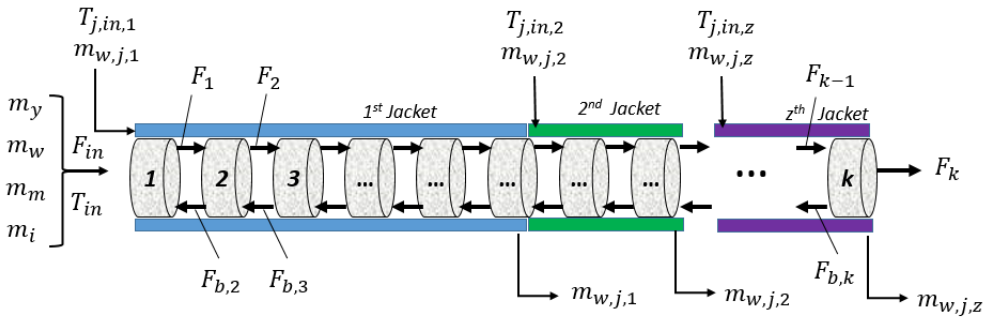

Figure 4.1: Tanks-in-series with backflow representation of the COBR.

In order to write down the mass and energy balances, a series of simplifying hypothesis must be enunciated so that a compromise between model complexity and accuracy must be achieved. In the present model, the following hypotheses were assumed to be valid:

- Volume additivity holds;
- Negligible effect of initiator on mixture volume;
- Existence of two liquid phases in equilibrium: organic and aqueous phases;
- Initiator is insoluble in water;
- Monomer is partially soluble in water;
- Polymer is insoluble in water;

- Monomer is mainly consumed by the propagation reaction;
- Heat of reaction released by reactions other than propagation is negligible;
- Chain initiation is much faster than initiator decomposition so that the overall rate of initiation is governed by initiator decomposition.

4.1.1 Kinetic Model

The polymerization of vinyl acetate follows a standard free radical polymerization mechanism (Table 4.1). The basic reaction steps are: initiator decomposition, chain initiation, propagation, transfer to monomer, transfer to polymer and termination (Odian, 2004). The major mode of termination in this case is disproportionation (Teymour, 1989). In Table 4.2, the kinetic rate constants are shown. The gel effect correlation from Friis and Hamielec (1976) was used to represent the decrease in the rate of termination. Even though some studies consider that the propagation step becomes impaired at high vinyl acetate monomer conversions due to the glass effect (Silva *et al.*, 2004), in the proposed kinetic model the propagation rate constant is not considered to be a function of monomer conversion. First of all, according to Friis (1973) and Kiparissides (1996), the propagation rate constant does not become affected by the conversion, even in the bulk process, when the polymerization is carried out at temperatures higher than the glass transition temperature of the polymer (301 K in the present case Lindemann (1999)). Besides, the analyzed experimental monomer conversion values are relatively small, as it will be shown in Section 4.2. This assumption can be easily relaxed, if necessary, to fit new sets of experimental data and extend the proposed simulation studies.

Table 4.1: Kinetic model used to represent the polymerization of vinyl acetate (Teymour, 1989).

Reaction Step	Mechanism[1]
Initiator decomposition	$I \xrightarrow{k_d} 2I^*$
Chain initiation	$I^* + M \xrightarrow{k_i} R_1$
Propagation	$R_x + M \xrightarrow{k_p} R_{x+1}$
Transfer to monomer	$R_x + M \xrightarrow{k_{tm}} P_x + R_1$
Transfer to polymer	$R_x + P_y \xrightarrow{k_{tp}} P_x + R_y$
Termination by disproportionation	$R_x + R_y \xrightarrow{k_{td}} P_x + P_y$

[1] R and P represent living and dead polymer chains, respectively.
I* and M represent the free radical and monomer, respectively.

Table 4.2: Kinetic rate constants used to perform the simulations.

Rate equation	Units	Ref.
$k_p(T_n) = 1.92 \times 10^9 \exp\left(\frac{-26359.2}{RT_n}\right)$	[m^3 kmol^{-1} s^{-1}]	Teymour (1989)
$k_{tm}(T_n) = 0.2 \times 10^{-3} k_p(T_n)$	[m^3 kmol^{-1} s^{-1}]	Ueda and Nagai (1999)
$k_{tp}(T_n) = 0.2 \times 10^{-3} k_p(T_n)$	[m^3 kmol^{-1} s^{-1}]	Ueda and Nagai (1999)
$k_{td}(T_n) = 2.2 \times 10^{11} \exp\left(\frac{-13388.8}{RT_n}\right) g_n$	[m^3 kmol^{-1} s^{-1}]	Teymour (1989)
$g_n = exp\left(-0.4407 x_n - 6.7530 x_n^2 - 0.3495 x_n^3\right)$	[-]	Friis and Hamielec (1976)
$k_d(T_n) = 7.44 \times 10^{15} \exp\left(\frac{-126390}{RT_n}\right)$, (DTBC)	[s^{-1}]	Nouryon catalog*
$k_d(T_n) = 3.12 \times 10^{14} \exp\left(\frac{-114590}{RT_n}\right)$, (CPND)	[s^{-1}]	Nouryon catalog*
$k_d(T_n) = 3.37 \times 10^{14} \exp\left(\frac{-109060}{RT_n}\right)$, (DIBP)	[s^{-1}]	Nouryon catalog*
$x_n = \frac{P_n}{P_n + M_n}$	[-]	

* Acessed on July 13, 2023. https://www.nouryon.com/content-search/?q=trigonox. Nouryon Company, Amsterdam, The Netherlands.

4.1.2 Mass Balances

The organic phase of the suspension (Phase 1, superscript 1) is constituted of monomer, polymer and initiator. On the other hand, the inorganic phase (Phase 2, superscript 2) comprises residual monomer, suspending agent and water. In order to represent the distribution of monomer between both phases, the solubility of vinyl acetate (k_{sol}) was included in the model. Let k represent the number of tanks in the simulation, then the overall species balances in Equations (4.1)–(4.6) can be written for $n = 1, 2, .., k$. The output flow rate, represented in Equation (4.7), was derived assuming that the volume of each tank remains constant (see Appendix B). Equations (4.11)-(4.15) are necessary to calculate the volume fractions of each phase (Equations (4.16) and (4.17)). Based on the volumes of each phase, the flow rates of each phase can be finally calculated as shown in Equations (4.18)-(4.21). It is important to emphasize that $F_{b,n}$ is a parameter in the model and must be calculated with help of constitutive equations or estimated with experimental data.

$$\phi\left(n\right) = \begin{cases} 1 & \text{if } n = 1 \\ 0 & \text{otherwise} \end{cases} \tag{4.1}$$

$$\begin{aligned} \frac{dM_n}{dt} = {} & m_m\phi(n) + \sum_{i=1}^{2}\left[F^i_{n-1}\frac{M^i_{n-1}}{V^i_{n-1}}(1-\phi(n)) + F^i_{b,n+1}\frac{M^i_{n+1}}{V^i_{n+1}}(1-\phi(k-n+1))\right. \\ & \left. -F^i_n\frac{M^i_n}{V^i_n} - F^i_{b,n}\frac{M^i_n}{V^i_n}(1-\phi(n))\right] - k_p(T_n)\frac{M^1_n}{V^1_n}\frac{\lambda^1_{0,n}}{V^1_n}V^1_n \end{aligned} \tag{4.2}$$

$$\begin{aligned} \frac{dI_n}{dt} = {} & m_i\phi(n) + F^1_{n-1}\frac{I^1_{n-1}}{V^1_{n-1}}(1-\phi(n)) + F^1_{b,n+1}\frac{I^1_{n+1}}{V^1_{n+1}}(1-\phi(k-n+1)) \\ & - F^1_n\frac{I^1_n}{V^1_n} - F^1_{b,n}\frac{I^1_n}{V^1_n}(1-\phi(n)) - k_d(T_n)I^1_n \end{aligned} \tag{4.3}$$

$$\begin{aligned} \frac{dP_n}{dt} = {} & F^1_{n-1}\frac{P^1_{n-1}}{V^1_{n-1}}(1-\phi(n)) + F^1_{b,n+1}\frac{P^1_{n+1}}{V^1_{n+1}}(1-\phi(k-n+1)) \\ & - F^1_n\frac{P^1_n}{V^1_n} - F^1_{b,n}\frac{P^1_n}{V^1_n}(1-\phi(n)) + k_p(T_n)\frac{M^1_n}{V^1_n}\frac{\lambda^1_{0,n}}{V^1_n}V^1_n \end{aligned} \tag{4.4}$$

$$\frac{dW_n}{dt} = m_w\phi(n) + F_{n-1}^2\frac{W_{n-1}^2}{V_{n-1}^2}(1-\phi(n)) + F_{b,n+1}^2\frac{W_{n+1}^2}{V_{n+1}^2}(1-\phi(k-n+1)) - F_n^2\frac{W_n^2}{V_n^2} - F_{b,n}^2\frac{W_n^2}{V_n^2}(1-\phi(n)) \tag{4.5}$$

$$\frac{dY_n}{dt} = m_y\phi(n) + F_{n-1}^2\frac{Y_{n-1}^2}{V_{n-1}^2}(1-\phi(n)) + F_{b,n+1}^2\frac{Y_{n+1}^2}{V_{n+1}^2}(1-\phi(k-n+1)) - F_n^2\frac{Y_n^2}{V_n^2} - F_{b,n}^2\frac{Y_n^2}{V_n^2}(1-\phi(n)) \tag{4.6}$$

$$\begin{aligned} F_n = \Bigg[& \left(MM_m\frac{m_m}{\rho_m} + MM_w\frac{m_w}{\rho_w}\right)\phi(n) + F_{n-1}(\Phi_{n-1}^1\alpha_{n-1} + \Phi_{n-1}^2\beta_{n-1})(1-\phi(n)) \\ & + F_{b,n+1}(\Phi_{n+1}^1\alpha_{n+1} + \Phi_{n+1}^2\beta_{n+1})(1-\phi(k-n+1)) \\ & - F_{b,n}(\Phi_n^1\alpha_n + \Phi_n^2\beta_n)(1-\phi(n)) - \gamma_n\Bigg] / (\Phi_n^1\alpha_n + \Phi_n^2\beta_n) \end{aligned} \tag{4.7}$$

$$\alpha_n = \frac{MM_m}{\rho_m}\frac{M_n^1}{V_n^1} + \frac{MM_m}{\rho_p}\frac{P_n^1}{V_n^1} \tag{4.8}$$

$$\beta_n = \frac{MM_m}{\rho_m}\frac{M_n^2}{V_n^2} + \frac{MM_w}{\rho_w}\frac{W_n^2}{V_n^2} \tag{4.9}$$

$$\gamma_n = k_p(T_n)\frac{M_n^1}{V_n^1}\frac{\lambda_{0,n}^1}{V_n^1}V_n^1\left(\frac{MM_m}{\rho_m} - \frac{MM_m}{\rho_p}\right) \tag{4.10}$$

$$M_n = M_n^1 + M_n^2 \tag{4.11}$$

$$M_n^2 = k_{sol}\frac{MM_w}{MM_m}W_n^2 \tag{4.12}$$

$$V_n^1 = MM_m\left(\frac{M_n^1}{\rho_m} + \frac{P_n^1}{\rho_p}\right) \tag{4.13}$$

$$V_n^2 = MM_m \frac{M_n^2}{\rho_m} + MM_w \frac{W_n^2}{\rho_w} \tag{4.14}$$

$$V_n = V_n^1 + V_n^2 \tag{4.15}$$

$$\Phi_n^1 = \frac{V_n^1}{V_n} \tag{4.16}$$

$$\Phi_n^2 = 1 - \Phi_n^1 \tag{4.17}$$

$$F_n^1 = \Phi_n^1 F_n \tag{4.18}$$

$$F_n^2 = F_n - F_n^1 \tag{4.19}$$

$$F_{b,n}^1 = \Phi_n^1 F_{b,n} \tag{4.20}$$

$$F_{b,n}^2 = F_{b,n} - F_{b,n}^1 \tag{4.21}$$

4.1.3 Moment Balances

In order to avoid the inconveniences of representing the whole molar mass distribution (MMD) of the final polymer product, the method of moments can be applied to describe the averages of the MMD. Compared to other MMD modeling approaches, the method of moments is of considerable simplicity and allows the calculation of the main polymer properties, including the number average molar mass (M_n) and weight average molar mass (M_w) (Ray, 1972). According to Mastan

and Zhu (2015), one of the major advantages of the method of moments relies on the fact that it avoids solving a high number of mass balances (one for each chain length). Nonetheless, the cost of doing so is the loss of the whole MMD representation. Based on the kinetic mechanism shown in Table 4.1, Equations (4.22)–(4.27) can be derived (see Appendix A).

Moments of living polymer chains

$$\begin{aligned}\frac{d\lambda_{0,n}}{dt} &= F^1_{n-1}\frac{\lambda^1_{0,n-1}}{V^1_{n-1}}(1-\phi(n)) + F^1_{b,n+1}\frac{\lambda^1_{0,n+1}}{V^1_{n+1}}(1-\phi(k-n+1)) \\ &- F^1_n\frac{\lambda^1_{0,n}}{V^1_n} - F^1_{b,n}\frac{\lambda^1_{0,n}}{V^1_n}(1-\phi(n)) + 2fk_d(T_n)I^1_n \\ &- k_{td}(T_n)\frac{\lambda^1_{0,n}}{V^1_n}\frac{\lambda^1_{0,n}}{V^1_n}V^1_n \end{aligned} \tag{4.22}$$

$$\begin{aligned}\frac{d\lambda_{1,n}}{dt} &= F^1_{n-1}\frac{\lambda^1_{1,n-1}}{V^1_{n-1}}(1-\phi(n)) + F^1_{b,n+1}\frac{\lambda^1_{1,n+1}}{V^1_{n+1}}(1-\phi(k-n+1)) \\ &- F^1_n\frac{\lambda^1_{1,n}}{V^1_n} - F^1_{b,n}\frac{\lambda^1_{1,n}}{V^1_n}(1-\phi(n)) + 2fk_d(T_n)I^1_n \\ &- k_{td}(T_n)\frac{\lambda^1_{0,n}}{V^1_n}\frac{\lambda^1_{1,n}}{V^1_n}V^1_n + k_{tm}(T_n)\frac{M^1_n}{V^1_n}\left(\frac{\lambda^1_{0,n}}{V^1_n} - \frac{\lambda^1_{1,n}}{V^1_n}\right)V^1_n \\ &+ k_p(T_n)\frac{M^1_n}{V^1_n}\frac{\lambda^1_0}{V^1_n}V^1_n + k_{tp}(T_n)\left(\frac{\lambda^1_{0,n}}{V^1_n}\frac{\mu^1_{2,n}}{V^1_n} - \frac{\lambda^1_{1,n}}{V^1_n}\frac{\mu^1_{1,n}}{V^1_n}\right)V^1_n \end{aligned} \tag{4.23}$$

$$\begin{aligned}\frac{d\lambda_{2,n}}{dt} &= F^1_{n-1}\frac{\lambda^1_{2,n-1}}{V^1_{n-1}}(1-\phi(n)) + F^1_{b,n+1}\frac{\lambda^1_{2,n+1}}{V^1_{n+1}}(1-\phi(k-n+1)) \\ &- F^1_n\frac{\lambda^1_{2,n}}{V^1_n} - F^1_{b,n}\frac{\lambda^1_{2,n}}{V^1_n}(1-\phi(n)) + 2fk_d(T_n)I^1_n \\ &- k_{td}(T_n)\frac{\lambda^1_{0,n}}{V^1_n}\frac{\lambda^1_{2,n}}{V^1_n}V^1_n + k_{tm}(T_n)\frac{M^1_n}{V^1_n}\left(\frac{\lambda^1_{0,n}}{V^1_n} - \frac{\lambda^1_{2,n}}{V^1_n}\right)V^1_n \\ &+ k_p(T_n)\frac{M^1_n}{V^1_n}\left(\frac{2\lambda^1_{1,n}}{V^1_n} - \frac{\lambda^1_{0,n}}{V^1_n}\right) \\ &+ k_{tp}(T_n)\left(\frac{\lambda^1_{0,n}}{V^1_n}\frac{\mu^1_{3,n}}{V^1_n} - \frac{\lambda^1_{2,n}}{V^1_n}\frac{\mu^1_{1,n}}{V^1_n}\right)V^1_n \end{aligned} \tag{4.24}$$

Moments of dead polymer chains

$$\begin{aligned}\frac{d\mu_{0,n}}{dt} &= F^1_{n-1}\frac{\mu^1_{0,n-1}}{V^1_{n-1}}(1-\phi(n)) + F^1_{b,n+1}\frac{\mu^1_{0,n+1}}{V^1_{n+1}}(1-\phi(k-n+1)) \\ &- F^1_n\frac{\mu^1_{0,n}}{V^1_n} - F^1_{b,n}\frac{\mu^1_{0,n}}{V^1_n}(1-\phi(n)) \\ &+ k_{tm}(T_n)\frac{M^1_n}{V^1_n}\frac{\lambda^1_{0,n}}{V^1_n}V^1_n + k_{td}(T_n)\frac{\lambda^1_{0,n}}{V^1_n}\frac{\lambda^1_{0,n}}{V^1_n}V^1_n \end{aligned} \tag{4.25}$$

$$\begin{aligned}\frac{d\mu_{1,n}}{dt} &= F^1_{n-1}\frac{\mu^1_{1,n-1}}{V^1_{n-1}}(1-\phi(n)) + F^1_{b,n+1}\frac{\mu^1_{1,n+1}}{V^1_{n+1}}(1-\phi(k-n+1)) \\ &- F^1_n\frac{\mu^1_{1,n}}{V^1_n} - F^1_{b,n}\frac{\mu^1_{1,n}}{V^1_n}(1-\phi(n)) \\ &+ k_{td}(T_n)\frac{\lambda^1_{0,n}}{V^1_n}\frac{\lambda^1_{1,n}}{V^1_n}V^1_n + k_{tm}(T_n)\frac{M^1_n}{V^1_n}\frac{\lambda^1_{1,n}}{V^1_n}V^1_n \\ &- k_{tp}(T_n)\left(\frac{\lambda^1_{0,n}}{V^1_n}\frac{\mu^1_{2,n}}{V^1_n} - \frac{\lambda^1_{1,n}}{V^1_n}\frac{\mu^1_{1,n}}{V^1_n}\right)V^1_n \end{aligned} \tag{4.26}$$

$$\begin{aligned}\frac{d\mu_{2,n}}{dt} &= F^1_{n-1}\frac{\mu^1_{2,n-1}}{V^1_{n-1}}(1-\phi(n)) + F^1_{b,n+1}\frac{\mu^1_{2,n+1}}{V^1_{n+1}}(1-\phi(k-n+1)) \\ &- F^1_n\frac{\mu^1_{2,n}}{V^1_n} - F^1_{b,n}\frac{\mu^1_{2,n}}{V^1_n}(1-\phi(n)) \\ &+ k_{td}(T_n)\frac{\lambda^1_{0,n}}{V^1_n}\frac{\lambda^1_{2,n}}{V^1_n}V^1_n + k_{tm}(T_n)\frac{M^1_n}{V^1_n}\frac{\lambda^1_{2,n}}{V^1_n}V^1_n \\ &- k_{tp}(T_n)\left(\frac{\lambda^1_{0,n}}{V^1_n}\frac{\mu^1_{3,n}}{V^1_n} - \frac{\lambda^1_{2,n}}{V^1_n}\frac{\mu^1_{1,n}}{V^1_n}\right)V^1_n \end{aligned} \tag{4.27}$$

Since the kinetic model considers transfer to polymer, a closure problem is created, i.e., the balance of dead moment of order j depends on the dead moment of order $j+1$. As a means of circumventing this problem, an empirical closure equation was employed (Equation (4.28)) (Hulburt and Katz, 1964). Finally, the average properties of the polymer can be calculated based on the moment equations. Equations (4.29)–(4.31) represent the number average molar mass (Mn_n), weight average molar mass (Mw_n) and the polydispersity index (PDI_n), respectively.

$$\mu^1_{3,n} = \mu^1_{2,n}\frac{(2\mu^1_{0,n}\mu^1_{2,n} - (\mu^1_{1,n})^2)}{\mu^1_{0,n}\mu^1_{1,n}} \tag{4.28}$$

$$Mn_n = \frac{\lambda_{1,n} + \mu_{1,n}}{\lambda_{0,n} + \mu_{0,n}} \tag{4.29}$$

$$Mw_n = \frac{\lambda_{2,n} + \mu_{2,n}}{\lambda_{1,n} + \mu_{1,n}} \tag{4.30}$$

$$PDI_n = \frac{Mw_n}{Mn_n} \tag{4.31}$$

4.1.4 Energy Balances

Temperature is one of the most important variables in polymerization processes (Leiza and Pinto, 2007). Indeed, all polymer properties are influenced by this variable. If the heat released by reaction is not removed from the system, serious operational problems can be triggered. One of the most common operational problems is the so called thermal runaway (Hutchinson and Penlidis, 2007). Under this condition, the controllability of the reactor is lost and the reactor must be shut down to avoid explosions and other material losses.

To avoid operational problems related to heat removal, special attention must be paid to the design of the cooling apparatus. For this endeavor, jackets are the cooling devices employed most often. In these jackets, a cooling liquid (generally water) flows at a lower temperature than the reactor, thus removing the heat generated by the reaction. In order to design a cooling jacket, the engineer must know the process conditions to produce a polymer product with a desired set of final properties beforehand (Hutchinson and Penlidis, 2007). For the sake of avoiding future problems in the case of changes in process flowsheet or operational conditions, these jackets are usually overdesigned (Leiza and Pinto, 2007).

Given the importance of temperature for most polymerization systems, it is of paramount concern that the model should include energy balances in order to calculate the reactor and jacket temperature along the length of the reactor. Equation (4.32) represents the energy balance for each tank in the model.

$$
\begin{aligned}
cp_{s,n}\frac{dT_n}{dt} &= m_w\phi(n)\int_{T_n}^{T_{in}} cp_w(T)dT + m_m\phi(n)\int_{T_n}^{T_{in}} cp_m(T)dT \\
&+ (1-\phi(n))\left(F_{n-1}^1\frac{M_{n-1}^1}{V_{n-1}^1} + F_{n-1}^2\frac{M_{n-1}^2}{V_{n-1}^2}\right)\int_{T_n}^{T_{n-1}} cp_m(T)dT \\
&+ (1-\phi(n))\left(F_{n-1}^1\frac{P_{n-1}^1}{V_{n-1}^1}\right)\int_{T_n}^{T_{n-1}} cp_p(T)dT \\
&+ (1-\phi(n))\left(F_{n-1}^2\frac{W_{n-1}^2}{V_{n-1}^2}\right)\int_{T_n}^{T_{n-1}} cp_w(T)dT \\
&+ (1-\phi(k-n+1))\left(F_{b,n+1}^1\frac{M_{n+1}^1}{V_{n+1}^1} + F_{b,n+1}^2\frac{M_{n+1}^2}{V_{n+1}^2}\right)\int_{T_n}^{T_{n+1}} cp_m(T)dT \\
&+ (1-\phi(k-n+1))\left(F_{b,n+1}^2\frac{W_{n+1}^2}{V_{n+1}^2}\right)\int_{T_n}^{T_{n+1}} cp_w(T)dT \\
&+ (1-\phi(k-n+1))\left(F_{b,n+1}^1\frac{P_{n+1}^1}{V_{n+1}^1}\right)\int_{T_n}^{T_{n+1}} cp_p(T)dT \\
&+ k_p(T_n)\frac{M_n^1}{V_n^1}\frac{\lambda_{0,n}^1}{V_n^1}V_n^1(-\Delta H) - \left(U_n\times 10^{-3}\right)A_n(T_n - T_{j,n})
\end{aligned} \tag{4.32}
$$

$$
cp_{s,n} = M_n cp_m(T_n) + P_n cp_p(T_n) + W_n cp_w(T_n) \tag{4.33}
$$

$$
A_n = \pi d_{r,ext} l_n \tag{4.34}
$$

$$
l_n = \frac{L}{k} \tag{4.35}
$$

$$
L = \sum_{z=1}^{3} L_z \tag{4.36}
$$

Attention must be paid to the fact that there are multiple cooling jackets in the model, as shown in Equations (4.37)–(4.39).

$$\frac{\rho_w V_{j,n} cp_w(T_{j,n})}{MM_w}\frac{dT_{j,n}}{dt} = m_{w,j}\left(\Omega(n)\int_{T_{j,n}}^{T_{j,in,z}} cp_w(T)dT \right.$$
$$\left. +(1-\Omega(n))\int_{T_{j,n}}^{T_{j,n-1}} cp_w(T)dT\right) + (U_n \times 10^{-3})A_n(T_n - T_{j,n}) \tag{4.37}$$

If n is in section z then:

$$m_{w,j} = m_{w,j,z} \tag{4.38}$$

$$\Omega(n) = \begin{cases} 1 & \text{if } n \text{ is the first tank in the zone} \\ 0 & \text{otherwise} \end{cases} \tag{4.39}$$

4.1.5 Dimensionless Groups

In order to describe the oscillatory flow in baffled tubes under oscillatory conditions, previous investigators used the net Reynolds number, oscillatory Reynolds number, and the Strouhal number as shown in Equations (4.40)–(4.42), respectively (Brunold *et al.*, 1989; Howes *et al.*, 1991; Mackley and Ni, 1991; Ni and Gough, 1997). In comparison to the conventional net Reynolds number that accounts for the continuous flow component, the oscillatory Reynolds number takes into account the frequency and amplitude of oscillation. Equation (4.43) represents the net flow velocity based on the cross section area of the reactor (Equation (4.44)).

$$Re_{s,n} = \frac{\rho_{s,n} v_{s,n} d_{r,int}}{\eta_{s,n}} \tag{4.40}$$

$$Re_{o,n} = \frac{2\pi f_o \chi_o \rho_{s,n} d_{r,int}}{\eta_{s,n}} \tag{4.41}$$

$$St = \frac{d_{r,int}}{4\pi\chi_o} \tag{4.42}$$

$$v_{s,n} = \begin{cases} \frac{F_n - F_{b,k+1}}{C_n} & \text{if } n < k \\ \frac{F_n}{C_n} & \text{if } n = k \end{cases} \tag{4.43}$$

$$C_n = \frac{\pi d_{r,int}^2}{4} \tag{4.44}$$

The continuous flow in circular tubes can be characterized as laminar in the region where $Re \leq 2300$, transition to turbulent in $2300 < Re \leq 10000$ and fully turbulent at $Re > 10000$. In oscillatory flow, Stonestreet and Van der Veeken (1999) identified that for $Re_o \leq 250$ the flow is 2D axi-symmetric with low intensity mixing, when $Re_o > 250$ the flow becomes 3D non axi-symmetric and at $Re_o \geq 2,000$ the flow becomes effectively turbulent.

Stonestreet and Van der Veeken (1999) and Stonestreet and Harvey (2002) also used the ratio of the oscillatory Reynolds number to the net Reynolds number as a design variable. This variable is known as velocity ratio (Equation (4.45)). In practical terms, it is desirable to have velocity ratios at least greater than 2 so that the oscillatory flow governs the mixing regime guaranteeing that the flow will be fully reversing (Harvey *et al.*, 2001).

$$\Psi_n = \frac{Re_{o,n}}{Re_{s,n}} \tag{4.45}$$

4.1.6 Heat Transfer

In comparison to other reactors, the COBR has the advantage of improving the heat transfer coefficients as reported by Mackley *et al.* (1990) and Mackley and Stonestreet (1995). Figure 4.2 illustrates, in a simplified manner, the cross section view of the reactor and its jacket. In order to compute the overall heat transfer coefficient between the jacket and the reactor, it is necessary to use correlations for the Nusselt number inside the reactor (considering it as a tube), the jacket Nusselt (annular area) and to consider the thermal conductivity of the wall.

Law *et al.* (2018) investigated the effects of fluid oscillation in the heat transfer coefficients and proposed the correlations described in Equations (4.46) and (4.47)

to fit their data. In these correlations, Pr represents the Prandtl number of the suspension (Equation (4.48)).

- $0 \leq Re_{o,n} \leq 1300$

$$Nu_{s,n} = 0.0022 Re_{s,n}^{0.7} Pr_{s,n}^{0.3} Re_{o,n}^{0.44} \tag{4.46}$$

- $Re_{o,n} \geq 1300$

$$Nu_{s,n} = 0.52 Re_{s,n}^{0.7} Pr_{s,n}^{0.3} \tag{4.47}$$

$$Pr_{s,n} = \frac{cp_{s,n}\eta_{s,n}}{\sigma_{s,n}} \tag{4.48}$$

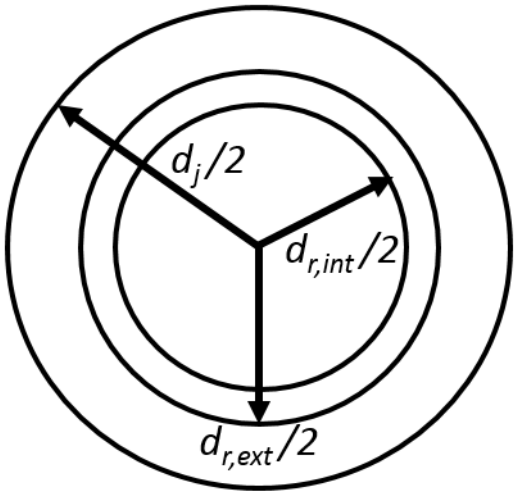

Figure 4.2: Cross section view of the reactor and jacket.

In order to determine the heat transfer coefficients in annular concentric tubes, three types of boundary conditions can be usually applied, namely (Gnielinski, 2010):

- Heat transfer from the inner tube, with the outer tube insulated;
- Heat transfer from the outer tube, with the inner tube insulated;
- Heat transfer from both inner and outer tubes with both walls at the same temperature.

The Reynolds number in annular regions, Equation (4.49), is slightly different from its counterpart defined in circular ducts. The equivalent of the duct diameter in circular ducts is the hydraulic diameter in annular ducts, which is the difference between the outer diameter (jacket) and the inner diameter (reactor) (Equation (4.50)). All the properties regarding the jacket side must be calculated at the temperature of the jacket.

$$Re_{j,n} = \frac{\rho_w v_{j,z} d_h}{\eta_{w,j,n}} \tag{4.49}$$

$$d_h = d_j - d_{r,ext} \tag{4.50}$$

$$v_{j,z} = \frac{m_{w,j} MM_w}{\rho_w A_j} \tag{4.51}$$

$$A_j = \frac{\pi}{4}\left(d_j^2 - d_{r,ext}^2\right) \tag{4.52}$$

Martin (1990) apud Gnielinski (2010) developed the following correlation, Equation (4.53), for the jacket side Nusselt number ($Nu_{j,n}$) employing the first boundary condition and assuming thermally and hydrodynamically developed laminar flow:

- $Re_{j,n} \leq 2300$

$$Nu_1 = 3.66 + 1.2\left(\frac{d_{r,ext}}{d_j}\right)^{-0.8} \tag{4.53}$$

$$Nu_{j,n} = Nu_1 \tag{4.54}$$

In the transition regime, Gnielinski (2010) suggested the following correlations to calculate the Nusselt number (Equation (4.60)):

- $2300 < Re_{j,n} < 10^4$

$$Nu_2 = f_g \sqrt[3]{\frac{Re_{j,n} Pr_{j,n} d_h}{l_n}} \tag{4.55}$$

$$Nu_3 = \left[\frac{2}{1 + 22 Pr_{j,n}}\right]^{1/6} \left(\frac{Re_{j,n} Pr_{j,n} d_h}{l_n}\right)^{1/2} \tag{4.56}$$

$$f_g = 1.615 \left[1 + 0.14 \left(\frac{d_{r,ext}}{d_j}\right)^{-1/2}\right] \tag{4.57}$$

$$Nu_{lam} = \left(Nu_1^3 + Nu_2^3 + Nu_3^3\right)^{1/3} \tag{4.58}$$

$$\Lambda = \frac{Re_{j,n} - 2300}{10^4 - 2300} \tag{4.59}$$

$$Nu_{j,n} = (1 - \Lambda) Nu_{lam}(Re_{j,n} = 2300) + \Lambda Nu_{turb}(Re_{j,n} = 10^4) \tag{4.60}$$

When the flow is in the fully turbulent regime, Equation (4.61) can be used to describe the Nusselt number (Gnielinski, 2009). f_{Nu} is the so called friction factor for turbulent flow in smooth tubes (Gnielinski, 2007). The ξ factor was estimated by Petukhov and Roizen (1964).

- $Re_{j,n} \geq 10^4$

$$Nu_{turb} = \frac{(f_{Nu}/8) Re_{j,n} Pr_{j,n}}{1 + 12.7\sqrt{f_{Nu}/8}(Pr_{j,n}^{2/3} - 1)} \left[1 + \left(\frac{d_h}{l_n}\right)^{2/3}\right] \xi \tag{4.61}$$

$$f_{Nu} = \left(1.8 \log_{10} Re_{j,n} - 1.5\right)^{-2} \tag{4.62}$$

$$\xi = 0.86 \left(\frac{d_{r,ext}}{d_j} \right)^{-0.16} \tag{4.63}$$

$$Nu_{j,n} = Nu_{turb} \tag{4.64}$$

By using the definitions of the Nusselt number in the reactor and in the jacket (Equations (4.65) and (4.66)), the overall heat transfer coefficient between the jacket and the reactor can be calculated according to Equation (4.67). Additionally, the suspension properties were calculated with the equations in Tables 4.3 and 4.4.

$$Nu_{s,n} = \frac{h_{s,n} d_{r,int}}{\sigma_{s,n}} \tag{4.65}$$

$$Nu_{j,n} = \frac{h_{j,n} d_h}{\sigma_{w,j,n}} \tag{4.66}$$

$$\frac{1}{U_n} = \frac{1}{h_{s,n}} + \frac{d_{r,int}}{d_{r,ext} h_{j,n}} + d_{r,int} \frac{ln(d_{r,ext}/d_{r,int})}{2k_{wall}} \tag{4.67}$$

4.1.7 Regulatory Control

Polymerization reactions are prone to instabilities mostly related to thermal, viscous, hydrodynamic and kinetic effects (Hutchinson and Penlidis, 2007; Leiza and Pinto, 2007). The safety of operation of unstable processes is guaranteed by regulatory control loops. This type of control loop keeps the main process variables at their setpoints guaranteeing secure operation (Skogestad and Postlethwaite, 2005; Seborg *et al.*, 2010). In order to maintain the reactor at the desired temperature, three proportional-integral controllers ($z = 1, 2, 3$) were implemented (Equation (4.68)), one for each zone in Figure 3.7. The manipulated and controlled variables are the jacket inlet temperatures ($T_{j,in,z}$) and the temperatures at specified positions in each zone z ($T_{m,z}$), respectively. The controllers gains are reported in Table 4.4.

Table 4.3: Suspension properties (poly(vinyl acetate)/vinyl acetate/water system).

Equation	Ref.
$\eta_{s,n} = \frac{\eta_{c,n}}{1-\Phi_n^1}\left(1+\frac{1.5\Phi_n^1\eta_{d,n}}{\eta_{c,n}+\eta_{d,n}}\right)$	Vermeulen *et al.* (1955)
$\eta_{c,n} = \eta_{w,n}\left(1+\frac{\Phi_n^1[\eta]_{pva}C_{pva,n}}{1-0.45[\eta]_{pva}C_{pva,n}}\right)$	Okaya (1992) apud Kiparissides and Pladis (2022)
$C_{pva,n} = Y_n^2/V_n^2$	
$\eta_{d,n} = \eta_{m,n}\left[1+2.5\Phi_{eff,n}+6.2(\Phi_{eff,n})^2\right];\ \ \Phi_{eff,n} = 1.8\Phi_{p,n}^1$	Kiparissides and Pladis (2022), Batchelor and Green (1972)
$\frac{1}{\rho_{d,n}} = \frac{1-x_n}{\rho_m}+\frac{x_n}{\rho_p}$	Bouyatiotis and Thornton (1967)
$\rho_{s,n} = \Phi_n^1\rho_{d,n}+(1-\Phi_n^1)\rho_{w,n}$	Maggioris *et al.* (2000)
$\underline{cp}_{s,n} = \sum_{e=m,w,p}\omega_e\underline{cp}_e(T_n)$	Green and Perry (2008)
$\sigma_{d,n} = \sum_{a=(m,p)}\sum_{e=(m,p)}\Phi_{a,n}^1\Phi_{e,n}^1\frac{2\sigma_a(T_n)\sigma_e(T_n)}{\sigma_a(T_n)+\sigma_e(T_n)}$	Li (1976)
$\frac{\sigma_{s,n}}{\sigma_{w,n}} = \frac{2+\frac{\sigma_{d,n}}{\sigma_{w,n}}-2\Phi_n^2\left(1-\frac{\sigma_{d,n}}{\sigma_{w,n}}\right)}{2+\frac{\sigma_{d,n}}{\sigma_{w,n}}+\Phi_n^2\left(1-\frac{\sigma_{d,n}}{\sigma_{w,n}}\right)}$	Wieme *et al.* (2007), Levy (1981), Wang *et al.* (2006)

Table 4.4: Additional constitutive relationships and parameters (poly(vinyl acetate)/vinyl acetate/water system).

Equation	Units	Ref.
$\ln(\eta_{m,n}) = -22.407 + \frac{1462.8}{T_n} + 1.7\ln(T_n)$	[kg m^{-1} s^{-1}]	Green and Perry (2008)
$\log_{10}(\eta_{w,n}) = -4.64 + \frac{262.37}{T_n - 133.98}$	[kg m^{-1} s^{-1}]	Korosi and Fabuss (1968)
$cp_m(T_n) = 161.33 + 0.2026(T_n - 273.15)$	[kJ kmol^{-1} K^{-1}]	Kalfas *et al.* (1993)
$cp_p(T_n) = 124.37 + 0.3440(T_n - 298.15)$	[kJ kmol^{-1} K^{-1}]	Kalfas *et al.* (1993)
$cp_w(T_n) = 276.37 - 2.09T_n + 8.125 \times 10^{-3}T_n^2$ $- 1.41 \times 10^{-5}T_n^3 + 9.37 \times 10^{-9}T_n^4$	[kJ kmol^{-1} K^{-1}]	Green and Perry (2008)
$\sigma_m(T_n) = 0.256 - 3.542 \times 10^{-4}T_n$	[J s^{-1} m^{-1} K^{-1}]	Green and Perry (2008)
$\sigma_p(T_n) = 0.159$	[J s^{-1} m^{-1} K^{-1}]	Lindemann (1999)
$\sigma_w(T_n) = -0.432 + 5.7255 \times 10^{-3}T_n - 8.078 \times 10^{-6}T_n^2$ $+ 1.861 \times 10^{-9}T_n^3$	[J s^{-1} m^{-1} K^{-1}]	Green and Perry (2008)
ΔH = -87864	[kJ kmol^{-1}]	Kalfas *et al.* (1993)
$[\eta]_{pva} = 1.332 \times 10^{-4}Mw_{pva}^{0.566}$	[m^3 kg^{-1}]	Nagy (1993)
$\rho_m = 934$, $\rho_p = 1190$, $\rho_w = 999$ (at 298.15 K)	[kg m^{-3}]	Kalfas *et al.* (1993), Green and Perry (2008), Lindemann (1999)
$MM_m = 86.09$, $MM_w = 18.0$	[kg kmol^{-1}]	Green and Perry (2008)
$R = 8.314$	[kJ kmol^{-1} K^{-1}]	Green and Perry (2008)
$k_{sol} = 2.9$	[wt.%]	Kalfas *et al.* (1993)
$k_{wall} = 1.09$ (borosilicate glass)	[J s^{-1} m^{-1} K^{-1}]	Green and Perry (2008)
$K_c = -0.5$	[-]	This work
$\tau_i = 300$	[s]	This work
$f = 0.8$	[-]	This work

$$T_{j,in,z} = T_{j,in,ref} + K_c \left[(T_{m,z} - T_{sp,z}) + \frac{1}{\tau_i} \int_0^t (T_{m,z} - T_{sp,z})\, dt \right] \tag{4.68}$$

By defining E_z (error) as $E_z = T_{m,z} - T_{sp,z}$, Equation (4.68) becomes:

$$T_{j,in,z} = T_{j,in,ref} + K_c \left[E_z + \frac{1}{\tau_i} \int_0^t E_z dt \right] \tag{4.69}$$

By appending E_z as a state variable in the system of differential-algebraic equations and providing an initial condition, the value of the integral in Equation (4.69) is obtained after integration until time t. Consequently, the value of the manipulated variable can be explicitly calculated. The system of algebraic-differential equations was implemented and solved in a Fortran environment with the DASSL solver (Petzold, 1982) with absolute tolerances of 1×10^{-7} for all the variables.

4.2 Literature Data

A complete description of the experimental apparatus can be found in Lobry *et al.* (2015) and Lobry (2012). Figure 3.7, in Chapter 3, shows a schematic representation of the experimental apparatus. The oscillatory baffled reactor provided by Nitech® Solutions was made of borosilicate glass. The liquid-liquid dispersion, heating, reaction, and cooling sections were 9.15, 12.2, 9.15, and 3.75 m long, respectively, leading to a total reactor length of 34.25 m. The straight sections were connected through U-shaped sections. Each straight section in Figure 3.7 comprised 4 subsections with a length of 700 mm. Each subsection was equipped with 23 baffles. The tube diameter was equal to 15 mm and the orifice opening was equal to 8 mm.

Given the low temperature at the liquid-liquid dispersion zone (Table 4.5), it was considered that no reaction took place in this zone. As such, the mathematical model considers only the heating, reaction and cooling zones of the reactor (total length of 25 m). For modeling purposes each zone was represented as a jacketed tube, so that 3 jackets (z=1,2,3) must be considered, one for each zone in Figure 3.7. The overall residence time in the reactor was about 45 min, 30 of which were devoted to the polymerization reaction. The authors reported the use of Di-(4-tert-

butyl-cyclohexyl)-peroxydicarbonate (DTBC) as initiator. Figure 4.3 displays the dynamic conversion data at reactor outlet and steady state profiles for two reported successful experiments.

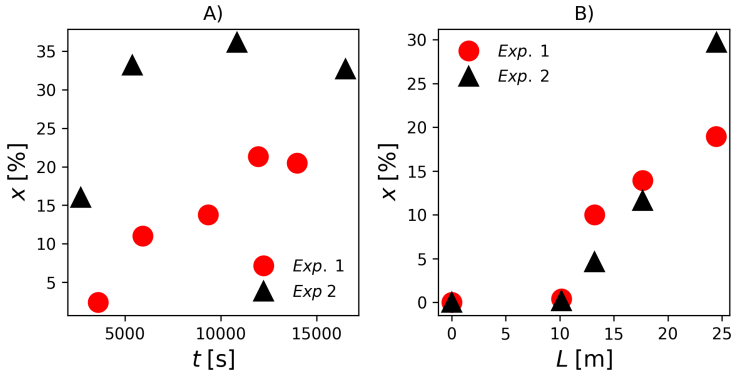

Figure 4.3: Conversion data at the outlet stream (A) and along the reactor length (B) (Lobry *et al.*, 2015; Lobry, 2012).

Table 4.5: Experimental conditions (Lobry *et al.*, 2015; Lobry, 2012).

	Exp. 1	Exp. 2
m_m [kmol s^{-1}]	4.25×10^{-6}	4.32×10^{-6}
m_w [kmol s^{-1}]	1.08×10^{-4}	1.13×10^{-4}
m_i/m_m [% mol]	0.06	0.11
m_y/m_m [ppm]	1,220	2,250
$T(Liq - Liq)$ [K]	295.15	295.15
$T(Heating)$ [K]	317.15	317.15
$T(Reaction)$ [K]	317.15	317.15
$T(Cooling)$ [K]	291.15	291.15
T_{in} [K]	295.15	295.15
χ_o [m]	3.0×10^{-2}	3.0×10^{-2}
f_o [Hz]	1	1
$d_{r,int}$ [m]	1.5×10^{-2}	1.5×10^{-2}
d_o [m]	8.0×10^{-3}	8.0×10^{-3}

The authors mentioned the possible occurrence of several operational problems while conducting the experiments. For example, the formation of gas bubbles inside the reactor is possible when the reaction temperature is higher than the boiling temperature of the reacting mixture, stopping the pulsating flow and causing the appearance of incrustations. Therefore, the operating pressure must be sufficiently high to avoid the formation of gas bubbles.

4.3 Results and Discussion

4.3.1 Effect of Backflow and Number of Tanks

In this subsection, a convergence analysis is performed. Firstly, the effect of the number of tanks (k) on the model response is investigated. In order to understand the effect of k on the simulation results, initially, simulations were performed by setting $F_{b,n}$ equal to zero. The reactor dimensions presented in Table 4.5 were utilized, except the temperature profile and initiator type and amount in order to obtain higher conversions. In this section, diisobutyryl peroxide (DIBP) was employed at concentration of 0.03% molar with respect to the monomer molar flow rate. The temperature setpoints of zones 1,2 and 3 (z=1,2,3) were made equal to $T_{sp,1} = T_{sp,2} = 323.15$ K and $T_{sp,3} = 291.15$ K. Additionally, the temperatures at the end of each zone were selected as controlled variables. In Figure 4.4, it is possible to observe that as the number of tanks increases, the conversion profile at the reactor outlet approaches the plug flow response. At lower number of tanks, the response exhibits dispersion and approaches the response of a stirred tank. Beyond $k = 70$, conversion curves almost overlap.

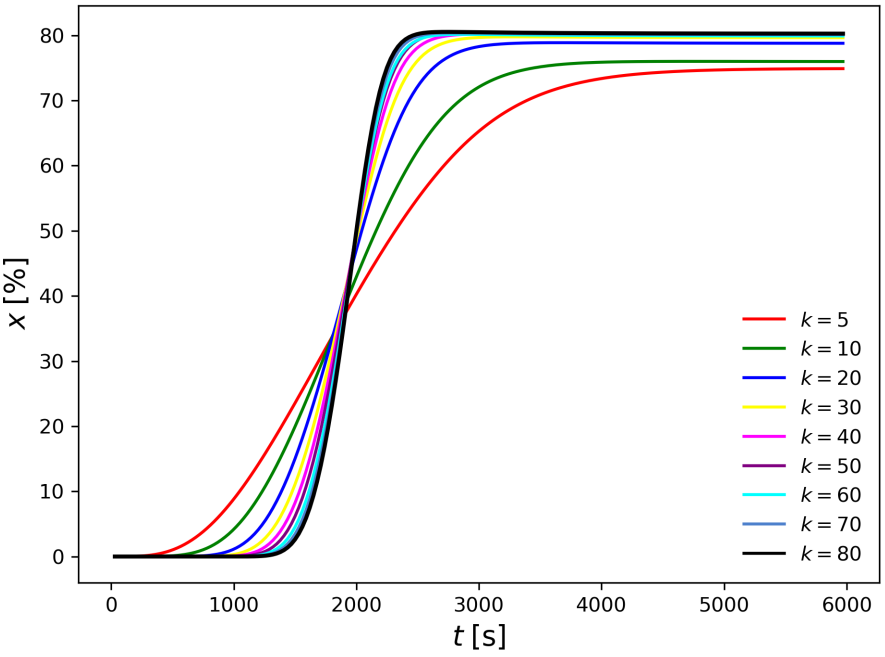

Figure 4.4: Effect of k on dynamic conversion profile at the reactor outlet.

In Figure 4.5, the steady state temperature profiles are shown. Similar to the conversion profiles, the simulations performed with $k = 70$ and $k = 80$ were almost identical, highlighting that the model response has converged. The 'staircase-like' temperature profiles in Figure 4.5 are due to the fact that in the tanks-in-series model the properties at every point of the tank are the same.

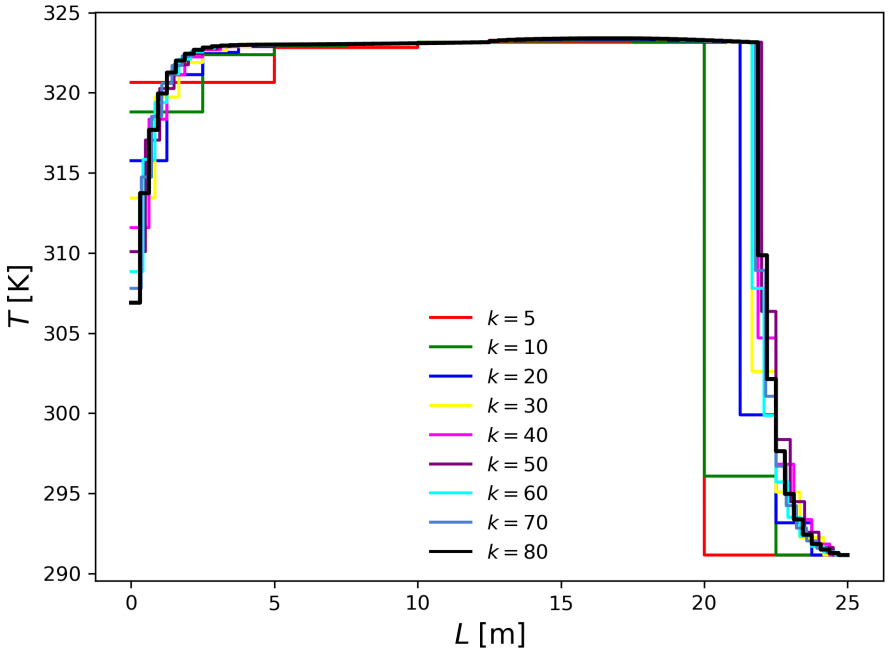

Figure 4.5: Effect of k on the steady state temperature profile.

In Figures 4.6 and 4.7, the number of tanks was fixed at 80 and the effect of the backflow was investigated. Before discussing the obtained results, it is important to emphasize that the backflow parameter in the tanks-in-series model is equivalent to the diffusion coefficient in the dispersion model. This parameter is employed to simulate mixing in the longitudinal direction. By increasing the backflow parameter, as shown in Figure 4.6, it can be noticed that the response starts to deviate from the plug flow behavior. Increasing the backflow is somewhat similar to decreasing the number of tanks in the simulations; in other words, the value of k must increase with the value of $F_{b,n}$ to assure the plug flow behavior of the reactor. It must be observed, however, that k can be interpreted on physical terms, as the number of independent reactor volumes constitutes a physical geometric parameter of the reactor vessel. The high backflow values were selected on purpose to illustrate the robustness of the proposed modeling approach. In Figure 4.7, it is shown that large backflow rates may exert a strong effect on the energy balances along the reactor length. This

occurs because, in these simulations, the controlled variables are the temperatures at the end of each zone and the high backflow causes strong interaction between the controlled and manipulated variables, causing mixing between consecutive reaction zones.

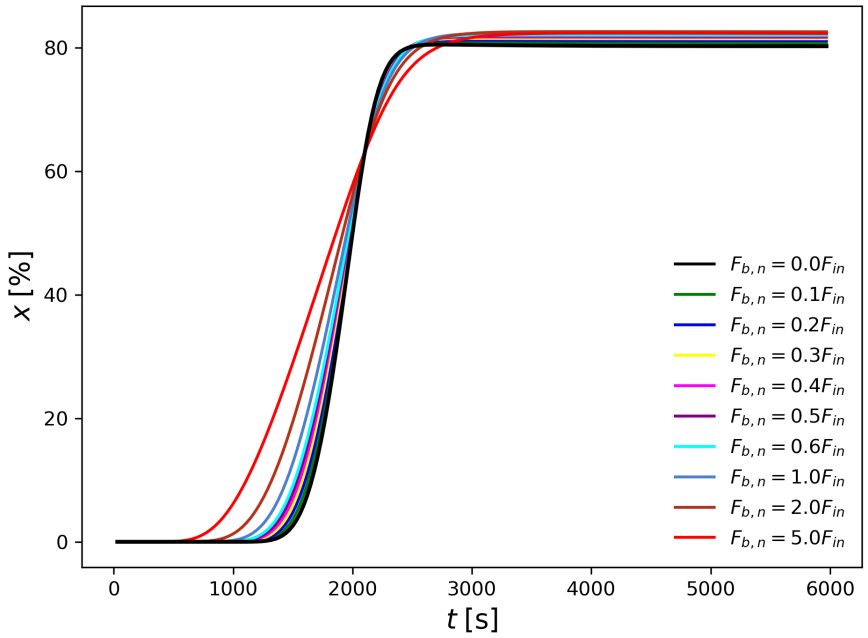

Figure 4.6: Effect of $F_{b,n}$ on dynamic conversion profile at the reactor outlet.

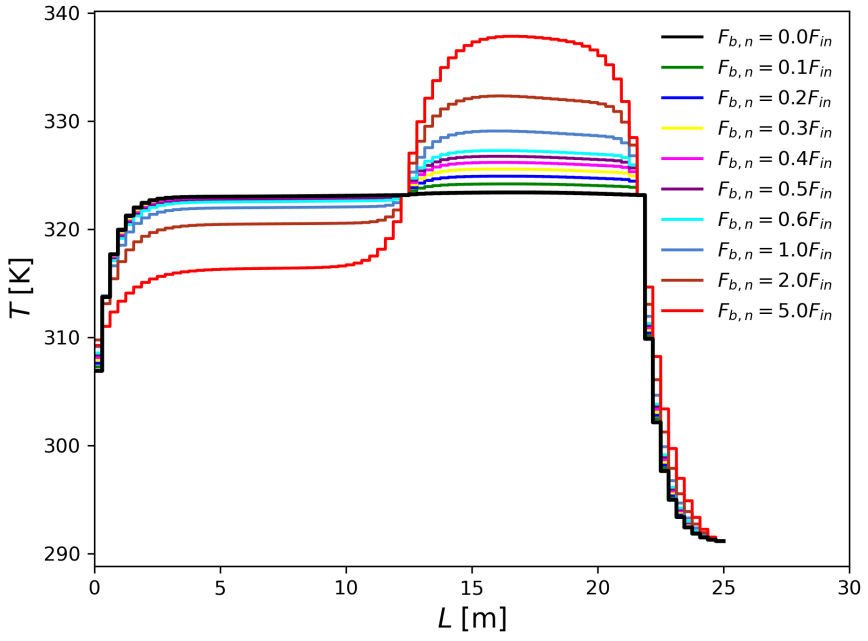

Figure 4.7: Effect of $F_{b,n}$ on the steady state temperature profile.

In Figures 4.8 and 4.9, the same simulations performed in Figures 4.6 and 4.7 were performed assuming that the controlled temperature was located at the position of 6 tanks before the last tank in the heating and reaction zones, respectively. In the cooling zone, the temperature of the last tank remained the controlled variable. It can be seen in Figure 4.9 that a more well-behaved temperature profile along the reactor length can be obtained. Therefore, the upcoming simulations in this work consider that the controlled temperatures are located 6 tanks before the last tank in zones 1 and 2.

The COBR was conceived as a reactor that can achieve near plug flow regime at net laminar flow conditions (Harvey *et al.*, 2001). With that in mind and the results shown so far, it can be concluded that the parameters $k = 80$ and $F_{b,n}$ below $0.5F_{in}$ give near plug flow responses in the simulated conditions. Therefore, from this point afterwards, all the simulations will be performed with $k = 80$ and $F_{b,n} = 0.3F_{in}$. The actual number of compartments in Lobry's work (Lobry, 2012; Lobry *et al.*, 2015) was around 1200, however, the convergence study has shown that near plug flow responses can be achieved with much less compartments. Consequently, one 'numerical compartment' represents nearly 15 'real physical compartments'.

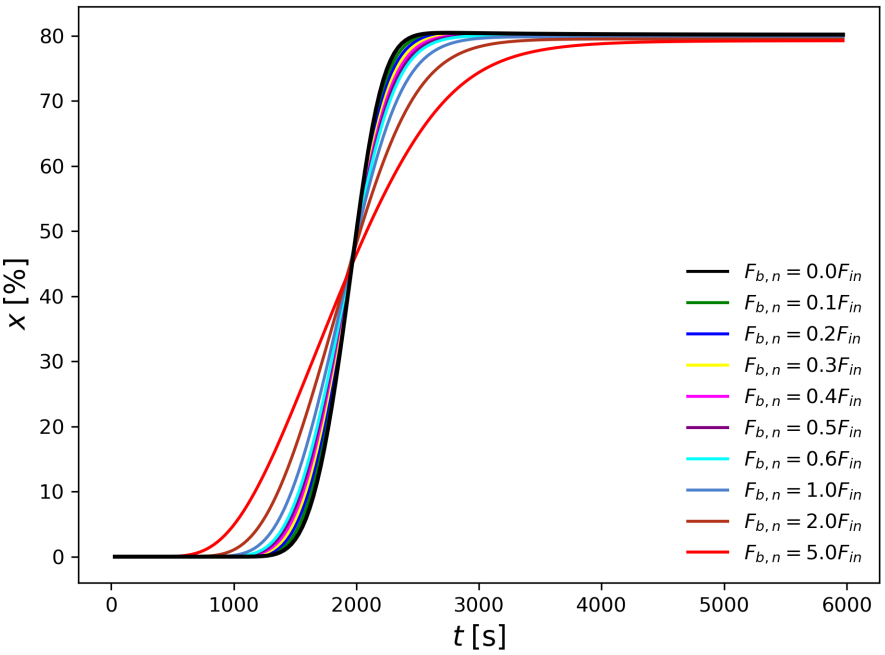

Figure 4.8: Effect of $F_{b,n}$ on dynamic conversion profile at the reactor outlet. Controlled temperatures located at intermediate positions in zones 1 and 2.

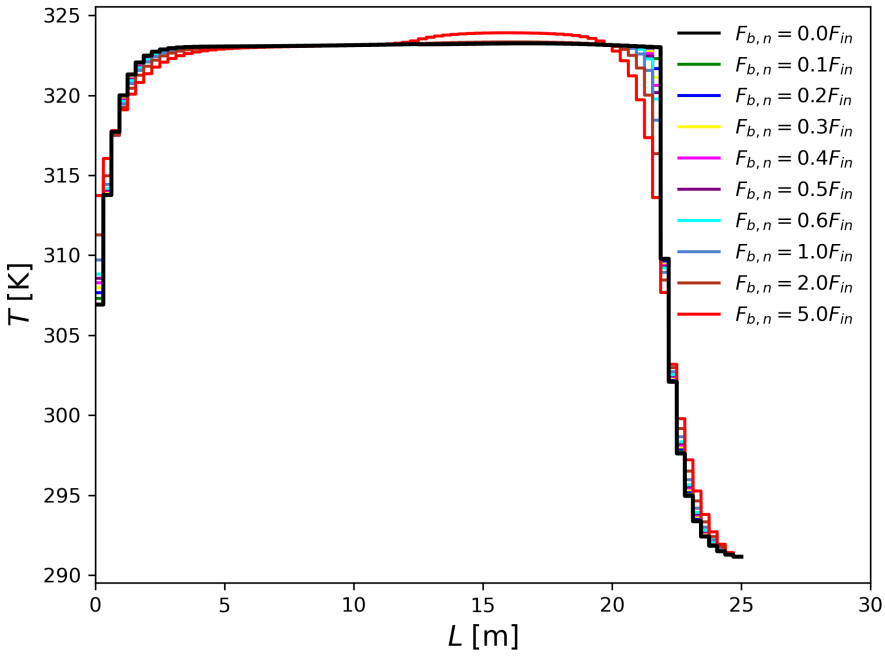

Figure 4.9: Effect of $F_{b,n}$ on the steady state temperature profile. Controlled temperatures located at intermediate positions in zones 1 and 2.

It must also be said that some works such as Reis *et al.* (2004, 2010) investigated the effect of backflow on the residence time distributions in mesoscale oscillatory baffled reactors. Additionally, Smith and Mackley (2006) and Slavnić *et al.* (2017) developed correlations based on experimental data to calculate the diffusion coefficient and the Peclet number as a way of characterizing the deviation from plug flow based on the operation conditions. However, these studies focused on homogeneous systems; the studies characterizing the flow behavior of heterogeneous systems, such as suspension polymerization, are scarce. For instance Kacker *et al.* (2017) investigated the residence time distributions in a DN15 oscillatory baffled flow crystallizer from Nitech® Solutions emphasizing the differences in operation conditions that give near plug flow regime in homogeneous and heterogeneous systems. Ejim *et al.* (2017) performed a design of experiments to understand the effect of baffle geometry on the flow behavior in solid-liquid systems in meso tubes. Similarly, Slavnić *et al.* (2019) studied the flow behavior of solids in a 2 m long oscillatory baffled reactor with 26 mm internal diameter and used the dispersion model to calculate the Peclet number of the solids. Finally, Jimeno *et al.* (2022) developed a numerical study using computational fluid dynamics software to simulate the effect of particle size on the flow behavior of the solids. In spite of that, these studies are limited and a correlation relating the backflow with the operational conditions has not been proposed yet. Consequently, the present work assumes that the deviations from plug flow behavior are small. Further studies will be performed to characterize

the flow behavior in terms of the operation conditions and the backflow parameter.

4.3.2 Fitting Experimental Data

In this section, the model predictions are compared to experimental data provided by Lobry and co-workers (Lobry *et al.*, 2015; Lobry, 2012). The experimental conditions shown in Table 4.5 were used as inputs to the model. Since the temperature in the heating and reaction zones was equal to 317.15 K (44^oC), the setpoints of the controllers of these zones ($T_{sp,z}$, $z = 1, 2$) were set to 317.15 K. The last zone, i.e., the cooling zone ($z = 3$), was maintained at a lower temperature 291.15 K, consequently, the setpoint of the last section was set to $T_{sp,z} = 291.15$ K. The initiator used was Di-(4-tert-butyl-cyclohexyl)-peroxydicarbonate (DTBC), whose decomposition rate constant is shown in Table 4.2. In these experimental conditions: $Re_o = 3675$, $Re_n = 258$, $St = 0.04$ and $\Psi = 14.2$ (calculated at $T = 317.15$K). Figure 4.10 shows the model predictions and the available experimental conversion data.

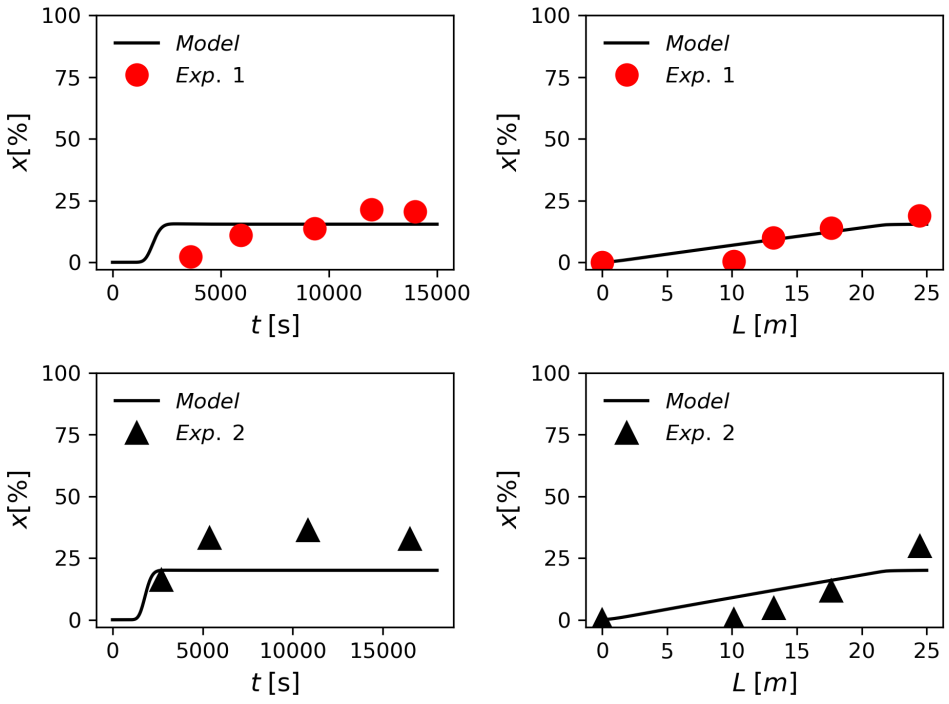

Figure 4.10: Calculated and experimental conversion values.

On the left side of Figure 4.10, the dynamic conversion data obtained at the reactor outlet are shown. On the right side, the steady state conversion data along the reactor length are shown. The final conversion predicted by the model in Exp. 1 was equal to 16%, which was in good agreement with the 20% obtained from experimental data without any sort of parameter fitting. However, the model responded faster in comparison to the data, which can be related to the startup procedure and to occurrence of more pronounced mixing effects. In spite of that, the steady state prediction for Exp. 1 was in very good agreement with the data. Yet regarding Figure 4.10, the final prediction of conversion in Exp. 2 was equal to 21% whereas the experimental data were close to 32%, although the steady state profiles were once more very similar. As a whole, given the fact that none of the model parameters were manipulated to represent the data, the obtained results can be indeed regarded as very good, encouraging the use of the model to perform other simulation studies.

Figure 4.11 depicts the model predictions for the average polymer molar masses at steady state conditions. The average molar masses were considerably high, M_w values close to 6.0×10^5 kg kmol^{-1}, because of the small concentration of radicals inside the reactor, the low monomer conversions and low reaction temperature (Figure 4.12). At $T = 317.15$ K, the half-life time of the employed initiator was $t_{1/2} = ln(2)/kd = 1020$ min, which was 30 times higher than the residence time in the reaction section. In other words, most of the initiator was passing through the reactor without decomposing and forming radicals.

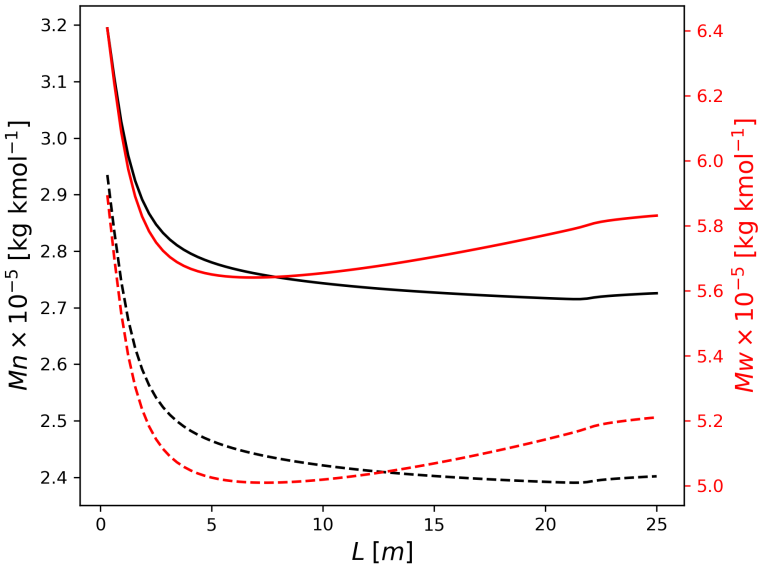

Figure 4.11: Steady state model predictions for Mn (left axis) and Mw (right axis) values in Exp. 1 (solid line) and Exp. 2 (dashed line).

Since the amount of initiator in Exp. 2 was twice the amount in Exp. 1, the average molar masses in Exp. 2 were slightly smaller (dashed lines in Figure 4.11). The dynamic temperature profiles of the reactor and cooling jackets are shown in Figure 4.12. It can be seen that the controllers were able to maintain the temperature of each zone at their respective setpoints.

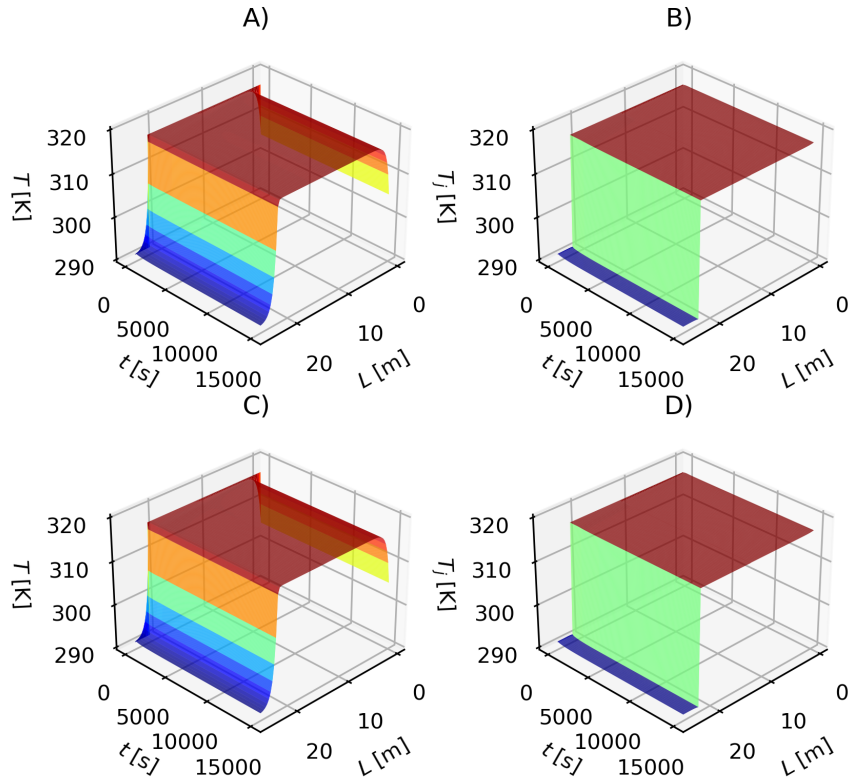

Figure 4.12: Simulated reactor (A,C) and jacket temperatures (B,D) in Exp. 1 (A,B) and Exp. 2 (C,D).

4.3.3 Effect of Initiator Type

In this part of the work, some aspects of the model were investigated at different conditions to understand the behavior of the COBR. In this set of simulations, the inlet temperature of the feed and the reactor temperature were assumed to be equal to 50°C (323.15 K), so that the setpoints of the controllers and the initial conditions were set to this value in order to guarantee a uniform temperature profile along the reactor length. Additionally, the volumetric fraction of water (Φ^2) was set to 0.6 which is close to values used in industry to perform suspension polymerizations. Simulations were performed for three initiator types, namely di-(4-tert-

butyl-cyclohexyl)-peroxydicarbonate (DTBC), cumyl peroxyneodecanoate (CPND) and diisobutyryl peroxide (DIBP) (Table 4.2). The ratio of initiator to monomer feed was fixed at 0.03% in molar basis. The inlet flow rate was kept the same in order to keep the same residence time described by Lobry *et al.* (2015).

At 50^{o}C, DTBC, CPND and DIBP have half-life times of 418.6, 123.5 and 14.6 min, respectively. Since the average residence time for the polymerization reaction is about 33 min, the half-life of the faster initiator, DIBP, is half the reactor average residence time. In other words, the initiator has enough time to decompose and to form radicals inside the reactor. In Figures 4.13 and 4.14, below, the dynamic conversion profiles at the outlet and steady state profiles along the reactor length are shown, respectively. With the fast initiator, DIPB, 96% conversion is achieved whereas monomer conversions achieved with CPND and DTBC were equal to 48 and 25%, respectively. These results clearly indicate that the initiator type must be carefully selected, considering its half-life time in comparison to the average residence time of the reactor in the process of designing COBR experiments.

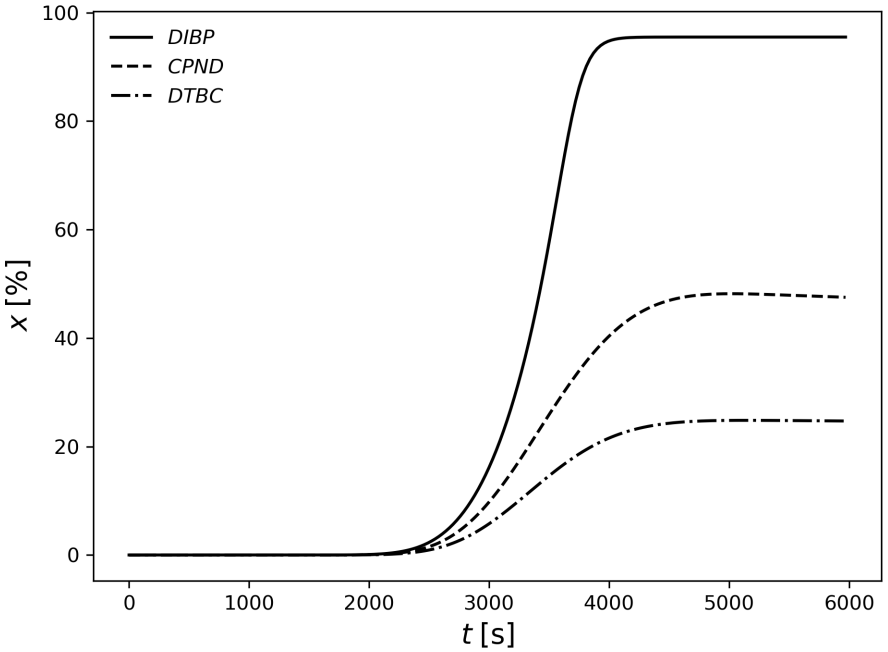

Figure 4.13: Effect of initiator type on dynamic conversion profile at the reactor outlet.

In Figure 4.15, the steady state reactor temperature profiles obtained from the simulations with each initiator type are shown. It can be seen that at low conversions very little stress is put on the cooling system; consequently, the reactor temperature

is kept nearly constant at 323.15 K. However, when using a fast initiator and reaching higher conversions, it is possible to observe variations of up to 4.4 degrees inside the second zone of the reactor. This behavior can be attributed to the gel effect, which causes the propagation rate to accelerate in comparison to the termination rate constant.

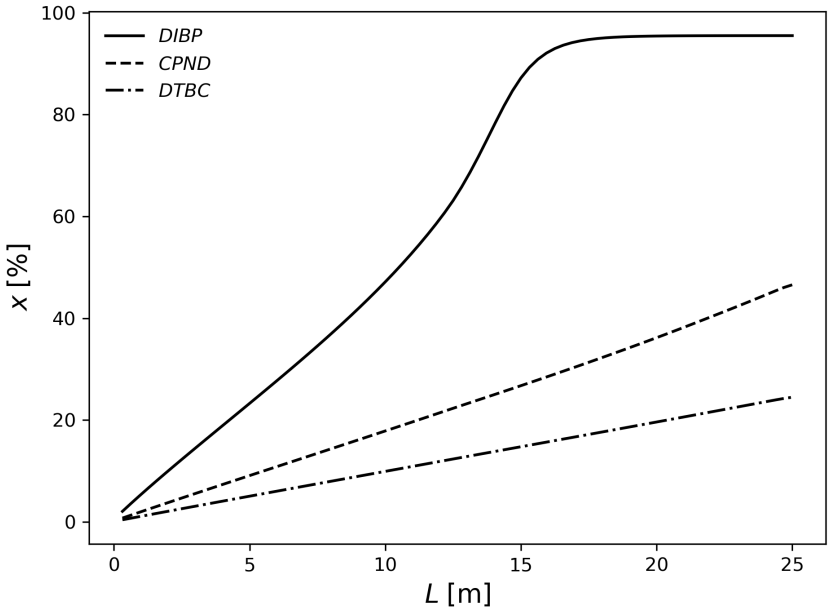

Figure 4.14: Effect of initiator type on the steady state conversion profile.

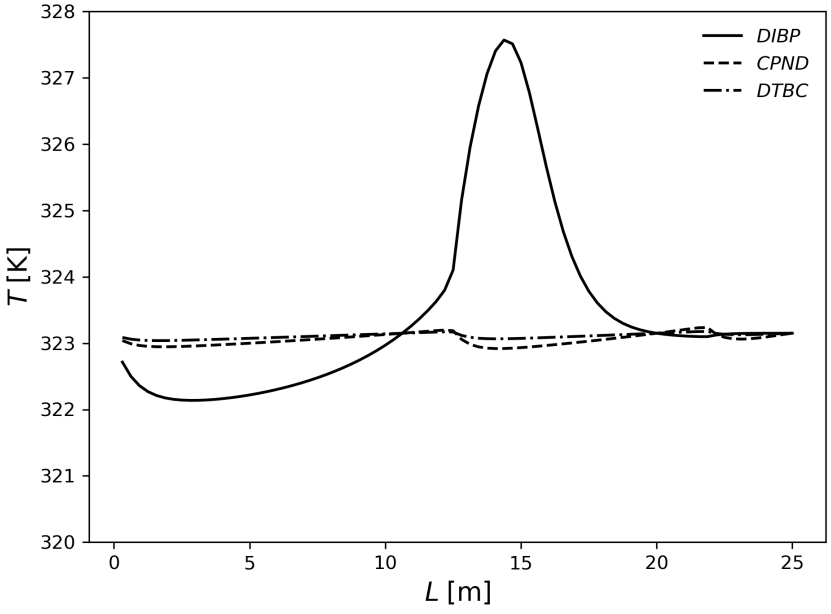

Figure 4.15: Effect of initiator type on the steady state reactor temperature profile.

The gel effect is of paramount importance for the operation of polymerization reactions because it can cause temperature runaways if the control systems are not able to maintain the reactor at the desired temperature. These results explain, in part, some of the difficulties reported by Lobry and co-workers (Lobry *et al.*, 2015; Lobry, 2012) when trying to operate the reactor at more severe operation conditions. Depending on the temperature of operation and pressure, as argued by the author, these temperature hotspots can cause the appearance of gas bubbles inside the reactor due to the vaporization of the monomer. The appearance of this gas phase stops the pulsation of the flow, jeopardizing the operation.

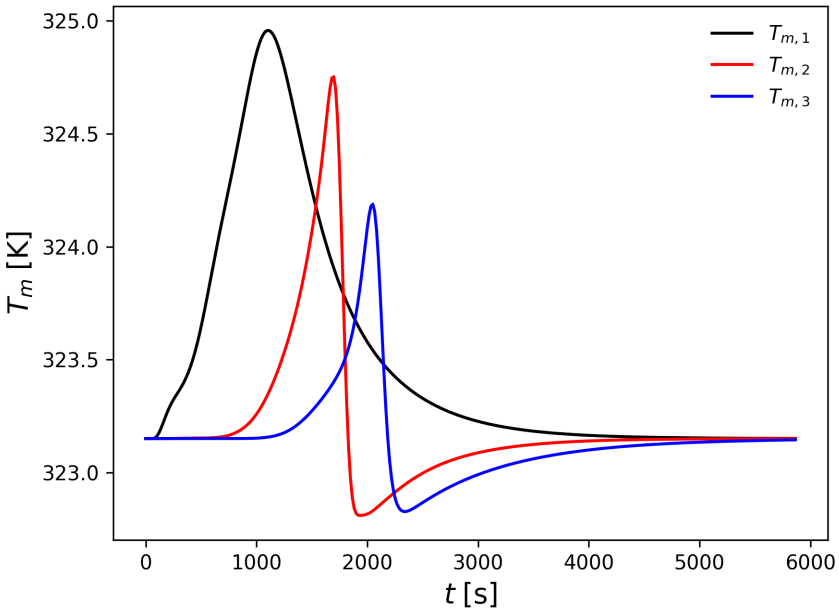

Figure 4.16: Controlled temperature in each zone.

In Figure 4.16, the controlled variables for the simulation performed with DIBP are shown. It is noticeable that these system variables reach a steady state in roughly 3 residence times showing that the control loops are achieving the control objective efficiently. It is also possible to observe a noticeable coupling between the controlled and manipulated variables in Figures 4.16 and 4.17. As the reaction starts, the reactor temperature is expected to increase due to the polymerization reaction; consequently, the manipulated jacket temperatures are reduced to remove the heat released by reaction. However, as the fluid from the first zone passes through the second and the third with its temperature approaching the setpoint, this information is passed to the second and third controllers which increase the inlet jacket temperatures at t=1700 and 2000 s, respectively. This observation shows that the system under consideration exhibits coupling and time delays since

the controlled variables are the temperatures near the end of each zone and the manipulated variables are the inlet jacket feed temperatures at the entrance of each zone; consequently, the residence time of the fluid in each zone (time delay) must be considered in designing control loops for this reactor. For the sake of this initial study, the control strategy was satisfactory. However, more robust strategies must be investigated in order to allow the proper operation at higher reactor temperatures and monomer conversions. It is also worth mentioning that the first zone has the lowest jacket inlet temperature because of its largest length (12.2 m), consequently, a large amount of heat must be removed from this zone.

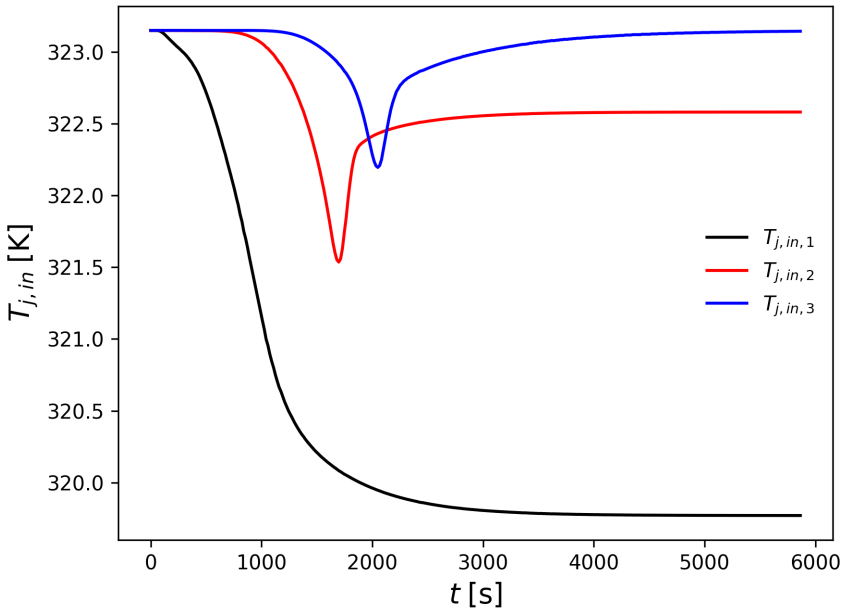

Figure 4.17: Jacket inlet temperature.

Figure 4.18 shows the spatial-temporal profile of heat generated by the reaction ($\dot{Q}_{gen} = (-\Delta H)R_{pol}$) in the simulation performed with DIBP. It is possible to observe that at steady state conditions the highest amount of heat is generated between 12 and 16 m which is responsible for the hotspot previously seen in Figure 4.15. This fact is a consequence of the high polymerization rates at this location of the reactor. On the other hand, the last section of the reactor exhibits low rates of heat generation as a consequence of the low polymerization rates. In this case, the low polymerization rates are due to the low concentration of initiator in this zone. This non-uniform heat generation profile implies that the overall heat transfer capacity of the reactor is not being fully utilized and must be carefully considered during the operation at high monomer conversion.

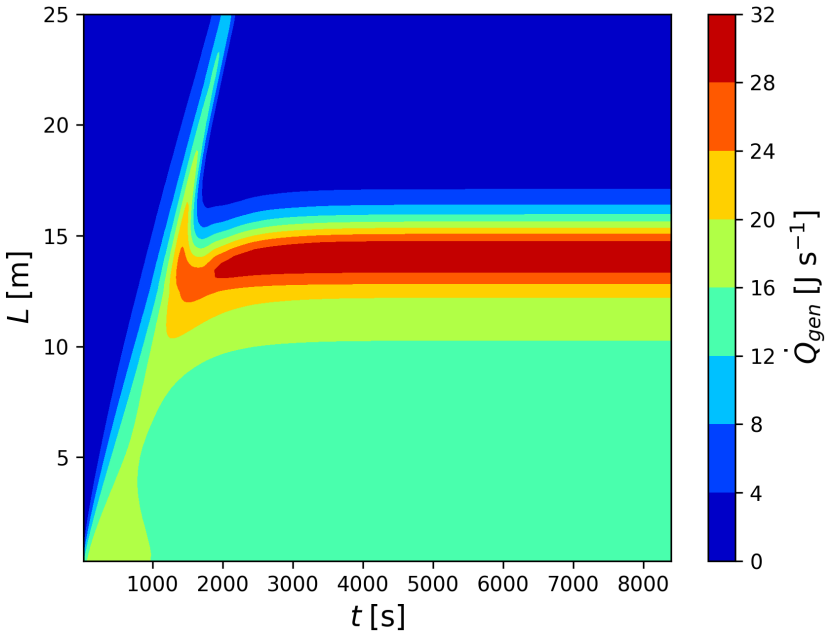

Figure 4.18: Heat generation profile in the simulation performed with DIBP.

In an attempt to obtain a more uniform heat generation profile along the reactor length, a new simulation was performed considering two initiator injection points, one at the reactor inlet and the other in the entrance of the third zone. In this case, the same total amount of initiator used in the previous simulation was employed with the difference that 70% was used at the reactor inlet and 30% was fed to the third zone. Figure 4.19 shows the heat generation profile obtained from this strategy, being possible to observe a more uniform heat generation profile, which suggests that the heat transfer capacity of the reactor can be better utilized and the temperature control can be improved.

In Figure 4.20, a comparison between the single initiator feed and the two feeds strategy is shown. In the case of the two feeds strategy, the acceleration of the conversion curve is diminished as a result of lower polymerization rates in intermediate positions of the reactor, which keeps the temperature profile closer to the setpoint. Given the lower concentration of initiator in the first sections of the reactor in comparison to the single feed strategy, the molar mass of the polymer is slightly higher in comparison to the molar mass obtained with a single initiator feed strategy.

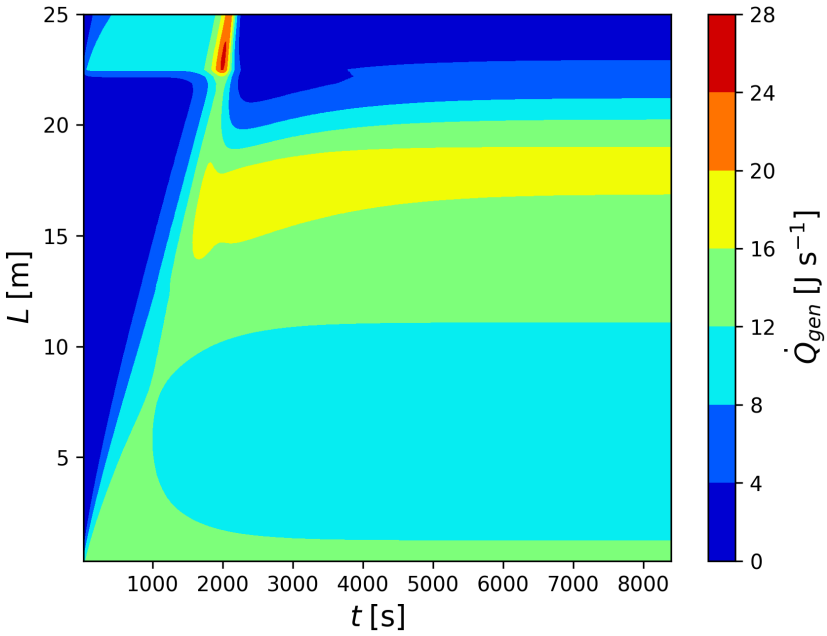

Figure 4.19: Heat generation profile in the simulation performed with DIBP and two initiator feed points.

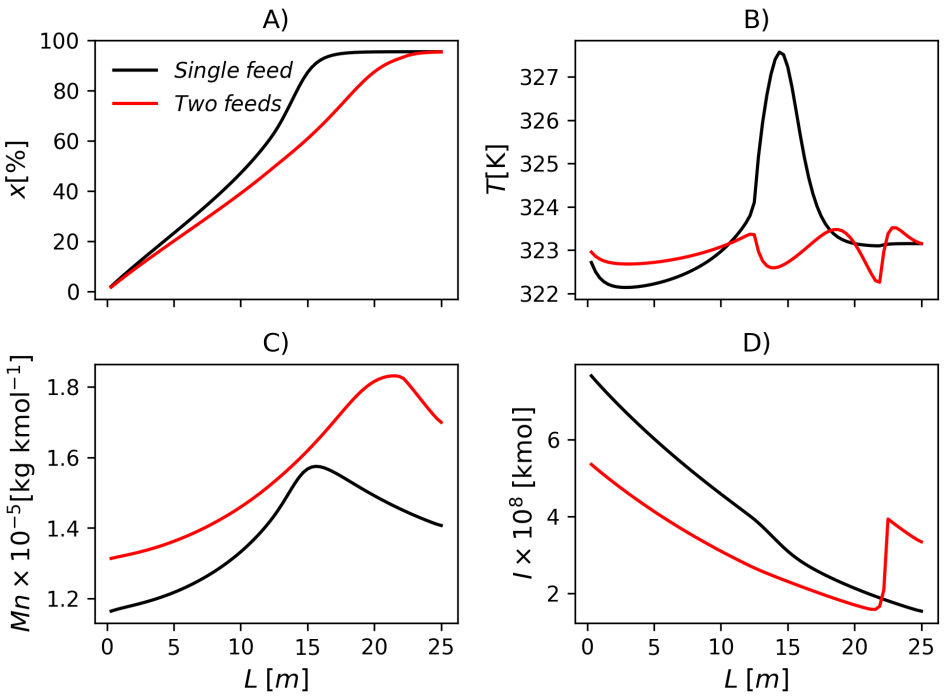

Figure 4.20: Comparison between steady state profiles in simulations performed with single initiator and two initiator feeds. A) Conversion, B) Reactor temperature, C) Number average molar mass, and D) Initiator.

4.3.4 Effect of Oscillation Velocity

In this subsection, the effect of the oscillatory conditions was investigated. Since the oscillation amplitude (χ_o) and frequency (f_o) appear together in Equation (4.41), the product $\chi_o f_o$ (oscillation velocity) was considered as a lumped parameter in this part of the work. According to Equation (4.46), the amplitude and frequency of oscillation affect the heat transfer characteristics of the reactor. In Figure 4.21, the Nusselt number (Nu_s) and heat transfer coefficient of the suspension (h_s) (reactor side) as well as the overall heat transfer coefficient (U) are shown for simulations performed with different $\chi_o f_o$. In the first simulation, when $Re_o = 2480$, the Nu_s, h_s and U are close to 35, 970 J s^{-1} m^{-2} K^{-1} and 320 J s^{-1} m^{-2} K^{-1}, respectively, indicating that the heat transfer rate at the tube side is high. For comparative purposes, the Nusselt number in a tube under developed laminar flow conditions is 3.66 (Bergman *et al.*, 2011). In the simulation performed with $Re_o = 1240$, the tube side Nusselt number is still high, although at this condition the oscillatory conditions are slightly below the point where the heat transfer due to oscillatory flow becomes asymptotic ($Re_o = 1300$ according to Equations (4.46) and (4.47)). Decreasing $\chi_o f_o$ even further to 0.0037 m s^{-1} causes Nu_s to approach 17, h_s drops to 477 J s^{-1} m^{-2} K^{-1} and U approaches 240 J s^{-1} m^{-2} K^{-1}. The calculated values of U show a good agreement with the experimental values reported by Briggs *et al.* (2021) in a similar apparatus setup.

4.4 Concluding Remarks

In the present chapter, a comprehensive model was built and implemented to represent suspension polymerizations in continuous oscillatory baffled reactors for the first time. The heat transfer rates, kinetics and polymer properties were considered in the proposed modeling approach. The model was able to represent the available literature data that reported monomer conversions for vinyl acetate polymerizations performed in COBR reactors. It was shown, in particular, that the initiator type and amounts play important roles for the development of temperature profiles along the reactor. Additionally, the use of multiple initiator feed points can lead to more uniform heat generation profiles, which can be useful to allow the tighter control of the reactor temperature and to avoid the appearance of hotspots. The effect of the oscillatory conditions was also investigated and it was shown that low oscillation velocities can cause the reduction of the heat transfer capacity of the reactor. This information can be particularly useful for further studies and

experiments regarding reactors of larger diameter.

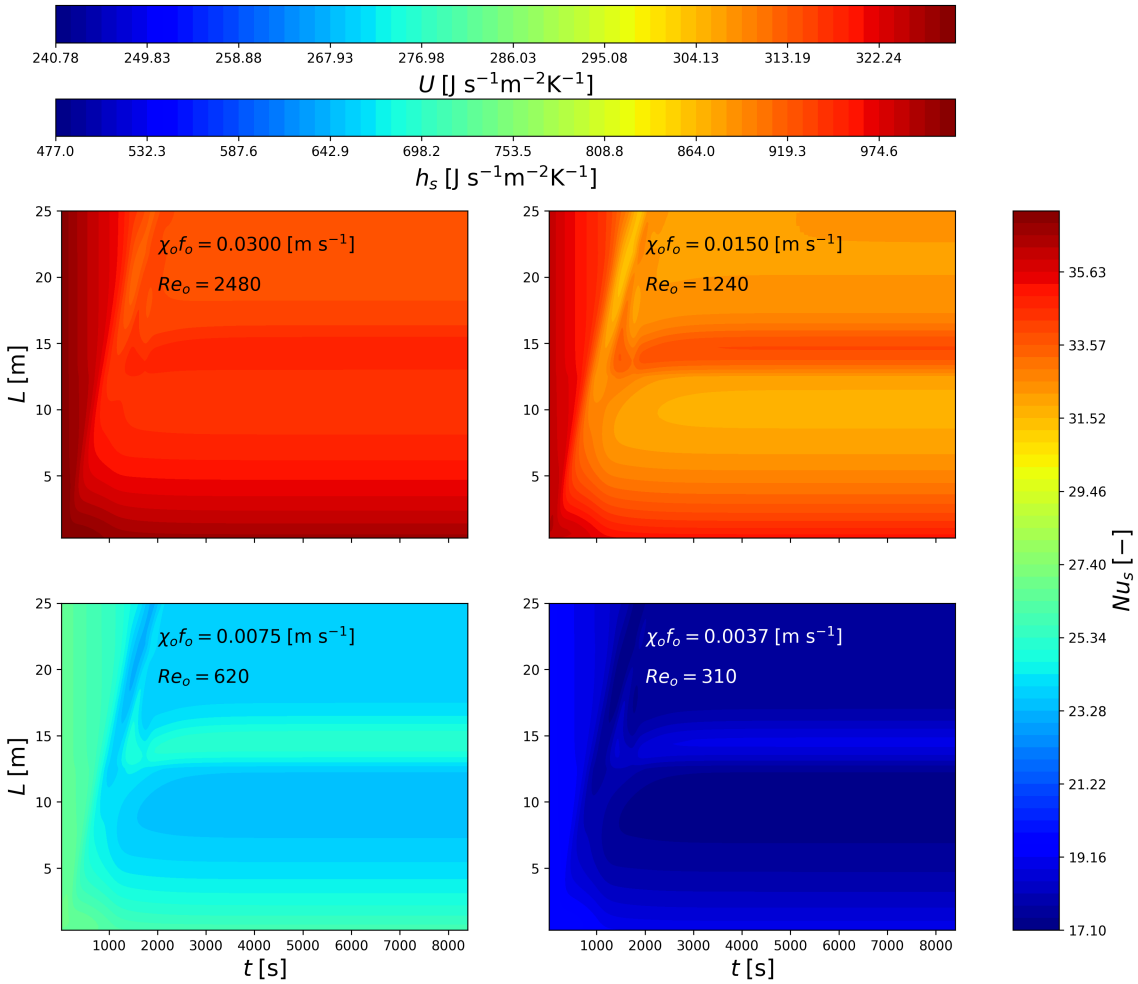

Figure 4.21: Effect of $\chi_o f_o$ on the reactor side Nusselt number and heat transfer coefficients.

List of Abbreviations

Abbreviation	Meaning
COBR	Continuous Oscillatory Baffled Reactor
DTBC	Di-(4-tert-butyl-cyclohexyl)-peroxydicarbonate
CPND	Cumyl peroxyneodecanoate
DIBP	Diisobutyryl peroxide
PVAC	Poly(vinyl acetate)

List of Symbols

Symbol	Meaning
A	Heat transfer area [m^2]
$\underline{cp}$	Heat capacity [kJ kg^{-1} K^{-1}]
cp	Heat capacity [kJ $kmol^{-1}$ K^{-1}]
C	Cross section area of the reactor [m^2]
C_{pva}	Concentration of poly(vinyl alcohol) [kg m^{-3}]
d_o	Orifice diameter [m]
$d_{r,ext}$	Reactor external diameter [m]
$d_{r,int}$	Reactor internal diameter [m]
d_{32}	Sauter mean diameter [m]
E	Error of the controller [K]
f_o	Frequency of oscillation [s^{-1}]
f	Initiator efficiency [-]
F	Flow rate [m^3 s^{-1}]
h	Heat transfer coefficient [J s^{-1} m^{-2} K^{-1}]
I	Initiator [kmol]
k	Total number of tanks [-]
k_d	Decomposition rate constant [s^{-1}]
k_p	Propagation rate constant [m^3 $kmol^{-1}$ s^{-1}]
k_{tm}	Transfer to monomer rate constant [m^3 $kmol^{-1}$ s^{-1}]
k_{sol}	Monomer solubility in water [wt.%]
k_{tp}	Transfer to polymer rate constant [m^3 $kmol^{-1}$ s^{-1}]
k_{td}	Termination by disproportionation rate constant [m^3 $kmol^{-1}$ s^{-1}]
k_{wall}	Thermal conductivity of the reactor wall [J s^{-1} m^{-1} K^{-1}]
K_c	Proportional gain of the controller [-]
l	Equivalent length [m]
L	Reactor length [m]

m	Molar or mass flow rate [kmol s^{-1} or kg s^{-1}]
M	Monomer [kmol]
MM	Molar mass [kg $kmol^{-1}$]
Mn	Number average molar mass [kg $kmol^{-1}$]
Mw	Weight average molar mass [kg $kmol^{-1}$]
Nu	Nusselt number [-]
P	Polymer [kmol]
Pr	Prandtl number [-]
$\dot{Q}_{gen}$	Heat generated by the reaction [J s^{-1}]
Re	Reynolds number [-]
Re_o	Oscillatory Reynolds number [-]
R_{pol}	Polymerization rate [kmol s^{-1}]
St	Strouhal number [-]
T	Temperature [K]
U	Overall heat transfer coefficient [J s^{-1} m^{-2} K^{-1}]
v	Velocity [m s^{-1}]
V	Volume [m^3]
x	Conversion [-]
Y	Suspending agent [kg]
W	Water [kmol]
Greek letters	
Φ	Volume fraction [-]
ϕ	Auxiliary function [-]
Ω	Auxiliary function [-]
χ_o	Center-to-peak amplitude of oscillation [m]
λ	Living polymer moments [kmol]
μ	Dead polymer moments [kmol]
η	Viscosity [kg m^{-1} s^{-1}]
$[\eta]_{pva}$	Intrinsic viscosity of poly(vinyl alcohol) [m^3 kg^{-1}]
σ	Thermal conductivity [J m^{-1} s^{-1} K^{-1}]
ρ	Density [kg m^{-3}]
τ_i	Integral time of the controller [s]
ΔH	Enthalpy of reaction [kJ $kmol^{-1}$]
Ψ	Velocity ratio [-]
Superscripts	
1	Phase 1 (organic phase)
2	Phase 2 (inorganic phase)
Subscripts	
0	Zero order moment

1	First order moment
2	Second order moment
3	Third order moment
b	Backflow
c	Continuous Phase
d	Dispersed Phase
h	Ref. to hydraulic diameter
i	Initiator
in	Inlet
j	Jacket
m	Monomer
n	Tank number
p	Polymer
r	Reactor
ref	Reference value
s	Suspension
sp	Setpoint
w	Water
y	Suspending agent
z	Reactor zone

4.5 References

Batchelor, G.K.; Green, J.T. The hydrodynamic interaction of two small freely-moving spheres in a linear flow field. Journal of Fluid Mechanics, 56, 2, 375-400, 1972.

Bergman, T.L.; Lavine, A.S.; Incropera, F.P.; Dewitt, D.P. Fundamentals of Heat and Mass Transfer, seventh ed., Wiley, Hoboken, USA, 2011.

Bouyatiotis, B.S.; Thornton, J.D. Liquid-liquid extraction studies in stirred tanks. Part I. droplet size and holdup. Institution of Chemical Engineers (London) Symposium Series, 26, 43-50, 1967.

Briggs, N.E.B.; McGinty, J.; McCabe, C.; Raval, V.R.; Sefcik, J.; Florence, A.J. Heat transfer and residence time distribution in plug flow continuous oscillatory baffled crystallizers. ACS Omega, 6, 28, 18352-18363, 2021.

Brunold, C.R.; Hunns, J.C.B.; Mackley, M.R.; Thompson, J.W. Experimental observations on flow patterns and energy losses for oscillatory flow in ducts containing sharp edges. Chemical Engineering Science, 44, 5, 1227-1244, 1989.

Ejim, L.N.; Yerdelen, S.; McGlone, T.; Onyemelukwe, I.; Johnston, B.; Florence, A.J.; Reis, N.M. A factorial approach to understanding the effect of inner geometry of baffled meso-scale tubes on solids suspension and axial dispersion in continuous, oscillatory liquid-solid plug flows. Chemical Engineering Journal, 308, 669-682, 2017.

Friis, N.; Hamielec, A.E. Gel-effect in emulsion polymerization of vinyl monomers. ACS Symposium Series, 24, 82-91, 1976

Friis, N. A kinetic study of the emulsion polymerization of vinyl acetate. Riso National Laboratory, Denmark, Forskningscenter Risoe. Reso-R No. 282, 1973.

Gnielinski, V. G2 Heat transfer in concentric annular and parallel plate ducts. in: VDI Heat Atlas, Second Edition, Springer-Verlag, Berlin, pp. 701-708, 2010.

Gnielinski, V. Heat transfer coefficients for turbulent flow in concentric annular ducts. Heat transfer engineering, 30, 6, 431-436, 2009.

Gnielinski, V. Berechnung des Druckverlustes in glatten konzentrischen Ringspalten bei ausgebildeter laminarer und turbulenter isothermer Strömung. Chemie Ingenieur Technik, 79, I-2, 91-95, 2007.

Green, D.W.; Perry, R.H. Perry's Chemical Engineers Handbook. 8th ed., McGraw Hill, New York, NY, USA, 2008.

Harvey, A.P.; Mackley, M.R.; Stonestreet, P. Operation and optimization of an oscillatory flow continuous reactor. Industrial and Engineering Chemistry Research, 40, 5371-5377, 2001.

Howes, T.; Mackley, M.R.; Roberts, E.P.L. The simulation of chaotic mixing and dispersion for periodic flows in baffled channels. Chemical Engineering Science, 46, 7, 1669-1677, 1991.

Hulburt, H.M.; Katz, S. Some problems in particle technology a statistical mechanical formulation. Chemical Engineering Science, 19, 555-574., 1964

Hutchinson, R.A.; Penlidis, A. Free-radical Polymerization: Homogeneous Sys-

tems. in: Asua, J.M. (Ed.), Polymer Reaction Engineering, Blackwell Publishing, Oxford, UK, pp. 118-178, 2007.

Jimeno, G.; Lee, Y.C.; Ni, X.W. The effect of particle size on flow in a continuous oscillatory baffled reactor using CFD. Canadian Journal of Chemical Engineering, 100, S258-S271, 2022.

Kacker, R.; Regensburg, S.I.; Kramer, H.J.M. Residence time distribution of dispersed liquid and solid phase in a continuous oscillatory flow baffled crystallizer. Chemical Engineering Journal, 317, 413-423, 2017.

Kalfas, G.; Yuan, G.; Ray, W.H. Modeling and experimental studies of aqueous suspension polymerization processes. 2. experiments in batch reactors. Industrial and Engineering Chemistry, 32, 1831-1838, 1993.

Kiparissides, C.; Pladis, P. On the prediction of suspension viscosity, grain morphology, and agitation power in SPVC reactors. Canadian Journal of Chemical Engineering, 100, 4, 714-730, 2022.

Kiparissides, C. Polymerization reactor modeling: a review of recent developments and future directions. Chemical Engineering Science, 51, 10, 1637-1659, 1996.

Korosi, A.; Fabuss, B.M. Viscosity of liquid water from 25^o to 150^o C measurements in pressurized glass capillary viscometer. Analytical Chemistry, 40, 1, 157-162, 1968.

Law, R.; Ahmed, S.M.R.; Tang, N.; Phan, A.N.; Harvey, A.P. Development of a more robust correlation for predicting heat transfer performance in oscillatory baffled reactors. Chemical Engineering and Processing: Process Intensification, 125, 133-138, 2018.

Leiza, J.; Pinto, A. Control of Polymerization Reactors. in: Asua, J.M. (Ed.), Polymer Reaction Engineering, Blackwell Publishing, Oxford, UK, pp. 315-361, 2007.

Levy, F.L. A modified Maxwell-Eucken equation for calculating the thermal conductivity of two-component solutions or mixtures. International Journal of Refrigeration, 4, 4, 223-225, 1981.

Li, C.C. Thermal conductivity of liquid mixtures. AIChE Journal, 22, 5, 927-

930, 1976.

Lindemann, M.K. Physical Constants of Some Important Polymers, in: Brandrup, J., Immergut , E.H., Grulke, A. (Eds.), Polymer Handbook. Wiley, New York, Ch. V, 1999.

Lobry, E.; Lasuye, T.; Gourdon, C.; Xuereb, C. Liquid-liquid dispersion in a continuous oscillatory baffled reactor - application to suspension polymerization. Chemical Engineering Journal, 259, 505-518, 2015.

Lobry, E. Batch to continuous vinyl chloride suspension polymerization process: a feasibility study. PhD Thesis, Université de Toulouse, 2012.

Mackley, M.R.; Tweddle, G.M.; Wyatt, I.D. Experimental heat transfer measurements for pulsatile flow in baffled tubes. Chemical Engineering Science, 45, 5, 1237-1242, 1990.

Mackley, M.R.; Ni, X. Mixing and dispersion in a baffled tube for steady laminar and pulsatile flow. Chemical Engineering Science, 46, 12, 3139-3151, 1991.

Mackley, M.R., Stonestreet, P. Heat transfer and associated energy dissipation for oscillatory flow in baffled tubes. Chemical Engineering Science, 50, 14, 2211-2224, 1995.

Maggioris, D.; Goulas, A.; Alexopoulos, A.H.; Chatzi, E.G.; Kiparissides, C. Prediction of particle size distribution in suspension polymerization reactors: effect of turbulence nonhomogeneity. Chemical Engineering Science, 55, 4611-4627, 2000.

Martin, H. Lecture on Heat Transfer. Universitaet Karlsruhe (TH), Germany, 1990.

Mastan, E.; Zhu, S. Method of moments: a versatile tool for deterministic modeling of polymerization kinetics. European Polymer Journal, 68, 139-160, 2015.

Mecklenburgh, J.C.; Hartland, S. Design of reactors with backmixing - I exact methods. Chemical Engineering Science, 23, 1, 57-65, 1968.

Nagy, D.J. A Mark-Houwink equation for poly(vinyl alcohol) from sec-viscometry. Journal of Liquid Chromatography, 16, 14, 3041-3058, 1993.

Ni, X.; Gough, P. On the discussion of the dimensionless groups governing

oscillatory flow in a baffled tube. Chemical Engineering Science, 52, 18, 3209-3212, 1997.

Odian, G. Principles of Polymerization, fourth ed. John Wiley and Sons, Hoboken, NJ, USA, 2004.

Okaya, T. General Properties of Polyvinyl alcohol in relation to its applications. in: Finch, C.A. (Ed.), Polyvinyl Alcohol Developments, Wiley, Oxford, UK, pp. 1-30, 1992.

Petukhov, B.S., Roizen, L.I. Generalized relationships for heat transfer in a turbulent flow of gas in tubes of annular section(heat transfer coefficients and adiabatic temperatures obtained for turbulent gas flow in tubes with annular section). High Temperature 2, 65-68, 1964.

Petzold, L. A description of DASSL: An Differential/Algebraic Equation Solver. Sandia National Laboratories, Livermore, CA, USA, 1982.

Ray, W.H. On the mathematical modeling of polymerization reactors. Journal of Macromolecular Science Part C, 8, 1, 1-56, 1972.

Reis, N.; Vicente, A.A.; Teixeira, J.A.; Mackley, M.R. Residence times and mixing of a novel continuous oscillatory flow screening reactor. Chemical Engineering Science, 59, 4967-4974, 2004.

Reis, N.; Vicente, A.A.; Teixeira, J.A. Liquid backmixing in oscillatory flow through a periodically constricted meso-tube. Chemical Engineering Science and Processing: Process Intensification, 49, 7, 793-803, 2010.

Seborg, D.E.; Mellichamp, D.A.; Edgar, T.F.; Doyle, F.J. Process Dynamics and Control, third ed. Wiley, Hoboken, NJ, USA, 2010.

Silva, F.M.; Lima, E.L.; Pinto, J.C. Acrylic acid/vinyl acetate suspension copolymerizations. 2. modeling and experimental results. Industrial and Engineering Chemistry Research, 43, 23, 7324-7342, 2004.

Skogestad, S.; Postlethwaite, I. Multivariable Feedback Control, Wiley, Hoboken, NJ, USA, 2005.

Slavnić, D.S.; Živković, L.V.; Bjelić, A.V.; Bugarski, B.M.; Nikačević, N.M. Residence time distribution and Peclet number correlation for continuous oscillatory

flow reactors. Journal of Chemical Technology and Biotechnology, 92, 2178-2188, 2017.

Smith, K.B.; Mackley, M.R. An experimental investigation into the scale-up of oscillatory flow mixing in baffled tubes. Chemical Engineering Research and Design, 84, A11, 1001-1011, 2006.

Stonestreet, P.; Van der Veeken, P.M.J. The effects of oscillatory flow and bulk flow components on residence time distribution in baffled tube reactors. Chemical Engineering Research and Design, 77, 8, 671-684, 1999.

Stonestreet, P.; Harvey, A.P. A mixing-based methodology for continuous oscillatory flow reactors. Chemical Engineering Research and Design, 80, 1, 31-44, 2002.

Teymour, F. The Dynamic Behavior of Free Radical Solution Polymerization Reactions in a Continuous Stirred Tank Reactor. PhD Thesis, University of Wisconsin (Madison), 1989.

Ueda, A.; Nagai, S. Polymerization and Depolymerization, in: Brandrup, J., Immergut , E.H., Grulke, A. (Eds.), Polymer Handbook. Wiley, New York, Ch. II, 1999.

Vermeulen, T.; Williams, G.M.; Langlois, G.E. Interfacial area in liquid-liquid and gas-liquid agitation. Chemical Engineering Progress, 51, 2, 85-94, 1955.

Wang, J.; Carson, J.K.; North, M.F.; Cleland, D.J. A new approach to modelling the effective thermal conductivity of heterogeneous materials. International of Heat and Mass Transfer, 49, 17-18, 3075-3083, 2006.

Wieme, J.; De Roo, T.; Marin, G.B.; Heynderickx, G.J. Simulation of pilot- and industrial-scale vinyl chloride batch suspension polymerization reactors. Industrial and Engineering Chemistry Research, 46, 4, 1179-1196, 2007.

Chapter 5

Poly(vinyl chloride) Suspension Polymerization in an Oscillatory Baffled Reactor

In this chapter, the previously developed model to represent the suspension polymerization of poly(vinyl acetate) (PVAC) in a continuous oscillatory baffled reactor (COBR) is extended to represent the polymerization of poly(vinyl chloride) (PVC). As discussed in Chapter 2, the polymerization of vinyl chloride is a heterogeneous process since the monomer presents very low solubility in water, and the polymer is also insoluble in its monomer. This scenario is quite different from the polymerization of vinyl acetate. Therefore, this entire chapter is devoted to the development of a comprehensive mathematical model to represent the polymerization of PVC in a continuous oscillatory baffled reactor. For the sake of conciseness, parallels are drawn between the present chapter and Chapters 2 and 4 when necessary. Furthermore, as an extension of the previous chapters, this part of the work disregards some aspects presented earlier to avoid redundancy.

5.1 Model Development

In a similar way as performed in Chapter 4, the following hypotheses were assumed to be valid during the development of the model used to represent the vinyl chloride polymerization in a COBR. Caution must be paid to the fact that, in the present chapter, three phases are considered simultaneously. This additional phase demands the inclusion of additional balance equations. Moreover, it is important to emphasize that the batch model developed to describe the suspension polymerization of vinyl chloride in a stirred tank reactor, presented in Chapter 2, considered a gaseous phase, which is neglected in this study. In the COBR, it is assumed that the gaseous phase is not present because the operation pressure is kept above the saturation pressures of vinyl chloride and water. The additional assumptions are:

- Volume additivity holds;
- Negligible effect of initiator on the overall mixture volume;
- Existence of three phases in equilibrium: monomer-rich (Phase 1), polymer-rich (Phase 2) and aqueous phase (Phase 3);
- Initiator is insoluble in water;
- Monomer is partially soluble in water;
- Polymer is insoluble in water;
- Monomer is mainly consumed mainly by the propagation reaction;
- Heat of reaction is mainly released by the propagation reaction;
- Chain initiation is much faster than initiator decomposition so that the overall rate of initiation is governed by initiator decomposition.

5.1.1 Kinetic Model

The kinetic mechanism presented in Table 2.1, in Chapter 2, to describe batch suspension polymerization of vinyl chloride in an industrial batch reactor was employed here to describe the polymerization of vinyl chloride in the COBR.

5.1.2 Equilibrium Calculations

The polymerization of vinyl chloride can be divided into three stages, as explained in Chapter 2. However, the inclusion of the the first stage, when the conversion (Equation (5.1)) is smaller than 0.001 can be neglected for practical purposes. Moreover, final conversions of interest are close to 90%. Therefore, in this chapter, the model neglects the first stage and considers that the initial conversion is equal to 0.001, so that it is implicitly assumed that there is a small amount of polymer inside the reactor since the start up.

Let $n = 1, 2, 3, ..., k$ represent the tank number in the series. By comparing the equation that represents the critical conversion in the COBR (Equation (5.3)) with its counterpart in the industrial batch reactor (Equation (5.4)) an interesting fact is put in evidence. As M_n^3/M_n^2 represents the molar ratio between monomer in the aqueous phase (Phase 3) and in the polymer-rich phase (Phase 2), and the solubility of monomer in water is very low, it can be concluded that the critical conversion ($x_{f,n}$) is very close to the equilibrium mass fraction of polymer in the polymer-rich phase ($x_{s,n}$) represented in Equation (5.2). In Equation (5.4), on the other hand, the term that multiplies $(1 - x_{s,n})$ is $(M_n^3 + M_n^4)/M_n^2$ and M_n^4 represents the monomer in the gaseous phase (Phase 4) which causes the critical conversion to be lower than $x_{s,n}$. This observation can be of paramount importance for the development of efficient operation strategies in the COBR because the identification of the critical conversion can be important to comprehend the evolution of the reaction. The equilibrium calculations required to compute the composition of each phase are described in Table 5.1.

$$x_n = \frac{P_n}{M_n + P_n} \tag{5.1}$$

$$x_{s,n} = \frac{\varphi_{p,n}\rho_p}{\varphi_{p,n}\rho_p + (1 - \varphi_{p,n})\rho_m} \tag{5.2}$$

$$x_{f,n} = x_{s,n}\left[\frac{1}{1 + \frac{M_n^3}{M_n^2}(1 - x_{s,n})}\right] \quad \text{(COBR)} \tag{5.3}$$

$$x_{f,n} = x_{s,n}\left[\frac{1}{1+\frac{M_n^3+M_n^4}{M_n^2}\left(1-x_{s,n}\right)}\right] \quad \text{(BATCH)} \tag{5.4}$$

Table 5.1: Equilibrium calculations at the different reaction stages in poly(vinyl chloride) polymerization.

$0.001 < x_n \leq x_{f,n}$	$x_n > x_{f,n}$
$M_n = M_n^1 + M_n^2 + M_n^3$	$M_n = M_n^1 + M_n^2 + M_n^3$
$V_n = V_n^1 + V_n^2 + V_n^3$	$V_n = V_n^1 + V_n^2 + V_n^3$
$W_n = W_n^3$	$W_n = W_n^3$
$P_n = P_n^2$	$P_n = P_n^2$
$I_n = I_n^1 + I_n^2$	$I_n = I_n^1 + I_n^2$
$I_n^1 = \frac{I_n V_n^1}{V_n^1 + K_I V_n^2}$	$I_n^1 = 0$
$M_n^2 = P_n^2\left(\frac{1-\varphi_{p,n}}{\varphi_{p,n}}\right)\left(\frac{\rho_m}{\rho_p}\right)$	$M_n^1 = 0$
$M_n^3 = k_{sol}\frac{MM_w}{MM_m}\frac{Z_t}{Z_m^{sat}}W_n^3$	$M_n^3 = k_{sol}\frac{MM_w}{MM_m}\frac{Z_t}{Z_m^{sat}}W_n^3$
$V_n^1 = \frac{M_n^1}{\rho_m}$	$V_n^1 = 0$
$V_n^2 = MM_m\left(\frac{M_n^2}{\rho_m} + \frac{P_n^2}{\rho_p}\right)$	$V_n^2 = MM_m\left(\frac{M_n^2}{\rho_m} + \frac{P_n^2}{\rho_p}\right)$
$V_n^3 = MM_w\frac{W_n^3}{\rho_w} + MM_m\frac{M_n^3}{\rho_m}$	$V_n^3 = MM_w\frac{W_n^3}{\rho_w} + MM_m\frac{M_n^3}{\rho_m}$
$ln(1-\varphi_{p,n}) + \varphi_{p,n} + \chi_{FH,n}\varphi_{p,n}^2 = 0$	
$\chi_{FH,n} = \frac{1286.4}{T_n} - 3.02$	

As the reaction proceeds, the polymer molecules form a segregated phase, namely the polymer-rich phase (Phase 2). The appearance of this polymer-rich phase characterizes the beginning of the so called Stage 2. As $x_{f,n}$ represents the critical conversion (Equation (5.3)), then from $x_n > 0.001$ to $x_n \leq x_{f,n}$, Phase 1 and Phase 2 are in equilibrium, so that the concentrations remain constant until $x_{f,n}$ is reached (Kiparissides *et al.*, 1997). The fraction of polymer in Phase 2 (Equation (2)) depends on the reaction temperature in accordance with the Flory-Huggins equation, which depends on an interaction parameter ($\chi_{FH,n}$) (Xie *et al.*, 1991) (see Table 5.1). This stage is characterized by the agglomeration of small particles (domains) to originate larger porous polymer particles (Yuan *et al.*, 1991). As the conversion increases, the volume of the polymer-rich phase increases and monomer from Phase 1 is transferred to Phase 2 to maintain the equilibrium. As discussed in the previous paragraph $x_{f,n} \approx x_{s,n}$, consequently, the range of validity of the equilibrium calculations shown in Table 5.1 can be expressed in terms of $x_{s,n}$ without any significant loss of information.

When the critical conversion is surpassed, the monomer-rich phase disappears and the reaction continues in the polymer-rich phase only (Table 5.1). Since it is assumed that there is no gaseous phase present in the COBR, no pressure effect is expected to occur after disappearance of Phase 2, in opposition to the usual batch operation, as the monomer from the gas phase migrates to the polymer-rich phase after disappearance of the monomer-rich phase causing the sustained decrease of the reactor pressure. At this stage, the polymerization reaction becomes diffusion controlled due to the decreasing mobility of the reacting molecules due to the continuous increase in polymer concentration.

5.1.3 Mass Balances

Based on the assumed hypotheses and the schematic representation of the COBR shown in Figure 4.1, the model equations can be derived. Attention must be paid to the fact that three phases are considered. Consequently, the following differential equations represent the overall balances of each component, Equations (5.5)-(5.11):

$$\phi\left(n\right) = \begin{cases} 1 & \text{if } n = 1 \\ 0 & \text{otherwise} \end{cases} \tag{5.5}$$

$$\begin{aligned} \frac{dM_n}{dt} = m_m\phi(n) + \sum_{i=1}^{3}\Bigg[& F_{n-1}^i \frac{M_{n-1}^i}{V_{n-1}^i}(1-\phi(n)) + F_{b,n+1}^i \frac{M_{n+1}^i}{V_{n+1}^i}(1-\phi(k-n+1)) \\ & -F_n^i \frac{M_n^i}{V_n^i} - F_{b,n}^i \frac{M_n^i}{V_n^i}(1-\phi(n))\Bigg] - \sum_{i=i}^{2} k_p^i(T_n)\frac{M_n^i}{V_n^i}\frac{\lambda_{0,n}^i}{V_n^i}V_n^i \end{aligned} \tag{5.6}$$

$$\begin{aligned} \frac{dI_n}{dt} = m_i\phi(n) + \sum_{i=1}^{2}\Bigg[& F_{n-1}^i \frac{I_{n-1}^i}{V_{n-1}^i}(1-\phi(n)) + F_{b,n+1}^i \frac{I_{n+1}^i}{V_{n+1}^i}(1-\phi(k-n+1)) \\ & -F_n^i \frac{I_n^i}{V_n^i} - F_{b,n}^i \frac{I_n^i}{V_n^1}(1-\phi(n)) - k_d^i(T_n)I_n^i\Bigg] \end{aligned} \tag{5.7}$$

$$\begin{aligned} \frac{dP_n}{dt} = m_p\phi(n) + \sum_{i=1}^{2}\Bigg[& F_{n-1}^i \frac{P_{n-1}^i}{V_{n-1}^i}(1-\phi(n)) + F_{b,n+1}^i \frac{P_{n+1}^i}{V_{n+1}^i}(1-\phi(k-n+1)) \\ & -F_n^i \frac{P_n^i}{V_n^i} - F_{b,n}^i \frac{P_n^i}{V_n^i}(1-\phi(n)) + k_p^i(T_n)\frac{M_n^i}{V_n^i}\frac{\lambda_{0,n}^i}{V_n^i}V_n^i\Bigg] \end{aligned} \tag{5.8}$$

In Equation (5.8), the polymer in Phase 1 (P_n^1) corresponds to the living polymer chains. In other words, P_n^1 is equal to $\lambda_{0,n}^1$. However, in free radical polymerizations the concentration of living radicals is very low (Odian, 2004) and the lifetime of these radicals is normally of the order of a fraction of a second (Hutchinson and Penlidis, 2007). Consequently, it is fair to assume that $P_n^1 \ll P_n^2$ so that the overall polymer balance can be written as Equation (5.9).

$$\begin{aligned}\frac{dP_n}{dt} &= m_p\phi(n) + F_{n-1}^2\frac{P_{n-1}^2}{V_{n-1}^2}(1-\phi(n)) + F_{b,n+1}^2\frac{P_{n+1}^2}{V_{n+1}^2}(1-\phi(k-n+1)) \\ &\quad - F_n^2\frac{P_n^2}{V_n^2} - F_{b,n}^2\frac{P_n^2}{V_n^2}(1-\phi(n)) + \sum_{i=i}^{2} k_p^i(T_n)\frac{M_n^i}{V_n^i}\frac{\lambda_{0,n}^i}{V_n^i}V_n^i \end{aligned} \tag{5.9}$$

$$\begin{aligned}\frac{dW_n}{dt} &= m_w\phi(n) + F_{n-1}^3\frac{W_{n-1}^3}{V_{n-1}^3}(1-\phi(n)) + F_{b,n+1}^3\frac{W_{n+1}^3}{V_{n+1}^3}(1-\phi(k-n+1)) \\ &\quad - F_n^3\frac{W_n^3}{V_n^3} - F_{b,n}^3\frac{W_n^3}{V_n^3}(1-\phi(n)) \end{aligned} \tag{5.10}$$

$$\begin{aligned}\frac{dY_n}{dt} &= m_y\phi(n) + F_{n-1}^3\frac{Y_{n-1}^3}{V_{n-1}^3}(1-\phi(n)) + F_{b,n+1}^3\frac{Y_{n+1}^3}{V_{n+1}^3}(1-\phi(k-n+1)) \\ &\quad - F_n^3\frac{Y_n^3}{V_n^3} - F_{b,n}^3\frac{Y_n^3}{V_n^3}(1-\phi(n)) \end{aligned} \tag{5.11}$$

By assuming that the tanks are completely filled, so that the tanks volumes remain constant, Equation (5.12) can be derived to represent the output flow rate in each tank. The complete derivation of Equations (5.12) to (5.25) can be found in the Appendix C.

$$\begin{aligned}&\left(\Phi_n^1\alpha_n + \Phi_n^2\beta_n + \Phi_n^3\gamma_n\right)F_n = \left(\frac{MM_m}{\rho_m}m_m + \frac{MM_w}{\rho_w}m_w + \frac{MM_m}{\rho_p}m_p\right)\phi(n) \\ &+ \left(\Phi_{n-1}^1\alpha_{n-1} + \Phi_{n-1}^2\beta_{n-1} + \Phi_{n-1}^3\gamma_{n-1}\right)F_{n-1}(1-\phi(n)) \\ &+ \left(\Phi_{n+1}^1\alpha_{n+1} + \Phi_{n+1}^2\beta_{n+1} + \Phi_{n+1}^3\gamma_{n+1}\right)F_{b,n+1}(1-\phi(k-n+1)) \\ &- \left(\Phi_n^1\alpha_n + \Phi_n^2\beta_n + \Phi_n^3\gamma_n\right)F_{b,n}(1-\phi(n)) + \xi_n \end{aligned} \tag{5.12}$$

$$\alpha_n = \frac{MM_m}{\rho_m}\frac{M_n^1}{V_n^1} \tag{5.13}$$

$$\beta_n = \frac{MM_m}{\rho_m}\frac{M_n^2}{V_n^2} + \frac{MM_m}{\rho_p}\frac{P_n^2}{V_n^2} \tag{5.14}$$

$$\gamma_n = \frac{MM_m}{\rho_m}\frac{M_n^3}{V_n^3} + \frac{MM_w}{\rho_w}\frac{W_n^3}{V_n^3} \tag{5.15}$$

$$\xi_n = \left(\frac{MM_m}{\rho_p} - \frac{MM_m}{\rho_m}\right)\left(\sum_{i=i}^{2} k_p^i(T_n)\frac{M_n^i}{V_n^i}\frac{\lambda_{0,n}^i}{V_n^i}V_n^i\right) \tag{5.16}$$

$$\Phi_n^1 = \frac{V_n^1}{V_n} \tag{5.17}$$

$$\Phi_n^2 = \frac{V_n^2}{V_n} \tag{5.18}$$

$$\Phi_n^3 = \frac{V_n^3}{V_n} \tag{5.19}$$

$$F_n^1 = F_n\Phi_n^1 \tag{5.20}$$

$$F_n^2 = F_n\Phi_n^2 \tag{5.21}$$

$$F_n^3 = F_n\Phi_n^3 \tag{5.22}$$

$$F^1_{b,n} = F_{b,n}\Phi^1_n \tag{5.23}$$

$$F^2_{b,n} = F_{b,n}\Phi^2_n \tag{5.24}$$

$$F^3_{b,n} = F_{b,n}\Phi^3_n \tag{5.25}$$

5.1.4 Moment Balances

The method of moments constitutes a well-known alternative solution to represent the main averages of the molar mass distribution when the full calculation of the molar mass distribution (MMD) is difficult or impractical (Saldívar-Guerra, 2020). As recently reviewed by Zapata-González and Saldívar-Guerra (2023), the representation of the whole MMD normally requires the solution of a large number of differential equations whose complexity can be challenging, depending on the kinetic mechanism. In these cases, the method of moments can constitute a powerful tool to calculate the averages of the MMD. The derivation of the moment equations for the kinetic mechanism of PVC polymerization presented in Chapter 1 is shown in the Appendix A. Based on the proposed COBR representation, the following differential equations (Equation (5.26)-(5.31)) can represent the moment balances in each tank. The following Equations apply for $i = 1, 2$.

Moments of living polymer chains

$$\begin{aligned}\frac{d\lambda^i_{0,n}}{dt} &= F^i_{n-1}\frac{\lambda^i_{0,n-1}}{V^i_{n-1}}(1-\phi(n)) + F^i_{b,n+1}\frac{\lambda^i_{0,n+1}}{V^i_{n+1}}(1-\phi(k-n+1)) \\ &- F^i_n\frac{\lambda^i_{0,n}}{V^i_n} - F^i_{b,n}\frac{\lambda^i_{0,n}}{V^i_n}(1-\phi(n)) + 2f^i_n k^i_d(T_n)I^i_n \\ &- \left(k^i_{tc}(T_n) + k^i_{td}(T_n)\right)\frac{\lambda^i_{0,n}}{V^i_n}\frac{\lambda^i_{0,n}}{V^i_n}V^i_n\end{aligned} \tag{5.26}$$

$$\frac{d\lambda^i_{1,n}}{dt} = F^i_{n-1}\frac{\lambda^i_{1,n-1}}{V^i_{n-1}}(1-\phi(n)) + F^i_{b,n+1}\frac{\lambda^i_{1,n+1}}{V^i_{n+1}}(1-\phi(k-n+1))$$
$$- F^i_n\frac{\lambda^i_{1,n}}{V^i_n} - F^i_{b,n}\frac{\lambda^i_{1,n}}{V^i_n}(1-\phi(n)) + 2f^i_n k^i_d(T_n)I^i_n + k^i_p(T_n)\frac{M^i_n}{V^i_n}\frac{\lambda^i_0}{V^i_n}V^i_n$$
$$+ k^i_{tm}(T_n)\frac{M^i_n}{V^i_n}\left(\frac{\lambda^i_{0,n}}{V^i_n} - \frac{\lambda^i_{1,n}}{V^i_n}\right)V^i_n - \left(k^i_{tc}(T_n) + k^i_{td}(T_n)\right)\frac{\lambda^i_{0,n}}{V^i_n}\frac{\lambda^i_{1,n}}{V^i_n}V^i_n \quad (5.27)$$

$$\frac{d\lambda^i_{2,n}}{dt} = F^i_{n-1}\frac{\lambda^i_{2,n-1}}{V^i_{n-1}}(1-\phi(n)) + F^i_{b,n+1}\frac{\lambda^i_{2,n+1}}{V^i_{n+1}}(1-\phi(k-n+1))$$
$$- F^i_n\frac{\lambda^i_{2,n}}{V^i_n} - F^i_{b,n}\frac{\lambda^i_{2,n}}{V^i_n}(1-\phi(n)) + 2f^i_n k^i_d(T_n)I^i_n$$
$$+ k^i_p(T_n)\frac{M^i_n}{V^i_n}\left(\frac{2\lambda^i_{1,n}}{V^i_n} + \frac{\lambda^i_{0,n}}{V^i_n}\right)V^i_n + k^i_{tm}(T_n)\frac{M^i_n}{V^i_n}\left(\frac{\lambda^i_{0,n}}{V^i_n} - \frac{\lambda^i_{2,n}}{V^i_n}\right)V^i_n$$
$$- \left(k^i_{tc}(T_n) + k^i_{td}(T_n)\right)\frac{\lambda^i_{0,n}}{V^i_n}\frac{\lambda^i_{2,n}}{V^i_n}V^i_n \quad (5.28)$$

Moments of dead polymer chains

$$\frac{d\mu^2_{0,n}}{dt} = F^2_{n-1}\frac{\mu^2_{0,n-1}}{V^2_{n-1}}(1-\phi(n)) + F^2_{b,n+1}\frac{\mu^2_{0,n+1}}{V^2_{n+1}}(1-\phi(k-n+1))$$
$$- F^2_n\frac{\mu^2_{0,n}}{V^2_n} - F^2_{b,n}\frac{\mu^2_{0,n}}{V^2_n}(1-\phi(n))$$
$$+ \sum_{i=1}^{2}\left[k^i_{tm}(T_n)\frac{M^i_n}{V^i_n}\frac{\lambda^i_{0,n}}{V^i_n}V^i_n + \left(\frac{1}{2}k^i_{tc}(T_n) + k^i_{td}(T_n)\right)\frac{\lambda^i_{0,n}}{V^i_n}\frac{\lambda^i_{0,n}}{V^i_n}V^i_n\right] \quad (5.29)$$

$$\frac{d\mu^2_{1,n}}{dt} = F^2_{n-1}\frac{\mu^2_{1,n-1}}{V^2_{n-1}}(1-\phi(n)) + F^2_{b,n+1}\frac{\mu^2_{1,n+1}}{V^2_{n+1}}(1-\phi(k-n+1))$$
$$- F^2_n\frac{\mu^2_{1,n}}{V^2_n} - F^2_{b,n}\frac{\mu^2_{1,n}}{V^2_n}(1-\phi(n))$$
$$+ \sum_{i=1}^{2}\left[k^i_{tm}(T_n)\frac{M^i_n}{V^i_n}\frac{\lambda^i_{1,n}}{V^i_n}V^i_n + \left(k^i_{tc}(T_n) + k^i_{td}(T_n)\right)\frac{\lambda^i_{0,n}}{V^i_n}\frac{\lambda^i_{1,n}}{V^i_n}V^i_n\right] \quad (5.30)$$

$$\frac{d\mu^2_{2,n}}{dt} = F^2_{n-1}\frac{\mu^2_{2,n-1}}{V^2_{n-1}}(1-\phi(n)) + F^2_{b,n+1}\frac{\mu^2_{2,n+1}}{V^2_{n+1}}(1-\phi(k-n+1))$$
$$- F^2_n\frac{\mu^2_{2,n}}{V^2_n} - F^2_{b,n}\frac{\mu^2_{2,n}}{V^2_n}(1-\phi(n))...$$

$$+\sum_{i=1}^{2}\left[k_{td}^{i}(T_n)\frac{\lambda_{0,n}^{i}}{V_n^i}\frac{\lambda_{2,n}^{i}}{V_n^i}V_n^i+k_{tm}^{i}(T_n)\frac{M_n^i}{V_n^i}\frac{\lambda_{2,n}^{i}}{V_n^i}V_n^i\right.$$
$$\left.+k_{tc}^{i}(T_n)\left(\frac{\lambda_{0,n}^{i}}{V_n^i}\frac{\lambda_{2,n}^{i}}{V_n^i}+\frac{\lambda_{1,n}^{i}}{V_n^i}\frac{\lambda_{1,n}^{i}}{V_n^i}\right)V_n^i\right] \tag{5.31}$$

With the statistical moments of the MMD, the average molar masses of the polymer, the K-Value (VK), and the polydispersity index (PDI) can be calculated as shown in Equations (5.32) through (5.35), respectively. The K-Value correlation (Equation (5.34)) is due to the work of Abi-Ramia (2012) and Castor (2014).

$$Mn_n = MM_m\frac{\sum_{i=1}^{2}\lambda_{1,n}^{i}+\mu_{1,n}}{\sum_{i=1}^{2}\lambda_{0,n}^{i}+\mu_{0,n}} \tag{5.32}$$

$$Mw_n = MM_m\frac{\sum_{i=1}^{2}\lambda_{2,n}^{i}+\mu_{2,n}}{\sum_{i=1}^{2}\lambda_{1,n}^{i}+\mu_{1,n}} \tag{5.33}$$

$$VK_n = 0.8482Mw_n^{0.385611} \tag{5.34}$$

$$PDI_n = \frac{Mw_n}{Mn_n} \tag{5.35}$$

5.1.5 Energy Balances

Temperature is a crucial variable for polymerization systems. In order to represent the variations of the reactor temperature as a function of the polymerization conditions, the energy balance in Equation (5.36) was included in the proposed modeling approach. The derivation of Equation (5.36) can be very intuitive if Figure 4.1 (in Chapter 4) is used as reference. Similarly, Equation (5.41) can be derived to describe the energy balance in the multiple reactor jackets.

$$cp_{s,n}\frac{dT_n}{dt} = \phi(n)\left[\int_{T_n}^{T_{in}}\Big(m_w cp_w(T) + m_m cp_m(T) + m_p cp_p(T)\Big)dT\right]$$
$$+ (1-\phi(n))\left(\sum_{i=1}^{3} F_{n-1}^{i}\frac{M_{n-1}^{i}}{V_{n-1}^{i}}\right)\int_{T_n}^{T_{n-1}} cp_m(T)dT$$
$$+ (1-\phi(n))\left(F_{n-1}^{2}\frac{P_{n-1}^{2}}{V_{n-1}^{2}}\right)\int_{T_n}^{T_{n-1}} cp_p(T)dT$$
$$+ (1-\phi(n))\left(F_{n-1}^{3}\frac{W_{n-1}^{3}}{V_{n-1}^{3}}\right)\int_{T_n}^{T_{n-1}} c_{p,w}(T)dT$$
$$+ (1-\phi(k-n+1))\left(\sum_{i=1}^{3} F_{b,n+1}^{i}\frac{M_{n+1}^{i}}{V_{n+1}^{i}}\right)\int_{T_n}^{T_{n+1}} cp_m(T)dT$$
$$+ (1-\phi(k-n+1))\left(F_{b,n+1}^{2}\frac{P_{n+1}^{2}}{V_{n+1}^{2}}\right)\int_{T_n}^{T_{n+1}} cp_p(T)dT$$
$$+ (1-\phi(k-n+1))\left(F_{b,n+1}^{3}\frac{W_{n+1}^{3}}{V_{n+1}^{3}}\right)\int_{T_n}^{T_{n+1}} cp_w(T)dT$$
$$+ (-\Delta H)\sum_{i=1}^{2} k_p^i(T_n)\frac{M_n^i}{V_n^i}\frac{\lambda_{0,n}^i}{V_n^i}V_n^i + (U_n\times 10^{-3})A_n(T_n - T_{j,n}) \tag{5.36}$$

$$cp_{s,n} = M_n cp_m(T_n) + P_n cp_p(T_n) + W_n cp_w(T_n) \tag{5.37}$$

$$A_n = \pi d_{r,ext} l_n \tag{5.38}$$

$$l_n = \frac{L}{k} \tag{5.39}$$

$$L = \sum_{z=1}^{nz} L_z \tag{5.40}$$

$$\frac{\rho_w V_{j,n} cp_w(T_{j,n})}{MM_w}\frac{dT_{j,n}}{dt} = m_j\left(\Omega(n)\int_{T_{j,n}}^{T_{j,in,z}} \underline{cp}_w(T)dT... \right.$$
$$\left. +(1-\Omega(n))\int_{T_{j,n}}^{T_{j,n-1}} cp_w(T)dT\right) + (U_n\times 10^{-3})A_n(T_n - T_{j,n}) \tag{5.41}$$

If n is in section z then:

$$m_j = m_{j,z} \tag{5.42}$$

$$\Omega(n) = \begin{cases} 1 & \text{if n is the first tank in the zone} \\ 0 & \text{otherwise} \end{cases} \tag{5.43}$$

5.1.6 Reaction Rates

The diffusion phenomena play an important role in the reaction rates in free radical polymerizations (Maschio and Moutier, 1989). The Free Volume Theory (Vrentas and Duda, 1977; Bueche, 1962) is usually employed to describe the diffusion limitation effect on the reaction rates. The free volume is a parameter that can be used to describe the mobility of the polymer and monomer molecules and, consequently, to model the decrease of rates of termination ('gel effect')(O'neil *et al.*, 1998; Maschio and Moutier, 1989). As monomer is converted to polymer and the reacting media becomes more viscous, the free volume diminishes considerably. The rates of propagation can also be influenced by diffusion limitations ('glass effect') when the polymerization temperature is below the glass transition temperature of the polymer (Kiparissides, 1996). More specifically, as the mobility of the monomer molecules also become impaired, the propagation rate falls considerably causing the reaction to "freeze" at conversions below 100%(Achilias and Kiparissides, 1992). Furthermore, the initiator efficiency can also be impaired at high polymer concentrations ('cage effect'). To account for these effects, the free volume was taken into consideration in the modeling approach (Equations (5.44)–(5.48)) (Xie *et al.*, 1991a; Fedors, 1979; Reding *et al.*, 1979; Ceccorulli *et al.*, 1977).

$$T_{gm,n} = 70.74 \tag{5.44}$$

$$T_{gp,n} = 87.1 - 0.132(T_n - 273.15) + 273.15 \tag{5.45}$$

$$V_{fm,n} = 0.025 + 9.98 \times 10^{-4}(T_n - T_{gm,n}) \tag{5.46}$$

$$V_{fp,n} = 0.025 + 5.47 \times 10^{-4}(T_n - T_{gp,n}) \tag{5.47}$$

$$V_{f,n} = V_{fp,n}\varphi_{p,n} + V_{fm,n}(1 - \varphi_{p,n}) \tag{5.48}$$

The kinetic parameters used in this chapter are the same shown in Chapter 2 and used to describe industrial scale batch reactors (Silva *et al.*, 2023). More specifically, k_t and k_p were taken from the works of Burnett and Wright (1954) and Sidiropoulou and Kiparissides (1990), respectively. k_{tm} was taken from Abdel-Alim and Hamielec (1972). In the rate equations presented below, Equations (5.49)–(5.56), the value of the universal gas constant R is already included in the exponential term. Furthermore, it is considered that $k_{tc} = 0.25k_t$ and $k_{td} = 0.75k_t$ (Park and Smith, 1970).

If $x_n \leq x_{f,n}$

$$k_t^1(T_n) = 1.3 \times 10^{12} exp\left(\frac{-2113.7}{T_n}\right) \tag{5.49}$$

$$k_t^2(T_n) = k_{t,ref}(T_n) = k_t^1(T_n)/F(T_n) \tag{5.50}$$

$$k_p^i(T_n) = k_{p,ref}(T_n) = 5.0 \times 10^7 exp\left(\frac{-3320}{T_n}\right) \tag{5.51}$$

$$k_{tm}^i(T_n) = k_{tm,ref}(T_n) = 5.78 exp\left(\frac{-2768}{T_n}\right) k_p^i(T_n) \tag{5.52}$$

$$k_d^i(T_n) = k_{d,ref}(T_n) = k_{d0} exp\left(\frac{-E_0}{T_n}\right) \tag{5.53}$$

$$k_{td}^{i}(T_n) = 0.75 k_{t}^{i}(T_n) \tag{5.54}$$

$$k_{tc}^{i}(T_n) = 0.25 k t_{t}^{i}(T_n) \tag{5.55}$$

$$f_{n}^{i} = f_{ref} \tag{5.56}$$

At conversions higher than x_f, the reaction rates become diffusion controlled and the reaction rates (Equations (5.57)–(5.63)) become dependent upon the free volume and parameters A^*, B^*, B_f^* and C^* as described by Equations (5.64)–(5.67) (Silva *et al.*, 2023).

If $x_n > x_{f,n}$

$$k_{t}^{2}(T_n) = k_{t,ref}(T_n) exp\left(-A_{n}^{*}\left(\frac{1}{V_{f,n}} - \frac{1}{V_{f,xf,n}}\right)\right) \tag{5.57}$$

$$k_{p}^{2}(T_n) = k_{p,ref}(T_n) exp\left(-B_{n}^{*}\left(\frac{1}{V_{f,n}} - \frac{1}{V_{f,xf,n}}\right)\right) \tag{5.58}$$

$$k_{tm}^{2}(T_n) = k_{tm,ref}(T_n) exp\left(-B_{n}^{*}\left(\frac{1}{V_{f,n}} - \frac{1}{V_{f,xf,n}}\right)\right) \tag{5.59}$$

$$k_{p}^{2}(T_n)(f_{n}^{2})^{1/2} = \left(k_{p,ref}(T_n) f_{ref}^{1/2}\right) exp\left(-B_{f,n}^{*}\left(\frac{1}{V_{f,n}} - \frac{1}{V_{f,xf,n}}\right)\right) \tag{5.60}$$

$$k_{d}^{2}(T_n) = k_{t,ref}(T_n) exp\left(-C_{n}^{*}\left(\frac{1}{V_{f,n}} - \frac{1}{V_{f,xf,n}}\right)\right) \tag{5.61}$$

$$k_{td}^2(T_n) = 0.75 k_{t,ref}(T_n) \tag{5.62}$$

$$k_{tc}^2(T_n) = 0.25 k_{t,ref}(T_n) \tag{5.63}$$

$$A_n^* = 6.64 \times 10^6 exp\left(\frac{-4850}{T_n}\right) \tag{5.64}$$

$$B_n^* = 1.85 \times 10^3 exp\left(\frac{-2450}{T_n}\right) \tag{5.65}$$

$$B_{f,n}^* = 4.01 \times 10^4 exp\left(\frac{-4081}{T_n}\right) \tag{5.66}$$

$$C_n^* = 477 exp\left(\frac{-2681}{T_n}\right) \tag{5.67}$$

5.1.7 Dimensionless Groups

Three dimensionless groups are commonly used to describe the oscillatory flow in baffled tubes under oscillatory conditions: the net Reynolds number, the oscillatory Reynolds number and the Strouhal number (Equations (5.68)–(5.70), respectively) (Avila *et al.*, 2022; Brunold *et al.*, 1989; Howes *et al.*, 1991, Mackley and Ni, 1991; Ni and Gough, 1997). The net Reynolds number can be understood as the ratio of inertial forces to viscous forces. In comparison to the conventional net Reynolds number that accounts for the continuous flow component, the oscillatory Reynolds number takes into account the frequency and amplitude of oscillation and describes the intensity of mixing (Avila *et al.*, 2022). The Strouhal number as defined in Equation (5.70) represents the ratio of tube diameter to oscillation amplitude (Stonestreet and Van der Veeken, 1999). Ni and Gough (1997) argued against these groups affirming that none of them includes the baffle orifice diameter and the baffle spacing, in spite of the importance of these two geometric parameters for the development of flow patterns. Equation (5.71) represents the net flow velocity

based on the cross section area of the reactor (Equation (5.72)).

$$Re_{s,n} = \frac{\rho_{s,n} v_{s,n} d_{r,int}}{\eta_{s,n}} \tag{5.68}$$

$$Re_{o,n} = \frac{2\pi f_o \chi_o \rho_{s,n} d_{r,int}}{\eta_{s,n}} \tag{5.69}$$

$$St = \frac{d_{r,int}}{4\pi\chi_o} \tag{5.70}$$

$$v_{s,n} = \begin{cases} \frac{F_n - F_{b,k+1}}{C_n} & \text{if } n < k \\ \frac{F_n}{C_n} & \text{if } n = k \end{cases} \tag{5.71}$$

$$C_n = \frac{\pi d_{r,int}^2}{4} \tag{5.72}$$

Regarding the continuous flow in circular tubes, three regimes can be usually identified depending on the value of the net Reynolds number (Green and Perry, 2008). When $Re \leq 2300$ the regime is laminar; whereas $Re > 10000$ characterizes the fully turbulent region. Additionally, $2300 < Re \leq 10000$ characterizes the transition regime. On the other hand, as the oscillatory Reynolds number depends on the oscillation velocity instead of the net velocity of the flow, the thresholds that characterize the oscillatory flow are different. For instance, Stonestreet and Van der Veeken (1999) identified that for $Re_o \leq 250$ the flow is 2D axi-symmetric with low intensity mixing, whereas $Re_o > 250$ the flow becomes 3D non axi-symmetric and for $Re_o \geq 2000$ the flow becomes effectively turbulent.

In addition to the three previously mentioned dimensionless groups, the so called velocity ratio, Equation (5.73), is employed as a design variable (Stonestreet and Van der Veeken, 1999; Stonestreet and Harvey, 2002). In practice, it is desirable to have velocity ratios at least greater than 2 so that the oscillatory flow governs the mixing regime, guaranteeing that the flow will be fully reversing (Harvey *et al.*, 2001).

$$\Psi_n = \frac{Re_{o,n}}{Re_{s,n}} \tag{5.73}$$

5.1.8 Heat Transfer

One of the most remarkable characteristics of the COBR is its higher heat transfer rates in comparison to other conventional tubular reactors (Mackley *et al.*, 1990; Mackley and Stonestreet, 1995; Law *et al.*, 2018). In order to represent the overall heat transfer coefficient in the proposed modeling approach, it becomes necessary to model the heat transfer coefficient at the tube side, at the jacket side and to consider the resistance to heat transfer due to the wall. In Chapter 3, a set of correlations proposed to describe the Nusselt number in the COBR were shown. The correlation proposed by Law *et al.* (2018) was selected to represent the Nusselt number at the tube side (Equations (5.74) and (5.75)) as it is expected to remain valid over a broad range of fluid properties and operation conditions. In these correlations, Pr represents the Prandtl number of the suspension (Equation (5.76)).

- $0 \leq Re_{o,n} \leq 1300$

$$Nu_{s,n} = 0.0022 Re_{s,n}^{0.7} Pr_{s,n}^{0.3} Re_{o,n}^{0.44} \tag{5.74}$$

- $Re_{o,n} \geq 1300$

$$Nu_{s,n} = 0.52 Re_{s,n}^{0.7} Pr_{s,n}^{0.3} \tag{5.75}$$

$$Pr_{s,n} = \frac{cp_{s,n}\eta_{s,n}}{\sigma_{s,n}} \tag{5.76}$$

According to Gnielinski (2010), in problems involving the heat transfer in annular concentric tubes, the following boundary conditions can often be applied:

- Heat transfer from the inner tube, with the outer tube insulated;
- Heat transfer from the outer tube, with the inner tube insulated;
- Heat transfer from both inner and outer tubes with both walls at the same temperature.

The Reynolds number in annular regions, Equation (5.77), is slightly different from its counterpart defined for circular ducts. The equivalent of the duct diameter in circular ducts is the hydraulic diameter in annular geometries, which is the difference between the outer diameter (jacket) and the inner diameter (reactor) (Equation (5.78)). All the properties regarding the jacket side must be calculated at the temperature of the jacket.

$$Re_{j,n} = \frac{\rho_w v_{j,z} d_h}{\eta_{w,j,n}} \tag{5.77}$$

$$d_h = d_j - d_{r,ext} \tag{5.78}$$

$$v_{j,z} = \frac{m_{w,j} MM_w}{\rho_w A_j} \tag{5.79}$$

$$A_j = \frac{\pi}{4}\left(d_j^2 - d_{r,ext}^2\right) \tag{5.80}$$

Martin (1990) apud Gnielinski (2010) developed the following correlation, Equation (5.81), for the jacket side Nusselt number ($Nu_{j,n}$) employing the first boundary condition and assuming thermally and hydrodynamically developed laminar flow:

- $Re_{j,n} \leq 2300$

$$Nu_1 = 3.66 + 1.2\left(\frac{d_{r,ext}}{d_j}\right)^{-0.8} \tag{5.81}$$

$$Nu_{j,n} = Nu_1 \tag{5.82}$$

In the transition regime, Gnielinski (2010) suggested the following correlations to calculate the Nusselt number (Equation (5.88)):

- $2300 < Re_{j,n} < 10^4$

$$Nu_2 = f_g \sqrt[3]{\frac{Re_{j,n} Pr_{j,n} d_h}{l_n}} \tag{5.83}$$

$$Nu_3 = \left[\frac{2}{1 + 22Pr_{j,n}}\right]^{1/6} \left(\frac{Re_{j,n} Pr_{j,n} d_h}{l_n}\right)^{1/2} \tag{5.84}$$

$$f_g = 1.615 \left[1 + 0.14 \left(\frac{d_{r,ext}}{d_j}\right)^{-1/2}\right] \tag{5.85}$$

$$Nu_{lam} = \left(Nu_1^3 + Nu_2^3 + Nu_3^3\right)^{1/3} \tag{5.86}$$

$$\Lambda = \frac{Re_{j,n} - 2300}{10^4 - 2300} \tag{5.87}$$

$$Nu_{j,n} = (1 - \Lambda) Nu_{lam}(Re_{j,n} = 2300) + \Lambda Nu_{turb}(Re_{j,n} = 10^4) \tag{5.88}$$

When the flow is in the fully turbulent regime, Equations (5.89) and (5.92) can be used to describe the Nusselt number (Gnielinski, 2009). f_{Nu}, Equation (5.90), is the so called friction factor for turbulent flow in smooth tubes (Gnielinski, 2007). The ξ factor was estimated by Pethukov and Roizen (1964), as described in Equation (5.91).

- $Re_{j,n} \geq 10^4$

$$Nu_{turb} = \frac{(f_{Nu}/8) Re_{j,n} Pr_{j,n}}{1 + 12.7\sqrt{f_{Nu}/8}(Pr_{j,n}^{2/3} - 1)} \left[1 + \left(\frac{d_h}{l_n}\right)^{2/3}\right] \xi \tag{5.89}$$

$$f_{Nu} = \left(1.8 \log_{10} Re_{j,n} - 1.5\right)^{-2} \tag{5.90}$$

$$\xi = 0.86 \left(\frac{d_{r,ext}}{d_j}\right)^{-0.16} \tag{5.91}$$

$$Nu_{j,n} = Nu_{turb} \tag{5.92}$$

By using the definitions of the Nusselt number in the reactor and in the jacket (Equations (5.93) and (5.94)), the overall heat transfer coefficient between the jacket and the reactor can be calculated according to Equation (5.95). Additionally, the suspension properties can be calculated with the equations presented in Tables 5.2 and 5.3.

$$Nu_{s,n} = \frac{h_{s,n} d_{r,int}}{\sigma_{s,n}} \tag{5.93}$$

$$Nu_{j,n} = \frac{h_{j,n} d_h}{\sigma_{w,j,n}} \tag{5.94}$$

$$\frac{1}{U_n} = \frac{1}{h_{s,n}} + \frac{d_{r,int}}{d_{r,ext} h_{j,n}} + d_{r,int} \frac{ln(d_{r,ext}/d_{r,int})}{2k_{wall}} \tag{5.95}$$

5.1.9 Regulatory Control

Polymerization reactions are prone to instabilities mostly related to thermal, viscous, hydrodynamic and kinetic effects (Hutchinson and Penlidis, 2007; Leiza and Pinto, 2007). The safety of operation of unstable processes is guaranteed by regulatory control loops. This type of control loop keeps the main process variables at their setpoints, guaranteeing the safe operation (Skogestad and Postlethwaite, 2005; Seborg *et al.*, 2010). In order to maintain the reactor at the desired temperature, nz proportional-integral controllers ($z = 1, 2, .., nz$) were implemented (Equation (5.96)), one for each straight section in the heating, reaction and cooling zones as described in Figure 3.7. The manipulated and controlled variables are the jacket inlet temperatures ($T_{j,in,z}$) and the temperatures at specified positions in each zone z ($T_{m,z}$), respectively. The controllers gains are reported in Table 5.3.

Table 5.2: Suspension properties (poly(vinyl chloride)/vinyl chloride/water system).

Equation	Reference
$\eta_{s,n} = \frac{\eta_{c,n}}{1-\Phi_{d,n}}\left(1+\frac{1.5\Phi_{d,n}\eta_{d,n}}{\eta_{c,n}+\eta_{d,n}}\right)$	Vermeulen *et al.* (1955)
$\Phi_{d,n} = \Phi_n^1 + \Phi_n^2$	This work
$\Phi_{c,n} = 1 - \Phi_{d,n}$	This work
$\eta_{c,n} = \eta_{w,n}\left(1+\frac{\Phi_{d,n}[\eta]_{pva}C_{pva,n}}{1-0.45[\eta]_{pva}C_{pva,n}}\right)$	Okaya (1992) apud Kiparissides and Pladis (2022)
$C_{pva,n} = Y_n^3/V_n^3$	
$\eta_{d,n} = \eta_{m,n}\left[1+2.5\Phi_{eff,n}+6.2(\Phi_{eff,n})^2\right];\ \ \Phi_{eff,n} = 1.8\Phi_{d,p,n}$	Kiparissides and Pladis (2022), Batchelor and Green (1972)
$\frac{1}{\rho_{d,n}} = \frac{1-x_n}{\rho_m} + \frac{x_n}{\rho_p}$	Bouyatiotis and Thornton (1967)
$\rho_{s,n} = \Phi_{d,n}\rho_{d,n} + (1-\Phi_{d,n})\rho_{w,n}$	Maggioris *et al.* (2002)
$\underline{cp}_{s,n} = \sum_{e=m,w,p}\omega_e\underline{cp}_e(T_n)$	Green and Perry (2008)
$\sigma_{d,n} = \sum_{a=(m,p)}\sum_{e=(m,p)}\Phi_{d,a,n}\Phi_{d,e,n}\frac{2\sigma_a(T_n)\sigma_e(T_n)}{\sigma_a(T_n)+\sigma_e(T_n)}$	Li (1976)
$\frac{\sigma_{s,n}}{\sigma_{w,n}} = \frac{2+\frac{\sigma_{d,n}}{\sigma_{w,n}}-2\Phi_n^3\left(1-\frac{\sigma_{d,n}}{\sigma_{w,n}}\right)}{2+\frac{\sigma_{d,n}}{\sigma_{w,n}}+\Phi_n^3\left(1-\frac{\sigma_{d,n}}{\sigma_{w,n}}\right)}$	Wieme *et al.* (2007), Levy (1981), Wang *et al.* (2006)
$\sigma_{\sigma,n} = \sigma_{\sigma,ref,n} - K_{\sigma,n}\frac{K_{A,n}C_{pva}}{1+K_{A,n}C_{pva}}$	Lazrak *et al.* (1998)

Table 5.3: Additional constitutive relationships and parameters (poly(vinyl chloride)/vinyl chloride/water system).

Equation	Units	Reference
$\eta_{m,n} = exp(0.26297 + \frac{276.55}{T_n} - 1.7282ln(T_n))$	[kg m^{-1} s^{-1}]	Green and Perry (2008)
$\log_{10}(\eta_{w,n}) = -4.64 + \frac{262.37}{T_n - 133.98}$	[kg m^{-1} s^{-1}]	Korosi and Fabuss (1968)
$cp_m(T_n) = -10.32 + 0.322T_n$	[kJ kmol^{-1} K^{-1}]	Green and Perry (2008)
$cp_p(T_n) = 10 + 0.166T$	[kJ kmol^{-1} K^{-1}]	Chang (1977)
$cp_w(T_n) = 276.37 - 2.09T_n + 8.125 \times 10^{-3}T_n^2$ $- 1.41 \times 10^{-5}T_n^3 + 9.37 \times 10^{-9}T_n^4$	[kJ kmol^{-1} K^{-1}]	Green and Perry (2008)
$\sigma_m(T_n) = 0.2333 - 3.92 \times 10^{-4}T_n$	[J s^{-1} m^{-1} K^{-1}]	Green and Perry (2008)
$\sigma_p(T_n) = 0.166$	[J s^{-1} m^{-1} K^{-1}]	Kiparissides *et al.* (1997)
$\sigma_w(T_n) = -0.432 + 5.7255 \times 10^{-3}T_n$ $- 8.078 \times 10^{-6}T_n^2 + 1.861 \times 10^{-9}T_n^3$	[J s^{-1} m^{-1} K^{-1}]	Green and Perry (2008)
ΔH = -96000	[kJ kmol^{-1} K^{-1}]	Collins *et al.* (1999)
$[\eta]_{pva} = 1.332 \times 10^{-4}MW_{pva}^{0.566}$	[m^3 kg^{-1}]	Nagy (1993)
$\rho_m = 840$, $\rho_p = 1380$, $\rho_w = 999$ (at x K)	[kg m^{-3}]	Green and Perry (2008)
$MM_m = 62.498$, $MM_w = 18.0$	[kg kmol^{-1}]	Green and Perry (2008)
$R = 8.314$	[kJ kmol^{-1} K^{-1}]	Green and Perry (2008)
$k_{sol} = 0.0088$	[kg kg^{-1}]	Nilsson *et al.* (1978)
$k_{wall} = 1.09$ (borosilicate glass)	[J s^{-1} m^{-1} K^{-1}]	Green and Perry (2008)
$K_c = -0.5$	[-]	This work
$\tau_i = 300$	[s]	This work
$f = 0.8$	[-]	This work
$F(T_n)^{1/2} = 41.2 - 0.0104(T_n - 273.15)^2 + 0.2656(T_n - 273.15)$	[-]	Silva *et al.* (2023)
$\sigma_{\sigma,ref,n} = -4.41 \times 10^{-5}T_n + 2.7 \times 10^{-2}$	[N m^{-1}]	fitted with data from Lazrak *et al.* (1998)
$K_{A,n} = 6.637 \times 10^{-6}T_n + 8.122 \times 10^{-3}$	[m^3 kg^{-1}]	fitted with data from Lazrak *et al.* (1998)
$K_{\sigma,n} = 1.042 \times 10^{-4}T_n + 2.519 \times 10^{-2}$	[N m^{-1}]	fitted with data from Lazrak *et al.* (1998)

$$T_{j,in,z} = T_{j,in,ref} + K_c \left[(T_{m,z} - T_{sp,z}) + \frac{1}{\tau_i} \int_0^t (T_{m,z} - T_{sp,z})\, dt \right] \tag{5.96}$$

By defining E_z (error) as $E_z = T_{m,z} - T_{sp,z}$, Equation (5.96) becomes:

$$T_{j,in,z} = T_{j,in,ref} + K_c \left[E_z + \frac{1}{\tau_i} \int_0^t E_z dt \right] \tag{5.97}$$

By appending E_z as a state variable in the system of differential-algebraic equations and providing an initial condition, the value of the integral in Equation (5.97) is obtained after integration until time t. Consequently, the value of the manipulated variable can be explicitly calculated. The system of algebraic-differential equations was implemented and solved in a Fortran environment with the DASSL solver (Petzold, 1982) with absolute tolerances of 1×10^{-7} for all the variables.

5.2 Results and Discussion

5.2.1 Effect of Backflow and Number of Tanks

In this subsection, a convergence analysis of the model is performed. The main goal is to investigate the model robustness. Thus, the effects of its two main parameters, i.e., the number of tanks (k) and the backflow rate (F_b), on model responses were investigated. In this set of simulations, the fraction of organics (Φ_d) in the feed was 16%, the same value used to perform vinyl acetate polymerizations reported by Lobry *et al.* (2015), while the initiator feed composition was equal to 0.0015% (mol/mol) with respect to the monomer feed. Di(2-ethylhexyl) peroxydicarbonate (DEHP, $k_{d0} = 1.83 \times 10^{15}$ s^{-1}, $E_0 = 122450$ J mol^{-1}, Nouryon (2023)) was used as initiator since it is used to produce PVC commercial grades in industrial plants. χ_o and f_o were set equal to 30 mm and 1 Hz, respectively. Similarly, the temperature of the feed was equal to 295.15 K to simulate the lower temperatures in the initial zones of the reactor. Additionally, the set point of the controllers were set to 340.15 K to resemble the operation condition normally used for the production of an industrial grade resin. The residence time in these simulations was 4 hours.

For practical purposes, the lower operating temperatures before reaching the reaction temperature is important to prevent the polymerization reaction before mixing the initiator homogeneously among the monomer droplets. If the reaction starts before attaining the homogeneous initiator conditions, the final properties of the resin can be compromised as the droplets with higher amounts of initiator will undergo higher rates of polymerization and will become so dense that plasticizer will not be absorbed in the final processing stages (Dirix *et al.*, 2016). This type of defect on resin properties can lead to the formation of "fish-eyes" (Eliassaf, 1973).

Initially, to investigate the effect of k on the model responses, simulations were performed by setting F_b equal to zero. Since the polymerization of vinyl chloride requires the tight control of the reaction temperature when the reaction rates reach the peak values at intermediate conversions as a consequence of the diffusional limitations, the reactor was divided into eight zones ($nz = 8$), i.e., each straight section in the heating, reaction and cooling zones as shown in Figure 3.7 was represented as an independent jacketed zone. Moreover, the temperatures at the end of each zone were selected as controlled variables. Figure 5.1 shows the dynamic conversion profiles at the outlet of the reactor for simulations performed with different values of k. As the number of tanks in the simulation increases, the response approaches the plug flow behavior.

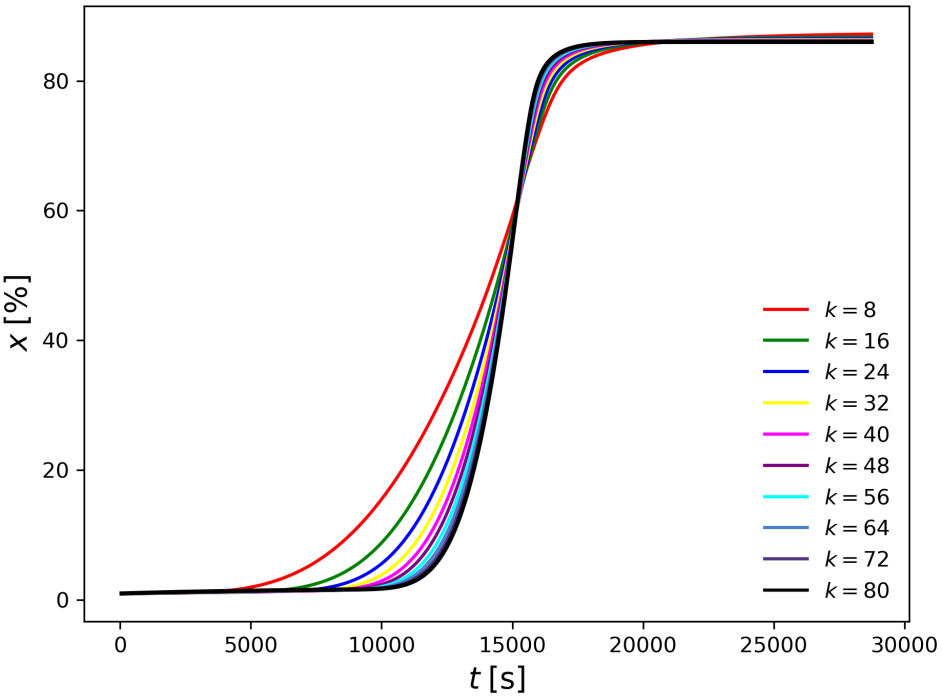

Figure 5.1: Effect of k on dynamic conversion profile at the reactor outlet.

In the simulation performed with only eight tanks, the model response approaches a mixed flow behavior. The minimum number of tanks used to perform the simulations was set to eight in order to represent each zone of the reactor with at least one tank. As it is assumed that every zone has equal length, simulations were performed with number of tanks that are multiples of eight in order to describe each zone with the same number of tanks.

In Figure 5.2, the steady state temperature profiles for simulations performed with different number of tanks are shown. First of all, it can be seen that the control objective can be achieved very precisely as the reactor temperature remains very close to the setpoint. Additionally, since the volume of each tank is the total volume of the reactor divided by the number of tanks, when the number of tanks decreases the equivalent volume of each simulated tank increases. The larger the tank, the higher the amount of heat released by the reaction. This observation explains the higher temperatures in the first zone of the reactor when the number of tanks is small. Since in both Figures 5.1 and 5.2 the model responses almost overlap when $k = 70$ and $k = 80$, all forthcoming simulations were performed with a total of 80 tanks (10 per section).

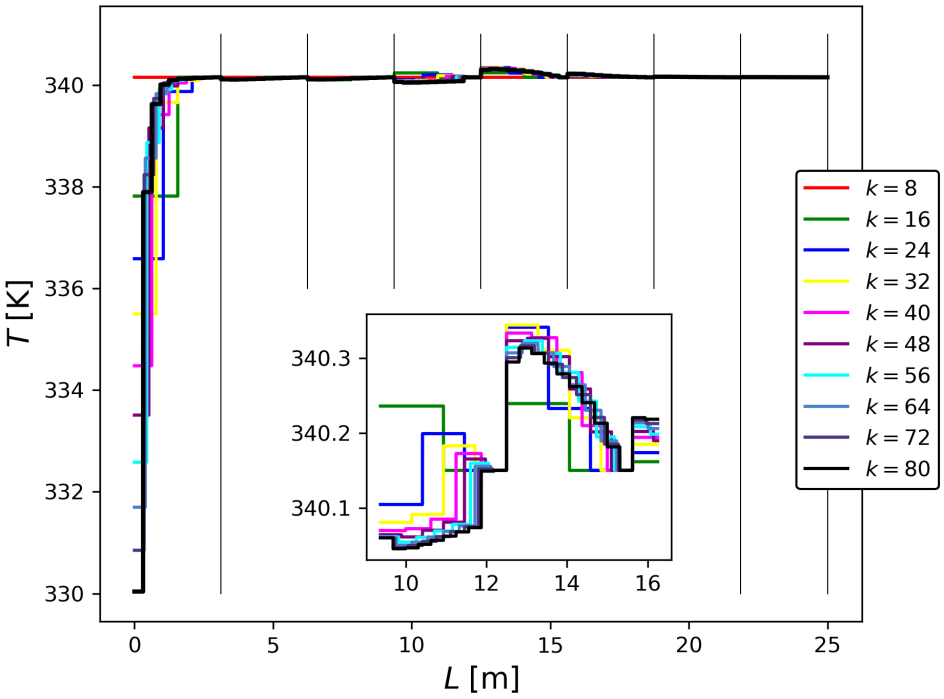

Figure 5.2: Effect k on the steady state temperature profile.

In Figure 5.3, the simulations were performed with $k = 80$ and with varying values of F_b. Since it was observed in the previous chapter that the backflow causes interaction between the controlled zones when the controlled variable is the temperature at the end of each zone, in these simulations, the temperatures at the center of each zone were selected as controlled variables. Figure 5.3 shows that increasing the F_b values causes the model response to exhibit dispersion, as expected, whereas at low backflow rates the model approaches the plug flow response. In Figure 5.4, the steady state temperature profiles were also very close to the setpoint values, emphasizing once more that the regulatory control loops were efficiently designed.

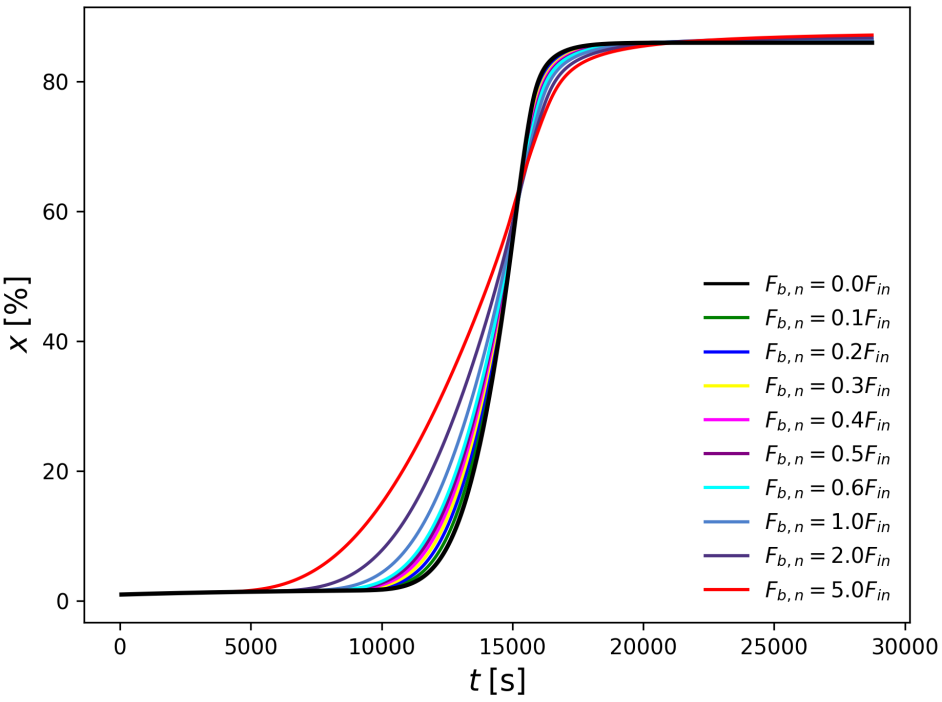

Figure 5.3: Effect of $F_{b,n}$ on dynamic conversion profile at the reactor outlet.

In the zoomed detail of Figure 5.4, it is possible to observe that the steady state temperature profiles obtained with different F_b values are eventually merged into the same value, which corresponds to the temperature setpoint at the center of each zone. When the backflow gets higher, the deviation from the setpoint also increases, as the interaction between the zones becomes stronger. From this point afterwards, all the simulations will be performed keeping $k = 80$ and $F_b = 0.3F_{in}$ as this combination of parameters gives near plug flow responses, as desired in a real production environment to keep molar mass and particle size distributions narrower.

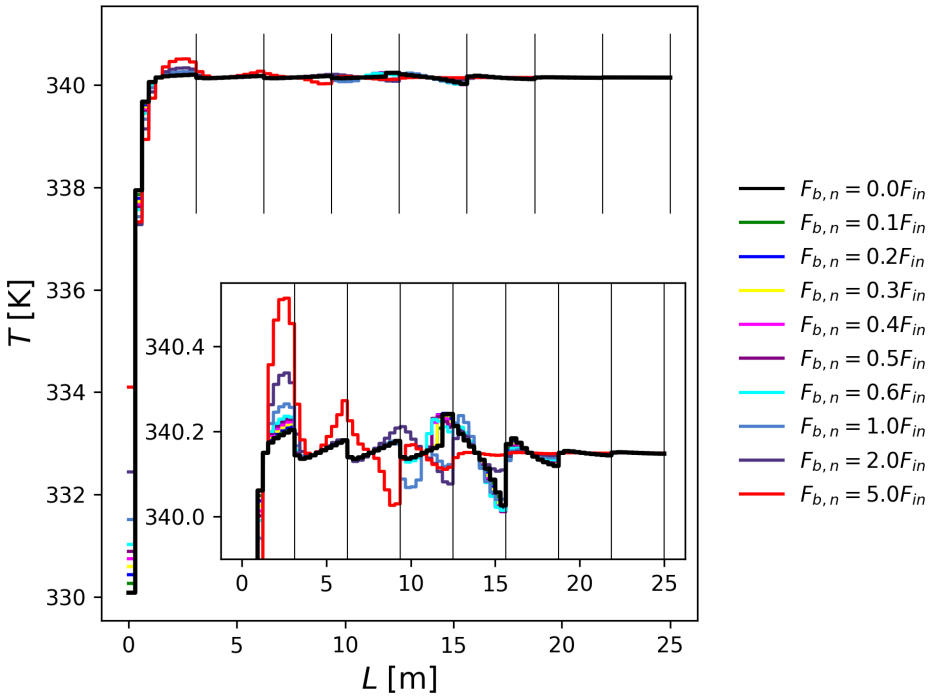

Figure 5.4: Effect of $F_{b,n}$ on the steady state temperature profile.

5.2.2 Effect of Residence Time

Similarly to the batch time in discontinuous processes, the residence time is a key productivity performance parameter in continuous processes. It is always desirable to obtain products with specified properties in the shortest time as a way of increasing process efficiency and productivity. Therefore, in this section, the effect of the residence time on model responses is investigated. With the exception of residence time, the same operation conditions of the previous subsection were assumed. In Figure 5.5 the dynamic conversion profiles at the reactor outlet are shown. The final conversions obtained for τ_{Res} = 4 h, 3 h, 2 h and 1 h were equal to 86, 84, 64 and 27%, respectively. The half-life time of the initiator at the analyzed reaction temperature was equal to 0.67 h. Therefore, when τ_{Res} = 4 h and τ_{Res} = 3 h, the residence times were nearly 6 and 4.5 times larger than the half-life of the initiator, respectively, which are sufficient for the initiator to decompose almost completely (Figure 5.6) and to initiate polymer chains, explaining the higher conversions obtained. On the other hand, when the residence time was smaller than 2 h, remarkable reduction of the final conversion values could be observed, in comparison to the previous cases, as the time required for initiator decomposition was shortened.

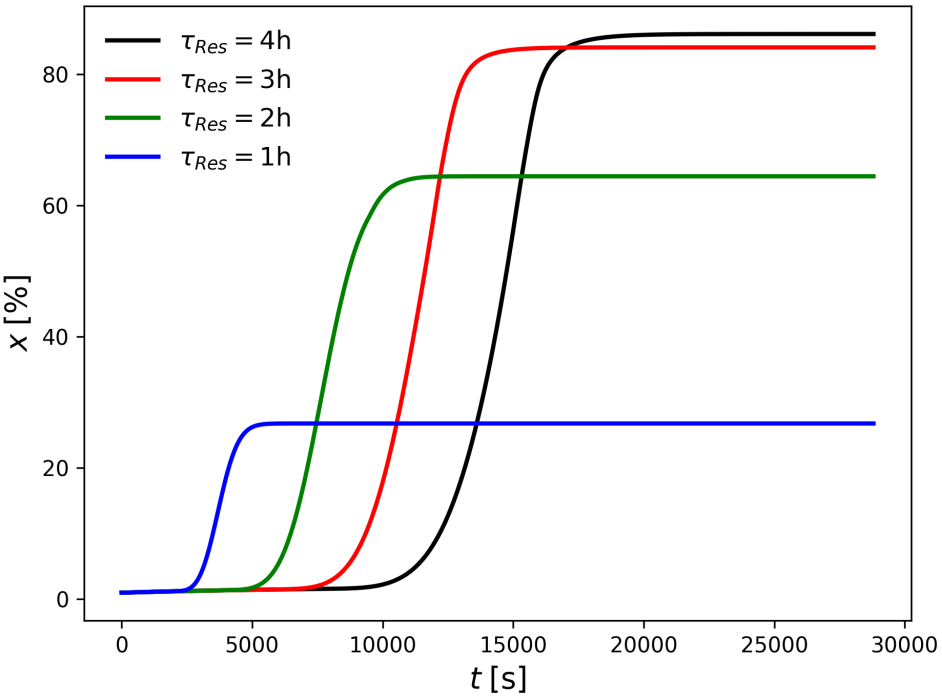

Figure 5.5: Effect of residence time on dynamic conversion profile at the reactor outlet.

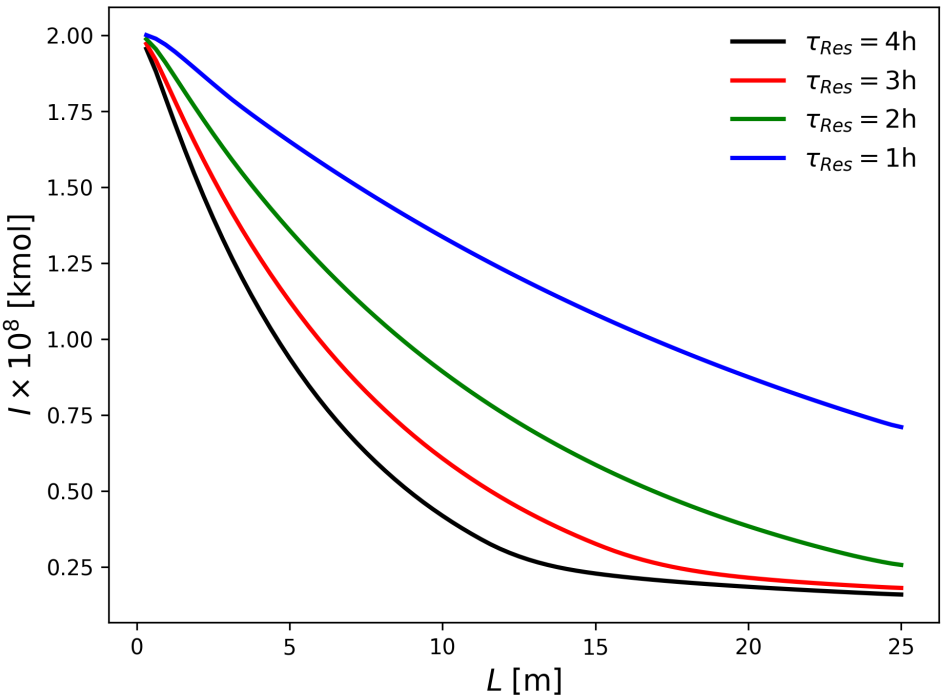

Figure 5.6: Effect of residence time on the steady state initiator amount profile.

Figure 5.7 depicts the steady state conversion profiles along the reactor length. At the lowest residence time, the curve exhibited an almost linear response along the reactor length, as the concentration of radicals was low and the reaction was far from the critical point where the diffusional effects begin. At higher conversions and residence times, the well-known S-shape form of the conversion curve observed in poly(vinyl chloride) polymerizations could be obtained, although the horizontal label represents the reactor length instead of time for a conventional batch reactor as depicted in Kiparissides *et al.* (1997) and in Chapter 2 of this Thesis.

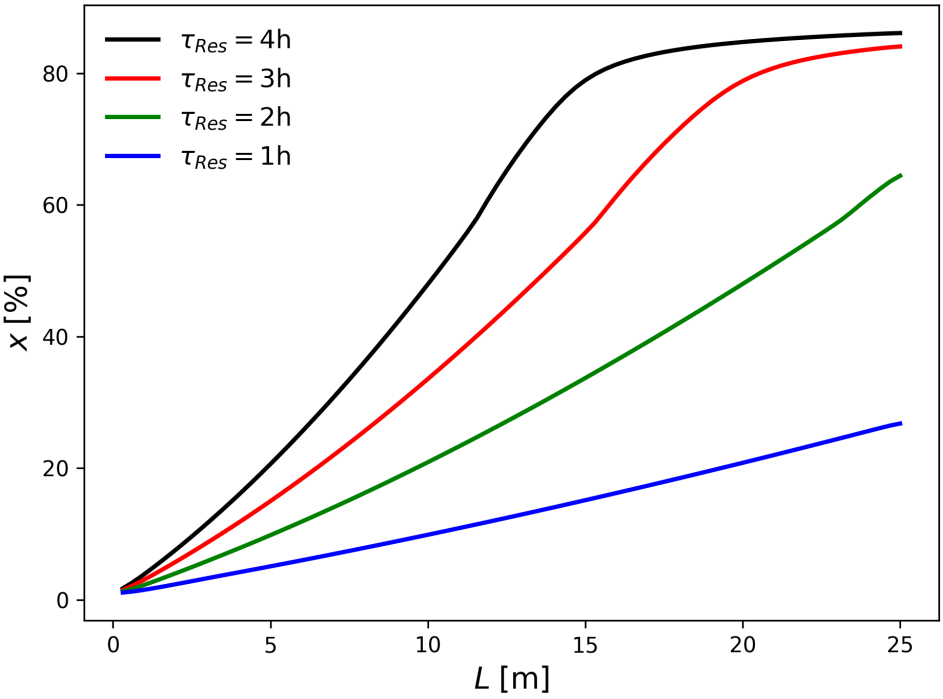

Figure 5.7: Effect of residence time on the steady state conversion profile.

Figures 5.8 and 5.9 show the K-Values and the weight average molar masses of the polymer. As these two variables represent essentially the same property, a remarkable similarity of the steady state profiles can be noticed. As the molar mass of poly(vinyl chloride) is mostly influenced by the temperature due to the high rates of transfer to monomer (Kiparissides *et al.*, 1997; Burgess, 1982), the profiles start to drop at the entrance of the reactor as the temperature increases. Then, these values slightly increase as the conversion advances and the availability of living radicals decreases.

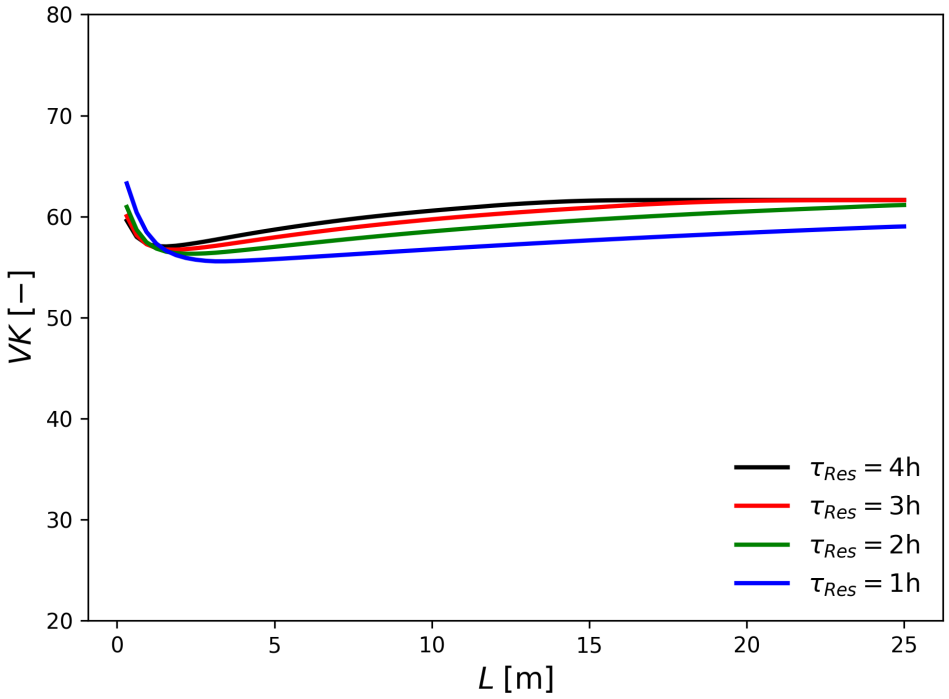

Figure 5.8: Effect of residence time on the steady state K-Value profile.

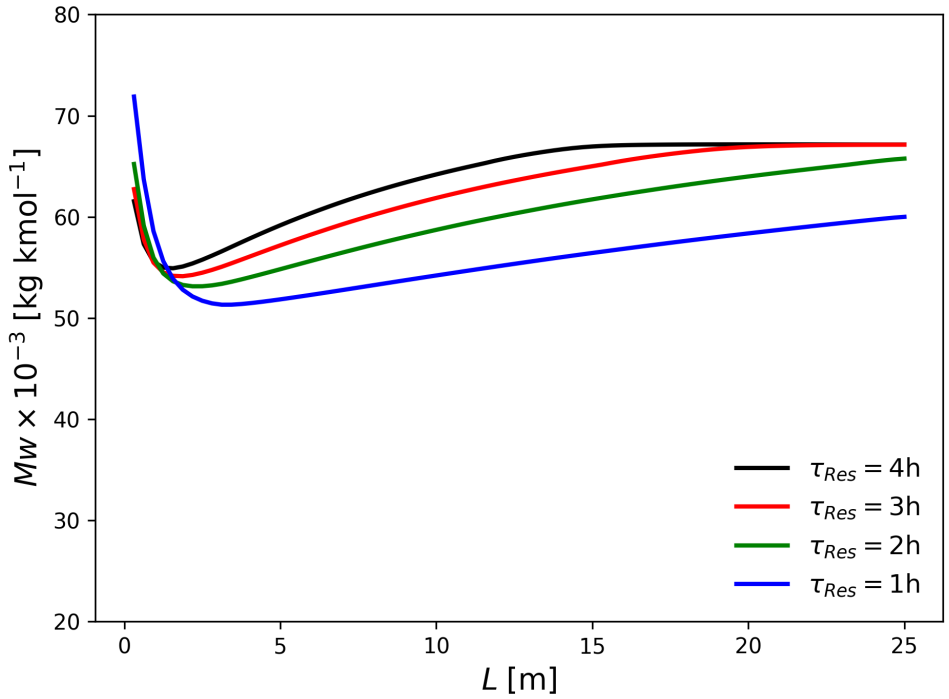

Figure 5.9: Effect of residence time on the steady state weight average molar mass profile.

The results presented so far indicate that the ratio between the residence time and the initiator half-life time plays an important role to explain the attained outlet conversion values. Moreover, by analyzing Figures 5.6 and 5.7 one can conclude that an attempt to increase productivity (higher conversion and low residence time) by increasing the amounts of initiator fed to the reactor may result in higher amounts of initiator in the final product, which can prejudice the final stability of the produced resins. Kobayashi *et al.* (1998) and Dirix *et al.* (2016) showed that the presence of high amounts of initiator in the final product can be detrimental to the color properties of the final resin and lead to high rates of polymerization and heat released, which can cause operational problems. Consequently, one possible solution to this problem is to use a more active initiator system (initiator with lower half-life time at the polymerization temperature).

In order to investigate the effect of the residence time on polymerization rate maintaining a final conversion of 85%, additional simulations were performed. More specifically, in this new set of simulations, the residence time was kept equal to 1 h, and cumyl peroxyneodecanoate (CPND, $k_{d0} = 3.12 \times 10^{14}$ s^{-1}, $E_0 = 114590$ J mol^{-1}, Nouryon (2023)) was used as initiator with inlet molar flow rate 0.045 % of the monomer molar flow rate. At the reaction temperature CPND has a half-life time of 0.25 h. Figure 5.10 shows the steady state profiles of polymerization rates in two simulations: one performed with a residence time of one hour and another with a residence time of three hours.

According to Figure 5.10, one can say that the peak in polymerization rate in the simulation performed with residence time of 1 h was three times higher than the peak observed in the simulation performed with residence time of 3 h. Since the amount of organic phase was kept constant in the simulations when the residence time was divided by three the polymerization rate had to be increased by a factor of approximately three times to attain the same final conversion value presented in the previous simulation. Moreover, the profile of polymerization rates in the simulation performed with the shortest residence time was steeper meaning that the heat generation would be more intense in an intermediate position of the reactor. Consequently, it is possible to affirm that attempts to decrease the residence time while maintaining the final conversion fixed, as a way to increase the productivity, can put more stress on the control system and should be carefully planned to avoid thermal runaways. Figures 5.11 and 5.12 show the spatial-temporal evolution of the polymerization rates along the reactor length.

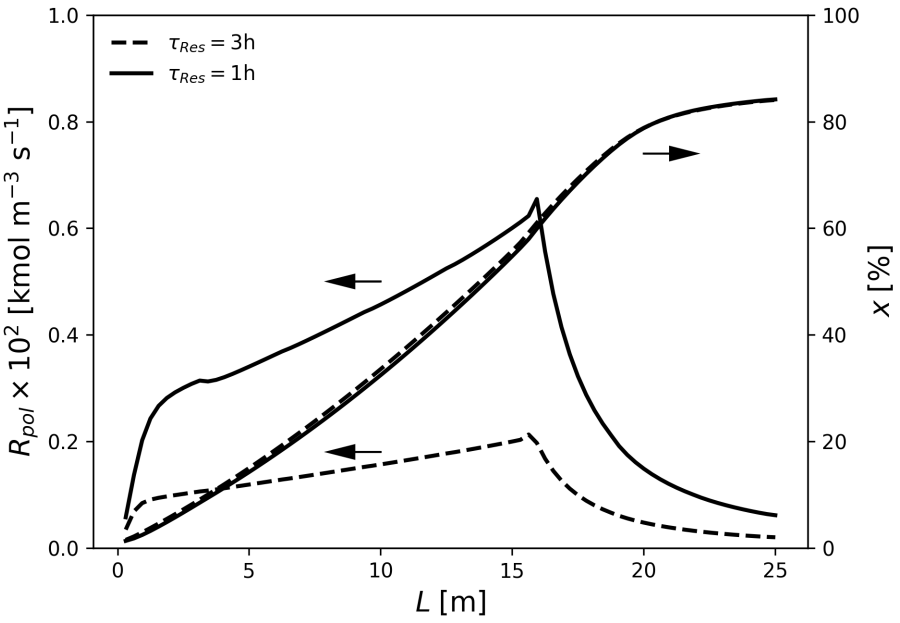

Figure 5.10: Steady state polymerization rate profile simulated with different residence times.

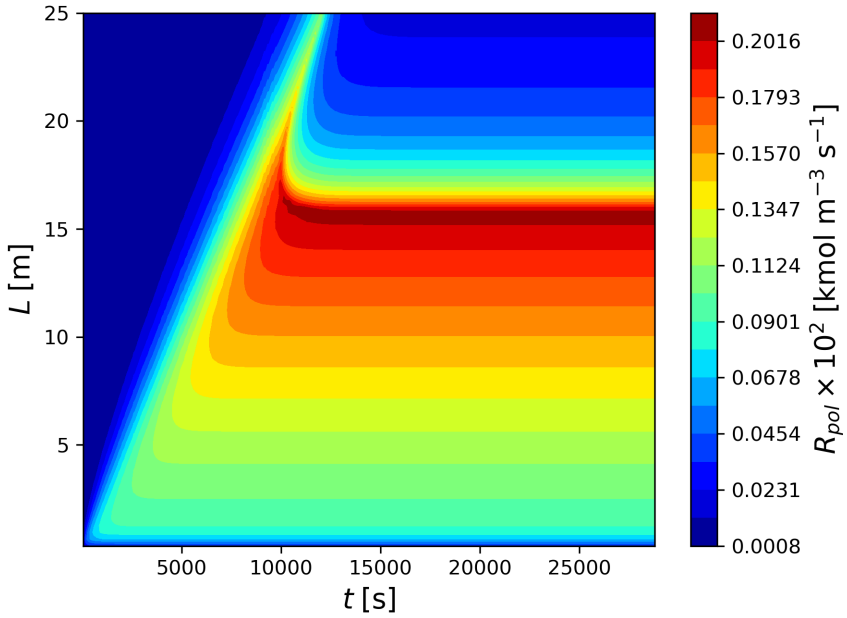

Figure 5.11: Spatial-temporal evolution of the polymerization rates in the simulation performed with residence time of 3 h.

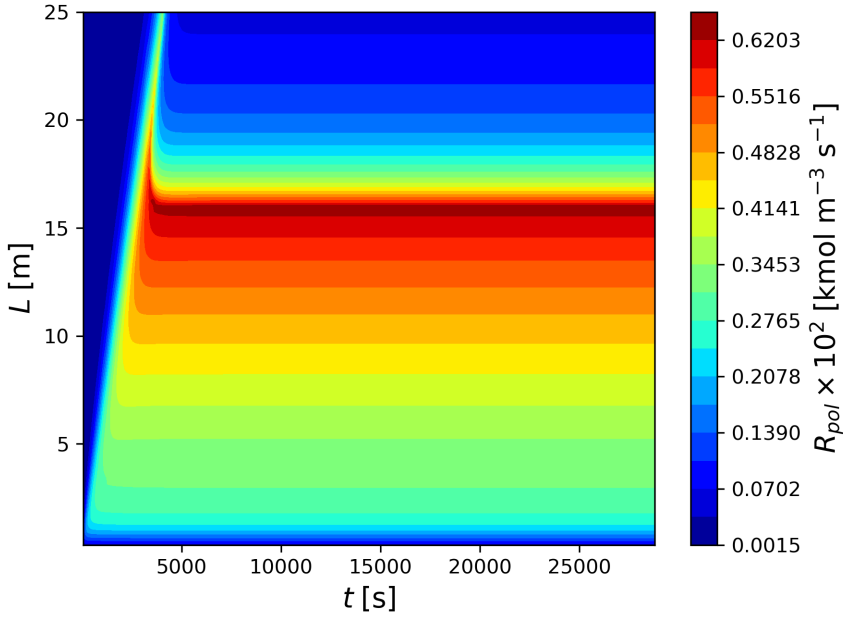

Figure 5.12: Spatial-temporal evolution of the polymerization rates in the simulation performed with residence time of 1 h.

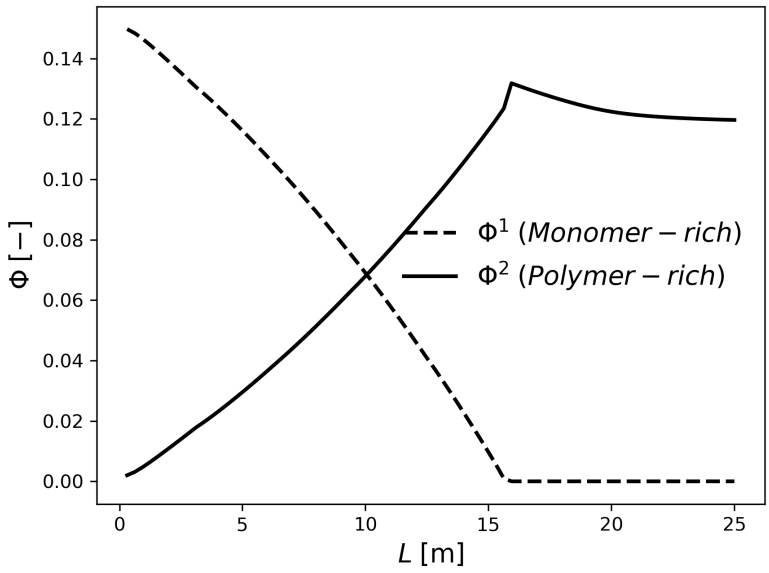

Figure 5.13: Steady state volume fractions of the phases that compose the organic phase.

According to Figures 5.11 and 5.12, the region of the reactor that concentrates the highest polymerization rates was the same in both simulations, as already shown in Figure 5.10. However, the magnitudes of the polymerization rates were different, as illustrated in the colorbars. The highest polymerization rates occurred near the

point where the monomer-rich phase disappeared. Figure 5.13 above shows the volume fractions of the phases that compose the organic phase in the simulation performed with residence time of 1 h. Once again the plot is very similar to the profiles observed in poly(vinyl chloride) polymerization in a batch reactor (Xie *et al.*, 1991) with the difference that the horizontal axis represents reactor length rather than time.

5.2.3 Effect of Initiator Type

In order to investigate the effect of the initiator type on the steady state conversion profiles and polymer properties, the simulation with residence time of 1 h and reaction temperature of 340.15 K was performed with CPND, DEHP, and TAPN (tert-amyl peroxyneodecanoate, $k_{d0} = 1.47 \times 10^{14}$ s^{-1}, $E_0 = 114380$ J mol^{-1}, Nouryon (2023)). The amounts of initiator fed to the reactor were fixed at 0.045 % with respect to the molar flow rate of monomer. In the simulated conditions, CPND, TAPN and DEHP have half-life times of 0.25, 0.48 and 0.67 h, respectively. In Figure 5.14, the steady state conversion, K-Value, initiator and weight averaged molar mass profiles are shown.

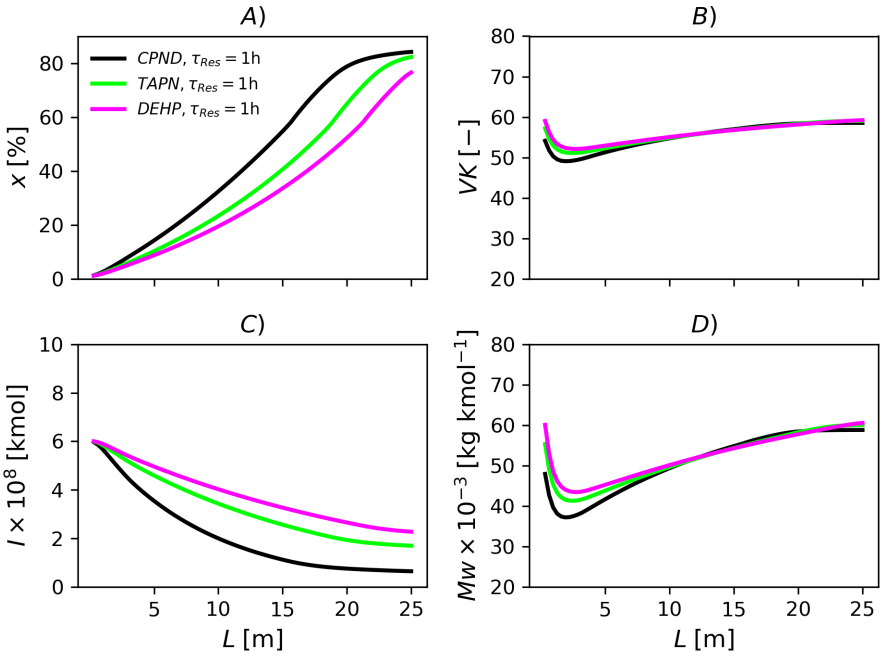

Figure 5.14: Effect of initiator type on the reaction performance. A) conversion, B) K-Value, C) initiator, and D) weight average molar mass.

According to Figure 5.14, the initiator with the higher half-life time in the simulated temperature, i.e., lower decomposition rate constant, provided the lower final conversion and higher concentrations of initiator in the final resin, as one might already expect. Negligible effects on the final K-Value and, consequently, weight average molar mass were observed since these variables are dependent upon the polymerization temperature and vary little with initiator concentration (Burgess, 1982).

The production of poly(vinyl chloride) of high molar mass requires low polymerization temperatures. In practice, this poses a challenge for plant engineers as low reaction temperature implies low polymerization rate and, consequently, low productivity since long reaction times are required. In order to circumvent this problem, initiator systems with high decomposition rate constants (fast initiators) are usually employed. One example of such initiators is Diisobutyryl peroxide (DIBP, $k_{d0} = 3.37 \times 10^{14}$ s^{-1}, $E_0 = 109060$ J mol^{-1}, Nouryon (2023)). In this subsection, three initiator feed strategies were simulated to produce poly(vinyl chloride) with weight average molar mass of 87000 g mol^{-1}. The temperature setpoint of the controllers were set to 324.15 K and the inlet temperature of the feed was equal to 295.15 K. Additionally, the volume fraction of organics (Φ_d) was made equal to 0.4 and the residence time was set to 3 h. In Strategy A, the initiator molar flow rate was 0.037% molar of the monomer feed flow rate and all the initiator was fed at the inlet of the reactor. Let I_A represent the total amount of initiator fed in strategy A. In Strategy B, $0.7I_A$ was fed at the inlet and $0.3I_A$ was fed at the entrance of the fifth zone ($z = 5$, $L = 12.5$ m) of the reactor. Finally, in strategy C, $0.7I_A$ was fed at the inlet and $0.1I_A$ at the entrance of the fifth zone.

In Figure 5.15, the steady state conversion, temperature, initiator and average molar mass profiles are shown. Regarding Strategy A, since the initiator is fast, the conversion curve is steeper in comparison to the previous simulations. Moreover, since the initiator decomposes almost completely in the first half of the reactor and the conversion reaches 80% at 12 m, the second half of the reactor is characterized by very small polymerization rates with the conversion varying from 80 to 85%. In Strategy B, the feed of fresh initiator at the intermediate position of the reactor results in a temperature hotspot of 2.5 K. This occurs because the termination rate was impaired but the initiator decomposition and chain propagation were still high at that point of the reactor which resulted in a peak in polymerization rate as shown in Figure 5.16. Regarding Strategy C, since the amount of fresh initiator fed was smaller, the increase in polymerization rate was smaller and the hotspot was not observed. Besides, the polymer produced in this strategy showed a higher molar

mass as displayed in Figure 5.15. Additionally, the strategy C made use of 20% less initiator than strategies A and B. Figure 5.16 shows the polymerization per volume of the organic phase. The intense peak in polymerization rate in Strategy B results in the hotspot seen in Figure 5.15.

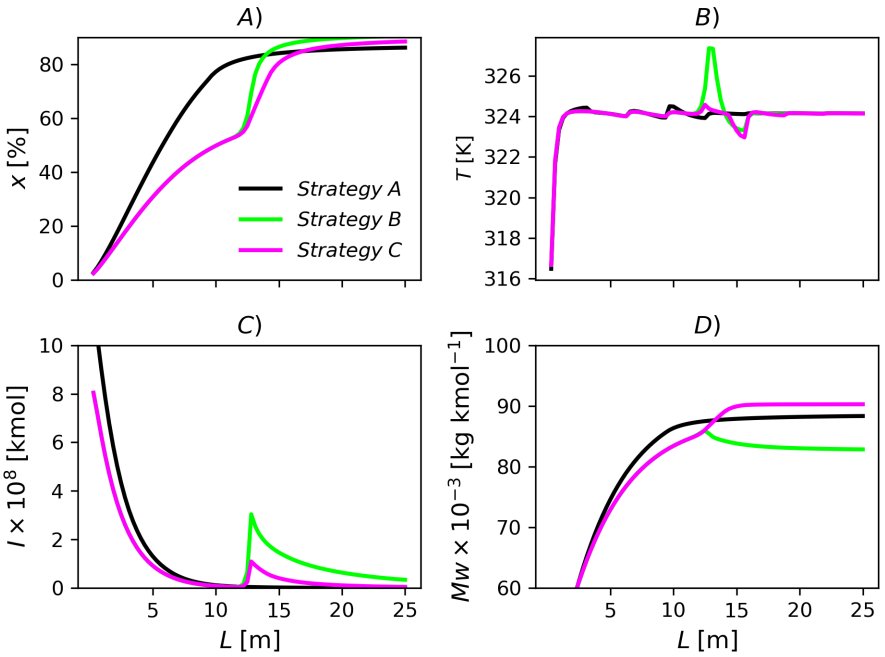

Figure 5.15: Effect of initiator feed strategy on the reaction performance. A) conversion, B) reactor temperature, C) initiator, and D) weight average molar mass.

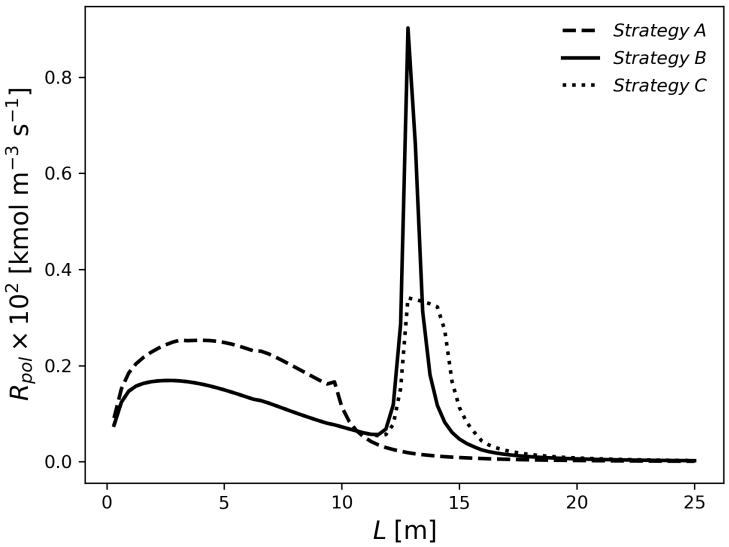

Figure 5.16: Steady state polymerization rates simulated with different initiator feed strategies.

5.2.4 Effect of Oscillation Velocity

In Figure 5.17, the spatial temporal profile of the heat transfer coefficients obtained in simulations performed at four distinct oscillatory conditions are depicted. In these simulations, the net Reynolds number was equal to 100 and the residence time was equal to 1 h. Moreover, the reaction temperature was made equal to 340.15 K and CPND was used as initiator at molar feed of 0.045% of the monomer molar flow rate. According to Figure 5.17, the Nusselt number dropped from 23 to about 10 when the oscillation velocity dropped from 0.03 m s^{-1} ($Re_o = 2757$) to 0.0037 m s^{-1} ($Re_o = 344$) and the overall heat transfer coefficient (U) dropped from 288 to 168 J s^{-1} m^{-2} K^{-1}. When the oscillatory Reynolds number dropped from 2757 to 1378, no significant change of the heat transfer coefficients was observed because this condition is still above the asymptotic condition of the Nusselt number, i.e., $Re_o > 1300$ according to Equation (5.75). In Figure 5.18, the simulations were performed with a lower net Reynolds number ($Re = 50$). It is possible to note that the Nusselt number dropped from nearly 14 to 6 when the oscillation velocity falls from 0.03 m s^{-1} to 0.0037 m s^{-1}. Moreover, the overall heat transfer coefficient drops from 229 to 122 J s^{-1} m^{-2} K^{-1} at these conditions. These results indicate that attention must be paid when operating the oscillatory baffled reactor at very low net Reynolds numbers. Even though the effect of oscillation enhances the heat transfer coefficient, operating the reactor at very low net velocities can exert a negative effect on the heat transfer performance of the reactor.

5.3 Concluding Remarks

In this chapter, a phenomenological model was developed to represent the suspension polymerization of vinyl chloride in a continuous oscillatory baffled reactor. The intrinsic kinetic features and multiphase behavior of the vinyl chloride/poly(vinyl chloride) reacting system were considered in the model development and the kinetic parameters estimated in Chapter 2 were used to perform the simulations. It was concluded that the heat released by the reaction can constitute an issue of concern when high reactor productivities are sought, although the implementation of independent proportional-integral temperature controllers for different reactor zones can be sufficient to assure the proper control of the reaction temperature. Particularly, vinyl chloride polymerization exhibits a heat generation peak due to its intrinsic kinetic features (such as strong diffusion limitation effects) that must be carefully considered during the design of larger reactors. Furthermore, it

was also highlighted that the use of fast initiator systems and multiple initiator feed points can be advantageous to produce resins with high molar masses at low polymerization temperatures. Finally, the proposed model indicates that different PVC grades can be produced at high rates in COBR reactors in continuous mode if initiator feed policies are developed.

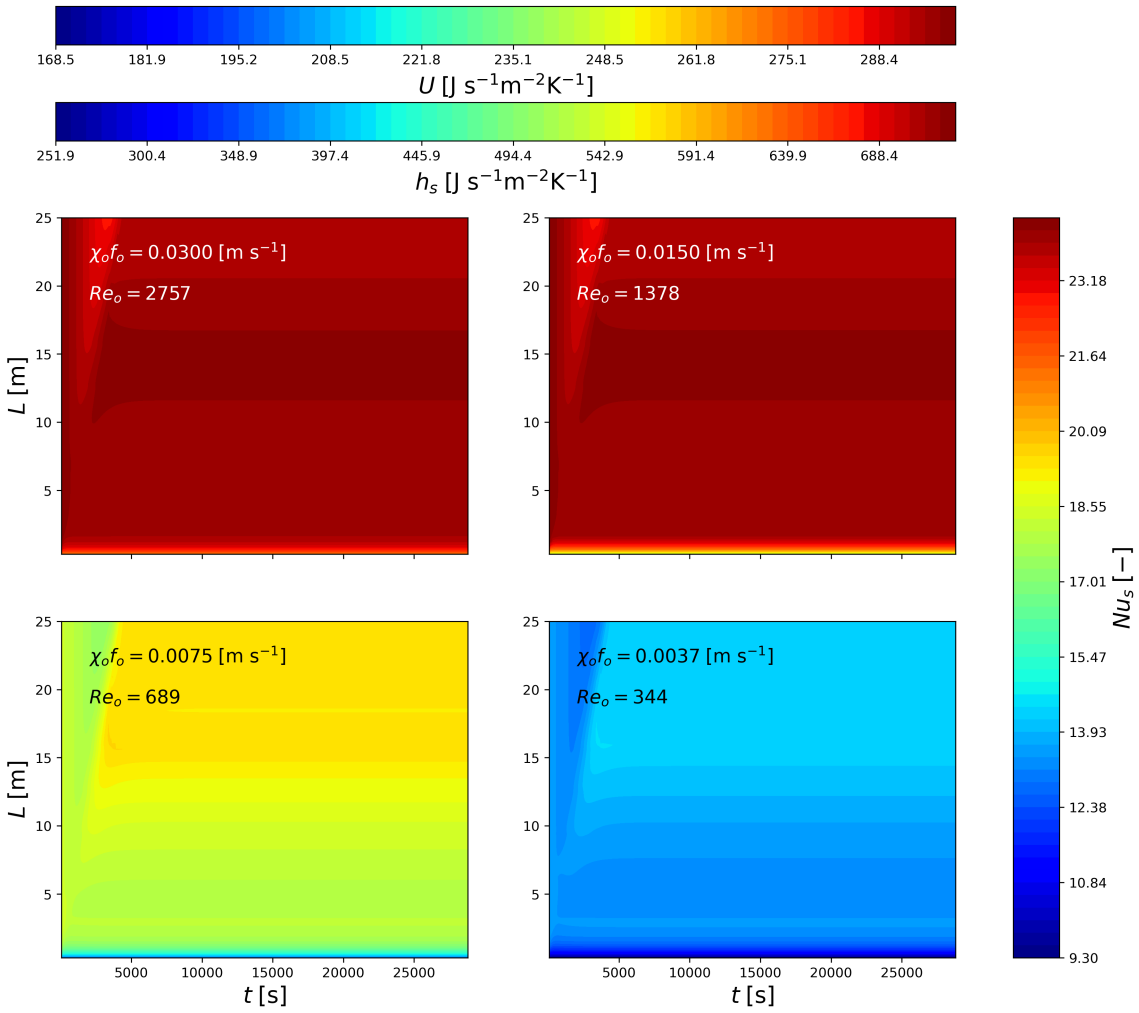

Figure 5.17: Effect of oscillation velocities on the heat transfer coefficients (Re = 100).

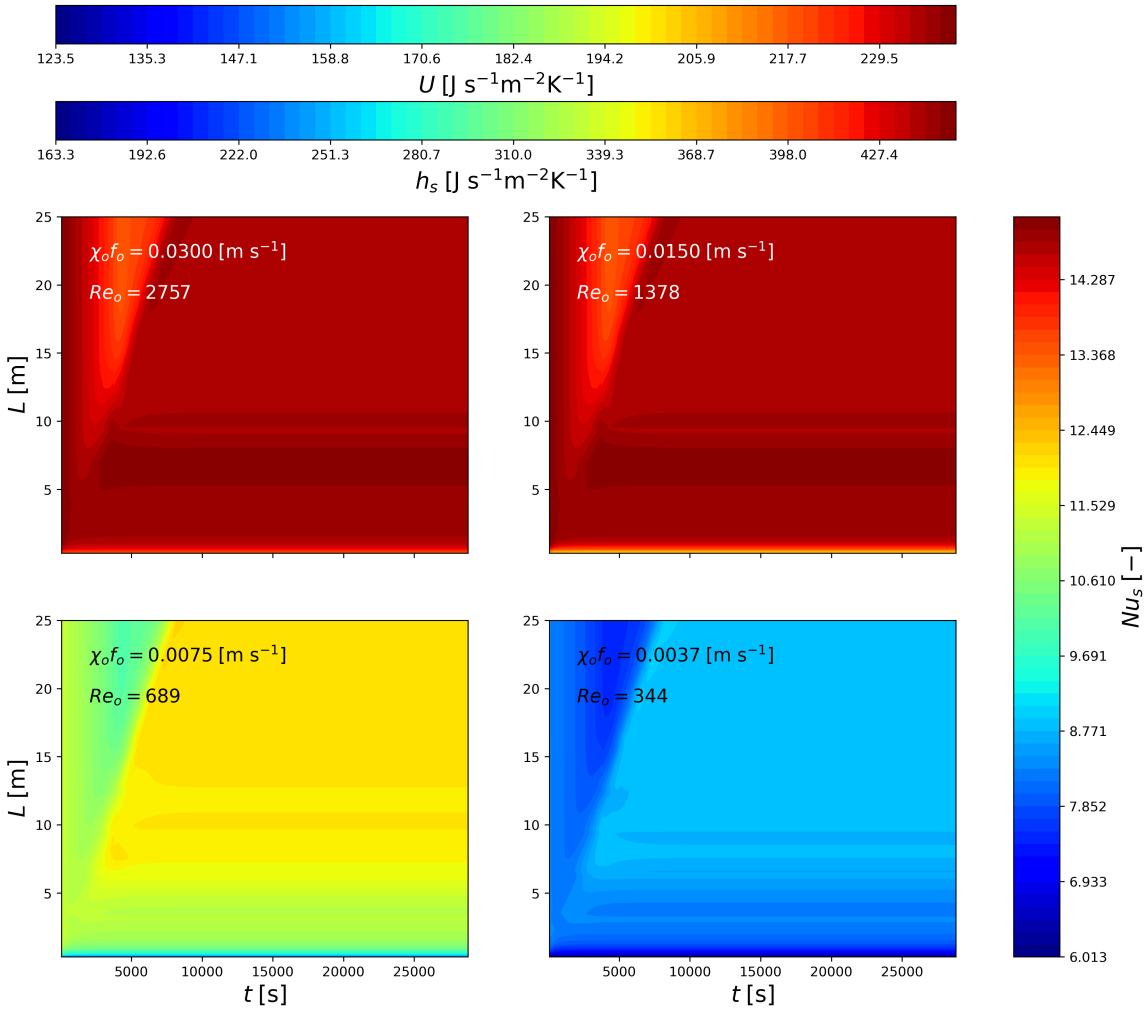

Figure 5.18: Effect of oscillation velocities on the heat transfer coefficients ($Re = 50$).

List of Abbreviations

Abbreviation	Meaning
COBR	Continuous Oscillatory Baffled Reactor
CPND	Cumyl peroxyneodecanoate
DEHP	Di(2-ethylhexyl) peroxydicarbonate
DIBP	Diisobutyryl peroxide
TAPN	Tert-amyl peroxyneodecanoate
PVC	Poly(vinyl chloride)
PVAC	Poly(vinyl acetate)

List of Symbols

Symbol	Meaning
A	Heat transfer area [m^2]
A^*, B^*, B_f^*, C^*	Free volume parameters [-]
$\underline{cp}$	Heat capacity [kJ kg^{-1} K^{-1}]
cp	Heat capacity [kJ $kmol^{-1}$ K^{-1}]
C	Cross section area of the reactor [m^2]
C_{pva}	Concentration of poly(vinyl alcohol) [kg m^{-3}]
d_o	Orifice diameter [m]
$d_{r,ext}$	Reactor external diameter [m]
$d_{r,int}$	Reactor internal diameter [m]
E	Error of the controller [K]
f_o	Frequency of oscillation [s^{-1}]
f	Initiator efficiency [-]
F	Flow rate [m^3 s^{-1}]
h	Heat transfer coefficient [J s^{-1} m^{-2} K^{-1}]
I	Initiator [kmol]
k	Total number of tanks [-]
k_d	Decomposition rate constant [s^{-1}]
k_p	Propagation rate constant [m^3 $kmol^{-1}$ s^{-1}]
k_{tm}	Transfer to monomer rate constant [m^3 $kmol^{-1}$ s^{-1}]
k_{sol}	Monomer solubility in water [kg kg^{-1}]
k_{tp}	Transfer to polymer rate constant [m^3 $kmol^{-1}$ s^{-1}]
k_{td}	Termination by disproportionation rate constant [m^3 $kmol^{-1}$ s^{-1}]
k_{tc}	Termination by combination rate constant [m^3 $kmol^{-1}$ s^{-1}]
k_{wall}	Thermal conductivity of the reactor wall [J s^{-1} m^{-1} K^{-1}]

K_c	Proportional gain of the controller [-]
l	Equivalent length [m]
L	Reactor length [m]
m	Molar or mass flow rate [kmol s^{-1} or kg s^{-1}]
M	Monomer [kmol]
MM	Molar mass [kg $kmol^{-1}$]
Mn	Number average molar mass [kg $kmol^{-1}$]
Mw	Weight average molar mass [kg $kmol^{-1}$]
nz	Number of zones [-]
Nu	Nusselt number [-]
P	Polymer [kmol]
Pr	Prandtl number [-]
$\dot{Q}_{gen}$	Heat generated by the reaction [J s^{-1}]
Re	Reynolds number [-]
Re_o	Oscillatory Reynolds number [-]
R_{pol}	Polymerization rate [kmol m^{-3} s^{-1}]
St	Strouhal number [-]
T	Temperature [K]
U	Overall heat transfer coefficient [J s^{-1} m^{-2} K^{-1}]
v	Velocity [m s^{-1}]
VK	K-Value [-]
V	Volume [m^3]
x	Conversion [-]
Y	Suspending agent [kg]
W	Water [kmol]
Z_t/Z_m^{sat}	Ratio of operating pressure to monomer saturation pressure [-]

Greek letters	
Φ	Volume fraction [-]
ϕ	Auxiliary function [-]
Ω	Auxiliary function [-]
χ_o	Center-to-peak amplitude of oscillation [m]
χ_{FH}	Flory-Huggins interaction parameter [-]
λ	Living polymer moments [kmol]
μ	Dead polymer moments [kmol]
η	Viscosity [kg m^{-1} s^{-1}]
$[\eta]_{pva}$	Intrinsic viscosity of poly(vinyl alcohol) [m^3 kg^{-1}]
σ	Thermal conductivity [J m^{-1} s^{-1} K^{-1}]
ρ	Density [kg m^{-3}]
τ_i	Integral time of the controller [s]

τ_{Res}	Residence time [h]
ΔH	Enthalpy of reaction [kJ kmol^{-1}]
Ψ	Velocity ratio [-]
Superscripts	
1	Phase 1 (Monomer-rich)
2	Phase 2 (Polymer-rich)
3	Phase 3 (Aqueous)
Subscripts	
0	Zero order moment
1	First order moment
2	Second order moment
3	Third order moment
b	Backflow
c	Continuous phase
d	Dispersed phase
h	Ref. to hydraulic diameter
i	Initiator
in	Inlet
j	Jacket
m	Monomer
n	Tank number
p	Polymer
r	Reactor
ref	Reference value
s	Suspension
sp	Setpoint
w	Water
y	Suspending agent
z	Reactor zone

5.4 References

Abi-Ramia, N.M. Modelagem, Simulação e Otimização da Polimerização em Suspensão do PVC, Master Thesis, Universidade Federal do Rio de Janeiro, May of 2012.

Achilias, D.S.; Kiparissides, C. Development of a general mathematical frame-

work for modeling diffusion-controlled free-radical polymerization reactions. Macromolecules, 25, 3739-3750, 1992.

Avila, M.; Kawas, B.; Fletcher, D.F.; Poux, M.; Xuereb, C. Design, performance characterization and applications of continuous oscillatory baffled reactors. Chemical Engineering and Processing: Process Intensification, 180, 108718, 2022.

Batchelor, G.K.; Green, J.T. The hydrodynamic interaction of two small freely-moving spheres in a linear flow field. Journal of Fluid Mechanics, 56, 2, 375-400, 1972.

Bouyatiotis, B.S.; Thornton, J.D. Liquid-liquid extraction studies in stirred tanks. Part I. droplet size and holdup. Institution of Chemical Engineers (London) Symposium Series, 26, 43-50, 1967.

Brunold, C.R.; Hunns, J.C.B.; Mackley, M.R.; Thompson, J.W. Experimental Investigations on Flow Patterns and Energy Losses for Oscillatory Flow in Ducts Containing Sharp Edges. Chemical Engineering Science, 44, 5, 1227-1244, 1989.

Bueche, F. Physical Properties of Polymers. Interscience Publishers: New York, NY, USA, pp. 112-120, 1962.

Burgess, R.H. Suspension polymerization of vinyl chloride. In: Manufacturing and Processing of PVC, Eds.: Burgess, R.H., Elsevier: Barking, England, pp. 1-27, 1982.

Burnett, G.M.; Wright, W.W. The photosensitized polymerization of vinyl chloride in tetrahydrofuran solution. III. determination of the kinetic coefficients. Proceedings of the Royal Society London. Series A. Mathematical and Physical Sciences, 221, 1144, 41-53, 1954.

Castor, C.A. Investigação Experimental e Modelagem de Sistemas Não-convencionais da Polimerização em Suspensão do Cloreto de Vinila. PhD Thesis, Universidade Federal do Rio de Janeiro, July of 2014.

Ceccorulli, G.; Pizzoli, M.; Pezzin, G. Effect of thermal history on T_g and corresponding C_P changes in PVC of different stereoregularities. Journal of Macromolecular Science Part B: Physics, 14, 4, 499-510, 1977.

Collins, E.A.; Daniels, C.A.; Witenhafer, D.E. Physical Constants of Poly(vinyl chloride), in: Brandrup, J., Immergut, E.H., Grulke, A. (Eds.), Poly-

mer Handbook, Wiley, New York, Ch. V.

Dirix, C.A.M.C.; Jacobus, J.; De Jong, T.; Meulenbrugge, L.; Vanduffel, K.A.K. Continuous process for the production of vinyl chloride (co)polymers. Akzo Nobel, United States Patent Number USRE45940E, 2016.

Eliassaf, J. "Fish-eyes" in poly(vinyl chloride). Journal of Applied Polymer Science, 17, 1225-1226, 1973.

Fedors, R.F. A universal reduced glass transition temperature for liquids. Journal of Polymer Science, 17, 719-722, 1979.

Gnielinski, V. G2 Heat transfer in concentric annular and parallel plate ducts. in: VDI Heat Atlas, Second Edition, Springer-Verlag, Berlin, pp. 701-708, 2010.

Gnielinski, V. Heat transfer coefficients for turbulent flow in concentric annular ducts. Heat transfer engineering 30, 6, 431-436, 2009.

Gnielinski, V., 2007. Berechnung des Druckverlustes in glatten konzentrischen Ringspalten bei ausgebildeter laminarer und turbulenter isothermer Strömung. Chemie Ingenieur Technik, 79, I-2, 91-95.

Green, D.W.; Perry, R.H. Perry's Chemical Engineers Handbook. 8th ed., McGraw Hill, New York, NY, USA, 2008.

Harvey, A.P., Mackley, M.R., Stonestreet, P. Operation and optimization of an oscillatory flow continuous reactor. Industrial and Engineering Chemistry Research, 40, 5371-5377, 2001.

Howes, T.; Mackley, M.R.; Roberts, E.P.L. The simulation of chaotic mixing and dispersion for periodic flows in baffled channels. Chemical Engineering Science, 46, 7, 1669-1677, 1991.

Hutchinson, R.A.; Penlidis, A. Free-radical Polymerization: Homogeneous Systems. in: Asua, J.M. (Ed.), Polymer Reaction Engineering, Blackwell Publishing, Oxford, UK, pp. 118-178, 2007.

Kiparissides, C. Polymerization reactor modeling: a review of recent developments and future directions. Chemical Engineering Science, 51, 10, 1637-1659, 1996.

Kiparissides, C.; Pladis, P., 2022. On the prediction of suspension viscosity, grain morphology, and agitation power in SPVC reactors. Canadian Journal of Chemical Engineering, 100, 4, 714-730, 2022.

Kiparissides, C.; Daskalakis, G.; Achilias, D.S.; Sidiropoulou, E. Dynamic simulation of industrial poly(vinyl chloride) batch suspension polymerization reactors. Industrial and Engineering Chemistry Research and Design, 36, 4, 1253-1267, 1997.

Kobayashi, T.; Amano, T.; Okuno, Y.; Kurihara, H.; Kurokawa, T. Process for preparing vinyl chloride polymer under specified pressure. Shin-Etsu Chemical Co., United States Patent Number 005739222A, 1998.

Korosi, A.; Fabuss, B.M. Viscosity of liquid water from 25° to 150°C measurements in pressurized glass capillary viscometer. Analytical Chemistry, 40, 1, 157-162, 1968.

Law, R.; Ahmed, S.M.R.; Tang, N.; Phan, A.N.; Harvey, A.P. Development of a more robust correlation for predicting heat transfer performance in oscillatory baffled reactors. Chemical Engineering and Processing: Process Intensification, 125, 133-138, 2018.

Lazrak, N.; Le Bolay, N.; Ricard, A. Droplet stabilization in high hold up fraction suspension polymerization reactors. European Polymer Journal, 34, 11, 1637-1647, 1998.

Leiza, J.; Pinto, A. Control of Polymerization Reactors. in: Asua, J.M. (Ed.), Polymer Reaction Engineering, Blackwell Publishing, Oxford, UK, pp. 315-361, 2007.

Levy, F.L. A modified Maxwell-Eucken equation for calculating the thermal conductivity of two-component solutions or mixtures. International Journal of Refrigeration, 4, 4, 223-225, 1981.

Li, C.C. Thermal conductivity of liquid mixtures. AIChE Journal, 22, 5, 927-930, 1976.

Mackley, M.R.; Tweddle, G.M.; Wyatt, I.D. Experimental heat transfer measurements for pulsatile flow in baffled tubes. Chemical Engineering Science, 45, 5, 1237-1242, 1990.

Mackley, M.R.; Ni, X. Mixing and dispersion in a Baffled Tube for Steady

laminar and pulsatile flow. Chemical Engineering Science, 46, 12, 3139-3151, 1991.

Mackley, M.R.; Stonestreet, P. Heat transfer and associated energy dissipation for oscillatory flow in baffled tubes. Chemical Engineering Science, 50, 14, 2211-2224, 1995.

Maggioris, D.; Goulas, A.; Alexopoulos, A.H.; Chatzi, E.G.; Kiparissides, C. Prediction of particle size distribution in suspension polymerization reactors: effect of turbulence nonhomogeneity. Chemical Engineering Science, 55, 4611-4627, 2000.

Martin, H. Lecture on Heat Transfer. Universitaet Karlsruhe (TH), Germany, 1990.

Maschio, G.; Moutier, C. Polymerization reactor: the influence of "gel effect" in batch and continuous solution polymerization of methyl methacrylate. Journal of Applied Polymer Science, 37, 825-840, 1989.

Nagy, D.J. A Mark-Houwink equation for poly(vinyl alcohol) from sec-viscometry. Journal of Liquid Chromatography, 16, 14, 3041-3058, 1993.

Ni, X.; Gough, P. On the discussion of the dimensionless groups governing oscillatory flow in a baffled tube. Chemical Engineering Science, 52, 18, 3209-3212, 1997.

Nilsson, H.; Silvergreen, C.; Törnell, B. Swelling of PVC latex particles by VCM. European Polymer Journal, 14, 9, 737-741, 1978.

Nouryon. Nouryon Company, Amsterdam, The Netherlands, Acessed on July 13, 2023, https://www.nouryon.com/contentsearch/.

Okaya, T. Modification of Polyvinyl Alcohol by Copolymerization. In: Polyvinyl Alcohol Developments; Ed.: Finch, C.A.; Wiley: Hoboken, New Jersey, USA, 1992.

O'neil, G.A.; Wisnudel, M.B.; Torkelson, J.M. An evaluation of free volume approaches to describe the gel effect in free radical polymerization. Macromolecules, 31, 4537-4545, 1998.

Park, G.S.; Smith, D.G. Vinyl chloride studies. II. initiation and termination in the homogeneous polymerization of vinyl chloride. Die Makromolekulare Chemie: Macromolecular Chemistry and Physics, 131, 1, 1-6, 1970.

Petukhov, B.S.; Roizen, L.I. Generalized relationships for heat transfer in a turbulent flow of gas in tubes of annular section(heat transfer coefficients and adiabatic temperatures obtained for turbulent gas flow in tubes with annular section). High Temperature 2, 65-68, 1964.

Petzold, L.R. Description of DASSL: A differential/Algebraic System Solver; Sandia National Labs.: Livermore, CA, USA, 1982.

Saldívar-Guerra, E. Numerical techniques for the solution of the molecular weight distribution in polymerization mechanisms, state of the art. Macromolecular Reaction Engineering, 14, 4, 2000010, 2020.

Seborg, D.E.; Mellichamp, D.A.; Edgar, T.F.; Doyle, F.J. Process Dynamics and Control, third ed. Wiley, Hoboken, NJ, USA, 2010.

Si, K. Kinetics and Mechanism of Vinyl Chloride Polymerization: Effects of additives on Polymerization Rate, Molecular Weight and Defect Concentration in the Polymer. Doctoral Dissertation, Case Western Reserve University, Cleveland, OH, USA, May 2007.

Silva, J.S.; Melo, P.A.; Pinto, J.C. Modeling of particle size distributions in industrial poly(vinyl chloride) suspension polymerization reactors. Processes, 11, 5, 1440, 2023.

Sidiropoulou, E.; Kiparissides, C. Mathematical modeling of PVC suspension polymerization: a unifying approach and some new results. Journal of Macromolecular Science - Chemistry, 27, 3, 257-288, 1990.

Skogestad, S., Postlethwaite, I. Multivariable Feedback Control, Wiley, Hoboken, NJ, USA, 2005.

Stonestreet, P.; Van der Veeken, P.M.J. The effects of oscillatory flow and bulk flow components on residence time distribution in baffled tube reactors. Chemical Engineering Research and Design, 77, 8, 671-684, 1999.

Stonestreet, P.; Harvey, A.P. A mixing-based methodology for continuous oscillatory flow reactors. Chemical Engineering Research and Design, 80, 1, 31-44, 2002.

Ugelstad, J.; Flogstad, H.; Hertzberg, T.; Sund, E. On the bulk polymerization of vinyl chloride. Die Makromoleckulare Chemie: Macromolecular Chemistry and

Physics, 164, 1, 171-181, 1973.

Vermeulen, T., Williams, G.M., Langlois, G.E. Interfacial area in liquid-liquid and gas-liquid agitation. Chemical Engineering Progress, 51, 2, 85-94, 1955.

Vrentas, J.S.; Duda, J.L. Diffusion in polymer-solvent systems. I. Reexamination of the free-volume theory. Journal of Polymer Science, 15, 403-416, 1977.

Xie, T.Y.; Hamielec, A.E.; Wood, P.E.; Woods, D.R. Experimental Investigation of Vinyl Chloride Polymerization at High Conversion: Mechanism, Kinetics and Modelling. Polymer, 32, 3, 537-557, 1991.

Yuan, H.G.; Kalfas, G.; Ray, W.H. Suspension Polymerization. Journal of Macromolecular Science, Part C: Polymer Reviews, 31, 2-3, 215-299, 1991.

Wang, J.; Carson, J.K.; North, M.F.; Cleland, D.J. A new approach to modelling the effective thermal conductivity of heterogeneous materials. International of Heat and Mass Transfer, 49, 17-18, 3075-3083, 2006.

Wieme, J.; De Roo, T.; Marin, G.B.; Heynderickx, G.J. Simulation of pilot- and industrial-scale vinyl chloride batch suspension polymerization reactors. Industrial and Engineering Chemistry Research, 46, 4, 1179-1196, 2007.

Zapata-Gonzalez, I.; Saldívar-Guerra, E. The method of moments used in polymerization reaction engineering for 70 years: an overview, tutorial, and minilibrary. Canadian Journal of Chemical Engineering, 101, 9, 5324-5356, 2023.

Chapter 6

Droplet and Particle Size Distributions in an Oscillatory Baffled Reactor: Population Balance Model

In this chapter, the population balance model developed in Chapter 2 is extended to describe the particle/droplet size distributions in continuous oscillatory baffled reactors (COBR). More specifically, in addition to representing the mass, energy, and statistical moment balances in each tank, a discrete representation of the droplet size distributions is appended to the set of model differential equations that describes the COBR. In contrast to the population balance model applied to a batch reactor where the size of the population is solely governed by breakage and coalescence, in this part of the work, the flow streams leaving and entering the reactor also affect the overall balance. It is important to emphasize that the present model considers all the suspension properties and kinetics presented in the previous chapter coupled with the distributed population balance model.

6.1 Model Development

6.1.1 Distributed Population Balance Model

Population balance models have become an attractive tool to describe particulate systems (Ramkrishna and Singh, 2014). Based on this modeling approach, it is possible to describe how the properties of a population vary with operational conditions and time (dynamic models). For instance, this modeling approach can be applied to crystallization, granulation, aerosol dynamics, and suspension polymerizations (Ramkrishna and Singh, 2014; Kiparissides, 2006). Depending on the systems in consideration and the phenomena taking place among the individuals of the population, different properties can be chosen as independent variables (Solsvik *et al.*, 2013). For example, crystal shape and size in crystallization systems (Zhou *et al.*, 2022; Costa *et al.*, 2007) and droplet or particle sizes in suspension polymerizations (Kiparissides, 2006; Machado *et al.*, 2000). A detailed derivation of the continuous population balance model based on different principles can be found in Solsvik and Jakobsen (2015).

Based on Figure 6.1, the population balance model to describe the number of droplets N of mass ϑ at tank n is shown in Equation (6.1). Equation (6.1) is the population balance model presented by Kumar and Ramkrishna (1996) with additional contributions due to flow leaving and entering each tank. Differently from the population balance model described in Chapter 2, Equation (6.1) represents a distributed population balance since the number of droplets with a specified mass is a function of time and position along the reactor (represented by the tank number n). According to this representation, $kc_n(\zeta, \vartheta)$ represents the coalescence rate constant of droplets with masses ζ and ϑ, respectively; $kb_n(\vartheta)$ represents the breakage rate constant of droplets of mass ϑ; $\beta(\zeta, \vartheta)$ is the daughter droplet distribution, representing the probability of a droplet of mass ϑ to be obtained from the breakage of a droplet of mass ζ; $\gamma(\zeta)$ is the number of daughter droplets resulting from the breakage of a droplet of mass ζ, and V_n is the volume of tank n. Therefore, the first term on the right-hand side of Equation (6.1) represents the number of droplets of mass ϑ in the feed. The second term is the number of droplets coming from the previous tank. The third term represents the droplets that come due to backflow from the posterior tank. The fourth and fifth terms represent the number of droplets that leave the tank due to the output flow rate and backflow streams, respectively. The remaining terms represent the consumption/generation due to breakage and coalescence. More specifically, the sixth term on the right-hand side of Equation (6.1)

represents the appearance of droplets of mass ϑ due to the coalescence of smaller ones. By analogy, the seventh term represents the disappearance of droplets of mass ϑ due to coalescence with other droplets. Finally, the eighth term represents the appearance of droplets of mass ϑ due to the breakage of bigger droplets, and the last term represents the disappearance due to breakage.

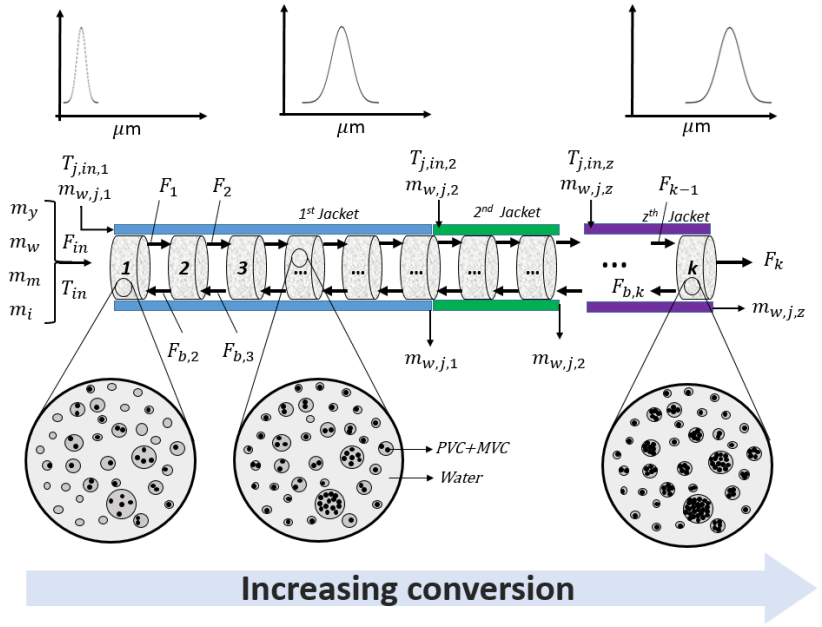

Figure 6.1: Schematic representation of the droplets and particles in the COBR.

$$\begin{aligned}
\frac{dN_n(\vartheta)}{dt} &= F_{in}\frac{N_{in}(\vartheta)}{V_n}\phi(n) + F_{n-1}\frac{N_{n-1}(\vartheta)}{V_{n-1}}(1-\phi(n)) \\
&+ F_{b,n+1}\frac{N_{n+1}(\vartheta)}{V_{n+1}}(1-\phi(k-n+1)) - F_n\frac{N_n(\vartheta)}{V_n} - F_{b,n}\frac{N_n(\vartheta)}{V_n}(1-\phi(n)) \\
&+ \frac{1}{2}\int_0^{\vartheta} kc_n(\zeta,\vartheta-\zeta)\frac{N_n(\zeta)}{V_n}\frac{N_n(\vartheta-\zeta)}{V_n}V_n d\zeta - \int_0^{\infty} kc_n(\zeta,\vartheta)\frac{N_n(\zeta)}{V_n}\frac{N_n(\vartheta)}{V_n}V_n d\zeta \\
&+ \int_{\vartheta}^{\infty} kb_n(\zeta)\beta(\zeta,\vartheta)\gamma(\zeta)\frac{N_n(\zeta)}{V_n}V_n d\zeta - kb_n(\vartheta)\frac{N_n(\vartheta)}{V_n}V_n
\end{aligned} \tag{6.1}$$

In addition to Equation (6.1), the following restriction (Equation (6.2)) must be satisfied in order to conserve the mass after breakage:

$$\int_0^{\zeta} \vartheta\gamma(\zeta)\beta\left(\zeta,\vartheta\right)d\vartheta = \zeta \tag{6.2}$$

By discretizing the internal variable mass as $\zeta_i = i\Delta\zeta$, $i = 1, ..., nc$ with $\Delta\zeta = \zeta_{max}/nc$, the following set of differential equations can be obtained (Equations (6.3) and (6.4)). This discretization approach is based on the mean value theorem (MI approach) on number frequency (Kumar and Ramkrishna, 1996). Hidy (1965) and Gelbard and Seinfeld (1979) used similar approaches to solve population balances. It is worth to mention that in the present model, if $\zeta_l + \zeta_i > \zeta_{max}$ then $kc_n(\zeta_l, \zeta_i) = 0$ to avoid forming particles with masses outside of the discretization range. $nc = 100$ was used to generate the discretization grid.

$$\begin{aligned}
&\frac{dN_n(\zeta_i)}{dt} = F_{in}\frac{N_{in}(\vartheta)}{V_n}\phi(n) + F_{n-1}\frac{N_{n-1}(\vartheta)}{V_{n-1}}(1-\phi(n)) \\
&+ F_{b,n+1}\frac{N_{n+1}(\vartheta)}{V_{n+1}}(1-\phi(k-n+1)) - F_n\frac{N_n(\vartheta)}{V_n} - F_{b,n}\frac{N_n(\vartheta)}{V_n}(1-\phi(n)) \\
&+ \frac{1}{2}\sum_{l=1}^{i-1} kc_n(\zeta_l, \zeta_{i-l})\frac{N_n(\zeta_l)}{V_n}\frac{N_n(\zeta_{i-l})}{V_n}V_n - \sum_{i=1}^{nc} kc_n(\zeta_l, \zeta_i)\frac{N_n(\zeta_l)}{V_n}\frac{N_n(\zeta_i)}{V_n}V_n \\
&+ \sum_{l=i+1}^{nc} kb_n(\zeta_l)\beta(\zeta_l, \zeta_i)\gamma(\zeta_l)\frac{N_n(\zeta_l)}{V_n}V_n - kb_n(\zeta_i)\frac{N_n(\zeta_i)}{V_n}V_n
\end{aligned} \tag{6.3}$$

$$\sum_{l=1}^{i} \zeta_l \gamma(\zeta_i)\beta(\zeta_i, \zeta_l) = \zeta_i \tag{6.4}$$

6.1.2 Breakage and Coalescence Rates

The models of breakage and coalescence proposed by Coulaloglou and Tavlarides (1977) were used to describe the mechanisms occurring at droplet level, Equations (6.5) and (6.6). For convenience, the equations shown in this part of the work are parametrized in terms of energy dissipation and the properties of the dispersion as reported by Alopaeus *et al.* (1999). In their original work Coulaloglou and Tavlarides investigated liquid-liquid dispersions in agitated vessels, as such, their models take into account impeller rotation and diameter. However, given the geometry of the COBR, it becomes favorable to express the breakage and coalescence models as functions of the energy dissipation.

According to Solsvik *et al.* (2013) and Azizi and Al Taweel (2011), Coulaloglou and Tavlarides' breakage model assumes a locally isotropic turbulent flow field and that the droplets are in the inertial subrange of turbulence with negligible viscous effects. Moreover, droplet deformation and breakage are caused by local pressure

fluctuations. This models is widely utilized to model liquid-liquid dispersions even though there is criticism regarding model predictions. For instance, Lasheras *et al.* (2002) and Tsouris and Tavlarides (1994) criticized the fact that the breakage model predicts a value of diameter in which the breakage rate is maximized. At diameters larger than this value, the breakage rate decreases.

$$kb_n^{'}(\zeta) = c_1 \zeta^{-2/9} \frac{\varrho_n^{1/3}}{1+\Phi_{d,n}} exp\left(-c_2 \frac{\sigma_{\sigma,n}(1+\Phi_{d,n})^2}{\rho_{d,n}\zeta^{5/9}\varrho_n^{2/3}}\right) \tag{6.5}$$

$$kc_n^{'}(\zeta,\vartheta) = c_3\left(\zeta^{1/3}+\vartheta^{1/3}\right)^2\left(\zeta^{2/9}+\vartheta^{2/9}\right)^{1/2}\frac{\varrho_n^{1/3}}{1+\Phi_{d,n}}\times exp\left(-c_4\frac{\eta_{c,n}\rho_{c,n}}{\sigma_{\sigma,n}^2}\frac{\varrho_n}{(1+\Phi_{d,n})^3}\left(\frac{\zeta^{1/3}\vartheta^{1/3}}{\zeta^{1/3}+\vartheta^{1/3}}\right)^4\right) \tag{6.6}$$

As the polymerization reaction proceeds, the morphology and properties of the droplets vary because of the changes in suspension properties. Since the density of the polymer is higher than the density of the monomer, when the fraction of polymer increases, the polymerizing droplets shrink. Additionally, the viscosity of the dispersed phase increases and surface tension increases (Maggioris *et al.*, 2000). In order to make the proposed modeling approach more realistic, the breakage and coalescence rate constants of Coulaloglou and Tavlarides were modified to take into account the effects of the conversion on the breakage and coalescence rates. More specifically, as proposed by Silva *et al.* (2023) and shown in Chapter 2, it was assumed that the breakage and coalescence rates decrease in the range of conversion from zero to 30% and become null thereafter (Equation (6.7) and Equation (6.8)). This assumption was based on the literature regarding poly(vinyl chloride) suspension polymerization. For instance, Máriási (1986) and Guo *et al.* (2017) have investigated experimentally the evolution of the droplets and particles in PVC polymerization and have agreed that after 30% conversion the mean particle diameter of the suspension remains constant independently of the stirring speed due to the rigidity of the droplets.

$$kb(\zeta) = \begin{cases} kb_n^{'}(\zeta)\left(1-\frac{x_n}{0.3}\right)^2 & \text{if } x \leq 0.3 \\ 0 & \text{otherwise} \end{cases} \tag{6.7}$$

$$kc_n(\zeta,\vartheta) = \begin{cases} kc_n'(\zeta,\vartheta)\left(1-\frac{x_n}{0.3}\right)^2 & \text{if } x \leq 0.3 \\ 0 & \text{otherwise} \end{cases} \tag{6.8}$$

6.1.3 Power Dissipation

According to Avila *et al.* (2022), the power dissipation is one of the most important parameters that govern heat transfer, mixing and scale-up. According to the literature review presented in Chapter 3, many works have attempted to describe the power dissipation in oscillatory baffled reactors both experimentally and theoretically (Mackley and Stonestreet, 1995; Jimeno *et al.*, 2018; Avila *et al.*, 2020; Muñoz-Cámara *et al.*, 2021). In this work, the power dissipation model derived based on the quasi steady state assumption (Jealous and Johnson, 1955) and reported by Mackley and Stonestreet (1995) is used, Equation (6.9). Is is worth mentioning that Equation (6.9) accounts only the power dissipation due to oscillatory flow neglecting the continuous flow contribution. For practical purposes, the COBR is expected to operate at low flow rates (long residence times), therefore, the power dissipation due to the net continuous flow can be neglected. According to Equation (6.9), the power dissipation varies linearly with the number of baffles per unit length of the reactor (N_b/L) and depends on the discharge coefficient of the orifice (C_d, usually assumed equal to 0.7). As the ratio of the orifice diameter to the tube diameter (restriction ratio $\alpha_o = d_o^2/d_{r,int}^2$) decreases, the power dissipation increases. Moreover, power dissipation increases to the third power with respect to the oscillation velocity ($f_o\chi_o$).

$$\varrho_n = \frac{2\rho_{s,n}N_b\left(2\pi f_o\chi_o\right)^3}{3\pi C_d^2 L}\left(\frac{1}{\alpha_o^2}-1\right) \tag{6.9}$$

6.1.4 Daughter Droplet Distribution

In this work, it was assumed that two unequal droplets are formed, so that $\gamma(\zeta) = 2$ (binary breakage). The daughter droplet distribution, Equation (6.10), was proposed by Mikos *et al.* (1986). In Equation (6.10), $\bar{\vartheta} = \frac{\zeta}{\gamma(\zeta)}$ and $\sigma_\beta = 0.4\bar{\vartheta}$. The authors carefully calculated these parameters in order to make sure that the distribution relies in the range from 0 to ζ guaranteeing that its integral is equal to

1.

$$\beta(\zeta,\vartheta)=\frac{1}{\sigma_\beta\sqrt{2\pi}}exp\left(-\frac{\left(\vartheta-\bar{\vartheta}\right)^2}{2\sigma_\beta^2}\right) \tag{6.10}$$

6.1.5 Mean Diameters

Finally, assuming that the particles are of spherical shape, the particle and droplet diameters can be calculated as Equations (6.11) and (6.12). Equations (6.13) and (6.14) were proposed by assuming that the PVC particles are spherical and a bed of these particles has a porosity of 40%. Since at $x \leq x_f$ the droplet has monomer and polymer, in this range of conversion $\epsilon_n = \epsilon_{f,n}$ if $\epsilon_{m,n} > \epsilon_{f,n}$, otherwise, $\epsilon_n = \epsilon_{m,n}$. Equation (6.15) represents the Sauter mean diameter ($d_{32,n}$) which is an average diameter.

$$d_{p,i,n}=\left[\frac{6x_n\zeta_i}{(1-\epsilon_n)\rho_p\pi}\right]^{1/3} \tag{6.11}$$

$$d_{d,i,n}=\left(\frac{6\zeta_i}{\rho_{d,n}\pi}\right)^{1/3} \tag{6.12}$$

$$\epsilon_{f,n}=0.4+0.6\left(1-\varphi_{p,n}\right) \tag{6.13}$$

$$\epsilon_{m,n}=\frac{\frac{1-x_n}{\rho_m}}{\frac{1-x_n}{\rho_m}+\frac{x_n}{\rho_p}} \tag{6.14}$$

$$d_{32,n}=\frac{\sum_{i=1}^{nc}N(\zeta_i)d_{i,n}^3}{\sum_{i=1}^{nc}N(\zeta_i)d_{i,n}^2} \tag{6.15}$$

6.1.6 Initial Condition

The initial and feed droplet size distributions were assumed to follow a Gaussian distribution (Equation (6.16)). In Equation (6.16), $\sigma_0^2 = 5.0 \times 10^{-11}$ and $\bar{\zeta} = 2.38 \times 10^{-10}$, in accordance with available literature data. The system of differential-algebraic equations was solved with the DASSL solver (Petzold, 1982) in a Fortran environment. Equation (6.16) applies for $n = 1, 2, 3, .., k$ tanks and $i = 1, 2, ..., nc$.

$$N_{in} = N_{0,n}(\zeta_i) = \frac{\Omega_i}{\sqrt{2\pi\sigma_0^2}} exp\left(-\frac{\left(\zeta_i - \bar{\zeta}\right)^2}{2\sigma_0^2}\right) \tag{6.16}$$

6.2 Results and Discussion

6.2.1 Breakage and Coalescence Parameters

Before discussing the set of breakage and coalescence parameters used to perform the simulations (c_1, c_2, c_3 and c_4), it is important to address some of the works that investigated droplet size distributions (DSD) in oscillatory baffled reactors. Figure 6.2 shows the predictions of Sauter mean diameter d_{32} obtained with the correlations shown in Table 6.1 evaluated in their range of applicability. A detailed overview of these works including the reactor geometry operation mode and liquid-liquid system was given in Chapter 3. Even though some of the works present these correlations in terms of the oscillation conditions, it is more convenient to express them in terms of the energy dissipation (ϱ) because it makes the comparison with other systems straightforward. By analysing Figure 6.2, one can conclude that there is variability in the predictions of the mean droplet diameters depending on the work. This variability can be attributed to the reactor size, geometry, operation mode, and the properties of the suspension (viscosity, density, dispersed phase fraction and surface tension).

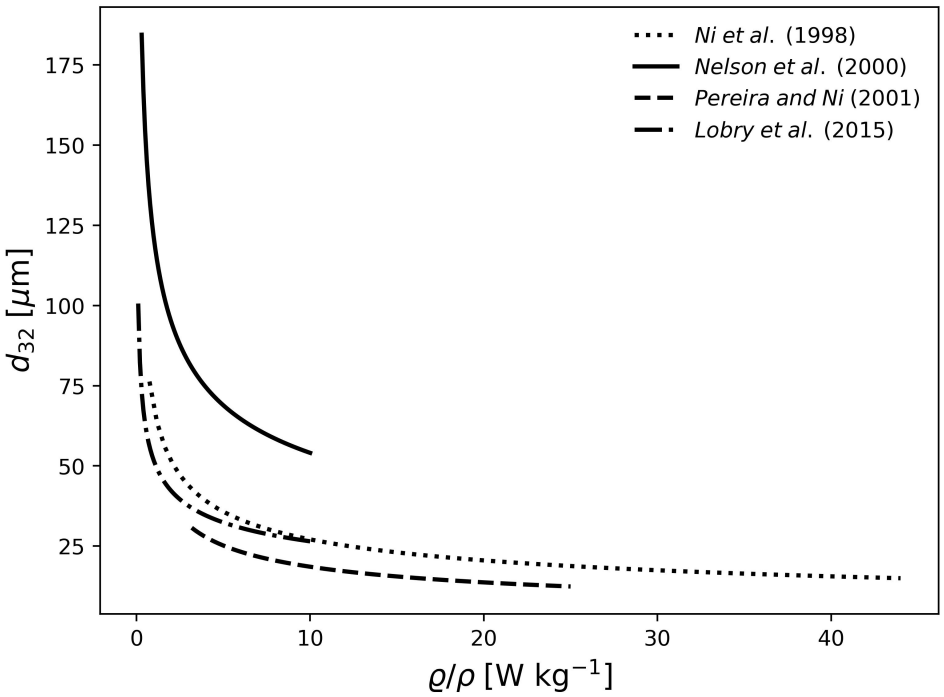

Figure 6.2: Predicted Sauter mean diameter by different correlations.

Table 6.1: Some mean droplet size correlations.

Reference	**Equation**
Ni *et al.* (1998)	$d_{32} = 6.8 \times 10^{-5} \left(\frac{\varrho}{\rho}\right)^{-0.4}$
Nelson *et al.* (2000)	$d_{32} = 12.1 \times 10^{-5} \left(\frac{\varrho}{\rho}\right)^{-0.35}$
Pereira and Ni (2001)	$d_{32} = 3.7 \times 10^{-5} \left(\frac{\varrho}{\rho}\right)^{-0.3} \left(\frac{\varrho}{\rho}\right)_{net}^{-0.14}$
Lobry *et al.* (2015)	$d_{32} = 5.16 \times 10^{-5} \left(\frac{\varrho}{\rho}\right)^{-0.29}$

Since there is no available droplet size distribution data regarding suspension polymerization of vinyl chloride in a COBRs in the open literature, a strategy was developed to, at least, investigate the qualitative behavior of the DSDs and particle size distributions (PSD) obtained in such devices. For this purpose, the parameters c_1 and c_2 of the breakage rate constant (Equation (6.5)) were adjusted to obtain breakage rate constants of the order of 10^{-4}-10^{-3} at diameters ranging from 20 to 100 μm as reported by Ni *et al.* (2002a). More specifically, Ni *et al.* (2002a) developed a population balance model and estimated the breakage rate constants to represent methyl methacrylate/water suspensions studied by Ni *et al.* (1998) using an optimization algorithm. Figure 6.3 shows the predictions of Equation (6.5) at different hold up fractions. In these simulations, c_1 and c_2 were assumed equal to

3.32×10^{-6} and 200.47, respectively. As expected, Equation (6.5) predicts that larger particles are more prone to breakage than smaller ones.

Ni *et al.* (2002b) also reported coalescence rate constants of the order of $10^{-12} - 10^{-14}$ for droplets of of size less than 500 μm for a wide range of operation conditions. Therefore, the parameters c_3 and c_4 were also adjusted in order to give coalescence rate constants of this order of magnitude. More specifically, c_3 and c_4 were assumed equal to 5.27×10^{-6} and 1.41×10^{7}, respectively. Figure 6.4 shown the coalescence rate constants (Equation (6.6)) calculated with these parameters. It is important to emphasize, once again, that the proposed approach intends to give an approximation of what is expected to occur at the droplet level when vinyl chloride is polymerized in an oscillatory baffled reactor.

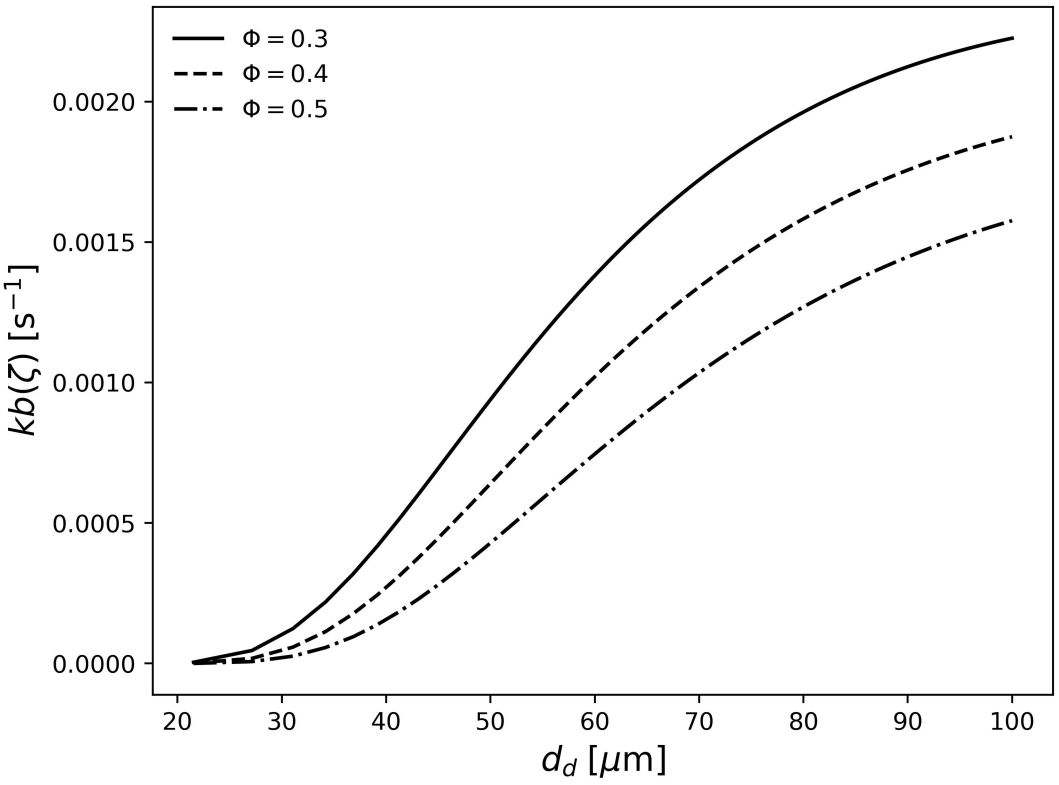

Figure 6.3: Breakage rate constant evaluated at different droplet diameters and dispersed phase fractions.

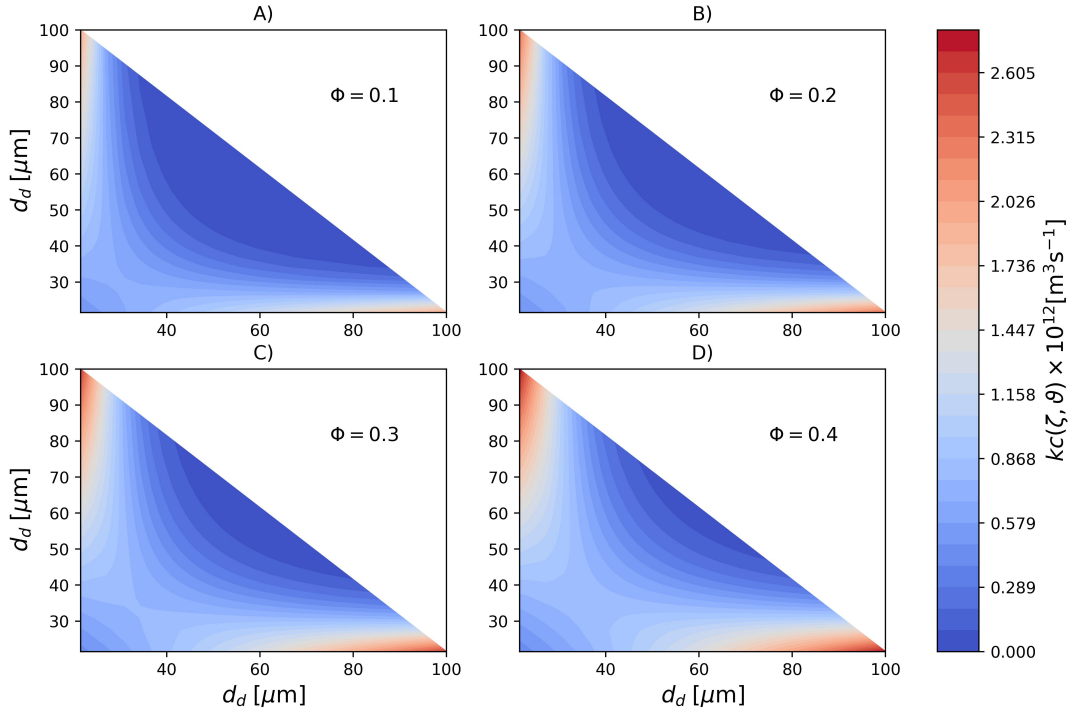

Figure 6.4: Coalescence rate constant evaluated at different droplet diameters and dispersed phase fractions.

6.2.2 Effect of Power Dissipation

Before performing perturbation tests, a simulation was performed to serve as basis for comparison. Figure 6.5 shows the steady state conversion profile along the reactor length for the simulation performed using di(2-ethylhexyl) peroxydicarbonate as initiator with a molar flow rate of 0.0065% of the monomer flow rate. In this simulation, the dispersed phase fraction (Φ_d, holdup) was 40% and the suspending agent, poly(vinyl alcohol), mass flow rate ($\dot{m}_y$) was 7.2×10^{-7} kg s^{-1}. The residence time was kept equal to 288 min. Since temperature control aspects have been thoroughly investigated in the previous chapter, this part of the work assumes isothermal operation (T = 331.15 K) in order to focus our attention on the phenomena that occur at the droplet and particle level. Additionally, in the last chapter it was shown that the COBR can achieve nearly isothermal temperature profiles if the control loops and operation conditions are properly tuned which justifies the assumption of isothermal operation used in this part of the work. Furthermore, due to computational limitations, the number of tanks (k) was made equal to 10 and the backflow rate was considered null ($F_{b,n} = 0$) to resemble a plug flow regime. According to Levenspiel (1998), a model with 10 tanks in series already shows a certain degree of plug flow behavior.

Regarding the oscillatory conditions, the reference simulation was performed with $\chi_o = 0.034$ m and $f_o = 1$ Hz. Considering the reactor geometry presented in Chapter 4 and these oscillatory conditions, the power dissipation per volume calculated using Equation 6.9 is $\varrho = 2100$ W m^{-3}. Figures 6.6 and 6.7 show the dynamic evolution of the droplet size distribution at the reactor outlet and the steady state profile along the reactor length, respectively. The z-axis in these plots represent the probability density function (PDF), i.e., the derivative of the cumulative distribution function (CDF).

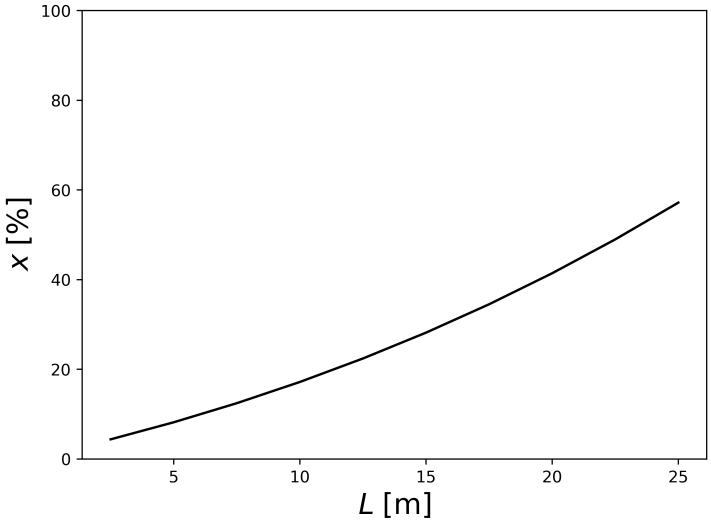

Figure 6.5: Steady state conversion profile.

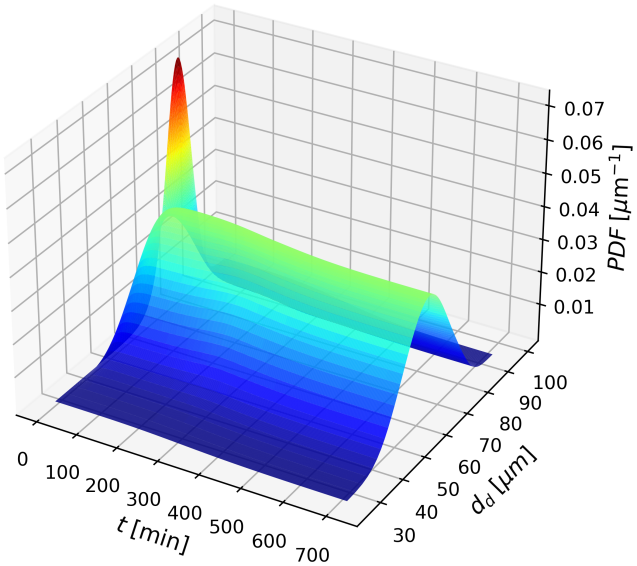

Figure 6.6: Dynamic droplet size distribution at the reactor outlet.

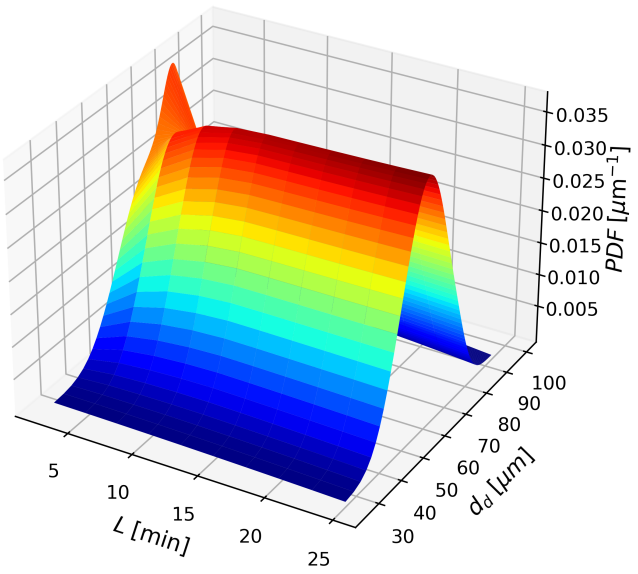

Figure 6.7: Steady state droplet size distribution along the reactor length.

In Figure 6.6, the highest peak at $t = 0$ corresponds to the initial distribution. It can be noticed that the breakage is very intense and the average of the droplet size distribution moves towards smaller particles very fast. Moreover, the distribution becomes broader, i.e. with larger variance. In Figure 6.7, the steady state distribution after $x = 30\%$ is does not vary along the reactor length. This is a consequence of the hypothesis assumed during the modeling step that after 30% conversion the rates of breakage and coalescence become null due to the rigidity of the polymerizing droplets (Equations (6.7) and (6.8)).

Figure 6.8 depicts a comparison among simulations performed assuming different oscillatory conditions, i.e., energy dissipation. The oscillation condition in which $\chi_o = 0.029$ m and $f_o = 1$ Hz corresponds to $\varrho = 1300$ W m^{-3}, whereas $\chi_o = 0.0385$ m and $f_o = 1$ Hz corresponds to $\varrho = 3056$ W m^{-3}. Parts A and B of Figure 6.8 show the particle size CDF and PDF at the reactor outlet, respectively. Additionally, Parts C and D show the Sauter mean diameter of the particles and droplets, respectively.

According to Part B, it is noticeable that the PDF obtained with $\varrho = 1300$ W m^{-3} is not symmetrical. In other words, the distribution shows a negative skewness. On the other hand, at $\varrho = 2100$, the distribution becomes symmetrical around the mean. Finally, at $\varrho = 3056$, the distribution exhibits slight positive skewness. These differences is the shape of the distribution can be attributed to the ratio between the rates of breakage and coalescence. When ϱ decreases from 2100 to 1300, the Sauter mean diameter of the droplets and particles (Figure 6.8, C and D), increases

13.06%. On the other hand, when ϱ increases from 2100 to 3056, the Sauter mean diameter of the droplets and particles decreases 9.47%.

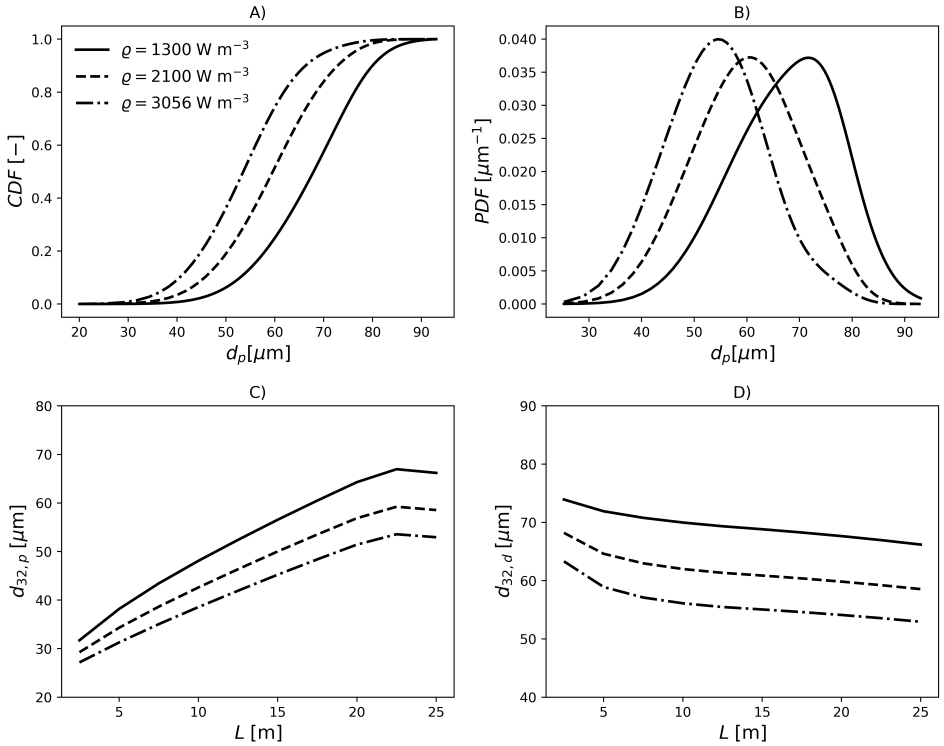

Figure 6.8: Effect of the power dissipation. A) particle size cumulative distribution function, B) particle size probability density function, C) steady state Sauter mean diameter of the particles, and D) steady state Sauter mean diameter of the droplets.

6.2.3 Effect of Dispersed Phase Fraction

The dispersed phase fraction (Φ_d) is a key variable in suspension polymerization processes. First of all, this variable is related to process productivity. In order to improve process economics it is always desirable to operate the system at high dispersed phase fractions respecting the constraints imposed by the phenomena that take place at the droplet level. In order to investigate the effect of the dispersed phase fraction on the final particle size distributions, simulations were performed assuming different Φ_d and keeping the remaining variables constant, i.e., $\varrho = 2100$ W m^{-3} in all simulations. More specifically, values of Φ_d up to 0.4 were investigated.

Figure 6.9 shows the particle size cumulative distribution function, particle size probability distribution function and average particle and droplet diameters. As the dispersed phase fraction decreases from 0.4 to 0.3, the final Sauter mean diameter of the particles and droplets decreases 7.53%. Additionally, when the dispersed phase fraction decreases from 0.4 to 0.2, the final Sauter mean diameter of the particles and droplets decreases 15.91%.

To understand these effects, it is important to look at Equations (6.5) and (6.6). First of all, in Equation (6.5), Φ_d appears in the denominator of the term that multiplies the exponential and in the denominator of the exponential term, consequently, the effect of increasing Φ is the reduction of the breakage rate. On the other hand, in Equation (6.6), Φ appears in the denominator both outside and inside the exponential term. Moreover, the term inside the exponential is raised to third power causing a net increase in the coalescence rate. Therefore, increasing the dispersed phase fraction causes a net increase in the average particle and droplet diameters.

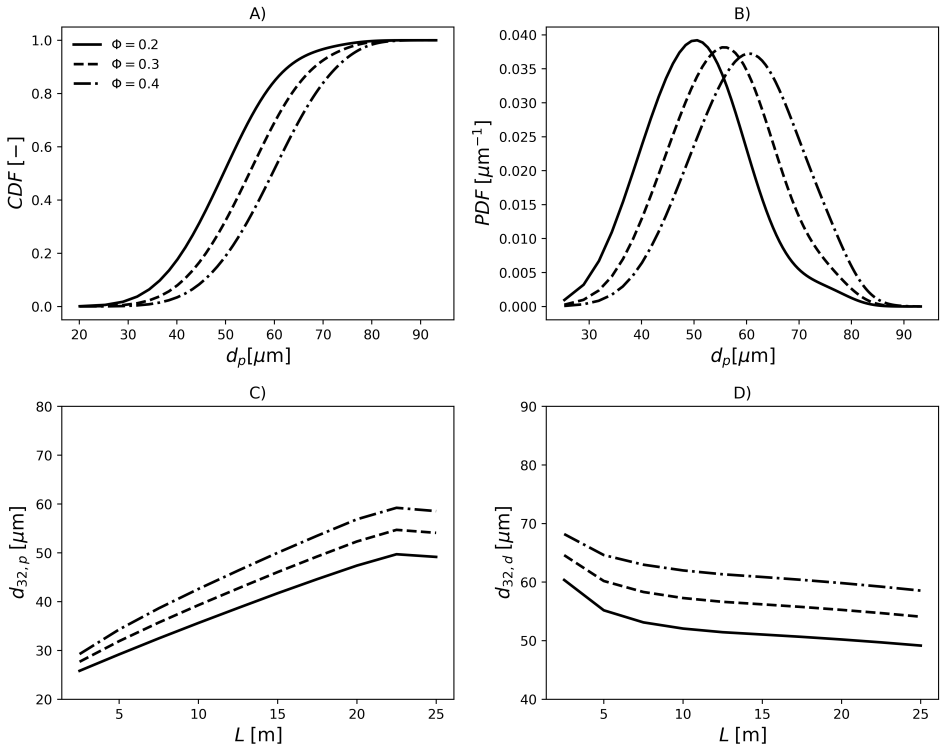

Figure 6.9: Effect of the dispersed phase fraction. A) particle size cumulative distribution function B), particle size probability density function, C) steady state Sauter mean diameter of the particles, and D) steady state Sauter mean diameter of the droplets.

6.2.4 Effect of Suspending Agent Flow Rate

The suspending agent has the task o stabilizing the droplets in the suspension. In the present model, it was considered that poly(vinyl alcohol) was used as suspending agent. More specifically, the effect of the its concentration on the surface tension of the droplets was represented as in Chapter 2 (See the last Equation in Table 5.2) and used by Silva *et al.* (2023) to represent particle size distributions in industrial batch reactors. In Figure 6.10, the simulation performed assuming $\varrho = 2100$ W m^{-3} was performed at two different poly(vinyl alcohol) mass flow rates. It can be noticed that reducing the poly(vinyl alcohol) flow rate by half results in larger particles. This occurs because smaller poly(vinyl alcohol) concentrations increase the surface tension of the droplets resulting in higher average diameters. In the simulated conditions, decreasing $\dot{m}_y$ from 7.2×10^{-7} to 3.6×10^{-7} results in an increase of 7.97% of the droplet and particle Sauter mean diameters.

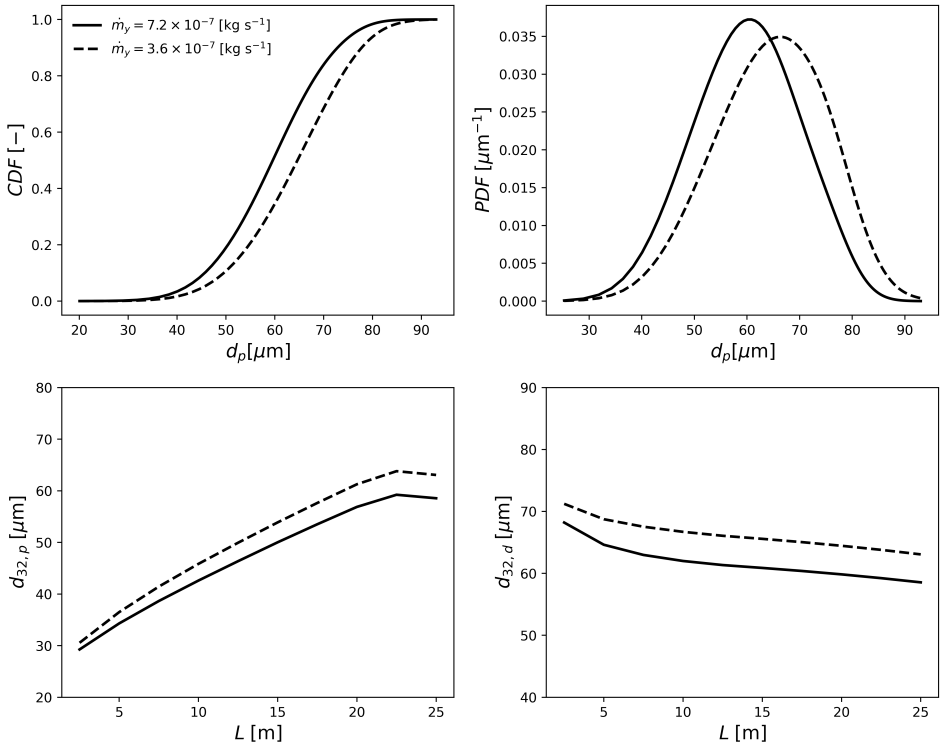

Figure 6.10: Effect of the suspending agent concentration. A) particle size cumulative distribution function B), particle size probability density function, C) steady state Sauter mean diameter of the particles, and D) steady state Sauter mean diameter of the droplets.

6.3 Concluding Remarks

In this chapter, a distributed population balance model was developed and implemented to describe the dynamic and steady state profiles of droplet and particle size distributions in a COBR. Breakage and coalescence kernels from the literature were employed to describe the droplet interactions. Moreover, the hypotheses employed and validated with batch industrial data (Chapter 2) were transported to the COBR system with the expectation that similar results would be obtained in the oscillatory baffled reactor. Even though a rigorous parameter estimation procedure was not performed, it is believed that the model predictions can, at least, give some qualitative insights on the behavior of droplet and particle size distributions in oscillatory baffled reactors.

List of Abbreviations

Abbreviation	Meaning
COBR	Continuous Oscillatory Baffled Reactor
CDF	Cumulative density function
DSD	Droplet size distribution
PDF	Probability density function
PSD	Particle size distribution
PVC	Poly(vinyl chloride)

List of Symbols

Symbol	Meaning
C_d	Orifice discharge coefficient [-]
d_{int}	Reactor internal diameter [m]
d_d	Droplet diameter [m]
d_p	Particle diameter [m]
d_{32}	Sauter mean diameter [m]
f_o	Frequency of oscillation [s^{-1}]
F	Flow rate [m^3 s^{-1}]
F_b	Backflow rate [m^3 s^{-1}]
F_{in}	Inlet flow rate [m^3 s^{-1}]

kb	Breakage rate constant [s^{-1}]
kc	Coalescence rate constant [m^3 s^{-1}]
L	Reactor length [m]
$N(\vartheta)$	Number of droplets with mass ϑ [-]
N_b	Number of baffles [-]
V	Tank volume [m^3]
x	Conversion [-]
Subscripts	
n	Tank number
Greek letters	
α	Restriction ratio [%]
$\beta(\zeta, \vartheta)$	Daughter droplet distribution [-]
χ_o	Center-to-peak amplitude of oscillation [m]
ϵ	Porosity [-]
η_c	Continuous phase viscosity [kg m^{-1} s^{-1}]
$\gamma(\zeta)$	Number of droplets per breakage [-]
ϱ	Power dissipation [W m^{-3}]
σ_σ	Surface tension [N m^{-1}]
σ_0^2	Variance [Kg^2]
ρ_c	Continuous phase density [kg m^{-3}]
ρ_d	Dispersed phase density [kg m^{-3}]
ζ, ϑ	Droplet masses [kg]
Φ_d	Dispersed phase volume fraction [-]

6.4 References

Avila, M., Kawas, B., Fletcher, D.F., Poux, M., Xuereb, C., Aubin, J. Design, performance characterization and applications of continuous oscillatory baffled reactors. Chemical Engineering and Processing - Process Intensification, 180, 108718, 2022.

Avila, M.; Fletcher, D.F.; Poux, M.; Xuereb, C.; Aubin, J. Predicting power consumption in continuous oscillatory baffled reactors. Chemical Engineering Science, 212, 115310, 2020.

Alopaeus, V.; Koskinen, J.; Keskinen, K.I. Simulation of the population balances for liquid-liquid systems in a nonideal stirred tank. part 1 description and qualitative validation of the model. Chemical Engineering Science, 54, 24, 5887-5899, 1999.

Azizi, F.; Al Taweel, A.M. Turbulently flowing liquid-liquid dispersions. part I: drop breakage and coalescence. Chemical Engineering Journal, 166, 2, 715-725, 2011.

Costa, C.B.B.; Maciel, M.R.W.; Maciel Filho, R. Considerations on the crystallization modeling: population balance solution. Computers and Chemical Engineering, 31, 206-218, 2007.

Coulaloglou, C.A.; Tavlarides, L.L. Description of interation processes in agitated liquid-liquid dispersions. Chemical Engineering Science, 32, 11, 1289-1297, 1977.

Gelbard, F.; Seinfeld, J.H. The general dynamic equation for aerosols. theory and application to aerosol formation and growth. Journal of Colloid and Interface Science, 68, 2, 363-382, 1979.

Guo, R.; Yu, E.; Liu, J.; Wei, Z. Agitation transformation during vinyl chloride suspension polymerization: Aggregation morphology and PVC properties. RSC Advances, 7, 39, 24022-24029, 2017.

Hidy, G.M. On the theory of the coagulation of noninteracting particles in brownian motion. Journal of Colloid Science, 20, 2, 123-144, 1965.

Jealous, A.C.; Johnson, H.F. Power requirements for pulse generation in pulse columns. Industrial and Engineering Chemistry, 47, 6, 1159-1166, 1955.

Jimeno, G.; Lee, Y.C.; Ni, X.W. On the evaluation of power density models for oscillatory baffled reactors using CFD. Chemical Engineering and Processing: Process Intensification, 134, 153-162, 2018.

Kiparissides, C. Challenges in particulate polymerization reactor modeling and optimization: a population balance perspective. Journal of Process Control, 16, 3, 205-224, 2006.

Kumar, S.; Ramkrishna, D. On the solution of population balance equations by discretization - I. a fixed pivot technique. Chemical Engineering Science, 51, 8,

1311-1332, 1996.

Lasheras, J.C.; Eastwood, C.; Martínez-Bazán, C.; Montañés, J.L. A review of statistical models for the break-up of an immiscible fluid immersed into a fully developed turbulent flow. International Journal of Multiphase Flow, 28, 2, 247-278, 2002.

Levenspiel, O. Chemical Reaction Engineering, Third Edition, Wiley, New York, USA, 1998.

Lobry, E.; Lasuye, T.; Gourdon, C.; Xuereb, C. Liquid-liquid dispersion in a continuous oscillatory baffled reactor- application to suspension polymerization. Chemical Engineering Journal, 259, 505-518, 2015.

Machado, R.A.F.; Pinto, J.C.; Araújo, P.H.H.; Bolzan, A. Mathematical modeling of polystyrene particle size distribution produced by suspension polymerization. Brazilian Journal of Chemical Engineering, 17, 395-407, 2000.

Mackley, M.R.; Stonestreet, P. Heat transfer and associated energy dissipation for oscillatory flow in baffled tubes. Chemical Engineering Science, 50, 14, 2211-2224, 1995.

Maggioris, D.; Goulas, A.; Alexopoulos, A.H.; Chatzi, E.G.; Kiparissides, C. Prediction of particle size distribution in suspension polymerization reactors: effect of turbulence nonhomogeneity. Chemical Engineering Science, 55, 4611-4627, 2000.

Máriási, B. On the particle formation mechanism of poly(vinyl chloride)(PVC) powder produced by suspension polymerization-development of external morphology of particles. Journal of Vinyl Technology, 8, 1, 20-26, 1986.

Mikos. A.G.; Takoudis, C.G.; Peppas, N.A. Reaction engineering aspects of suspension polymerization. Journal of Applied Polymer Science, 31, 8, 2647-2659, 1986.

Muñoz-Cámara, J.; Solano, J.P.; Pérez-García, J. Analytical calculation of the flow superposition effect on the power consumption in oscillatory baffled reactors. Chemical Engineering Science, 229, 116084, 2021.

Nelson, G.; Ni, X.; Mustafa, I. Experimental measurement of droplet size distribution of a MMA suspension in a batch oscillatory reactor of 0.21m diameter. 10^{th} European Conference on Mixing, Eds: H.E.A. van den Akker and J.J. Derksen,

Elsevier, 2000.

Ni, X.; Zhang, Y.; Mustafa, I. An investigation of the droplet size and size distribution in methylmethacrylate suspensions in a batch oscillatory-baffled reactor. Chemical Engineering Science, 53, 16, 2903-2919, 1998.

Ni, X.; Murray, K.R.; Zhang, Y.; Bennett, D.; Howes, T. Polymer product engineering utilising oscillatory baffled reactors. Powder Technology, 124, 3, 281-286, 2002a.

Ni, X.; Mignard, D.; Saye, B.; Johnstone, J.C.; Pereira, N. On the evaluation of droplet breakage and coalescence rates in an oscillatory baffled reactor. Chemical Engineering Science, 57, 11, 2101-2114, 2002b.

Pereira, N.E.; Ni, X. Droplet size distribution in a continuous oscillatory baffled reactor. Chemical Engineering Science, 56, 3, 735-739, 2001.

Petzold, L.R. Description of DASSL: A differential/Algebraic System Solver; Sandia National Labs.: Livermore, CA, USA, 1982.

Ramkrishna, D.; Singh, M.R. Population balance modeling: current status and future prospects. Annual Review of Chemical and Biomolecular Engineering, 5, 123-146, 2014.

Silva, J.S.; Melo, P.A.; Pinto, J.C. Modeling of particle size distributions in industrial poly(vinyl chloride) suspension polymerization reactors. Processes, 11, 5, 1440, 2023.

Solsvik, J.; Tangen, S.; Jakobsen, H.A. On the constitutive equations for fluid particle breakage. Reviews in Chemical Engineering, 29, 5, 241-356, 2013.

Solsvik, J.; Jakobsen, H.A. The foundation of the population balance equation: a review. Journal of Dispersion Science and Technology, 36, 4, 510-520, 2015.

Tsouris, C.; Tavlarides L.L. Breakage and coalescence models for drops in turbulent dispersions. AIChE Journal, 40, 3, 395-406, 1994.

Zhou, H.Y.; Zhou, G.Z.; Wang, X.Z. Multi-objective optimization of protein cooling crystallization with morphological population balance models. Journal of Crystal Growth, 588, 126664, 2022.

Chapter 7

Conclusions

"This above all: to thine one self be true."

W. Shakespeare, The Tragedy of Hamlet

In this work, several aspects of continuous suspension polymerization in oscillatory baffled reactors were investigated. The kinetics, heat transfer, equilibrium relationships, averages of the molar mass distribution and particle size distributions were taken into consideration to describe two polymerization systems: poly(vinyl acetate)/vinyl acetate/water and poly(vinyl chloride)/vinyl chloride/water. The modeling approach developed was able to describe the literature data regarding the polymerization of vinyl acetate with fair accuracy. The oscillatory baffled reactor has improved heat transfer capacity, even at low net Reynolds number, which can be of paramount importance to control highly exothermic reactions such as polymerizations. Proper tuning of the operation conditions can lead to isothermal temperature profiles. Moreover, since the oscillation conditions can be adjusted to keep dispersion at a minimum, i.e., low backmixing, the reactor is suitable to obtain products with very similar properties, i.e., molar mass distribution and particle size distribution. Additionally, the heat transfer can be decoupled from the residence time which creates a degree of freedom in the operation allowing the proper control of temperature and product size distributions simultaneously.

Dividing the initiator feed can lead to more uniform heat generation profiles improving the heat transfer capacity and making the COBR attractive to conduct reactions governed by strong gel and glass effects. The proposed modeling approach can be extended to perform design of experiments, parameter estimation and process

control strategies. However, there is still a long road to reach continuous suspension polymerization at industrial level.

The main hurdles ahead include the non-newtonian behavior of polymer melts and the settling of larger polymer particles as the conversion advances and the droplets become denser. Flow assurance at higher hold up and conversion is a challenge that can be tackled by investigating different baffle designs and using multiple pistons to promote the oscillation and to avoid the oscillation dampening.

The process scale-up also constitutes an important area of investigation. It should be investigated weather increasing reactor diameter and throughput or operating several small diameter reactors in series is more efficient than the current industrial batch process. To answer this question, the costs of construction and operation must be evaluated. Moreover, experimental and modeling studies should also be carried out to understand the effects of the operation conditions on the product final properties and fouling. In this respect, computational fluid dynamic studies can be a powerful tool to investigate the effects of the operation conditions, baffle design and reactor geometry on the rates of energy dissipation and shear rates, and how these variables influence the particle size distributions and particle morphology.

Appendix A

Demonstration of the Moment Equations

Here, a demonstration of the moment equations for a free radical polymerization kinetic scheme in a batch system is given. The extension of the moment equations to continuous systems is straightforward, i.e., it is simply necessary to add an inlet and an outlet term in the equations. The kinetic schemes studied in this Thesis are simplified versions of this more general kinetic scheme taken from Kiparissides et al. (1997) and shown in Table A.1. The interested reader should consult Mastan and Zhu (2015) for more details about the method of moments.

Table A.1: Free radical polymerization mechanism.

Step	Reaction
Initiator decomposition	$I \xrightarrow{kd} 2I^*$
Chain initiation	$I^* + M \xrightarrow{ki} R_1$
Propagation	$R_x + M \xrightarrow{kp} R_{x+1}$
Transfer to monomer	$R_x + M \xrightarrow{ktm} P_x + R_1$
Transfer to polymer	$R_x + P_y \xrightarrow{ktp} P_x + R_y$
	$R_y + P_x \xrightarrow{ktp} P_y + R_x$
Termination by disproportionation	$R_x + R_y \xrightarrow{ktd} P_x + P_y$
Termination by combination	$R_x + R_y \xrightarrow{ktc} P_{x+y}$
Inhibition	$R_x + Z \xrightarrow{kz} P_x + Z^*$

Before performing the radical balances, it is necessary to define the moments of a polymer molecular mass distribution (MMD). The κ^{th} order moment of living and dead polymer radicals is given by Equations A.1 and A.2, respectively.

$$\lambda_\kappa = \sum_{x=1}^{\infty} x^\kappa R_x \tag{A.1}$$

$$\mu_\kappa = \sum_{y=1}^{\infty} y^\kappa P_y \tag{A.2}$$

These definitions allow the representation of the distributions of living and dead polymer radicals in terms of the statistical moments.

A.1 Living Polymer Balances

For the living polymer radicals it is necessary to perform two balances. One for the radicals with a single monomer molecule and another for the remaining radicals:

$$\begin{aligned}\frac{dR_1}{dt} &= 2fkdI - kp\frac{M}{V}\frac{R_1}{V}V - k_z\frac{Z}{V}\frac{R_1}{V}V + ktm\frac{M}{V}\left(\sum_{i=1}^{\infty}\frac{R_x}{V} - \frac{R_1}{V}\right)V \\ &+ ktp\left(\frac{P_1}{V}\sum_{y=1}^{\infty}\frac{R_y}{V} - \frac{R_1}{V}\sum_{y=1}^{\infty} y\frac{P_y}{V}\right)V \\ &- (ktc + ktd)\frac{R_1}{V}\sum_{y=1}^{\infty}\frac{R_y}{V}V\end{aligned} \tag{A.3}$$

$$\begin{aligned}\frac{dR_x}{dt} &= kp\frac{M}{V}\left(\frac{R_{x-1}}{V} - \frac{R_x}{V}\right)V - kz\frac{Z}{V}\frac{R_1}{V}V - ktm\frac{M}{V}\frac{R_x}{V}V \\ &+ ktp\left(x\frac{P_x}{V}\sum_{y=1}^{\infty}\frac{R_y}{V} - \frac{R_x}{V}\sum_{y=1}^{\infty} y\frac{P_y}{V}\right)V \\ &- (ktc + ktd)\frac{R_x}{V}\sum_{y=1}^{\infty}\frac{R_y}{V}V, \quad x > 1\end{aligned} \tag{A.4}$$

By deriving Equation A.1 with respect to time, we obtain:

$$\frac{d\lambda_\kappa}{dt} = \frac{d\left(\sum_{x=1}^{\infty} x^\kappa R_x\right)}{dt} = \sum_{x=1}^{\infty} x^\kappa \frac{dR_x}{dt} = \frac{dR_1}{dt} + \sum_{x=2}^{\infty} x^\kappa \frac{dR_x}{dt} \tag{A.5}$$

By substituting Equations A.3 and A.4 in Equation A.5 and grouping the similar terms one can write:

$$\begin{aligned}
\frac{d\lambda_\kappa}{dt} &= 2fkdI - kz\frac{Z}{V}\left(\frac{R_1}{V} + \sum_{x=2}^{\infty} x^\kappa \frac{R_x}{V}\right)V + kp\frac{M}{V}\left(\sum_{x=2}^{\infty} x^\kappa \frac{R_{x-1}}{V} - \sum_{x=2}^{\infty} x^\kappa \frac{R_x}{V} - \frac{R_1}{V}\right)V \\
&+ ktm\frac{M}{V}\left(\sum_{x=1}^{\infty} \frac{R_x}{V} - \frac{R_1}{V} - \sum_{x=2}^{\infty} x^\kappa \frac{R_x}{V}\right)V \\
&+ ktp\left(\frac{P_1}{V}\sum_{y=1}^{\infty}\frac{R_y}{V} - \frac{R_1}{V}\sum_{y=1}^{\infty} y\frac{P_y}{V} + \sum_{x=2}^{\infty} x^{\kappa+1}\frac{P_x}{V}\sum_{y=1}^{\infty}\frac{R_y}{V} - \sum_{x=2}^{\infty} x^\kappa \frac{R_x}{V}\sum_{y=1}^{\infty} y\frac{P_y}{V}\right)V \\
&- (ktc + ktd)\left(\frac{R_1}{V}\sum_{y=1}^{\infty}\frac{R_y}{V} + \sum_{x=2}^{\infty} x^\kappa \frac{R_x}{V}\sum_{y=1}^{\infty}\frac{R_y}{V}\right)V
\end{aligned} \tag{A.6}$$

Now, it becomes necessary to represent each term in Equation A.6 in terms of the moments.

Term that multiplies kp

By performing a simple change of variables, summing the negative terms and applying the binomial theorem it can be easily shown that:

$$\begin{aligned}
\sum_{x=2}^{\infty} x^\kappa \frac{R_{x-1}}{V} - \sum_{x=2}^{\infty} x^\kappa \frac{R_x}{V} - \frac{R_1}{V} &= \sum_{x=1}^{\infty}(x+1)^\kappa \frac{R_x}{V} - \sum_{x=1}^{\infty} x^\kappa \frac{R_x}{V} \\
&= \sum_{x=1}^{\infty}\sum_{r=0}^{\kappa}\binom{\kappa}{r} x^{\kappa-r}\frac{R_x}{V} - \sum_{x=1}^{\infty} x^\kappa \frac{R_x}{V} \\
&= \sum_{r=0}^{\kappa}\left[\binom{\kappa}{r}\frac{\lambda_{\kappa-r}}{V}\right] - \frac{\lambda_\kappa}{V}
\end{aligned} \tag{A.7}$$

Term that multiplies ktm

$$\begin{aligned}
\sum_{x=1}^{\infty}\frac{R_x}{V} - \frac{R_1}{V} - \sum_{x=2}^{\infty} x^\kappa \frac{R_x}{V} &= \sum_{x=1}^{\infty}\frac{R_x}{V} - \sum_{x=1}^{\infty} x^\kappa \frac{R_x}{V} \\
&= \frac{\lambda_0}{V} - \frac{\lambda_\kappa}{V}
\end{aligned} \tag{A.8}$$

Term that multiplies ktp

$$\frac{P_1}{V}\sum_{y=1}^{\infty}\frac{R_y}{V}-\frac{R_1}{V}\sum_{y=1}^{\infty}y\frac{P_y}{V}+\sum_{x=2}^{\infty}x^{\kappa+1}\frac{P_x}{V}\sum_{y=1}^{\infty}\frac{R_y}{V}-\sum_{x=2}^{\infty}x^{\kappa}\frac{R_x}{V}\sum_{y=1}^{\infty}y\frac{P_y}{V}=$$
$$=\sum_{y=1}^{\infty}\frac{R_y}{V}\left(\frac{P_1}{V}+\sum_{x=2}^{\infty}x^{\kappa+1}\frac{P_x}{V}\right)-\sum_{y=1}^{\infty}y\frac{P_y}{V}\left(\frac{R_1}{V}+\sum_{x=2}^{\infty}x^{\kappa}\frac{R_x}{V}\right)$$
$$=\sum_{y=1}^{\infty}\frac{R_y}{V}\sum_{x=1}^{\infty}x^{\kappa+1}\frac{P_x}{V}-\sum_{y=1}^{\infty}y\frac{P_y}{V}\sum_{x=1}^{\infty}x^{\kappa}\frac{R_x}{V}$$
$$=\frac{\lambda_0}{V}\frac{\mu_{\kappa+1}}{V}-\frac{\mu_1}{V}\frac{\lambda_\kappa}{V} \tag{A.9}$$

Term that multiplies (ktc + ktd)

$$\frac{R_1}{V}\sum_{y=1}^{\infty}\frac{R_y}{V}+\sum_{x=2}^{\infty}x^{\kappa}\frac{R_x}{V}\sum_{y=1}^{\infty}\frac{R_y}{V}=\sum_{y=1}^{\infty}\frac{R_y}{V}\left(\frac{R_1}{V}+\sum_{x=2}^{\infty}x^{\kappa}\frac{R_x}{V}\right)$$
$$=\sum_{y=1}^{\infty}\frac{R_y}{V}\sum_{x=1}^{\infty}x^{\kappa}\frac{R_x}{V}=\frac{\lambda_0}{V}\frac{\lambda_\kappa}{V} \tag{A.10}$$

Term that multiplies kz

$$\frac{R_1}{V}+\sum_{x=2}^{\infty}x^{\kappa}\frac{R_x}{V}=\sum_{x=1}^{\infty}x^{\kappa}\frac{R_x}{V}=\frac{\lambda_\kappa}{V} \tag{A.11}$$

By substituting Equations A.7 through A.11 into Equation A.6, we obtain:

$$\frac{d\lambda_\kappa}{dt}=2fkdI+kp\frac{M}{V}\left(\sum_{r=0}^{\kappa}\left[\binom{\kappa}{r}\frac{\lambda_{\kappa-r}}{V}\right]-\frac{\lambda_\kappa}{V}\right)V+ktm\frac{M}{V}\left(\frac{\lambda_0}{V}-\frac{\lambda_\kappa}{V}\right)V$$
$$+ktp\left(\frac{\lambda_0}{V}\frac{\mu_{\kappa+1}}{V}-\frac{\mu_1}{V}\frac{\lambda_\kappa}{V}\right)V-(ktc+ktd)\frac{\lambda_0}{V}\frac{\lambda_\kappa}{V}V-kz\frac{Z}{V}\frac{\lambda_\kappa}{V}V \tag{A.12}$$

A.2 Dead Polymer Balances

Similarly to the living polymer balances, it is necessary to perform the dead polymer balance

$$\frac{dP_x}{dt}=ktm\frac{M}{V}\frac{R_x}{V}V+ktp\left(\frac{R_x}{V}\sum_{y=1}^{\infty}y\frac{P_y}{V}-x\frac{P_x}{V}\sum_{y=1}^{\infty}\frac{R_y}{V}\right)V+ktd\frac{R_x}{V}\sum_{y=1}^{\infty}\frac{R_y}{V}V$$
$$+\frac{1}{2}ktc\sum_{y=1}^{\infty}\frac{R_y}{V}\frac{R_{x-y}}{V}V \tag{A.13}$$

By applying the definition of dead polymer moments:

$$\frac{d\mu_\kappa}{dt} = ktm\frac{M}{V}\sum_{x=1}^{\infty} x^\kappa \frac{R_x}{V}V + ktp\left(\sum_{x=1}^{\infty} x^\kappa \frac{R_x}{V}\sum_{y=1}^{\infty} y\frac{P_y}{V} - \sum_{x=1}^{\infty} x^{\kappa+1}\frac{P_x}{V}\sum_{y=1}^{\infty}\frac{R_y}{V}\right)V$$
$$+ ktd\sum_{x=1}^{\infty} x^\kappa \frac{R_x}{V}\sum_{y=1}^{\infty}\frac{R_y}{V}V + \frac{1}{2}ktc\sum_{x=2}^{\infty} x^\kappa \sum_{y=1}^{\infty}\frac{R_y}{V}\frac{R_{x-y}}{V}V \tag{A.14}$$

In Equation A.14, all the terms except the one that multiplies ktc are explicit definitions of moments. In order to express the term that multiplies ktc in terms of moments, it is helpful to use auxiliary tables when $\kappa = 0, 1, 2$ to calculate the 0^{th}, 1^{st} and 2^{nd} order moments, respectively. These moments will be enough to represent the averages of the MMD.

For $\kappa = 0$, Tale A.1 will be useful to find a closed form of the double summation below:

$$\sum_{x=2}^{\infty}\sum_{x=1}^{\infty}\frac{R_y}{V}\frac{R_{x-y}}{V}$$

Table A.2: Auxiliary table[1], $\kappa = 0$.

	$y=1$	$y=2$	$y=3$	$y=4$	$y=5$	...	$y=n$
$x=2$	R_1R_1						
$x=3$	R_1R_2	R_2R_1					
$x=4$	R_1R_3	R_2R_2	R_3R_1				
$x=5$	R_1R_4	R_2R_3	R_3R_2	R_4R_1			
$x=6$	R_1R_5	R_2R_4	R_3R_3	R_4R_2	R_5R_1		
$\vdots$	$\vdots$	$\vdots$	$\vdots$	$\vdots$	$\vdots$		
$x=m$	R_1R_{m-1}	R_2R_{m-2}	R_3R_{m-3}	R_4R_{m-4}	R_5R_{m-5}	...	R_nR_{m-n}

[1] The V in the denominator was omitted to for the sake of simplicity.

By summing the terms in the columns and then adding them up, we get:

$$\sum_{x=2}^{\infty}\sum_{x=1}^{\infty}\frac{R_y}{V}\frac{R_{x-y}}{V} = \frac{R_1}{V}\frac{\lambda_0}{V} + \frac{R_2}{V}\frac{\lambda_0}{V} + \frac{R_3}{V}\frac{\lambda_0}{V} + \frac{R_4}{V}\frac{\lambda_0}{V} + \frac{R_5}{V}\frac{\lambda_0}{V} + ... = \frac{\lambda_0}{V}\frac{\lambda_0}{V} \tag{A.15}$$

Substituting this result in Equation A.14 with $\kappa = 0$, we obtain:

$$\frac{d\mu_0}{dt} = ktm\frac{M}{V}\frac{\lambda_0}{V}V + \left(ktd + \frac{ktc}{2}\right)\frac{\lambda_0}{V}\frac{\lambda_0}{V}V \tag{A.16}$$

Similarly, for $\kappa = 1$, we have:

$$\sum_{x=2}^{\infty} x \sum_{x=1}^{\infty}\frac{R_y}{V}\frac{R_{x-y}}{V}$$

Table A.3: Auxiliary table, $\kappa = 1$

	$y=1$	$y=2$	$y=3$	$y=4$	$y=5$	...	$y=n$
$x=2$	$2R_1R_1$						
$x=3$	$3R_1R_2$	$3R_2R_1$					
$x=4$	$4R_1R_3$	$4R_2R_2$	$4R_3R_1$				
$x=5$	$5R_1R_4$	$5R_2R_3$	$5R_3R_2$	$5R_4R_1$			
$x=6$	$6R_1R_5$	$6R_2R_4$	$6R_3R_3$	$6R_4R_2$	$6R_5R_1$		
$\vdots$	$\vdots$	$\vdots$	$\vdots$	$\vdots$	$\vdots$		
$x=m$	mR_1R_{m-1}	mR_2R_{m-2}	mR_3R_{m-3}	mR_4R_{m-4}	mR_5R_{m-5}	...	mR_nR_{m-n}

$$\sum_{x=2}^{\infty} x \sum_{x=1}^{\infty} \frac{R_y}{V}\frac{R_{x-y}}{V} = \frac{R_1}{V}\left(2\frac{R_1}{V} + 3\frac{R_2}{V} + 4\frac{R_3}{V} + 5\frac{R_4}{V} + 6\frac{R_5}{V} + ...\right) +$$
$$\frac{R_2}{V}\left(3\frac{R_1}{V} + 4\frac{R_2}{V} + 5\frac{R_3}{V} + 6\frac{R_4}{V} + ...\right) +$$
$$\frac{R_3}{V}\left(4\frac{R_1}{V} + 5\frac{R_2}{V} + 6\frac{R_3}{V} + ...\right) +$$
$$\frac{R_4}{V}\left(5\frac{R_1}{V} + 6\frac{R_2}{V} + ...\right) +$$
$$\frac{R_5}{V}\left(6\frac{R_1}{V} + ...\right)$$
$$= \sum_{y=1}^{\infty} \frac{R_y}{V} \sum_{x=1}^{\infty} \left(x\frac{R_x}{V} + y\frac{R_x}{V}\right)$$
$$= \sum_{y=1}^{\infty} \frac{R_y}{V} \left[\sum_{x=1}^{\infty} x\frac{R_x}{V} + \sum_{x=1}^{\infty} y\frac{R_x}{V}\right]$$
$$= \sum_{y=1}^{\infty} \frac{R_y}{V} \left[\frac{\lambda_1}{V} + y\sum_{x=1}^{\infty} \frac{R_x}{V}\right]$$
$$= \frac{\lambda_1}{V}\sum_{y=1}^{\infty} \frac{R_y}{V} + \sum_{y=1}^{\infty} y\frac{R_y}{V}\sum_{x=1}^{\infty} \frac{R_x}{V}$$
$$= \frac{\lambda_1}{V}\frac{\lambda_0}{V} + \frac{\lambda_1}{V}\frac{\lambda_0}{V} = 2\frac{\lambda_1}{V}\frac{\lambda_0}{V} \tag{A.17}$$

By substituting this result in Equation A.14 with $\kappa = 1$, we obtain:

$$\frac{d\mu_1}{dt} = ktm\frac{M}{V}\frac{\lambda_1}{V}V + ktp\left(\frac{\lambda_1}{V}\frac{\mu_1}{V} - \frac{\lambda_0}{V}\frac{\mu_2}{V}\right)V + (ktc + ktd)\frac{\lambda_0}{V}\frac{\lambda_1}{V} \tag{A.18}$$

Finally, for $\kappa = 2$:

$$\sum_{x=2}^{\infty} x^2 \sum_{x=1}^{\infty} \frac{R_y}{V}\frac{R_{x-y}}{V}$$

Table A.4: Auxiliary table, $\kappa = 2$.

	$y=1$	$y=2$	$y=3$	$y=4$	$y=5$	...	$y=n$
$x=2$	$2^2R_1R_1$						
$x=3$	$3^2R_1R_2$	$3^2R_2R_1$					
$x=4$	$4^2R_1R_3$	$4^2R_2R_2$	$4^2R_3R_1$				
$x=5$	$5^2R_1R_4$	$5^2R_2R_3$	$5^2R_3R_2$	$5^2R_4R_1$			
$x=6$	$6^2R_1R_5$	$6^2R_2R_4$	$6^2R_3R_3$	$6^2R_4R_2$	$6^2R_5R_1$		
$\vdots$	$\vdots$	$\vdots$	$\vdots$	$\vdots$	$\vdots$		
$x=m$	$m^2R_1R_{m-1}$	$m^2R_2R_{m-2}$	$m^2R_3R_{m-3}$	$m^2R_4R_{m-4}$	$m^2R_5R_{m-5}$	...	$m^2R_6R_{m-n}$

$$\begin{aligned}
\sum_{x=2}^{\infty} x^2 \sum_{x=1}^{\infty} \frac{R_y}{V}\frac{R_{x-y}}{V} &= \frac{R_1}{V}\left(2^2\frac{R_1}{V} + 3^2\frac{R_2}{V} + 4^2\frac{R_3}{V} + 5^2\frac{R_4}{V} + 6^2\frac{R_5}{V} + ...\right) + \\
&\quad \frac{R_2}{V}\left(3^2\frac{R_1}{V} + 4^2\frac{R_2}{V} + 5^2\frac{R_3}{V} + 6^2\frac{R_4}{V} + ...\right) + \\
&\quad \frac{R_3}{V}\left(4^2\frac{R_1}{V} + 5^2\frac{R_2}{V} + 6^2\frac{R_3}{V} + ...\right) + \\
&\quad \frac{R_4}{V}\left(5^2\frac{R_1}{V} + 6^2\frac{R_2}{V} + ...\right) + \\
&\quad \frac{R_5}{V}\left((6^2\frac{R_1}{V} + ...\right) \\
&= \sum_{y=1}^{\infty}\frac{R_y}{V}\sum_{x=1}^{\infty}(y+x)^2\frac{R_x}{V} \\
&= \sum_{y=1}^{\infty}\frac{R_y}{V}\sum_{x=1}^{\infty}(x^2+2xy+y^2)\frac{R_x}{V} \\
&= \sum_{y=1}^{\infty}\frac{R_y}{V}\left[\sum_{x=1}^{\infty}x^2\frac{R_x}{V} + y\sum_{x=1}^{\infty}2x\frac{R_x}{V} + y^2\sum_{x=1}^{\infty}\frac{R_x}{V}\right] \\
&= \sum_{y=1}^{\infty}\frac{R_y}{V}\left[\frac{\lambda_2}{V} + 2y\frac{\lambda_1}{V} + y^2\frac{\lambda_0}{V}\right] \\
&= \lambda_2\sum_{y=1}^{\infty}R_y + 2\lambda_1\sum_{y=1}^{\infty}y\frac{R_y}{V} + \frac{\lambda_0}{V}\sum_{y=1}^{\infty}y^2\frac{R_y}{V} \\
&= \frac{\lambda_2}{V}\frac{\lambda_0}{V} + 2\frac{\lambda_1}{V}\frac{\lambda_1}{V} + \frac{\lambda_0}{V}\frac{\lambda_2}{V} = 2\frac{\lambda_0}{V}\frac{\lambda_2}{V} + 2\frac{\lambda_1}{V}\frac{\lambda_1}{V}
\end{aligned} \tag{A.19}$$

$$\frac{d\mu_2}{dt} = ktm\frac{M}{V}\frac{\lambda_2}{V}V + ktp\left(\frac{\lambda_2}{V}\frac{\mu_1}{V} - \frac{\mu_3}{V}\frac{\lambda_0}{V}\right) + ktc\left(\frac{\lambda_0}{V}\frac{\lambda_2}{V} + \frac{\lambda_1}{V}\frac{\lambda_1}{V}\right) + ktd\frac{\lambda_0}{V}\frac{\lambda_2}{V} \tag{A.20}$$

References

Kiparissides, C.; Daskalakis, G.; Achilias, D.S.; Sidiropoulou, E. Dynamic Simulation of Industrial Poly(vinyl chloride) Batch Suspension Polymerization Reactors. Industrial and Engineering Chemistry Research, 36, 1253-1267, 1997.

Mastan, E.; Zhu, S. Method of Moments: A Versatile Tool for Deterministic Modeling of Polymerization Kinetics. European Polymer Journal, 68, 139-16-, 2015.

Appendix B

Output Flow Rate: Vinyl Acetate Polymerization

The volume change of each tank can be represented as:

$$\frac{dV_n}{dt} = \frac{MM_m}{\rho_m}\frac{dM_n}{dt} + \frac{MM_m}{\rho_p}\frac{dP_n}{dt} + \frac{MM_w}{\rho_w}\frac{dW_n}{dt} \tag{B.1}$$

By imposing that $dV_n/dt = 0$ and substituting the mass balances, we obtain:

$$\begin{aligned}
0 =& \frac{MM_m}{\rho_m}\left(m_m\phi(n) + F^1_{n-1}\frac{M^1_{n-1}}{V^1_{n-1}}(1-\phi(n)) + F^1_{b,n+1}\frac{M^1_{n+1}}{V^1_{n+1}}(1-\phi(k-n+1))\right.\\
&\left. -F^1_n\frac{M^1_n}{V^1_n} - F^1_{b,n}\frac{M^1_n}{V^1_n}(1-\phi(n)) - kp(T_n)\frac{M^1_n}{V^1_n}\frac{\lambda^1_{0,n}}{V^1_n}V^1_n\right)\\
&+ \frac{MM_m}{\rho_m}\left(F^2_{n-1}\frac{M^2_{n-1}}{V^2_{n-1}}(1-\phi(n)) + F^2_{b,n+1}\frac{M^2_{n+1}}{V^2_{n+1}}(1-\phi(k-n+1))\right.\\
&\left. -F^2_n\frac{M^2_n}{V^2_n} - F^2_{b,n}\frac{M^2_n}{V^2_n}(1-\phi(n))\right)\\
&+ \frac{MM_w}{\rho_w}\left(m_w\phi(n) + F^2_{n-1}\frac{W^2_{n-1}}{V^2_{n-1}}(1-\phi(n)) + F^2_{b,n+1}\frac{W^2_{n+1}}{V^2_{n+1}}(1-\phi(k-n+1))\right.\\
&\left. -F^2_n\frac{W^2_n}{V^2_n} - F^2_{b,n}\frac{W^2_n}{V^2_n}(1-\phi(n))\right)\\
&+ \frac{MM_m}{\rho_p}\left(m_p\phi(n) + F^1_{n-1}\frac{P^1_{n-1}}{V^1_{n-1}}(1-\phi(n)) + F^1_{b,n+1}\frac{P^1_{n+1}}{V^1_{n+1}}(1-\phi(k-n+1))\right.\\
&\left. -F^1_n\frac{P^1_n}{V^1_n} - F^1_{b,n}\frac{P^1_n}{V^1_n}(1-\phi(n)) + k_p(T_n)\frac{M^1_n}{V^1_n}\frac{\lambda^1_{0,n}}{V^1_n}V^1_n\right)
\end{aligned} \tag{B.2}$$

$$
\begin{aligned}
0 = & \left(m_m \frac{MM_m}{\rho_m} + m_p \frac{MM_m}{\rho_p} + m_w \frac{MM_w}{\rho_w} \right) \phi(n) \\
& + F^1_{n-1} \left(\frac{MM_m}{\rho_m} \frac{M^1_{n-1}}{V^1_{n-1}} + \frac{MM_m}{\rho_p} \frac{P^1_{n-1}}{V^1_{n-1}} \right) (1 - \phi(n)) \\
& + F^1_{b,n+1} \left(\frac{MM_m}{\rho_m} \frac{M^1_{n+1}}{V^1_{n+1}} + \frac{MM_m}{\rho_p} \frac{P^1_{n+1}}{V^1_{n+1}} \right) (1 - \phi(k-n+1)) \\
& - F^1_n \left(\frac{MM_m}{\rho_m} \frac{M^1_n}{V^1_n} + \frac{MM_m}{\rho_p} \frac{P^1_n}{V^1_n} \right) \\
& - F^1_{b,n} \left(\frac{MM_m}{\rho_m} \frac{M^1_n}{V^1_n} + \frac{MM_m}{\rho_p} \frac{P^1_n}{V^1_n} \right) (1 - \phi(n)) \\
& + F^2_{n-1} \left(\frac{MM_m}{\rho_m} \frac{M^2_{n-1}}{V^2_{n-1}} + \frac{MM_w}{\rho_w} \frac{W^2_{n-1}}{V^2_{n-1}} \right) (1 - \phi(n)) \\
& + F^2_{b,n+1} \left(\frac{MM_m}{\rho_m} \frac{M^2_{n+1}}{V^2_{n+1}} + \frac{MM_w}{\rho_w} \frac{W^2_{n+1}}{V^2_{n+1}} \right) (1 - \phi(k-n+1)) \\
& - F^2_n \left(\frac{MM_m}{\rho_m} \frac{M^2_n}{V^2_n} + \frac{MM_w}{\rho_w} \frac{W^2_n}{V^2_n} \right) \\
& - F^2_{b,n} \left(\frac{MM_m}{\rho_m} \frac{M^2_n}{V^1_n} + \frac{MM_w}{\rho_w} \frac{W^2_n}{V^2_n} \right) (1 - \phi(n)) \\
& - k_p(T_n) \frac{M^1_n}{V^1_n} \frac{\lambda^1_{0,n}}{V^1_n} V^1_n \left(\frac{MM_m}{\rho_m} - \frac{MM_m}{\rho_p} \right)
\end{aligned} \tag{B.3}
$$

By defining:

$$
\alpha_n = \frac{MM_m}{\rho_m} \frac{M^1_n}{V^1_n} + \frac{MM_m}{\rho_p} \frac{P^1_n}{V^1_n} \tag{B.4}
$$

$$
\beta_n = \frac{MM_m}{\rho_m} \frac{M^2_n}{V^2_n} + \frac{MM_m}{\rho_w} \frac{W^2_n}{V^2_n} \tag{B.5}
$$

$$
\gamma_n = k_p(T_n) \frac{M^1_n}{V^1_n} \frac{\lambda^1_{0,n}}{V^1_n} V^1_n \left(\frac{MM_m}{\rho_m} - \frac{MM_m}{\rho_p} \right) \tag{B.6}
$$

$$
\Phi^1_n = \frac{V^1_n}{V_n} \tag{B.7}
$$

$$
\Phi^2_n = \frac{V^2_n}{V_n} \tag{B.8}
$$

$$F_n^1 = \Phi_n^1 F_n \tag{B.9}$$

$$F_n^2 = \Phi_n^2 F_n \tag{B.10}$$

Substituting into Equation B.3:

$$\begin{aligned}
0 = &\left(m_m \frac{MM_m}{\rho_m} + m_p \frac{MM_m}{\rho_p} + m_w \frac{MM_w}{\rho_w} \right) \phi(n) \\
&+ \Phi_{n-1}^1 F_{n-1}^1 \alpha_{n-1} \left(1 - \phi(n)\right) + \Phi_{n+1}^1 F_{b,n+1}^1 \alpha_{n+1} \left(1 - \phi(k-n+1)\right) \\
&- \Phi_n^1 F_n^1 \alpha_n - \Phi_n^1 F_{b,n}^1 \alpha_n \left(1 - \phi(n)\right) \\
&+ \Phi_{n-1}^2 F_{n-1}^2 \beta_{n-1} \left(1 - \phi(n)\right) + \Phi_{n+1}^2 F_{b,n+1}^2 \beta_{n+1} \left(1 - \phi(k-n+1)\right) \\
&- \Phi_n^2 F_n^2 \beta_n - \Phi_n^2 F_{b,n}^2 \beta_n \left(1 - \phi(n)\right) - \gamma_n
\end{aligned} \tag{B.11}$$

Finally, we obtain:

$$\begin{aligned}
F_n = &\left(\Phi_n^1 \alpha_n + \Phi_n^2 \beta_n \right)^{-1} \left[\left(m_m \frac{MM_m}{\rho_m} + m_p \frac{MM_m}{\rho_p} + m_w \frac{MM_w}{\rho_w} \right) \right. \\
&+ F_{n-1} \left(\Phi_{n-1}^1 \alpha_{n-1} + \Phi_{n-1}^2 \beta_{n-1} \right) \left(1 - \phi(n)\right) \\
&+ F_{b,n+1} \left(\Phi_{n+1}^1 \alpha_{n+1} + \Phi_{n+1}^2 \beta_{n+1} \right) \left(1 - \phi(k-n+1)\right) \\
&\left. - F_b \left(\Phi_n^1 \alpha_n + \Phi_n^2 \beta_n \right) \left(1 - \phi(n)\right) - \gamma_n \right]
\end{aligned} \tag{B.12}$$

Appendix C

Output Flow Rate: Vinyl Chloride Polymerization

The volume change of each tank can be represented as:

$$\frac{dV_n}{dt} = \frac{MM_m}{\rho_m}\frac{dM_n}{dt} + \frac{MM_m}{\rho_p}\frac{dP_n}{dt} + \frac{MM_w}{\rho_w}\frac{dW_n}{dt} \tag{C.1}$$

By imposing that $dV_n/dt = 0$ and substituting the mass balances, we obtain:

$$\begin{aligned}
0 =& \frac{MM_m}{\rho_m}\left(m_m\phi(n) + F^1_{n-1}\frac{M^1_{n-1}}{V^1_{n-1}}\left(1-\phi(n)\right) + F^1_{b,n+1}\frac{M^1_{n+1}}{V^1_{n+1}}\left(1-\phi(k-n+1)\right)\right.\\
&\left. -F^1_n\frac{M^1_n}{V^1_n} - F^1_{b,n}\frac{M^1_n}{V^1_n}\left(1-\phi(n)\right) - k^1_p(T_n)\frac{M^1_n}{V^1_n}\frac{\lambda^1_{0,n}}{V^1_n}V^1_n\right)\\
&+ \frac{MM_m}{\rho_m}\left(F^2_{n-1}\frac{M^2_{n-1}}{V^2_{n-1}}\left(1-\phi(n)\right) + F^2_{b,n+1}\frac{M^2_{n+1}}{V^2_{n+1}}\left(1-\phi(k-n+1)\right)\right.\\
&\left. -F^2_n\frac{M^2_n}{V^2_n} - F^2_{b,n}\frac{M^2_n}{V^2_n}\left(1-\phi(n)\right) - k^2_p(T_n)\frac{M^2_n}{V^2_n}\frac{\lambda^2_{0,n}}{V^2_n}V^2_n\right)\\
&+ \frac{MM_m}{\rho_m}\left(F^3_{n-1}\frac{M^3_{n-1}}{V^3_{n-1}}\left(1-\phi(n)\right) + F^3_{b,n+1}\frac{M^3_{n+1}}{V^3_{n+1}}\left(1-\phi(k-n+1)\right)\right.\\
&\left. -F^3_n\frac{M^3_n}{V^3_n} - F^3_{b,n}\frac{M^3_n}{V^3_n}\left(1-\phi(n)\right)\right)\\
&+ \frac{MM_w}{\rho_w}\left(m_w\phi(n) + F^2_{n-1}\frac{W^3_{n-1}}{V^3_{n-1}}\left(1-\phi(n)\right) + F^3_{b,n+1}\frac{W^3_{n+1}}{V^3_{n+1}}\left(1-\phi(k-n+1)\right)\right.\\
&\left. -F^3_n\frac{W^3_n}{V^3_n} - F^3_{b,n}\frac{W^3_n}{V^3_n}\left(1-\phi(n)\right)\right)
\end{aligned}$$

$$+\frac{MM_m}{\rho_p}\left(m_p\phi(n)+F^2_{n-1}\frac{P^2_{n-1}}{V^1_{n-1}}\left(1-\phi(n)\right)+F^2_{b,n+1}\frac{P^2_{n+1}}{V^2_{n+1}}\left(1-\phi(k-n+1)\right)\right.$$
$$\left.-F^2_n\frac{P^2_n}{V^2_n}-F^2_{b,n}\frac{P^2_n}{V^2_n}\left(1-\phi(n)\right)+k^2_p(T_n)\frac{M^2_n}{V^2_n}\frac{\lambda^2_{0,n}}{V^2_n}V^2_n++k^1_p(T_n)\frac{M^1_n}{V^1_n}\frac{\lambda^1_{0,n}}{V^1_n}V^1_n\right) \tag{C.2}$$

$$\begin{aligned}
0=&\left(m_m\frac{MM_m}{\rho_m}+m_p\frac{MM_m}{\rho_p}+m_w\frac{MM_w}{\rho_w}\right)\phi(n)\\
&+F^1_{n-1}\left(\frac{MM_m}{\rho_m}\frac{M^1_{n-1}}{V^1_{n-1}}\right)\left(1-\phi(n)\right)+F^1_{b,n+1}\left(\frac{MM_m}{\rho_m}\frac{M^1_{n+1}}{V^1_{n+1}}\right)\left(1-\phi(k-n+1)\right)\\
&-F^1_n\left(\frac{MM_m}{\rho_m}\frac{M^1_n}{V^1_n}\right)-F^1_{b,n}\left(\frac{MM_m}{\rho_m}\frac{M^1_n}{V^1_n}\right)\left(1-\phi(n)\right)\\
&+F^2_{n-1}\left(\frac{MM_m}{\rho_m}\frac{M^2_{n-1}}{V^2_{n-1}}+\frac{MM_m}{\rho_p}\frac{P^2_{n-1}}{V^2_{n-1}}\right)\left(1-\phi(n)\right)\\
&+F^2_{b,n+1}\left(\frac{MM_m}{\rho_m}\frac{M^2_{n+1}}{V^2_{n+1}}+\frac{MM_m}{\rho_p}\frac{P^2_{n+1}}{V^2_{n+1}}\right)\left(1-\phi(k-n+1)\right)\\
&-F^2_n\left(\frac{MM_m}{\rho_m}\frac{M^2_n}{V^2_n}+\frac{MM_m}{\rho_p}\frac{P^2_n}{V^2_n}\right)\\
&-F^2_{b,n}\left(\frac{MM_m}{\rho_m}\frac{M^2_n}{V^2_n}+\frac{MM_m}{\rho_p}\frac{P^2_n}{V^2_n}\right)\left(1-\phi(n)\right)\\
&+F^3_{n-1}\left(\frac{MM_m}{\rho_m}\frac{M^3_{n-1}}{V^3_{n-1}}+\frac{MM_w}{\rho_w}\frac{W^3_{n-1}}{V^3_{n-1}}\right)\left(1-\phi(n)\right)\\
&+F^3_{b,n+1}\left(\frac{MM_m}{\rho_m}\frac{M^3_{n+1}}{V^3_{n+1}}+\frac{MM_w}{\rho_w}\frac{W^3_{n+1}}{V^3_{n+1}}\right)\left(1-\phi(k-n+1)\right)\\
&-F^3_n\left(\frac{MM_m}{\rho_m}\frac{M^3_n}{V^3_n}+\frac{MM_w}{\rho_w}\frac{W^3_n}{V^3_n}\right)\\
&-F^3_{b,n}\left(\frac{MM_m}{\rho_m}\frac{M^3_n}{V^3_n}+\frac{MM_w}{\rho_w}\frac{W^3_n}{V^3_n}\right)\left(1-\phi(n)\right)\\
&-k^1_p(T_n)\frac{M^1_n}{V^1_n}\frac{\lambda^1_{0,n}}{V^1_n}V^1_n\left(\frac{MM_m}{\rho_m}-\frac{MM_m}{\rho_p}\right)\\
&-k^2_p(T_n)\frac{M^2_n}{V^2_n}\frac{\lambda^2_{0,n}}{V^2_n}V^2_n\left(\frac{MM_m}{\rho_m}-\frac{MM_m}{\rho_p}\right)
\end{aligned} \tag{C.3}$$

By defining:

$$\alpha_n=\frac{MM_m}{\rho_m}\frac{M^1_n}{V^1_n} \tag{C.4}$$

$$\beta_n=\frac{MM_m}{\rho_m}\frac{M^2_n}{V^2_n}+\frac{MM_m}{\rho_p}\frac{P^2_n}{V^2_n} \tag{C.5}$$

$$\gamma_n = \frac{MM_m}{\rho_m}\frac{M_n^3}{V_n^3} + \frac{MM_w}{\rho_w}\frac{W_n^3}{V_n^3} \tag{C.6}$$

$$\xi_n = \left(\frac{MM_m}{\rho_m} - \frac{MM_m}{\rho_p}\right)\left(k_p^1(T_n)\frac{M_n^1}{V_n^1}\frac{\lambda_{0,n}^1}{V_n^1}V_n^1) + k_p^2(T_n)\frac{M_n^2}{V_n^2}\frac{\lambda_{0,n}^2}{V_n^2}V_n^2\right) \tag{C.7}$$

$$F_n^1 = \Phi_n^1 F_n \tag{C.8}$$

$$F_n^2 = \Phi_n^2 F_n \tag{C.9}$$

$$F_n^3 = \Phi_n^3 F_n \tag{C.10}$$

$$\Phi_n^1 = \frac{V_n^1}{V_n} \tag{C.11}$$

$$\Phi_n^2 = \frac{V_n^2}{V_n} \tag{C.12}$$

$$\Phi_n^3 = \frac{V_n^3}{V_n} \tag{C.13}$$

Ans substituting into Equation C.3:

$$
\begin{aligned}
0 = & \left(m_m \frac{MM_m}{\rho_m} + m_p \frac{MM_m}{\rho_p} + m_w \frac{MM_w}{\rho_w} \right) \phi(n) \\
& + \Phi^1_{n-1} F^1_{n-1} \alpha_{n-1} \left(1 - \phi(n)\right) + \Phi^1_{n+1} F^1_{b,n+1} \alpha_{n+1} \left(1 - \phi(k-n+1)\right) \\
& - \Phi^1_n F^1_n \alpha_n - \Phi^1_n F^1_{b,n} \alpha_n \left(1 - \phi(n)\right) \\
& + \Phi^2_{n-1} F^2_{n-1} \beta_{n-1} \left(1 - \phi(n)\right) + \Phi^2_{n+1} F^1_{b,n+1} \beta_{n+1} \left(1 - \phi(k-n+1)\right) \\
& - \Phi^3_n F^3_n \gamma_n - \Phi^3_n F^3_{b,n} \gamma_n \left(1 - \phi(n)\right) \\
& + \Phi^3_{n-1} F^3_{n-1} \gamma_{n-1} \left(1 - \phi(n)\right) + \Phi^3_{n+1} F^3_{b,n+1} \gamma_{n+1} \left(1 - \phi(k-n+1)\right) \\
& - \Phi^3_n F^3_n \gamma_n - \Phi^3_n F^3_{b,n} \gamma_n \left(1 - \phi(n)\right) - \xi_n
\end{aligned} \tag{C.14}
$$

Lastly, we obtain:

$$
\begin{aligned}
F_n = & \left(\Phi^1_n \alpha_n + \Phi^2_n \beta_n + \Phi^3_n \gamma_n \right)^{-1} \left[\left(m_m \frac{MM_m}{\rho_m} + m_p \frac{MM_m}{\rho_p} + m_w \frac{MM_w}{\rho_w} \right) \right. \\
& + F_{n-1} \left(\Phi^1_{n-1} \alpha_{n-1} + \Phi^2_{n-1} \beta_{n-1} + \Phi^3_{n-1} \gamma_{n-1} \right) \left(1 - \phi(n)\right) \\
& + F_{b,n+1} \left(\Phi^1_{n+1} \alpha_{n+1} + \Phi^2_{n+1} \beta_{n+1} + \Phi^3_{n+1} \gamma_{n+1} \right) \left(1 - \phi(k-n+1)\right) \\
& \left. - F_b \left(\Phi^1_n \alpha_n + \Phi^2_n \beta_n + \Phi^3_n \gamma_n \right) \left(1 - \phi(n)\right) - \xi_n \right]
\end{aligned} \tag{C.15}
$$